UNIVERSITY OF MINNESOTA
ST. ANTHONY FALLS HYDRAULIC LABORATORY

Project Report No. 305

ANALYSIS AND SIMULATION OF MIXING OF STRATIFIED LAKES OR RESERVOIRS BY AIR BUBBLE PLUMES

by

Kresimir Zic

and

Heinz G. Stefan

Prepared for

LEGISLATIVE COMMISSION ON MINNESOTA RESOURCES
St. Paul, Minnesota

December 1990

Minneapolis, Minnesota

ABSTRACT

The goal of the research presented in this report is to analyze, understand, and simulate the flow field induced by a bubble plume in a lake or reservoir. This is useful and necessary for the design of lake or reservoir aeration and destratification projects. Three mathematical models were developed and laboratory experiments were performed.

Experiments similar to the ones presented here are not available in the literature but were necessary to understand the governing physical processes and to verify the mathematical models. What makes these experiments unique, in comparison with other bubble plume measurements, is the description of the entire flow field (not just the flow in vicinity of the bubble plume), the inclusion of stratified ambient water, and the evaluation of destratification over time.

The first model developed is a modified version of a dynamic 1–D mathematical model originally formulated by Goossens[1979]. The improved model is based on the research described here and is linked to a general dynamic lake model MINLAKE. It is a tool useful for lake restoration projects, particularly for evaluation of different restoration techniques.

The second model is also an integral model of a bubble plume. The flow field induced by an air bubble plume in stratified ambient water is presented in the general context of mixing mechanics of water jets and plumes.

The third model is a 2–D numerical model that gives insight into the subregions of the flow field. The 2–D model solves the Reynolds' equations by using the buoyancy–extended version of the k–ϵ model as a closure of the turbulent quantities. The effect of the bubbles in the fluid flow is modeled by imposing internal forces in the region where the air bubbles are present.

A discussion of lake aeration as an oxygen transfer technique is beyond the scope of the research described herein.

TABLE OF CONTENTS

List of Figures

List of Figures (Cont'd)

List of Figures (Cont'd)

List of Tables

1. INTRODUCTION

1.1. Lake/reservoir stratification and water quality

The presence of excessive nutrients in a lake, known as eutrophication, is a widely observed problem. Eutrophication is a natural aging process, but human activities accelerate it. Increased nutrient levels caused by the influx of domestic and industrial wastes and runoff encourage the growth of a variety of micro–organisms. These, in turn, may lead to undesirable conditions ranging from "pea soup" water to coatings of blue–green algae on the surface of a lake to the presence of unpleasant odor and taste in water supplies. Dead plants, fish, and other organic matter settle to the bottom, and become a nutrient source for oxygen consuming bacteria. As a result, oxygen deficiencies are likely in the lower water layers of a productive lake or reservoir. This may have substantial adverse effects on lake biota and general water quality [Torrest and Wen, 1976].

These problems intensify when thermal stratification occurs as is typical for lakes in the temperate regions. Strong thermal (density) gradients inhibit vertical mixing, resulting in the formation of strata in the reservoir. In summer the *epilimnion*, the upper region, contains warm water generally high in dissolved oxygen (DO) due to gas exchange with the atmosphere and photosynthesis. Below the epilimnion is a region of rapidly decreasing temperatures, called the *thermocline* or *metalimnion*. The lowest region, the *hypolimnion*, consists of cooler water which, because of low rates of exchange with the overlying, aerated water due to thermal stratification, and high oxygen demand, is often low or deficient in DO.

Monomictic lakes which mix once each year are found at the extremes of the temperate zone, in the tropical and in very cold regions. In areas where temperatures fall below 4° C in winter, there can be two periods of mixing per year. These dimictic lakes "inversely" stratify in the winter due to the fact that as water cools below 4° C, it becomes lighter.

The major significance of stratification, as far as water quality is concerned, is that the thermocline acts as a physical barrier between the epilimnion and hypolimnion. The hypolimnion is cut off from the surface, and the oxygen depleted by normal biological activities cannot be replenished. As a result, this water tends towards anoxia and its attendant water quality problems.

In some cases, the breakdown of stratification which (in dimictic lakes) occurs in the spring and fall and is called "turnover" mixes anoxic hypolimnetic waters which are high in oxygen demand throughout the reservoir, causing fishkills.

The primary goal of efforts to alleviate this problem is to increase oxygen levels throughout the water column and to eliminate anaerobic conditions.

Various restoration techniques have been developed to deal with the problems associated with eutrophication. They can be divided into two groups: methods that emphasize nutrient control (external and internal) and methods that emphasize direct control or removal of biomass [Cooke et al., 1986].

Artificial circulation (mixing), attempts to control algal biomass by reducing internal nutrient loading associated with anaerobic conditions but does not affect external loading sources. The implementation of artificial circulation has had mixed results. Negative impacts of its use include, e.g., enhancement of blue–green algae, turbidity, and even fishkills [Pastorok et al., 1980]. Although some adverse effects can be attributed to the secondary effects of the technique, others are almost certainly due to faulty design of aeration devices or their improper application following inadequate assessment of the biological community and its response mechanisms [Pastorok et al., 1982].

Various mixing devices and their applications have been reviewed in detail [Tolland, 1977; Lorenzen and Fast, 1977; Pastorok et al., 1980; Pastorok et al., 1982]. They may be pneumatic, mechanical or use buoyant water. Pneumatic devices propel water by releasing air bubbles which drag the water along with them in their ascent to the surface. Mechanical pumps and water jets induce circulation by plume entrainment and proper placement of intake–discharge locations.

The goal of the research presented here is to analyze, understand, and simulate the flow field induced by a bubble plume in a lake/reservoir to use these devices with less uncertainty. With this goal in mind, three mathematical models were developed and laboratory experiments were performed.

Experiments similar to the ones presented here are not available in the literature but were necessary to understand the governing physical processes and to verify the mathematical models. What makes these experiments unique, in comparison with other bubble plume measurements, is the description of the entire flow field (not only the flow in vicinity of the bubble plume), the inclusion of stratified ambient water, and the evaluation of destratification over time.

The first model developed is a modified dynamic 1–D mathematical model originally formulated by Goossens[1979]. The improved model, based on the research described here, is a general dynamic lake model and is intended to be a tool for lake restoration practitioners in evaluating different restoration techniques.

The second model is an integral model of the bubble plume in stratified water. It resulted from the effort to present the findings about the flow field induced by air bubble plumes in stratified ambient water in the more general context of mixing mechanics of water jets and plumes.

The third model is a 2–D air bubble mixing model that gives an insight into the subregions of the flow field which are difficult to measure in the laboratory. The 2–D model solves the Reynolds equations by using the buoyancy–extended version of the k–ϵ model as a closure of the turbulent quantities. The effect of the bubble motion in the fluid flow is modeled through the interaction of the forces in the region where the air bubbles are present.

A discussion of lake aeration as an oxygen transfer technique is beyond the scope of the research described here and can be found elsewhere [EPA, 1981; Pastorok et al., 1982; Burns and Powling, 1981; Lorenzen and Fast, 1977].

1.2. Use of air bubble plumes for destratification of lakes and reservoirs

This study deals with release of air bubbles in order to create circulation in a stratified lake or reservoir. The rising air mass generates vertical water currents which diverge horizontally upon reaching the surface. As this upwelled water is colder (denser) than the surface water it starts to plunge after initial horizontal spreading as shown in Fig. 1.1. As the process continues complete circulation can be achieved, and destratification progresses towards reaching a uniform temperature.

The release of the air can be from the end of a pipe [Bernhardt, 1967], through a horizontal perforated pipe (line diffuser) producing an "air curtain" [Knoppert et al., 1970; Fast, 1968, 1971a, 1971b; Davis, 1980], or through a single diffuser (point diffuser) producing an "air column" [Kranenburg, 1978; Goossens, 1979].

Although the expression "aeration" with air bubble plumes is commonly used, diffused air systems are not aerators but pumps. Rising bubbles produce a circulation in the lake or reservoir in such a way that thermal stratification is modified. Gas transfer from the air bubbles takes place, of course, but often represents a small fraction of the surface gas exchange induced by the plume.

1.3. Mechanics of air bubble plumes: Literature review

Plumes induced by the release of the air bubbles have a large variety of applications. They can be used to augment convective heat and mass transfer in mixing technology [Kipke, 1983]; as pneumatic barriers against density currents [Larsen, 1960]; in pneumatic breakwater applications [Baines and Hamilton, 1959]; in controlling shoaling in estuaries and harbors [Brunn, 1975]; in preventing of icing [Ashton, 1974]. A more complete list of references of applications can be found in Tekeli and Maxwell [1978].

This study deals with an air bubble plume as a source of artificial mixing for control of stratification and water quality in shallow lakes and reservoirs. References which treat the practical applications of such a device can be found in Pastorok et al. [1982], Henderson–Sellers [1984], Cooke et al. [1986].

A bubble plume can be either a two dimensional "curtain" (bubbles are released from a line diffuser) or an axisymmetric "column" (bubbles are released from a single diffuser). It has been shown that both types of a devices, "curtain" [Davis, 1980] or "column" [Goossens, 1979], can be used to destratify reservoirs.

A detailed review of the relevant literature has been given by Tekeli and Maxwell [1978], Goossens [1979], Johnson [1980], Milgram [1983], Hussain and Narang [1984], Poon [1985]. Previous work can be classified according to a few common features.

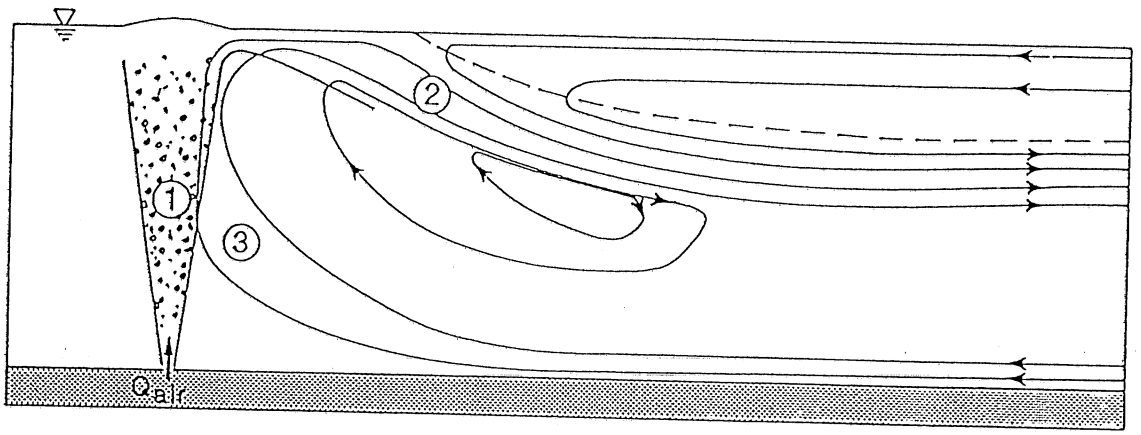

Figure 1.1 Flow field induced by an air bubble column in a stratified lake (after Goossens, 1979)

Referring to the temperature of the environment there are two groups of studies: isothermal and stratified environments. The research of Baines and Hamilton [1959], Kobus [1968, 1973], Cederwall and Ditmars [1970], Ashton [1974], Hussain and Siegel [1976], Hussain and Narang [1977], Brevik [1977], Milgram [1983], Wen and Torrest [1987], Laureshen and Rowe [1987] was conducted in isothermal environments.

On the other hand, it has been shown that the strength of the stratification has a significant influence on the bubble plume behavior [Cederwall and Ditmars, 1970; McDougall, 1978; Graham, 1978; Kranenburg, 1978; Rayyan and Speece, 1977; Hussain and Narang, 1984, Zic et Stefan, 1989a]. Asaeda and Imberger [1988] described various cases of the flow field which can occur depending on the relative strength of the bubble plume versus the ambient stratification. Zic et Stefan [1989a] showed that practical applications of air bubble systems as destratification devices belong to the group described by Asaeda and Imberger [1988] as cases with a strong air bubble plume and a relatively weak stratification. The cases with strong stratification described in the literature were obtained with saline concentration [McDougall, 1978; Kranenburg, 1978; Asaeda and Imberger, 1988].

In all the aforementioned investigations, the bubble plume has been treated separately, without effect on the environment. Goossens [1979] presented a composite model for the mixing of a lake with a bubble column which treats the bubble plume and its vicinity, the so called "nearfield". Davis [1980] proposed a method to design an air bubbles system based on the known stability (potential energy of the stratified lake minus potential energy of the well mixed one). The air bubbles system is then designed as the one which will overcome the existing stability in the lake. Zic and Stefan [1988, 1989a] modified Goossens' [1979] nearfield model and combined it with a dynamic water quality model MINLAKE [Riley and Stefan, 1987]. Similarly Patterson and Imberger [1989] combined McDougall's [1978] bubble plume model with a reservoir dynamic model DYRESM [Imberger and Patterson, 1981]. In both cases evolution of the temperature stratification in time and in response to the bubble plume and weather is being predicted.

1.3.1. *Experimental studies*

Experiments have been performed in the laboratory and in the field.

Kobus [1968] did experiments in isothermal basins 8m x 280m x 4.7m and 2m x 1m x 10m, varying the orifice size and position, with airflow rates up to 6.2×10^{-3} m^3/s at atmospheric pressure. For each airflow rate profiles of velocity versus radius were measured, and each of these was fitted with a Gaussian curve whose width and centerline velocity were chosen so as to minimize the error between the curve and the measured data. Kobus found it necessary to average his data over five minute intervals because the flow was "subject to considerable fluctuations". These fluctuations could be caused not only by local turbulence, but also by lateral wandering of the plume. If wandering did occur, the long term time–average measurements would show greater widths and smaller centerline velocities than actually existed with respect to the instantaneous locations of the wandering plume centerline; a fact which must be considered in interpreting the data.

Takeshi [1972] performed experiments in two stratified reservoirs in Japan. The smaller Shikazawa reservoir had a volume of $550x10^4m^3$ and a mean depth of 10 m. The air was conducted by a 64 mm diameter vinyl pipe to the bottom of the reservoir, 9 m below the surface. The diameter of the holes was 3.5 mm and the holes were 350 mm apart. A compressor supplied 4.6 m^3/s of air. The larger reservoir used was Ikari reservoir with a volume of $5500x10^4m^3$ and a mean depth of 17.74 m. The same equipment was used. The goal of the experiments was to control the temperature of the water released from the reservoirs. The results for two cases were found to be inconsistent. This was explained by a difference in the quantity of water flowing through the reservoirs.

Topham [1975] performed experiments with air bubble plumes in Saanich Inlet off Vancouver Island using air–nozzle depths up to 60 m and airflow rates up to 0.66 m^3/s at atmospheric pressure. Profiles of flow velocities versus radius were measured at several heights from a horizontally suspended 12 m long beam which supported 20 vertical current meters. A 6 minute average of the data from each current meter was used as the velocity at a radius equal to the distance from the beam center to the meter. Although fluctuations around mean values were large and varied substantially from test to test, the data are in qualitative agreement with data of similar scale experiments [Milgram 1983].

Rayyan and Speece [1977] used a square tank with dimensions of 1.22m x 1.22m x 2.44m. With different degrees of stratification in the tank the airflow rates used varied from $1.67x10^{-6}$ to $5.0x10^{-6}$ m^3/s. The field study was conducted in Lake Travis, near Austin, Texas, with a depth of 30 m, during the months of July and August, when the lake was stratified. Three types of air outlets, at a depth of 26.7 m, were used: open end, ceramic diffuser and PVC diffuser with airflow rates of $2.42x10^{-4}$, $1.33x10^{-4}$ and $8.33x10^{-5}$ m^3/s respectively. Temperature measurements were made with thermistors and a digital voltmeter. A dye study in the lake and replicated in the lab showed that complete uncoupling of the plume in the thermocline took place. The primary plume carrying the cold water of the hypolimnion was seen to stop in the thermocline. The bubbles continued to rise and an injection of dye immediately above the thermocline was seen to be carried all the way to the surface (secondary plume). The thermocline acted therefore as a ceiling to the rising plume.

Graham [1978] produced experiments using a vessel with a 0.127 m in diameter, depth of 0.387 m and orifice diameter of 0.476 cm. Saline solutions were used. The rather small volume of the cylinder resulted in the liquid being very agitated at high airflow rates. It was observed that the layer above the thermocline became rapidly homogeneous while material from the upper layer did not mix in the layer below the thermocline so easily.

McDougall's [1978] experiments were carried out in a Perspex tank of square horizontal cross–section 0.6x0.6 m which was normally filled to a height of approximately 1.3 m with a linearly stratified salt solution. Airflow rates of $2.5x10^{-5}$ m^3/s were introduced through a nozzle in the tank floor. Experiments showed that fluid can leave the plume and spread out horizontally, while the center of the plume, where the bubbles are concentrated, continues to rise.

Kranenburg [1978] performed a series of experiments under stratified conditions in a cylindrical tank with a radius of 5.0 m and water depths of 0.2 m and 0.3 m. Sodium chloride dissolved in tap water was used to obtain density difference. In all experiments the relative density difference was about 0.005. Compressed air was injected through a porous glass filter, 5 cm in diameter, which was mounted in the bottom. The airflow rates used were 20×10^{-6} to 253×10^{-6} m^3/s. Experiments showed that the bubble column produced by the air injection entrains hypolimnetic water from below and also water from a recirculating flow close to the surface. A radial jet at the free surface forces the less dense epilimnion to move to the point of equilibrium between the buoyancy and momentum forces where the plunging occurs. At the plunge point a part of the outflowing water mixes with epilimnetic water. A portion of the mixed water forms an interlayer of intermediate density between epilimnion and hypolimnion.

Goossens [1979] performed experiments at different scales:

a) small scale experiments in a rectangular tank 0.5m x 0.5m x 0.5m with transparent walls. A round sintered glass plate (diameter 4 cm) with pore diameter of 16 μ and 40 μ was used as distributor. Depth of the injector varied: 0.28, 0.38 and 0.48 m below the surface. The airflow rate varied from 1.4×10^{-5} m^3/s to 7.2×10^{-5} m^3/s.

b) medium scale experiments in a tank of 2.5 m in diameter, 2 m height and a maximum water depth of 1.75 m above the injector. The injector was a round glass plate (6 cm in diameter). Air flow rates varied from 2.3×10^{-4} to 9.2×10^{-4} m^3/s.

c) large scale experiments in a tank 5 m deep and 4 m in diameter; airflow rates varied from 2.3×10^{-4} m^3/s to 0.9×10^{-3} m^3/s

d) in the field – reservoir Petrusplaat, with airflow rates of 0.085, 0.17 and 0.13 m^3/s.

Experimental results agree with findings by Kranenburg [1978] described previously. Data obtained were vertical velocities versus radial distance at various depths for the vertical plume and horizontal velocities versus horizontal distance from the plume axis for the horizontal jet. In the field studies temperature profiles were measured at various locations and different times after the start of the air bubble system.

Fannelop and Sjoen [1980] conducted experiments in an isothermal laboratory basin having a width of 10.5 m and depth of 10 m using airflow rates up to 0.022 m^3/s. Fluid velocity at various points was measured, and averaged over 10 min time intervals. The actual data were fitted by Gaussian curves with a normalized standard deviation of about 5%.

Milgram and Van Houten [1982] performed experiments on bubble plumes in a 1.65 m diameter laboratory tank with a nozzle depth of 3.66 m

at airflow rates up to 0.0022 m^3/s. In addition to measuring profiles of flow speed versus radius at several heights, they also measured profiles of momentum flux and of gas fraction. Profiles of flow speed, momentum flux and gas fraction were fitted with Gaussian curves, with the standard deviation of the fits averaging about 3% of the centerline values. Special filtering of measurements was used in order to avoid the influence of the wandering of the plume.

Milgram [1983] presented experimental data obtained for an axisymmetric bubble plume in an isothermal environment. Milgram's experiments took place in Bugg Spring, which is a natural sinkhole spring located at Florida. Experiments for measuring velocity profiles were conducted with a gas outlet depth of 50 m and airflow rates up to 0.59 m^3/s.

Maruyama et al. [1984] investigated mixing by a bubble plume in comparison with a liquid jet. Four cylindrical tanks 0.3, 0.56, 0.8 and 1.04 m in inside diameter were used. The volumetric flow rate of air was varied from $1x10^{-6}$ to 0.1 m^3/s. Three nozzles were provided: two air orifices of 1 and 2.5 cm internal diameter and a 3 cm diameter sintered porous–plate sparger with a mean pore diameter of 100 μ. Mixing was studied by using a tracer response method. The results indicate that the induced liquid flow rate varies as the first power of the submergence depth of the nozzle and as the 1/3 power of both the gas flow rate and the horizontal cross–section of the tank.

Godon and Milgram [1987] carried out the experiments in a cubical tank measuring 1.22 m along each edge and in a rectangular tank with 1.18x1.22 m base dimensions and 2.44 m high. Tests were done at airflows of $3.2x10^{-4}$, $4.8x10^{-4}$, $1.1x10^{-3}$ and $2.0x10^{-3}$ m^3/s. Air was released through holes in a 12.7 mm ID perforated pipe at the bottom of the tank. They found that the mixing time is primarily governed by the gas flow rate, the plume length and the tank base dimensions; and it is quite insensitive to tank height.

Wen and Torrest [1987] studied line diffusers in isothermal tanks 0.3 m wide, 2.4 m long and 0.6 or 1.2 m high. Their work included the influence of diffuser characteristics, a wide range of aeration rates in a larger scale channel of 0.46 m width and 3.7 m length. The airflow rates were $2.55x10^{-3}$–$6.18x10^{-3}$ m^3/s. Surface velocity decay was described and the circulation cell size from the diffuser was shown to be about four times the water depth.

Asaeda and Imberger [1988] studied bubble plumes in both a linearly stratified and a two–layered ambient fluid. The experiments were carried out in a 1.0x1.0 m glass tank containing water to a depth of 0.8 m. Air bubbles were released from a bubble maker consisting of a hollow tube 2.4 cm in diameter. The airflow rates varied from $2.5x10^{-8}$ to $1.28x10^{-5}$ m^3/s for linear stratification and from $1.83x10^{-7}$ to $1.97x10^{-6}$ m^3/s for two–layered stratification. In a linearly stratified fluid, three well–defined regions of the flow were evident; the upmowed flow core consisting of a mixture of air bubbles and dense fluid, an annular downdraft, and the intrusion flow. At very large gasflow rates a single intrusion was observed. As the gas flow was

decreased, the buoyancy flux was insufficient to carry the lower fluid to the surface and multiple intrusions were observed, exiting the dowdraft region at equally spaced elevations. At very low gasflow rates the intrusions became unsteady and much less well defined. When bubbles were released in a two layered fluid, two distinct regimes were observed. For a strong stratification and a small gasflow rate the lower plume did not penetrate the interface and only entrained a little of the upper fluid before intruding in a thin layer immediately below the interface. A second plume formed in the upper layer. For the weak stratification and a large gas flow rate, the plume formed in the lower layer was able to pierce the interface, mix with the upper fluid, and rise to the surface. Once at the surface it was observed to spread out radially and then plunge back forming a thick intrusion above the interface.

Zic et al. [1989b] measured the time evolution and the surface temperature distributions in laboratory tanks up to 1.4 m depth and up to 4.5 m in diameter. The data have been analyzed to give stratified flow patterns and entrainment rates needed in unsteady one–dimensional farfield models. It has been found that the flow field follows the same pattern as described previously by Kranenburg [1979], Goossens [1979] and Asaeda and Imberger [1988].

Brown et al. [1989] measured velocity profiles with an electromagnetic probe in Upper Bear Creek reservoir. The dye concentrations measurements were performed to estimate the water flow rates. The water depth was 21 m and the reservoir had a volume of approximately 42×10^6 m^3. Two tests were made, with Q_{air} of 0.012 and 0.3 m^3/s. The velocity profiles indicated that the depth of the flow away layer was between 1.5 and 2.5 m. The estimations of the upwelled flow rates were found to be bigger than the equations by Goossens [1979] and Kobus [1968] would predict. The measurements were affected by wind.

1.3.2. *Theoretical and numerical studies*

In theoretical and numerical studies most authors used integral formulations of the conservation equations, with specific assumptions as to the form of the mean liquid velocity and gas fraction profiles (e.g. top hat or Gaussian). The key point is the treatment of entrainment in these models.

Cederwall and Ditmars [1970] developed an integral theory for bubble plumes based on the similarity with buoyant plumes extending an integral theory for single–phase buoyant plumes by Morton et al. [1956]. Abraham's [1972a] model is also based on a plume with negligible entry momentum. Abraham [1972b] extended his theory by including an energy equation for (buoyant) jets. Kobus [1968] presented a model which is similar to that of Cederwall and Ditmars [1970]. The relative bubble velocity was assumed to be negligible compared to the water velocity for small air rates and the entrainment coefficient was adjusted in terms of slip velocity in order to find an appropriate solution. A second appropriate solution was found for large air rates when the averaged bubble velocity is considered constant. Kobus' experimental data were in agreement with these two hypotheses. Hussain and Siegel [1976] treated the axisymmetric plume as a double–zoned liquid jet in which the inner zone consisted of a single row of big bubbles (with wakes) rising from a single orifice. The value of the entrainment coefficient for a

single phase jet was taken as a basis, corrected for the gas density ratio and for the relative bubble motion in the inner zone. Hussain and Narang [1977] extended this work to the two–dimensional case. McDougall [1978] proposed a double–zone model plume composed of an inner circular plume (which contains all the bubbles of gas) and an outer annular plume. Brevik [1977] used the kinetic energy equation, instead of the assumption that the rate of entrainment be proportional to the vertical center line velocity. This is a main difference from Cederwall and Ditmars' [1970] work. Wilkinson [1979] analyzed previous work and concluded that the internal structure of bubble plumes is strongly influenced by the relative importance of surface tension and buoyant forces in the region of bubble formation and flow establishment. This ratio can be expressed as a form of source Weber number. He found that at high Weber number, i.e. at high rate of airflow, the structure of the bubble plumes was not self–preserving and the similarity with simple plumes was not longer valid. Wilkinson's reasoning, however, was not supported by experimental findings by Topham [1975]. Goossens [1979] presented plume equations without assuming either radial profiles of liquid velocity or gas distribution of the total momentum flux associated with the mean flow. The entrainment coefficient was found to be equal or slightly greater than that of a single phase free jet. Goossens' bubble plume model treats the mixing in the vicinity of the plume called "nearfield". Kranenburg [1979] developed a model which combines Goossens' [1979] nearfield model with a model which treats the rest of the lake called "farfield". Coupling conditions at the transition from nearfield to farfield were derived by considering the transition as an "internal weir". Fannelop and Sjoen [1980] determined appropriate similarity solutions and numerically integrated solutions to a set of equations that neglected the slip velocity of the gas, but otherwise were the same as those used by Cederwall and Ditmars [1970]. Milgram and Van Houten [1982] developed a theory that included the effect of gas fraction on mass and momentum fluxes, and approximated the turbulent transport of mean momentum flux by assuming that a fixed fraction of this flux was carried by turbulence. Milgram [1983] presented an integral method with an entrainment coefficient and momentum amplification factor taken to be variables that depend on the local values of the relevant physical variables, e.g. gas flow rate and void fraction. Hussain and Narang [1984] extended the analysis of Hussain at al. [1976] and [1977] to include the effect of moderate temperature stratification in the farfield for both the axisymmetric jet and for the two–dimensional jet. Rowe et al. [1989] analyzed experimental data from the literature and found that the general properties of air bubble plumes can be described as a function of a dimensionless number called a "bubble Reynolds number". This analysis is presented in Appendix B.

1.3.3. *Summary of the previous work*

Previously cited work is mainly concerned with the bubble plume itself, treating it through integral models where the determination of the entrainment coefficient is the key point. Few investigators i.e. Kranenburg [1979], Goossens [1979], Davis [1980] developed (simplified) models of the mixing of a stratified lake by an air bubbles plume. Zic and Stefan [1988, 1989a] and Patterson and Imberger [1989] combined bubble plume models with dynamic lake/reservoir temperature stratification models to evaluate destratification in response to air bubbles plumes and weather.

1.4. Study outline

The goal of this study is to develop a better understanding and simulation capability of the processes involved in lake destratification induced by an air bubble plume.

Chapter 2 presents a dynamic 1–D model suitable to evaluate the destratification of a lake or reservoir in response to an air bubble plume and weather.

In Chapter 3 a numerical 2D model is presented. It is developed to analyze the details of the flow field induced by the air bubble plume in the farfield.

Chapter 4 describes laboratory experiments performed in stratified tanks. The position and the development of the plunging region, the layer structure in the farfield and water entrainment by the bubble plume were of particular interest.

Chapter 5 gives a synthesis of the results obtained in the previous chapters and emphasizes the similarities and differences with mixing induced by buoyant jets.

Chapter 6 presents suggestions for the design of air bubble systems as a lake destratification device.

Chapter 7 summarizes the work done and suggests further research.

2. COMPOSITE 1–D MODEL

2.1. Overview

As mentioned in Section 1.3 (Literature review) there have been few attempts in the past to give a composite model of the mixing of a lake or reservoir by an air bubble plume. Most investigators have been mainly concerned with the bubble plume itself. The computer program which will be presented herein can be used as a tool for the analysis of an air bubble system in a stratified lake or reservoir. The influence of the weather relative to the strength of an air bubble destratification system is demonstrated herein by synoptic simulation of heat transfer into and within a lake, as well as circulation and mixing induced by the upwelling water plume created by the rising bubbles. In addition, the simulations made demonstrate that the effectiveness of an air column destratification system with a given air flow rate is strongly dependent on the number of release points. Seasonal timing of the release and total air flow rate are also important as illustrated herein. In the numerical model, the lake is divided into a nearfield and a farfield. The nearfield model includes the bubble plume and the flow in its vicinity. The farfield model treats the rest of the lake and takes into account the flow from the plume towards the lake and from the lake towards the plume. Simulations are based on the nearfield model developed by Goossens [1979]. The nearfield model is combined with a multilayer dynamic farfield temperature stratification model to account for heat transfer through the water surface during the mixing period. The farfield model is driven by daily weather input data.

2.2. Introduction

If air is injected from the bottom of a two layered stratified lake, water with high density from the hypolimnion will be brought to the surface. This "heavier" water flows off and collides with the lighter epilimnion water. Consequently the heavy water will pass (plunge) under the epilimnion and spread as an intermediate layer (Fig. 2.1). Experimental evidence of this "interflow" was provided by Kranenburg [1979], Goossens [1979] and by the experiments presented in Chapter 4. Since there is mixing between discharged and epilimnetic water, the interflow density is intermediate between the epilimnion and hypolimnion densities. In the farfield this produces a new layer since density differences suppress turbulence and mixing at the boundaries. Near the stagnation (plunging) area, however, higher turbulence provides some mixing [Goossens, 1979].

A simplified flow pattern under stratified conditions was shown in Fig. 1.1. The major characteristics of the flow are the eddy like motion in the vicinity of the air release and a three layer flow in the region further away from the bubble plume. It has to been pointed out that there is no

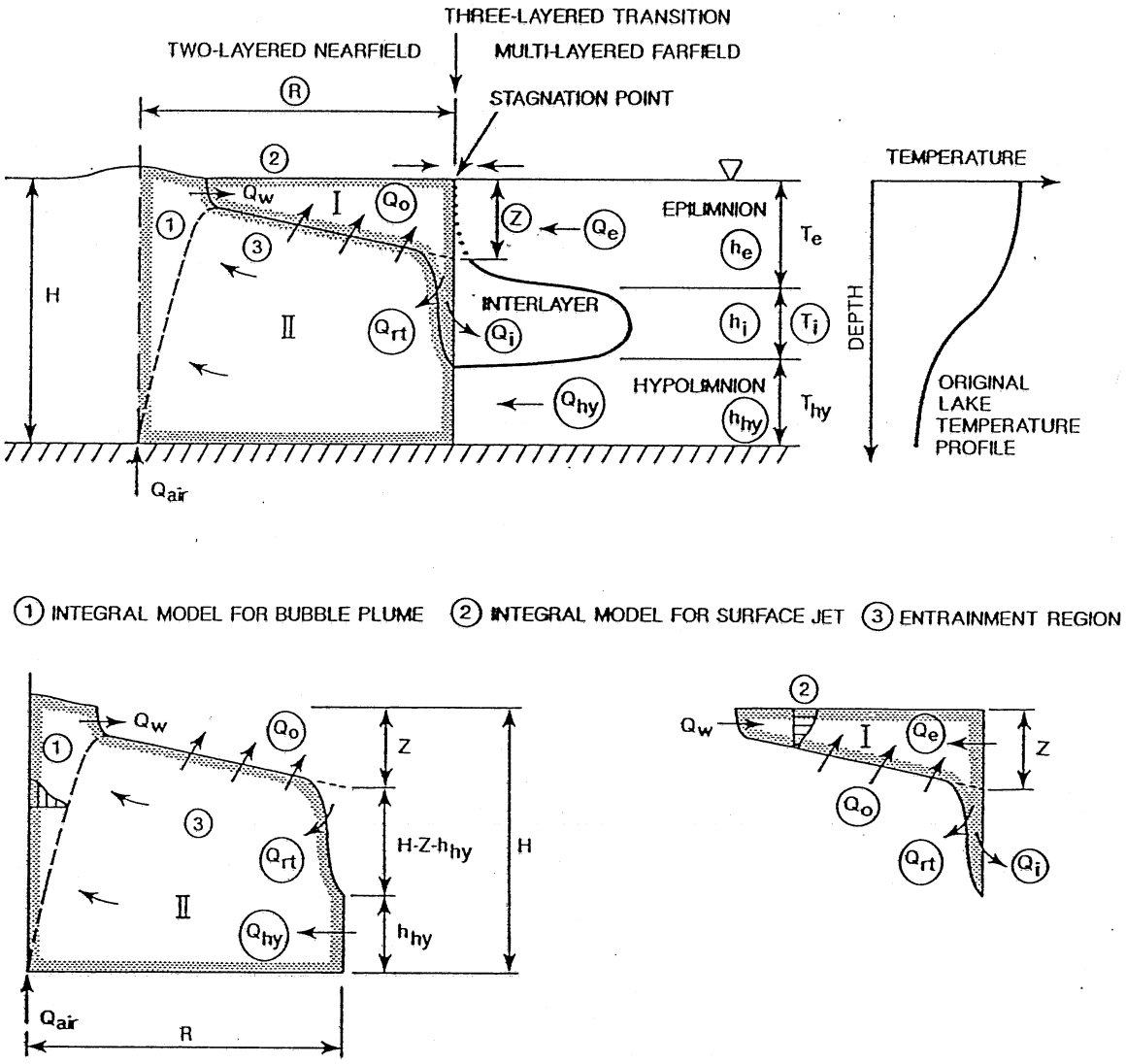

Figure 2.1 Schematic presentation of the flow field as used in model formulation

significant difference between the flow pattern in the case of isothermal and stratified receiving water in the vicinity of an air bubble plume [Goossens, 1979]. (This phenomenon can also be seen in the results of the 2–D numerical model in Chapter 3, Fig.3.13 to 3.16). The density difference between the epilimnion and hypolimnion influences the flow pattern. The plunging of the surface radial jet is governed by the interaction between the buoyancy force and momentum of the flow. Accordingly the greater density difference causes bigger negative buoyancy of the surface radial jet and earlier plunging. Increase of the air release rate by a small amount will not change the momentum of the flow significantly, and therefore will not affect the position of the plunging point much, but the flow rates in the three layers will be affected [Goossens, 1979]. The thickness of the epilimnion affects the density of the interflow (mixing) layer flowing into the lake. A thicker epilimnion decreases the mixing layer density, which then slides over the denser hypolimnetic water. A thin epilimnion, on the other hand, provides for a heavier mixing layer which mixes with the hypolimnion more easily.

2.3. Mathematical model

The mathematical model of the air bubble column and near– and farfield circulation was developed by Goossens [1979]. The basic features of the model will be summarized here. The first assumption of the model is that it is possible to distinguish two regions in the lake (Fig. 2.1):

1. the region in the vicinity of the air bubble column, treated as two–layer system and called nearfield, and

2. the bulk of the lake, which is treated as a multi–layered temperature (density) stratified environment and called farfield.

The boundary between the two regions is set through the stagnation point (plunge point) of the horizontal surface flow away from the plume (Fig. 2.1).

2.3.1. *Nearfield model*

The nearfield consists of four main regions also shown in Fig. 2.1:

1. a plume of water induced by air bubbles (marked as 1),

2. a horizontal surface jet, which begins where the upward flow induced by the bubbles is deflected by the water surface and which plunges into the surroundings because it is negatively buoyant (marked as 2),

3. two mixing regions, in which ambient water is drawn towards the bubble plume and entrained by it (marked as I and II), and

4. transition from nearfield to farfield at the stagnation point.

a) Bubble plume

The bubble plume is analyzed as a two–phase buoyant plume analogous to a single–phase buoyant plume. Its entrainment coefficient is equal or slightly greater than that of a single–phase plume [Goossens, 1979]. The ambient stratification is assumed not to have an influence on the plume development. Two coupled equations for the rate of change of the equivalent diameter d and velocity of the plume v can be obtained:

$$-\frac{d(d)}{dz} = \frac{\frac{-gQ_{inj}z_o}{2z(v+v_r)} + K_1 v^2 \left(\frac{1 + 4Q_{inj}z_o}{\pi z(v+v_r)}\right)^{1/2}}{\frac{\pi d^2}{4}} \tag{2.1}$$

$$-\frac{dv}{dz} = \frac{\frac{-gQ_{inj}z_o}{z(v+v_r)} - K_1 v^2 \left(\frac{1 + 4Q_{inj}z_o}{\pi z(v+v_r)}\right)^{1/2}}{\frac{\pi d^2 v}{4}} \tag{2.2}$$

where z = vertical coordinate directed downwards from the surface (with z = 10.2 m at the surface), Q_{inj} = volumetric gas injection rate under injection conditions, z_o = position of diffuser, v_r = relative bubble velocity = 0.3 m/s, K_1 = entrainment coefficient = 0.25.

On the basis of equations (2.1) and (2.2), assuming that the expansion of the air is adiabatic, and supported by measurements in the laboratory and in the field the following relation between the submergence depth of diffuser H, the volumetric gas rate at atmospheric pressure Q_{air} and the volumetric outflow from the bubble plume at the surface Q_w was obtained [Goossens, 1979]

$$Q_w = 0.47\ H^{4/3}\ Q_{air}^{1/3} \tag{2.3}$$

b) Surface radial jet

Once the plume reaches the surface, it starts to spread horizontally. The assumption under which the mathematical model is developed are the following: isothermal ambient water, stationary conditions with radial symmetry, no Coriolis force influence, and a sufficiently turbulent flow to neglect viscous effects.

The Navier Stokes equations can then be combined to:

$$u_r\frac{\partial u_r}{\partial r} + u_z\frac{\partial u_r}{\partial z} + \frac{\overline{\partial u_r' u_z'}}{\partial z} = 0 \tag{2.4}$$

The continuity equation is

$$\frac{1}{r}\frac{\partial(u_r r)}{\partial r} + \frac{\partial u_z}{\partial z} = 0 \tag{2.5}$$

where u_r, u_z are radial and vertical velocity components, respectively, r = radial distance from the vertical bubble plume axis, z = vertical coordinate (z = 0 at the surface), $\overline{u_r' u_z'}$ = Reynolds stresses. Equations (2.4) and (2.5) are solved assuming a similarity for the velocity and shear stress profiles. Regardless of the reservoir depth, the assumption is made that the hypolimnetic flow towards a bubble plume has no influence on the velocity profile of the surface jet. Solution of the equations (2.4) and (2.5), in terms of the total surface flow at the stagnation point (r = R), is [Goossens, 1979]

$$Q_o + Q_w = 2\pi m R \left[\tanh\left(\frac{Z}{kR}\right) - \frac{Z}{H}\tanh\left(\frac{H}{kR}\right)\right] \tag{2.6}$$

with a jet thickness

$$Z = kR \tanh^{-1}\left[\sqrt{1 - \frac{kR}{H}\tanh\left(\frac{H}{kR}\right)}\right] \tag{2.7}$$

where $m = 0.69\ k^{0.5}\ Q_{air}^{0.35}\ H^{0.5}$ with k = 0.0725 (Q_{air} in m^3/s, H in m),

Q_o = flow rate of water entrained by the radial surface jet.

c) Mixing regions

Mixing zone **I** entrains the discharge from the vertical plume (Q_w), from the radial surface jet (Q_o) and from the epilimnion (Q_e) and yields the return flow (Q_{rt}) to the mixing zone **II** and the interlayer flow (Q_i) to the farfield. Mixing zone **II** entrains hypolimnetic water (Q_{hy}) and return flow (Q_{rt}) and yields a discharge ($Q_w + Q_o$) to mixing zone **I**. The mass balances of mixing zones **I** and **II** yields expressions for the interlayer density ρ_i and the density of the outflowing discharge at the surface ρ_o (referring to Fig. 2.1)

$$(Q_w + Q_o + Q_e)\rho_i = (Q_w + Q_o)\rho_o + Q_e\rho_e \tag{2.8}$$

$$(Q_w + Q_o)\rho_o = (Q_w + Q_o - Q_{hy})\rho_i + Q_{hy}\rho_{hy} \tag{2.9}$$

where ρ_e and ρ_{hy} are the epilimnion and hypolimnion densities, respectively. Based on Eq. (2.8) and (2.9) the interlayer density ρ_i is equal to

$$\rho_i = \frac{Q_e\ \rho_e + Q_{hy}\ \rho_{hy}}{Q_e + Q_{hy}} \tag{2.10}$$

The assumption is made that the entrainment from the epilimnion Q_e is proportional to the total flow on the surface at the stagnation point

$$Q_e = c_1\ (Q_w + Q_o) \tag{2.11}$$

where c_1 = entrainment coefficient (in the range 0.05–0.2). The return flow Q_{rt}, on the other hand, is assumed to be proportional to the hypolimnetic flow

$$Q_{rt} = c_2 \frac{Q_{hy}}{h_{hy}} (H - Z - h_{hy}) \tag{2.12}$$

where c_2 = entrainment coefficient (in the range 1–8), h_{hy} = thickness of the hypolimnion at the transition from nearfield to farfield.

d) Conditions at transition from nearfield to farfield

The horizontal extent of the mixing regions as characterized by the location of the stagnation point can be determined by assuming equilibrium between nearfield (F^n) and farfield (F^f) forces

$$F^n = F^f \tag{2.13}$$

at r = R. Each of these forces consists of a dynamic part (resulting from the water flow) and a static part (resulting from the water density). The dynamic part is, however, significantly smaller then the static one [Goossens, 1979]. The assumption was made that the stratification in the nearfield can be described as a two layer system, obtained from the original temperature profile in the lake, with thicknesses H_{eo} and H_{ho} for epilimnion and hypolimnion, respectively (see Fig. 2.2). At some time after the air is turned on, the initial thicknesses H_{eo} and H_{ho} will change to some new values h_e and h_{hy} at the point of transition to the farfield. Accordingly, the nearfield force can be written as

$$F^n = 2\pi Rg \{0.5\rho_o Z^2 + [\rho_o Z + 0.5\rho_i(H - H_{ho} - Z)]H_{eo} + [\rho_o Z + \rho_i(H - H_{ho} - Z) + 0.5\rho_{hy}H_{ho}]H_{ho}\} \tag{2.14}$$

The farfield force is given as

$$F^f = 2\pi Rg \{0.5\rho_o h_e^2 + [\rho_e h_e + 0.5\rho_i h_i]h_i + [\rho_e h_e + \rho_i h_i + 0.5\rho_{hy}h_{hy}]h_{hy}\} \tag{2.15}$$

where h_i = thickness of the interlayer at the transition to farfield at some time when the air is released (see Fig. 2.1). Inserting Eq. (2.14) and (2.15) in Eq. (2.13) allows a solution of the stagnation point distance R. The only unknowns remaining are :

(1) the thicknesses of the epilimnion h_e and hypolimnion h_{hy} in the transition to the farfield. If it is assumed that the mixing layer is located at the position that would result from a direct mixing of the appropriate epilimnion and hypolimnion flows, then

$$h_e = H_{eo} - \frac{\rho_{hy} - \rho_i}{\rho_{hy} - \rho_e} h_i \tag{2.16}$$

$$h_{hy} = H_{ho} - \frac{\rho_i - \rho_e}{\rho_{hy} - \rho_e} h_i \tag{2.17}$$

and from the lake geometry

$$H = H_{ho} + H_{eo} = h_e + h_i + h_{hy} \tag{2.18}$$

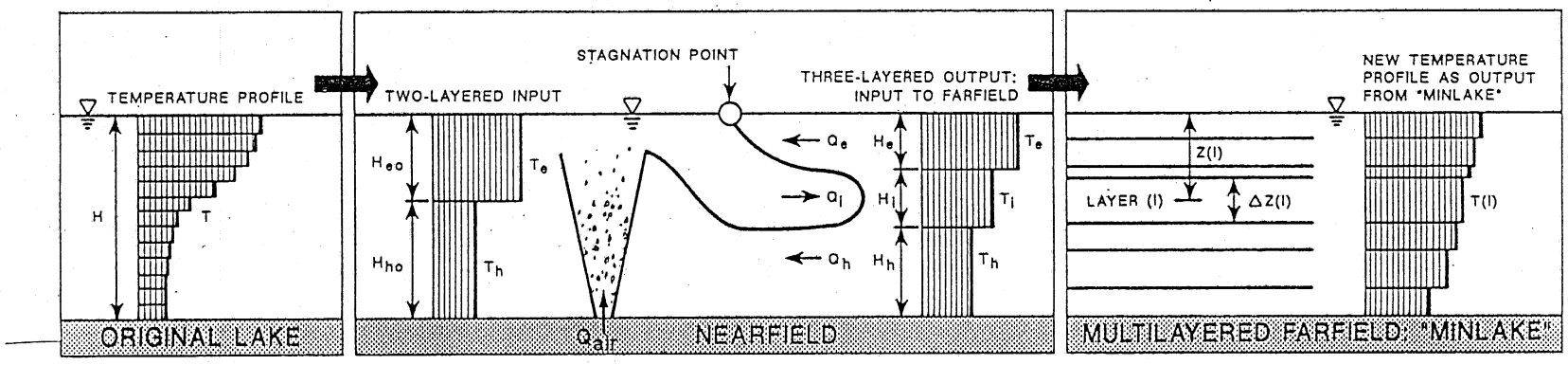

Figure 2.2 Schematic presentation of information flow

(2) the thickness of the interlayer h_i in the transition to the farfield. Kranenburg [1979] compared the diving of the interlayer underneath the epilimnion with an open channel flow over a broadcrested weir. In this case, the epilimnion corresponded to the weir and the mixing region in the nearfield to the hydraulic jump in front of it. At the transition R there is critical flow if the farfield flow in the interlayer does not influence the flow at the transition. The condition for the presence of the critical flow is [Goossens, 1979]

$$F_e^2F_i^2 + F_e^2F_{hy}^2 + F_{hy}^2F_e^2 - \frac{\rho_{hy} - \rho_i}{\rho_{hy}} F_e^2 - \frac{\rho_{hy} - \rho_e}{\rho_{hy}} F_i^2 - \frac{\rho_i - \rho_e}{\rho_{hy}} F_{hy}^2 + \frac{(\rho_i - \rho_e)(\rho_{hy} + \rho_i)}{\rho_{hy}^2} = 0 \tag{2.19}$$

where the densimetric Froude numbers in the epilimnion (F_e), interlayer (F_i) and hypolimnion (F_{hy}) are defined, respectively, as

$$F_e = \frac{1}{(2\pi R)^2} \frac{\rho_{hy} Q_e^2}{(\rho_{hy} - \rho_e) g h_e^3} \tag{2.20}$$

$$F_i = \frac{1}{(2\pi R)^2} \frac{\rho_{hy} Q_i^2}{(\rho_{hy} - \rho_e) g h_i^3} \tag{2.21}$$

$$F_{hy} = \frac{1}{(2\pi R)^2} \frac{\rho_{hy} Q_{hy}^2}{(\rho_{hy} - \rho_e) g h_{hy}^3} \tag{2.22}$$

where the interlayer flow Q_i is equal to

$$Q_i = Q_{hy} + Q_e \tag{2.23}$$

The nearfield model described above is for axisymmetric flow. It can be modified to plane (2–D) flow for line diffusers. The horizontal extent of the nearfield is usually less than 1–2 lake depths from the air injection, as observed in a field study [Goossens, 1979] and experiments described in Chapter 4.

The above simplified model of the nearfield takes into account the most basic hydraulic phenomena. The input values are the initial temperature profile in the lake, which must be transformed into a two–layer system, and the volumetric air release rate Q_{air}. Outputs of the nearfield model are the thicknesses and the flow rates from the hypolimnion, the epilimnion, and the interlayer in the transition to the farfield as shown in Fig. 2.2. The flow in the epilimnion and the hypolimnion is towards the air bubble column, and the flow in the interlayer is from the air bubble column towards the lake (farfield).

Differences between the original Goossens' [1979] model and the one presented here are as follows:

1. The nearfield process is treated as unsteady whereas a steady–state assumption was made by Goossens.

2. Entrainment rate from the epilimnion, which is specified by the coefficient c_1 in Eq. (2.10) is small and virtually constant for all investigated cases ($c_1 = 0.05$) and therefore does not have to be obtained in an iteration loop as proposed previously. This value is in good agreement with work done on plunging flows by Akiyama and Stefan [1987]. They found that the entrainment coefficient for non–diverging, plunging flows varies in the range from 0 to 0.08.

3. Coefficient c_2 in Eq. (2.11) varies according to Goossens from 1 to 8 and has to be evaluated based on experiments. It has been found, however, that c_2 can be found in an iteration loop such that a maximum interlayer flow rate is obtained, and this will usually correspond to a value $c_2 \approx 1$. This means that the ratio of return flow velocity to hypolimnetic withdrawal velocity is about unity for field cases.

4. Entrainment of water from below the diffuser is included in the model according to experimental results presented in Section 4.3.5.

Laboratory experiments presented in Chapter 4 verified that the basic assumptions of the nearfiled model are physically realistic.

2.3.2. *Farfield model*

As a farfield model, a dynamic lake temperature stratification model MINLAKE [Ford and Stefan, 1980; Riley and Stefan, 1987] is used. The model includes surface heat exchange due to short and long wave radiation, evaporation, convection, and wind mixing at the water surface. Program MINLAKE treats the lake as a one–dimensional multilayered system of variable layer thicknesses and layer temperatures.

The dynamics for all variables (including temperature) in the farfield can be expressed by an one–dimensional advection–diffusion equation:

$$A \frac{\partial \phi}{\partial t} + v \frac{\partial(\phi A)}{\partial z} = \frac{\partial}{\partial z}\left(KA \frac{\partial \phi}{\partial z}\right) \pm \text{source/sinks} \qquad (2.24)$$

where

ϕ = general variable (ϕ can be $\rho c_p T$, where ρc_p = specific heat and T = temperature), v = vertical velocity, z = depth, K = turbulent diffusion coefficient, and A = horizontal area of the control volume.

The vertical velocities in Eq. (2.24) are obtained assuming that Q_e = the flow rate of the water entrained from the epilimnion, Q_h = the flow rate of the entrained water from the hypolimnion, and Q_i = the flow rate which represents the inflow in the farfield from the bubble plume, will produce uniform horizontal velocities. From the continuity equation, going from the bottom to the top (or opposite) the vertical velocities can then be found.

The time step of the simulation is one day. Input to the simulation includes weather parameters, lake morphometry, and inflow rate. The model has been applied and verified with data from numerous lakes from 0.25 km^2 to 17 km^2 surface area and maximum depths from 2 to 80 m [e.g. Ford and Stefan, 1980; Stefan et al., 1982; Riley and Stefan, 1988].

Vertical diffusion is incorporated in the main program MINLAKE, but there is some additional shear stress in the flow field induced by the horizontal movement of the three layers with different directions, velocities and densities. The following approach was used to account for this effect. The vertical diffusion coefficient is at first defined according to the stability method given in HEC–5Q, Users Manual (U.S. Army Corps of Engineers, 1982). Stability E is equal to $E = -\frac{1}{\rho}\frac{d\rho}{dz}$, where ρ is density. An incremental diffusion coefficient is defined as $\Delta K_z = k\ K_z$ where K_z is the original diffusion coefficient from HEC–5Q. The coefficient k was found to be approximately 0.05 for the investigated cases.

2.3.3. *Composite computer program*

A computer subroutine, called BUBBLES, was written to simulate the nearfield and the three–layer flow from the nearfield into the farfield. Additional steps are the calculations of the vertical velocities, required for MINLAKE, and additional diffusion as described above. Merging the subroutine BUBBLES with MINLAKE produces a program which combines artificial lake mixing by air bubble diffusers with the naturally occurring stratification by heating, wind mixing, and natural convection by cooling. The program can therefore be used e.g. to determine air requirements to maintain or produce a fully–mixed lake. The information flow in the combined program is shown schematically in Figure 2.2; BUBBLES and MINLAKE are applied sequentially. For each computational time step (one day) at first the original temperature in the lake is described with a two–layer system. The nearfield part of the model then computes the flow rates and thicknesses at the transition to farfield. Calculation of the vertical velocities follows as required for the calculation of the flow in the farfield which results with new temperature profile at the end of the computational time step. The procedure is repeated for the next time step until the end of simulation period is reached.

Details of the subroutine BUBBLES are described by Zic and Stefan [1987] and Zic [1989c].

2.3.4. *Model validation*

The computer program was applied to two cases for validation: a) aeration of reservoir Petrusplaat in the Netherlands [Goossens, 1979] and b) aeration of Lake Calhoun, Minneapolis, Minnesota [Shapiro and Pfannkuch, 1973].

The basic data for reservoir Petrusplaat are: mean depth = 12.4 m, maximum depth = 15.0 m, surface area = 1.05 km^2, volume = $13.0 \times 10^6 m^3$, and air flow rate Q_{air} = 0.17 m^3/s = 0.097 $m^3 min^{-1} ha^{-1}$ = 1.38 $ft^3 min^{-1} acre^{-1}$. The diffuser was situated at the deepest point of the reservoir. Calculated and measured temperature profiles induced by the air bubble column are shown in Fig. 2.3.

The basic data for Lake Calhoun are: mean depth = 10.0 m, maximum depth = 27.4 m, surface area = 1.71 km^2, volume = $17.1 \times 10^6 m^3$. An estimated 0.0147 to 0.059 m^3/s = 0.005 to 0.021 $m^3 min^{-1} ha^{-1}$ = 0.067 to 0.27 ft^3 $min^{-1} acre^{-1}$ of air were used. Aeration of Lake Calhoun during the summer of 1972 lasted from August 4 to September 13. The aerator was a 30 m long, 5 cm diameter, perforated tube. Results of the calculations and measurements are shown in Fig. 2.4. Mean values ($\Delta \bar{T}$) and standard deviations ($\sigma_{\Delta T}$) of absolute differences between measured and calculated temperatures are shown for each temperature profile. The tendency towards restratification in response to surface heat input is apparent in both cases and shall be further investigated.

2.4. Model application – Analysis of mixing efficiency for lake Calhoun

Mixing efficiency can be calculated as a change of the stability of the lake. A stability parameter S is calculated [Ditmars, 1970] as

$$S = \rho \, g \, V_R \, (H_i - H_s) \tag{2.25}$$

where ρ = density of water, g = acceleration due to gravity, V_R = reservoir volume, H_i = center of mass for isothermal lake or reservoir, H_s = center of mass for a stratified lake or reservoir. Percentage of mixing achieved is defined as

$$P = \frac{S_o - S_t}{S_o} \times 100 \tag{2.26}$$

where S_o = initial stability, S_t = stability at time t. This stability parameter will be used herein as a relative measure to compare various aeration scenarios for the same lake and for the same meteorological conditions.

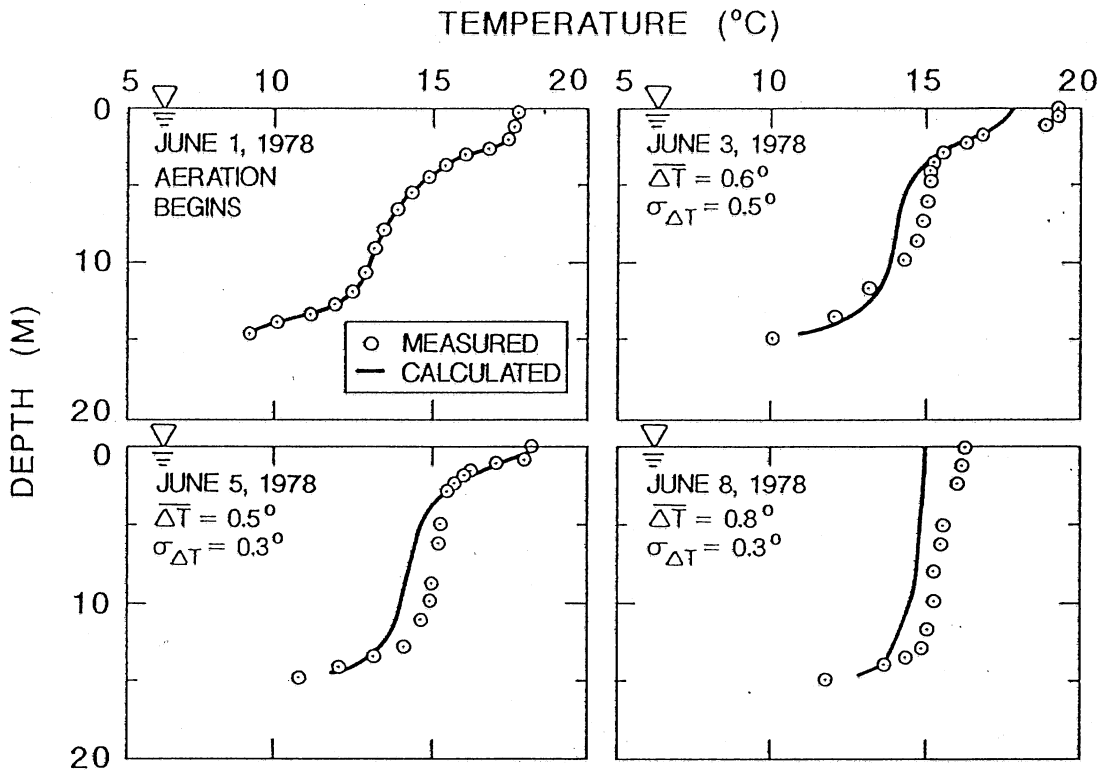

Figure 2.3 Simulation of destratification of the reservoir Petrusplaat (data from Goossens, 1979)

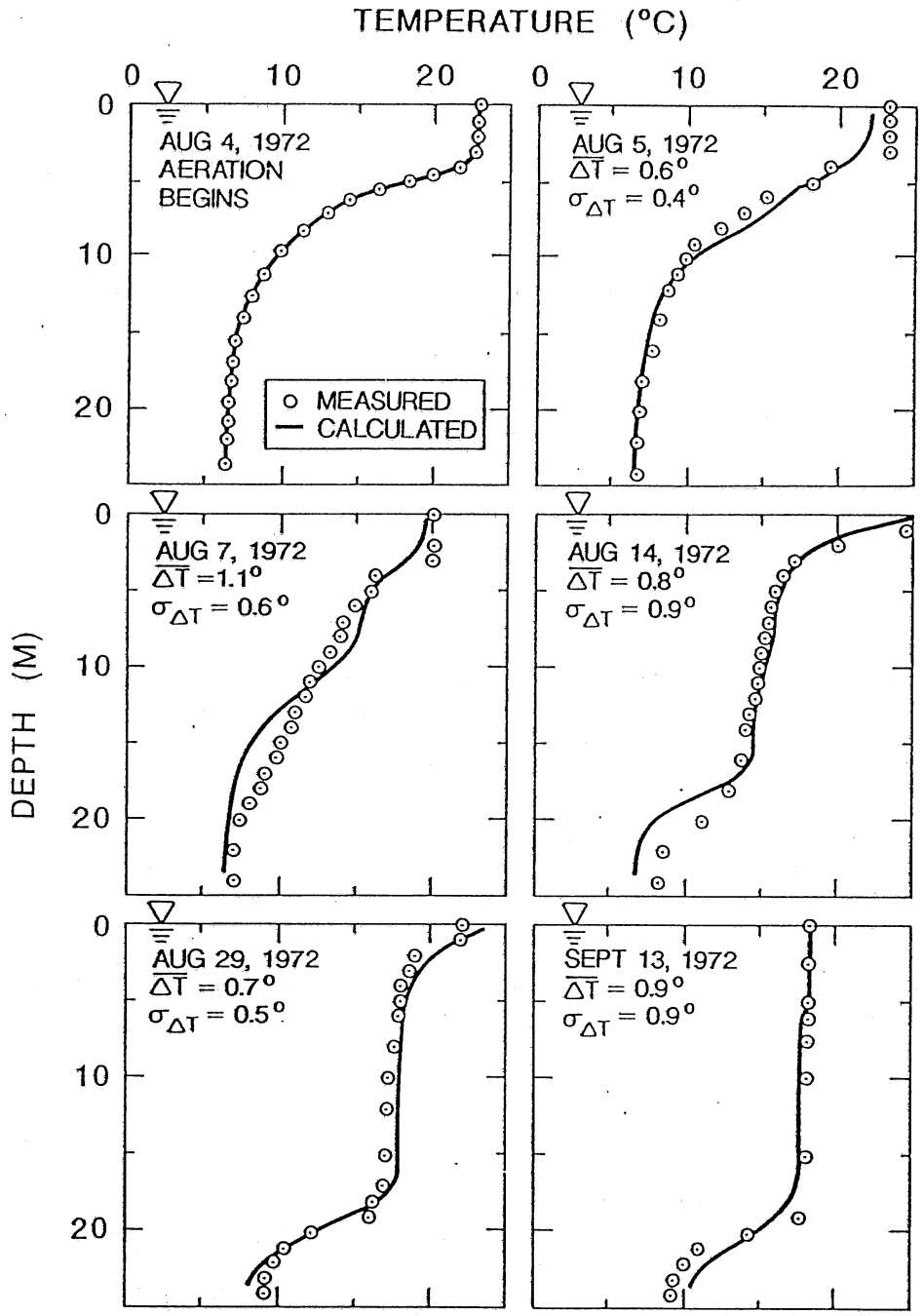

Figure 2.4 Simulation of destratification of the Lake Calhoun (data from Shapiro and Pfannkuch, 1973)

Lake Calhoun in Minneapolis, Minnesota, and weather data from August 4 to September 13, 1971 (see Fig. 2.5) are used as a first example. Figure 2.6 shows the development of the destratification process for different air injection rates. The percentage of mixing P and the interlayer flow rate Q_i are plotted versus time beginning with August 4, 1971. The results in the top three graphs used the actual meteorological conditions as input; the three bottom graphs assumed zero surface heat transfer. Without surface heat exchange, the destratification progresses much more continuously than with heat transfer. Natural heat input through the water surface tends to re–establish or retain stratification. With real meteorological conditions, high mixing efficiencies, e.g. 90 percent, are achieved only intermittently. It is most noteworthy that increasing the air flow rate by as much as 3300 percent did not raise mixing efficiencies appreciably or overcome the weather effect. Figure 2.7 further illustrates the diminishing return on increasing air flow rates. Identical mixing efficiencies as a function of the air flow rate released from a single diffuser are plotted. The mostly retarding effect of the heat exchange through the water surface on mixing is apparent.

Instead of having only one point of air release, the air flow can also be distributed over a number of diffusers. The benefits of increasing the number of diffusers, rather than the air flow rate at a single diffuser are apparent in Fig. 2.8. Increasing the number of diffusers (beyond three) or the air flow rate (beyond 0.5 m^3/s) did not have an appreciable effect on the time necessary to achieve 80 percent mixing efficiency. This was also found by Patterson and Imberger [1989]. Based on the analysis for a single plume in an unstratified region, they showed that for n diffusers, each discharging Q_{air} the total water entrainment will be proportional to $n \cdot Q_{air}$; on the other hand, a total flow of $n \cdot Q_{air}$ from a single diffuser will yield only a total entrainment proportional to $n^{1/3}\ Q_{air}^{1/3}$. For the same net air flow, it is therefore desirable to increase the number of diffusers to maximize the total water entrainment.

Interlayer flow rate, Q_i, is a measure of advective water exchange induced by an air bubble system. It is of interest to determine how much flow Q_i is produced as a function of air release rate Q_{air}. Table 2.1 gives ratios of air flow rate Q_{air} at atmospheric pressure and interlayer water flow rate Q_i. The ratios are high and increase dramatically as the air flow rate is reduced. Using small air release rates of each release point is therefore of benefit. The reason for this behavior is the nature of the entrainment process. Water is entrained in the wake of the bubbles rising in the fluid. As the number of bubbles is increased at higher air flow rates, bubble wakes interfere with each other, especially in the core of the plume, and entrain relatively less water per bubble. If the foregoing arguments are pushed to the extreme, an infinite number of air injection points would appear best. This is not the case. With an excessive number of diffusers, the buoyancy of each air release becomes too weak to form a coherent, rising water plume. The total water entrainment diminishes. Therefore one can think of an optimal number of diffusers which is attained when the simulated mixing efficiency remains about the same despite an increase in the number of air release points (e.g. three diffusers in Fig. 2.8).

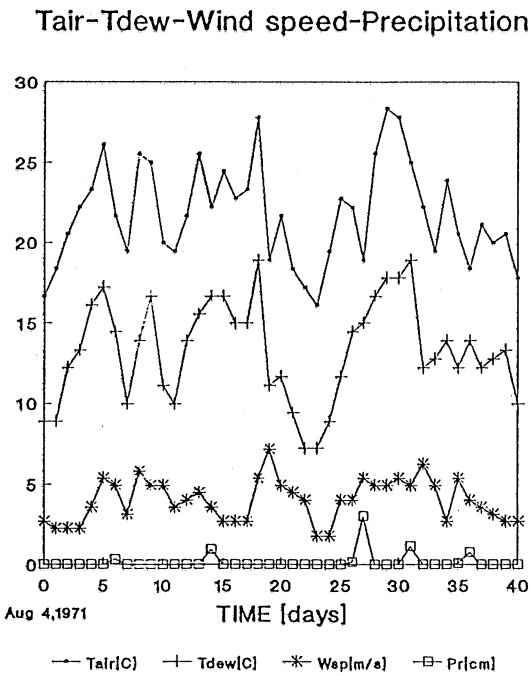

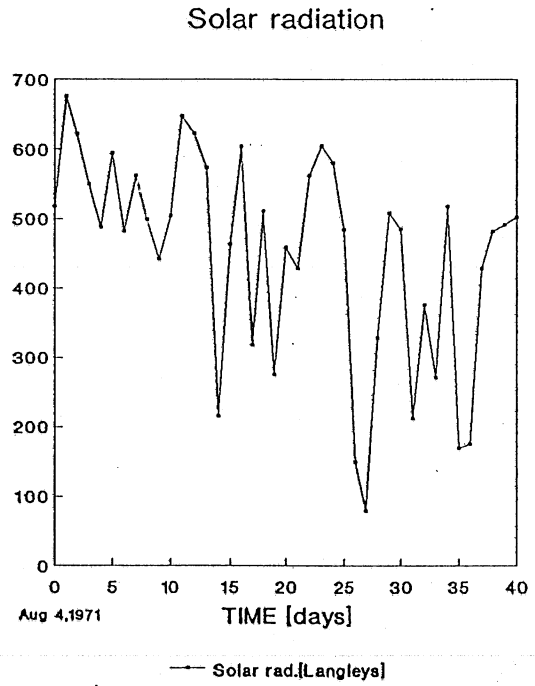

Figure 2.5 Weather data used in simulation

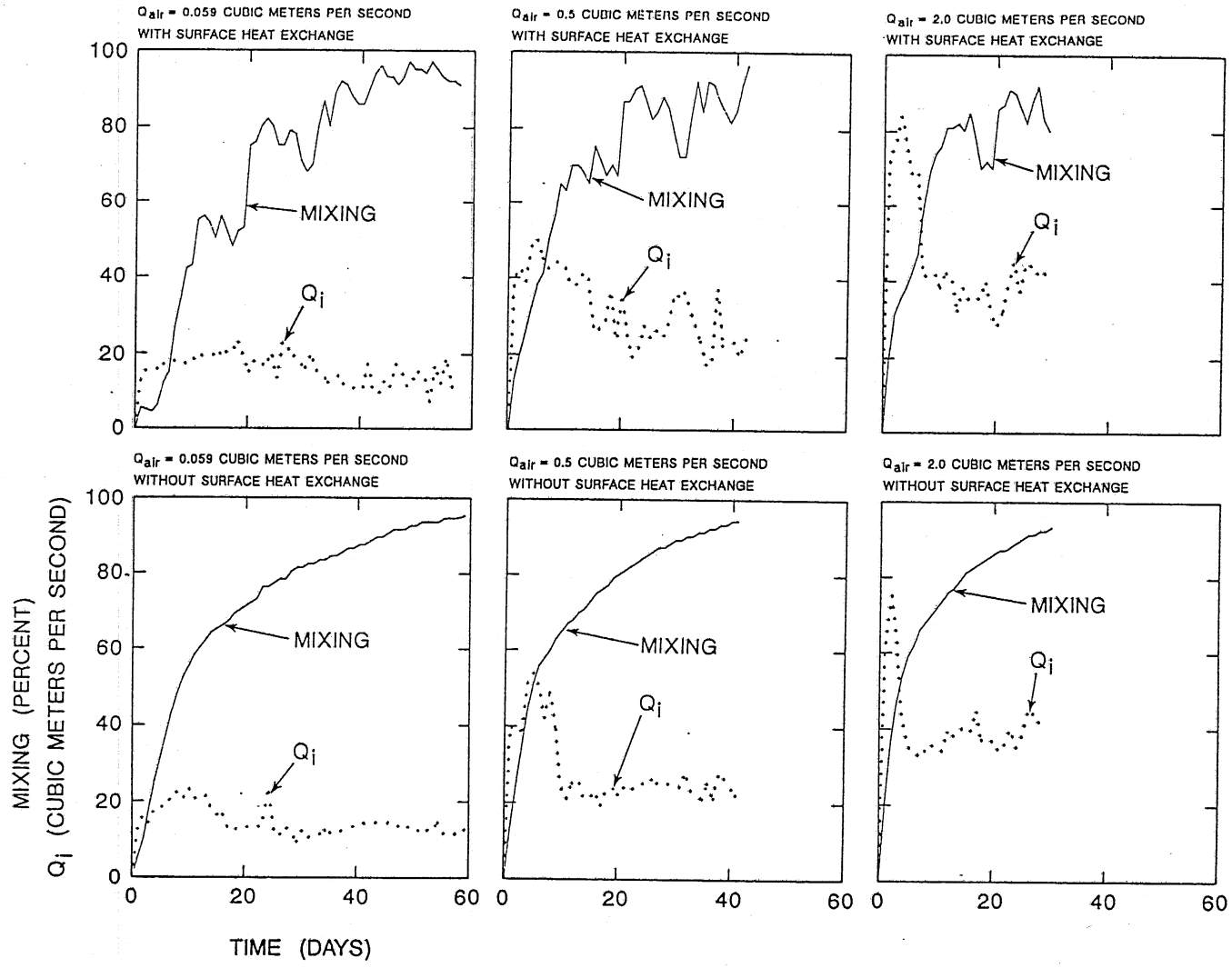

Figure 2.6 Development of mixing as a function of time at three air release rates with and without natural heat exchange through water surface (example: calhoun, 1971)

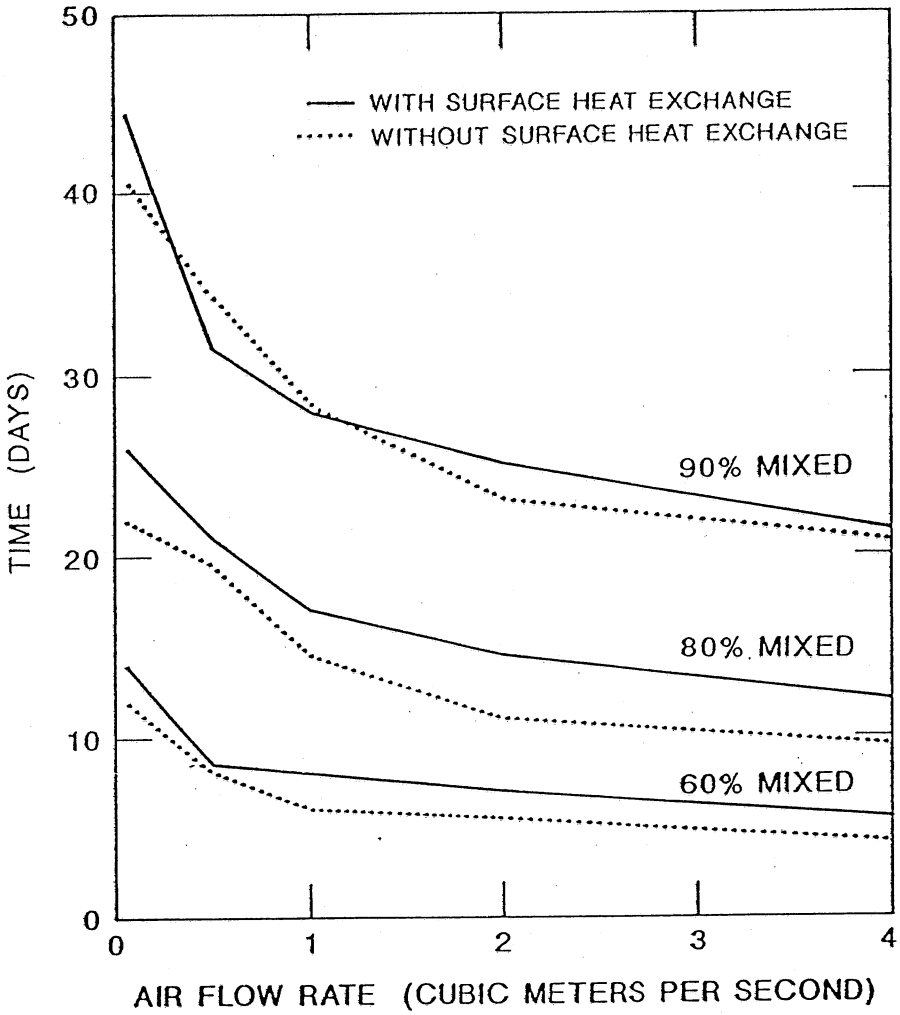

Figure 2.7 Time to achieve 60 or 80 percent mixing as a function of air flow rate and surface heat exchange (example: Lake Calhoun, 1971)

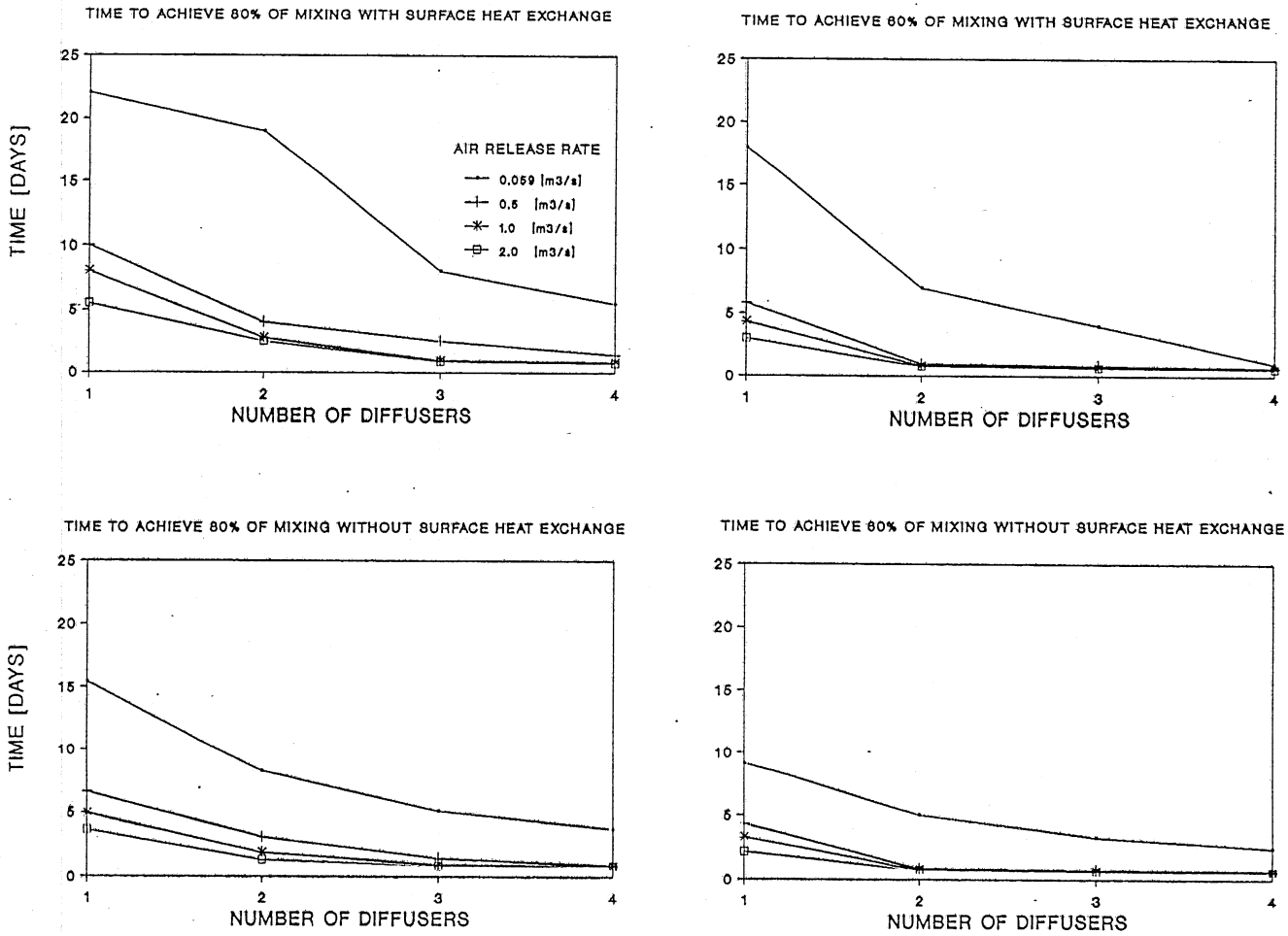

Figure 2.8 Time required to achieve 60 or 80 percent of mixing as a function of the number of diffusers (example: Lake Calhoun, 1971)

TABLE 2.1 Air Release Q_{air} and Total Entrained Water Flow Q_i

$Q_{air}(m^3/s)$	$Q_{air}[m^3min^{-1}\ ha^{-1}]$	$Q_i(m^3/s)$	Q_i/Q_{air}
4.0	1.40	47	14
2.0	0.70	49	25
1.0	0.35	43	43
0.5	0.18	36	72
0.059	0.02	18	305

Figure 2.9 illustrates the actual time evolution of mixing for several single and multiple diffusers and air flow rates.

The foregoing illustrations are for a case study in which aeration was started rather late in the summer season (August 4). Time t=0 on Figs. 2.5, 2.6 and 2.9 corresponds to that date. What would have happened had the aerator system been started two months earlier, say on June 1? Figure 2.10 answers that question by presenting mixing efficiency versus time for both starting times. At the lowest of the three air injection rates investigated (0.059 m^3/s) only a 50 percent destratification efficiency would have been achieved within 40 days from June 1. Operation beginning August 4 at the same air flow rate would have achieved 50 percent within about 20 days. The delay is due to heat input through the water surface from June 1 to August 1 which tends to re–establish a stratification during the early summer season. At the higher air injection rates (0.5 m^3/s and 2 m^3/s) mixing was more forceful, and the starting date less influential; in less than 10 days, 50 percent mixing was achieved in all cases.

In Fig. 2.11, lake temperature structures (isotherms) are illustrated for three conditions: (a) no aeration (measured temperatures), (b) aeration at 0.059 or 0.5 m^3/s beginning June 1, 1971 (temperatures are simulated) and (c) aeration at 0.059 or 0.5 m^3/s beginning August 4, 1971 (temperatures are simulated). In all simulations, aeration lasted 40 days (as applied in the field study in August 1972, see Fig. 2.4). Once the aerator is turned off, only the meteorological and inflow conditions continue to govern the thermal structure of the lake. Timing of the aeration has a large effect on temperature structure and heat storage as shown by the position of the 15° C and 20° C isotherms in Fig. 2.11. By comparison, air injection rate seemed less influential on the seasonal temperature structure.

In summary it can be said that efforts to mix (wholly) a temperature stratified lake in summer by air bubble column systems is counteracted by restratification due to surface heat input. This "tug–of–war" situation can be analyzed by simulation of heat transfer into and within a lake and circulation and mixing by the upwelling water plume created by the rising bubbles. Examples of such destratification have been illustrated herein. The influence of the weather relative to the strength of the air bubble system as measured by the air release rate has been demonstrated in particular. The influence of total air release rate, number of release points and timing of release has been

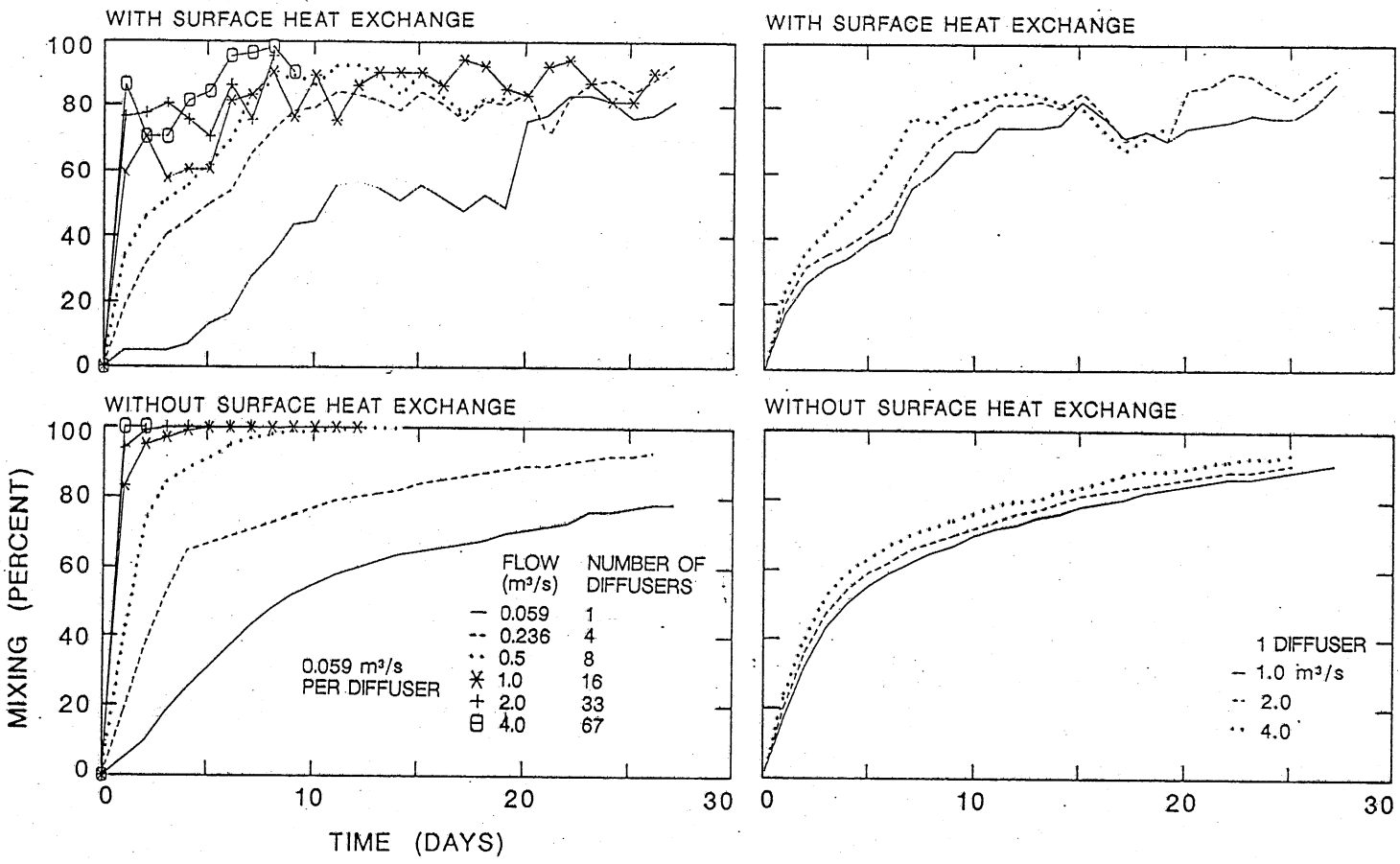

Figure 2.9 Development of mixing as a function of time for increasing numbers of air diffusers (example: Lake Calhoun, 1971)

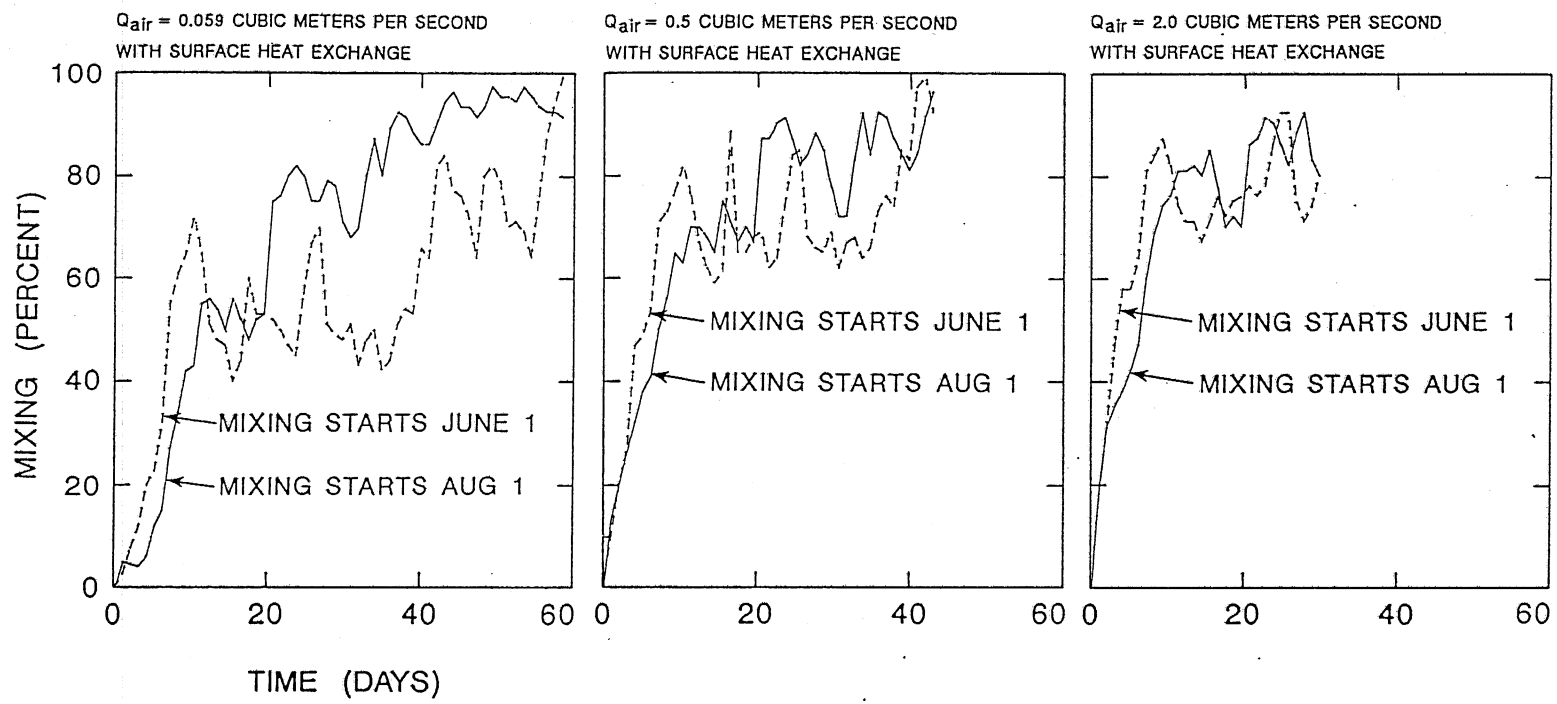

Figure 2.10 Mixing efficiencies as a function of time at two starting dates of aeration (example: Lake Calhoun, 1971)

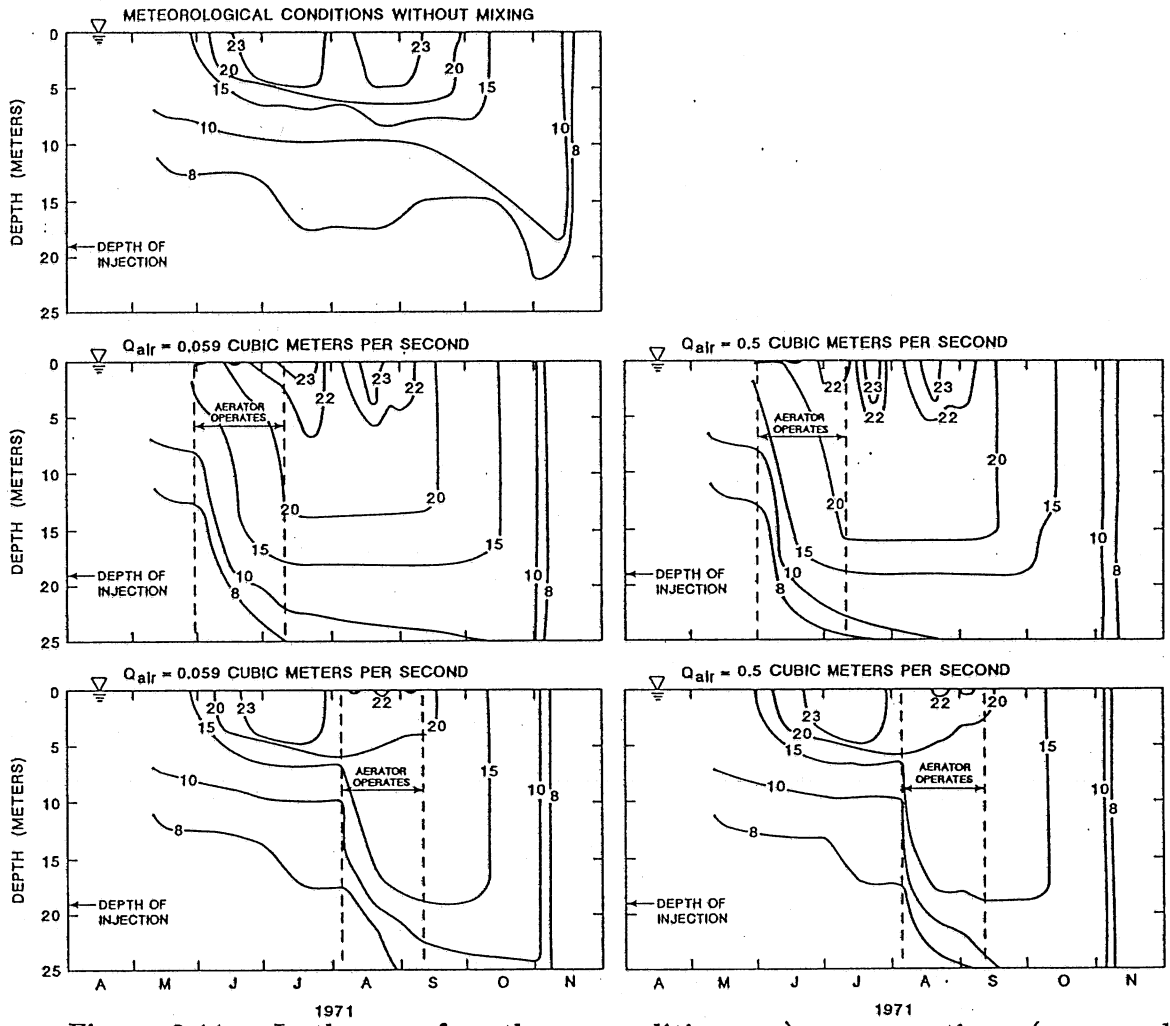

Figure 2.11 Isotherms for three conditions a) no aeration (measured conditions), b) aeration at 0.059 or 0.5 m^3/s beginning June 1, 1971, and c) aeration at 0.059 or 0.5 m^3/s beginning August4, 1971. (example: Lake Calhoun)

shown. The results agree with findings of other investigations [Patterson and Imberger, 1989]. Simulations such as shown herein can be put to practical use in the design and selection of lake/reservoir aeration systems.

3. NUMERICAL 2–D MODEL

3.1. Overview

Although a one–dimensional model such as discussed in Chapter 2 can give a good prediction of the bulk characteristics of the mixing process in a lake due to air bubble release, the details of the flow field, especially its development in time, and the influence of the different strengths of the stratification, cannot be determined with a one–dimensional model.

The 2–D model presented in this chapter gives details of the flow field and destratification and therefore offers the possibility to understand better the interactions between various parameters in the destratification process.

The computer program is based on the code given by Patankar [1980]. The unsteady version is used here [Farell, 1986]. Bubble dynamics in the air bubble plume has been examined to define a characteristics of the flow, and to define an appropriate model. The water movement induced by the air bubbles is then incorporated in the code with the PSI (particles in cell) method [Crowe, 1983] which treats air bubbles as a source of mass, momentum and energy in the flow field. Such a model is compared with measurements. The comparisons show good agreement.

3.2. Governing equations of the fluid flow

Most of the flows of practical relevance in hydraulics are turbulent [Rodi, 1980]. Turbulent flows are always dissipative. Viscous stresses perform deformative work which increases internal energy of the fluid at the expense of a kinetic energy of the turbulence.

Equations which describe the incompressible fluid flow, written in tensor notation are:

– continuity equation (conservation of mass)

$$\frac{\partial u_i}{\partial x_i} = 0 \tag{3.1}$$

– Navier – Stokes equations (conservation of momentum)

$$\frac{\partial u_i}{\partial t} + u_j \frac{\partial u_i}{\partial x_j} = -\frac{1}{\rho_r}\frac{\partial p}{\partial x_i} + \nu \frac{\partial^2 u_i}{\partial x_j \partial x_j} + g_i \frac{\rho - \rho_r}{\rho_r} \tag{3.2}$$

– thermal energy conservation

$$\frac{\partial T}{\partial t} + u_i \frac{\partial T}{\partial x_i} = \alpha \frac{\partial^2 T}{\partial x_i \partial x_i} \tag{3.3}$$

where u_i = instantaneous velocity component in the x_i direction, p = hydrostatic pressure, ρ = density, ρ_r = reference density, g_i = acceleration due to gravity in x_i direction, ν = molecular kinematic viscosity, α = thermal diffusivity, T = temperature.

Bousinesq [1903] introduced the approximation of neglecting variations of density in so far as they affect inertia, but retaining them in the buoyancy term. The density/temperature relationship can be written as

$$\rho = \rho_r[1 - \beta(T - T_r)] \tag{3.4}$$

where T_r = reference temperature, β = coefficient of thermal expansion (for water $\beta \approx 1.5\text{x}10^{-4}/^{\circ}\text{C}$). With equation (3.4), equation (3.2), can be rewritten as

$$\frac{\partial u_i}{\partial t} + u_j \frac{\partial u_i}{\partial x_j} = -\frac{1}{\rho_r}\frac{\partial p}{\partial x_i} + \nu \frac{\partial^2 u_i}{\partial x_j \partial x_j} + g_i\beta(T_r - T) \tag{3.5}$$

where $g_i\beta(T_r - T)$ is a buoyancy term.

Although equations (3.1), (3.3) and (3.5) describe completely the turbulent flow, from a practical point of view they cannot be successfully used. Osborn Reynolds [1901] proposed a statistical approach which requires that instantaneous variables are transformed into mean and fluctuating parts or

$$\begin{aligned} u_i &= \bar{u}_i + u_i' \\ p &= \bar{p} + p' \\ T &= \bar{T} + T' \end{aligned} \tag{3.6}$$

By use of equations (3.6) in (3.1), (3.3) and (3.5), the following equations can be obtained [Hinze, 1979]:

– continuity equation

$$\frac{\partial \bar{u}_i}{\partial x_i} = 0 \tag{3.7}$$

– momentum equations

$$\frac{\partial \bar{u}_i}{\partial t} + \bar{u}_j \frac{\partial \bar{u}_i}{\partial x_j} = -\frac{1}{\rho_r}\frac{\partial \bar{p}}{\partial x_i} + \frac{\partial}{\partial x_j}\left(\nu \frac{\partial \bar{u}_i}{\partial x_j} - \overline{u_i' u_j'}\right) + g_i\beta(T_r - T) \tag{3.8}$$

– temperature equation

$$\frac{\partial \bar{T}}{\partial t} + \bar{u}_j \frac{\partial \bar{T}}{\partial x_i} = \frac{\partial}{\partial x_i}\left(\alpha \frac{\partial \bar{T}}{\partial x_i} - \overline{u_i' T'}\right) \tag{3.9}$$

The equations are exact since no assumptions have been introduced in deriving them, but they do not represent a closed set of equations. Due to nonlinearity of equations (3.8) and (3.9) the unknown correlations between fluctuating velocities $\overline{u_i'u_j'}$ and between velocity and temperature $\overline{u_j'T'}$ are introduced.

The problem of defining those unknown correlations in terms of mean flow variables is called the closure problem and represents the basic goal for the practical solution of the turbulent flow.

Two of the most important effects of the turbulence on the mean flow are [Ferziger, 1987]:

(i) it absorbs kinetic energy from the mean flow and converts it to thermal energy (dissipation),

(ii) it increases the rate of transport of mass, momentum, and energy normal to the streamlines of the flow (diffusion).

As both of these effects are mediated by the viscosity in laminar flows, it is natural to assume that the effect of turbulence on the mean flow can be represented as an increased, or eddy, viscosity. This leads to

$$\overline{u_i'u_j'} = -\nu_t\left(\frac{\partial \overline{u}_i}{\partial x_j} + \frac{\partial \overline{u}_j}{\partial x_i}\right) + \frac{2}{3}\,k\delta_{ij} \tag{3.10}$$

as a model of the Reynolds stresses in the turbulent flows where ν_t = turbulent or eddy viscosity, $k = \overline{u_i u_i}/2$, δ_{ij} = Kronecker delta.

In analogy to equation (3.10) the turbulent heat transport is often assumed to be

$$\overline{u_i'T'} = -\Gamma\,\frac{\partial T}{\partial x_i} \tag{3.11}$$

where Γ is the turbulent diffusivity of heat and can be defined as

$$\Gamma = \frac{\nu_t}{\sigma_t} \tag{3.12}$$

where σ_t is a turbulent Prandtl number.

The turbulence problem now concerns the value of ν_t. The simplest descriptions of turbulence are those which characterize it by its kinetic energy, $\rho V^2/2$, and an average length scale L. In terms of these, dimensional analysis shows that the eddy viscosity, which carries dimensions L^2/T, must be written as

$$\nu_t = C \cdot V \cdot L \tag{3.13}$$

where V and L are velocity and length scale of the turbulence, respectively, and C is an empirical constant or a function of dimensionless parameters.

In recent years between various schemes the most widely used is the so–called k–ϵ model which relates the turbulent kinetic energy k, and the turbulent energy dissipation rate $\epsilon = \nu_t(\overline{\partial u_i}/\partial x_j)^2$ by

$$\nu_t = c_\mu \frac{k^2}{\epsilon} \tag{3.14}$$

where c_μ is an empirical coefficient.

The values of k and ϵ are obtained from differential equations which incorporate the effects of convection, diffusion, shear and buoyancy in the flow field. The k–ϵ model is described by Rodi [1980].

The complete equations for the plane symmetric and the axisymmetric case are provided here.

3.2.1. *Plane symmetric case*

The plane symmetric case corresponds to the 2–D Cartesian coordinate system.

Mean flow equations

If we drop the overbar symbol from the usual notation for the mean flow variables it can be written as follows:

– continuity equation

$$\frac{\partial u}{\partial x} + \frac{\partial v}{\partial y} = 0 \tag{3.15}$$

– momentum equations

$$\frac{\partial u}{\partial t} + u\frac{\partial u}{\partial x} + v\frac{\partial u}{\partial y} = -\frac{1}{\rho_r}\frac{\partial p}{\partial x} + \frac{\partial}{\partial x}\left(\nu_{eff}\frac{\partial u}{\partial x}\right) + \frac{\partial}{\partial y}\left(\nu_{eff}\frac{\partial u}{\partial y}\right) + \frac{\partial}{\partial x}\left(\nu_t\frac{\partial u}{\partial x}\right) + \frac{\partial}{\partial y}\left(\nu_t\frac{\partial v}{\partial x}\right) \tag{3.16}$$

$$\frac{\partial v}{\partial t} + u\frac{\partial v}{\partial x} + v\frac{\partial v}{\partial y} = -\frac{1}{\rho_r}\frac{\partial p}{\partial y} + \frac{\partial}{\partial x}\left(\nu_{eff}\frac{\partial v}{\partial x}\right) + \frac{\partial}{\partial y}\left(\nu_{eff}\frac{\partial v}{\partial y}\right) + \frac{\partial}{\partial x}\left(\nu_t\frac{\partial u}{\partial y}\right) + \frac{\partial}{\partial y}\left(\nu_t\frac{\partial v}{\partial y}\right) + \beta g(T_r - T) \tag{3.17}$$

– temperature equation

$$\frac{\partial T}{\partial t} + u\frac{\partial T}{\partial x} + v\frac{\partial T}{\partial y} = \frac{\partial}{\partial x}\left(\alpha_{eff}\frac{\partial T}{\partial x}\right) + \frac{\partial}{\partial y}\left(\alpha_{eff}\frac{\partial T}{\partial y}\right) \tag{3.18}$$

where

$$\nu_{eff} = \nu + \nu_t \tag{3.19}$$

$$\alpha_{eff} = \frac{\nu}{Pr} + \frac{\nu_t}{\sigma_t} \tag{3.20}$$

where Pr = Prandtl number for a laminar flow.

Turbulence model equations

The k–ϵ model is used, and extended to include buoyancy effects. The basic equation is written already as Eq. (3.14) where k is now defined as

$$k = \frac{1}{2}\left(\overline{u'^2} + \overline{v'^2}\right)^2 \tag{3.21}$$

and ϵ = dissipation rate per unit mass. The differential equations for k and ϵ can be written as follows:

– the k equation

$$\frac{\partial k}{\partial t} + u\frac{\partial k}{\partial x} + v\frac{\partial k}{\partial y} = \frac{\partial}{\partial x}\left(\nu_{eff}\frac{\partial k}{\partial x}\right) + \frac{\partial}{\partial y}\left(\nu_{eff}\frac{\partial k}{\partial y}\right) + P + G - \epsilon \tag{3.22}$$

where $\nu_{eff} = \nu + \frac{\nu_t}{\sigma_k}$ and σ_k is an empirical coefficient.

– the ϵ equation

$$\frac{\partial \epsilon}{\partial t} + u\frac{\partial \epsilon}{\partial x} + v\frac{\partial \epsilon}{\partial y} = \frac{\partial}{\partial x}\left(\nu_{eff}\frac{\partial \epsilon}{\partial x}\right) + \frac{\partial}{\partial y}\left(\nu_{eff}\frac{\partial \epsilon}{\partial y}\right) + c_{1\epsilon}\frac{\epsilon}{k}\left(P + c_{3\epsilon}G\right) - c_{2\epsilon}\frac{\epsilon^2}{k} \tag{3.23}$$

where $\nu_{eff} = \nu + \frac{\nu_t}{\sigma_\epsilon}$ and σ_ϵ is an empirical coefficient.

In equations (3.22) and (3.23) P denotes the production of turbulent energy from the mean flow and can be defined as

$$P = \nu_t\left[2\left(\frac{\partial u}{\partial x}\right)^2 + 2\left(\frac{\partial u}{\partial x} + \frac{\partial v}{\partial y}\right) + \left(\frac{\partial v}{\partial y}\right)^2\right] \tag{3.24}$$

The G term represents the production or destruction of turbulent energy by buoyancy forces and can be defined as:

$$G = \beta g \frac{\nu_t}{\sigma_t} \frac{\partial T}{\partial y} \tag{3.25}$$

In the previous equations $c_{1\varepsilon}$, $c_{2\varepsilon}$, σ_k and σ_ε represent empirical coefficients.

Equation summary

If we denote the dependent variable as φ then all the equations from the previous chapter can be written in the form:

$$\frac{\partial \varphi}{\partial t} + u \frac{\partial \varphi}{\partial x} + v \frac{\partial \varphi}{\partial y} = \text{pressure term}$$

$$+ \frac{\partial}{\partial x}\left(\Gamma \frac{\partial \varphi}{\partial x}\right) + \frac{\partial}{\partial y}\left(\Gamma \frac{\partial \varphi}{\partial y}\right) + S \tag{3.26}$$

where Γ is a diffusion coefficient and S the source term. The pressure term exists just in the case when φ represents velocity.

Referring to the general equation (3.26) Table 3.1 gives a summary of the equations treated in this chapter.

Table 3.1 Diffusion coefficients and source terms in the governing equations for a plane symmetric case

variable	symbol	diffusion coefficient, Γ	source term, S
horizontal velocity	u	$\nu_{eff} = \nu + \nu_t$	$\frac{\partial}{\partial x}\left(\nu_t \frac{\partial u}{\partial x}\right) + \frac{\partial}{\partial y}\left(\nu_t \frac{\partial v}{\partial x}\right)$
vertical velocity	v	$\nu_{eff} = \nu + \nu_t$	$\frac{\partial}{\partial x}\left(\nu_t \frac{\partial u}{\partial y}\right) + \frac{\partial}{\partial y}\left(\nu_t \frac{\partial v}{\partial y}\right) + \beta g (T_r - T)$
temperature	T	$\frac{\nu}{Pr} + \frac{\nu_t}{\sigma_t}$	none
turb.kin. energy	k	$\nu + \frac{\nu_t}{\sigma_k}$	$P + G - \epsilon$ (*)
turb.energy diss.rate	ϵ	$\nu + \frac{\nu_t}{\sigma_\epsilon}$	$c_{1\varepsilon} \frac{\epsilon}{k}(P + c_{3\varepsilon} G) - c_{2\varepsilon} \frac{\epsilon^2}{k}$
(*) $P = \nu_t \left[2\left(\frac{\partial u}{\partial x}\right)^2 + 2\left(\frac{\partial u}{\partial x} + \frac{\partial v}{\partial y}\right) + \left(\frac{\partial v}{\partial y}\right)^2\right]$			$G = \beta g \frac{\nu_t}{\sigma_t} \frac{\partial T}{\partial y}$

3.2.2 *Axisymmetric case*

The axisymmetric case corresponds to the cylindrical coordinate system with a unit angle Ψ.

Mean flow equations

With substitutions $u = \overline{v}_z$ and $v = \overline{v}_r$ and with the overbar symbol dropped for convenience, the equations can be written:

– continuity equation

$$\frac{1}{r}\frac{\partial}{\partial r}(rv) + \frac{\partial u}{\partial z} = 0 \tag{3.27}$$

– momentum equations

a) in vertical direction

$$\frac{\partial u}{\partial t} + u\frac{\partial u}{\partial z} + v\frac{\partial u}{\partial r} = -\frac{1}{\rho_r}\frac{\partial p}{\partial z} + \frac{1}{r}\frac{\partial}{\partial r}\left(\nu_{eff}\, r\frac{\partial u}{\partial r}\right) + \frac{\partial}{\partial z}\left(\nu_{eff}\frac{\partial u}{\partial z}\right) + \frac{1}{r}\frac{\partial}{\partial r}\left(\nu_t r\frac{\partial v}{\partial z}\right) + \frac{\partial}{\partial z}\left(\nu_t\frac{\partial u}{\partial z}\right) + \beta g(T_r - T) \tag{3.28}$$

b) in radial direction

$$\frac{\partial v}{\partial t} + u\frac{\partial v}{\partial z} + v\frac{\partial v}{\partial r} = -\frac{1}{\rho_r}\frac{\partial p}{\partial r} + \frac{1}{r}\frac{\partial}{\partial r}\left(\nu_{eff} r\frac{\partial v}{\partial r}\right) + \frac{\partial}{\partial z}\left(\nu_{eff}\frac{\partial v}{\partial z}\right) - \nu_{eff}\frac{v}{r^2} + \frac{1}{r}\frac{\partial}{\partial r}\left(\nu_t r\frac{\partial v}{\partial r}\right) + \frac{\partial}{\partial z}\left(\nu_t\frac{\partial u}{\partial z}\right) - \frac{\nu_t v}{r^2} \tag{3.29}$$

–temperature equation

$$\frac{\partial T}{\partial t} + u\frac{\partial T}{\partial z} + v\frac{\partial T}{\partial r} = \frac{1}{r}\frac{\partial}{\partial r}\left(\alpha_{eff} r\frac{\partial T}{\partial r}\right) + \frac{\partial}{\partial z}\left(\alpha_{eff}\frac{\partial T}{\partial z}\right) \tag{3.30}$$

where ν_{eff}, α_{eff} and Pr are as defined before.

Turbulence model equations

As shown in chapter 3.2.1 the k–ϵ model is used, with

$$\nu_t = c_\mu\frac{k^2}{\epsilon} \tag{3.31}$$

where k, ϵ, c_μ are as before. Now the differential equations for k and ϵ can be written in the following form:

– the k equation

$$\frac{\partial k}{\partial t} + u\,\frac{\partial k}{\partial z} + v\,\frac{\partial k}{\partial r} = \frac{1}{r}\,\frac{\partial}{\partial r}\,(\nu_{eff} r\,\frac{\partial k}{\partial r}) + \frac{\partial}{\partial z}\,(\nu_{eff}\,\frac{\partial k}{\partial z}) + P + G - \epsilon \qquad (3.32)$$

where $\nu_{eff} = \nu + \frac{\nu_t}{\sigma_k}$ and σ_k is an empirical coefficient.

– the ϵ equation

$$\frac{\partial \epsilon}{\partial t} + u\,\frac{\partial \epsilon}{\partial z} + v\,\frac{\partial \epsilon}{\partial r} = \frac{1}{r}\,\frac{\partial}{\partial r}\,(\nu_{eff} r\,\frac{\partial \epsilon}{\partial r}) + \frac{\partial}{\partial z}\,(\nu_{eff}\,\frac{\partial \epsilon}{\partial z}) + + c_{1\epsilon}\,\frac{\epsilon}{k}\,(P + c_{3\epsilon}G) - c_{2\epsilon}\,\frac{\epsilon^2}{k} \qquad (3.33)$$

where $\nu_{eff} = \nu + \frac{\nu_t}{\sigma_\epsilon}$ and σ_ϵ is an empirical coefficient.

As mentioned before P denotes the production of the turbulent energy from the mean flow and can be defined as

$$P = \nu_t\{2\,[(\frac{\partial u}{\partial z})^2 + (\frac{\partial v}{\partial r})^2 + (\frac{v}{r})^2] + (\frac{\partial u}{\partial z} + \frac{\partial v}{\partial r})^2\} \qquad (3.34)$$

Again the G term represents the production or destruction of the turbulent energy by buoyancy forces and it can be defined as:

$$G = \beta g\,\frac{\nu_t}{\sigma_t}\,\frac{\partial T}{\partial z} \qquad (3.35)$$

In the previous equations $c_{1\epsilon}$, $c_{1\epsilon}$, σ_k and σ_ϵ represent empirical coefficients.

Equation summary

As for the plane symmetric case all the equations of this chapter can be written in the form given by equation (3.26) with individual terms presented in the Table 3.2.

Table 3.2 Diffusion coefficients and source terms in the governing equations for an axisymmetric case

variable	symbol	diffusion coefficient, Γ	source term, S
radial velocity	v	$\nu_{eff} = \nu + \nu_t$	$\frac{1}{r}\frac{\partial}{\partial r}\left(\nu_t r \frac{\partial v}{\partial r}\right) + \frac{\partial}{\partial z}\left(\nu_t \frac{\partial u}{\partial z}\right) - \nu_{eff}\frac{v}{r^2} - \nu_t \frac{v}{r^2}$
vertical velocity	u	$\nu_{eff} = \nu + \nu_t$	$\frac{1}{r}\frac{\partial}{\partial r}\left(\nu_t r \frac{\partial v}{\partial z}\right) + \frac{\partial}{\partial z}\left(\nu_t \frac{\partial u}{\partial z}\right) + \beta g(T_r - T)$
temperature	T	$\frac{\nu}{Pr} + \frac{\nu_t}{\sigma_t}$	none
turb.kin. energy	k	$\nu + \frac{\nu_t}{\sigma_k}$	$P + G - \epsilon$ (*)
turb.energy diss.rate	ϵ	$\nu + \frac{\nu_t}{\sigma_\epsilon}$	$c_{1\epsilon}\frac{\epsilon}{k}(P + c_{3\epsilon}G) - c_{2\epsilon}\frac{\epsilon^2}{k}$

$$P = \nu_t\{2\left[\left(\frac{\partial u}{\partial z}\right)^2 + \left(\frac{\partial v}{\partial r}\right)^2 + \left(\frac{v}{r}\right)^2\right] + \left(\frac{\partial u}{\partial z} + \frac{\partial v}{\partial r}\right)^2\} \qquad G = \beta g \frac{\nu_t}{\sigma_t}\frac{\partial T}{\partial z}$$

The standard constants used in the k–ϵ model are listed in Table 3.3 [Rodi, 1980].

Table 3.3 Constants in k–ϵ model

c_μ	$c_{1\epsilon}$	$c_{2\epsilon}$	$c_{3\epsilon}$	σ_k	σ_ϵ
0.09	1.44	1.92	0.8	1.0	1.3

3.2.3 *Boundary and initial conditions*

Boundary conditions

The boundary conditions have to be specified at the free surface, bottom and a wall at the right. The left boundary is a line of symmetry for all the variables. The boundary conditions are presented for each individual variable.

a) Velocity

The free surface is treated as a symmetry boundary, according to the so–called "rigid lid" assumption [McGuirk and Rodi, 1983; Farell, 1986]. Bottom and wall are treated as no–slip boundaries. This was accomplished using the wall functions of Patankar and Spalding [1972]. These use known behaviour near a wall to compute the velocity at the near wall grid point. This eliminates the requirement of having to laboriously compute out from the wall through the steep gradients of the viscous sublayer.

The treatment of the tangential velocity v at the near–wall grid point is defined through

$$v = \frac{u_*}{\kappa} \ln\left(\frac{u_* \, y_p}{\nu} E\right) \tag{3.36}$$

where the Von Karman constant was taken as $\kappa = 0.4$ and $E = 9.0$, u_* is the shear velocity. In the case that

$$y^+ = \frac{y_p \, u_*}{\nu} \tag{3.37}$$

is less than 11.5, the tangential velocity v is set to its viscous subrange value of

$$v = \frac{u_*^2 \, y_p}{\nu} \tag{3.38}$$

In the constant stress layer, the stress at the point P is approximately equal to that at the wall so the definition of the shear velocity u_*, was generalized [Patankar and Spalding, 1972] to

$$u_* = c_\mu^{1/4} k^{1/2} \tag{3.39}$$

Since the tangential velocity component is close to zero near the wall, then from equation of the continuity

$$\frac{\partial u}{\partial y} = 0 \tag{3.40}$$

where u represents the normal velocity component and y direction normal to the wall.

b) Temperature

The surface, wall and bottom are taken as adiabatic.

c) Turbulent kinetic energy

A zero gradient conditions for k was imposed at the free surface, at the bottom and at the wall.

d) Kinetic energy dissipation rate

The kinetic energy dissipation rate was given a symmetry condition at the free surface. At the bottom and at the wall the dissipation at the near wall grid point was computed from the condition that the length scale is a linear function of distance from the wall, or

$$\epsilon = \frac{u_*^3}{k\ y_p} \tag{3.41}$$

where y_p, k and u_* are as defined before.

Figure 3.1 shows a typical computational grid size with boundary conditions for all the variables.

Initial conditions

Initial conditions are given as the initial temperature profile in the reservoir plus the condition of calm water ($u = v = 0$).

3.3. Numerical model of the bubble plume

The flow of the air bubbles in the water represents an example of two–phase flow. To analyze such a flow there are two possible approaches. One, which is known as Eulerian approach, treats the fluid phase and bubbles as continuum. Through the void fraction (fraction of bubbles in a certain volume of the water) the relationship between two phases is given. For each phase then continuity and momentum equations have to be solved. The second approach, known as Lagrangian, treats the fluid phase as a continuum in which the bubbles are moving under the influence of the driving forces. As far as bubbles move along their trajectories, the mass, momentum and energy transfer, from the bubbles to the fluid phase and vice versa, can be calculated.

The Lagrangian approach, called also trajectory model [Crowe, 1986], incorporates the most natural computational scheme for each phase, namely, a relaxation method for the continuous (fluid) phase and marching method for the dispersed (bubbles) phase. Thus the elliptic nature of the fluid flow and the parabolic nature of the flow of the bubbles in the fluid are retained [Crowe, 1982].

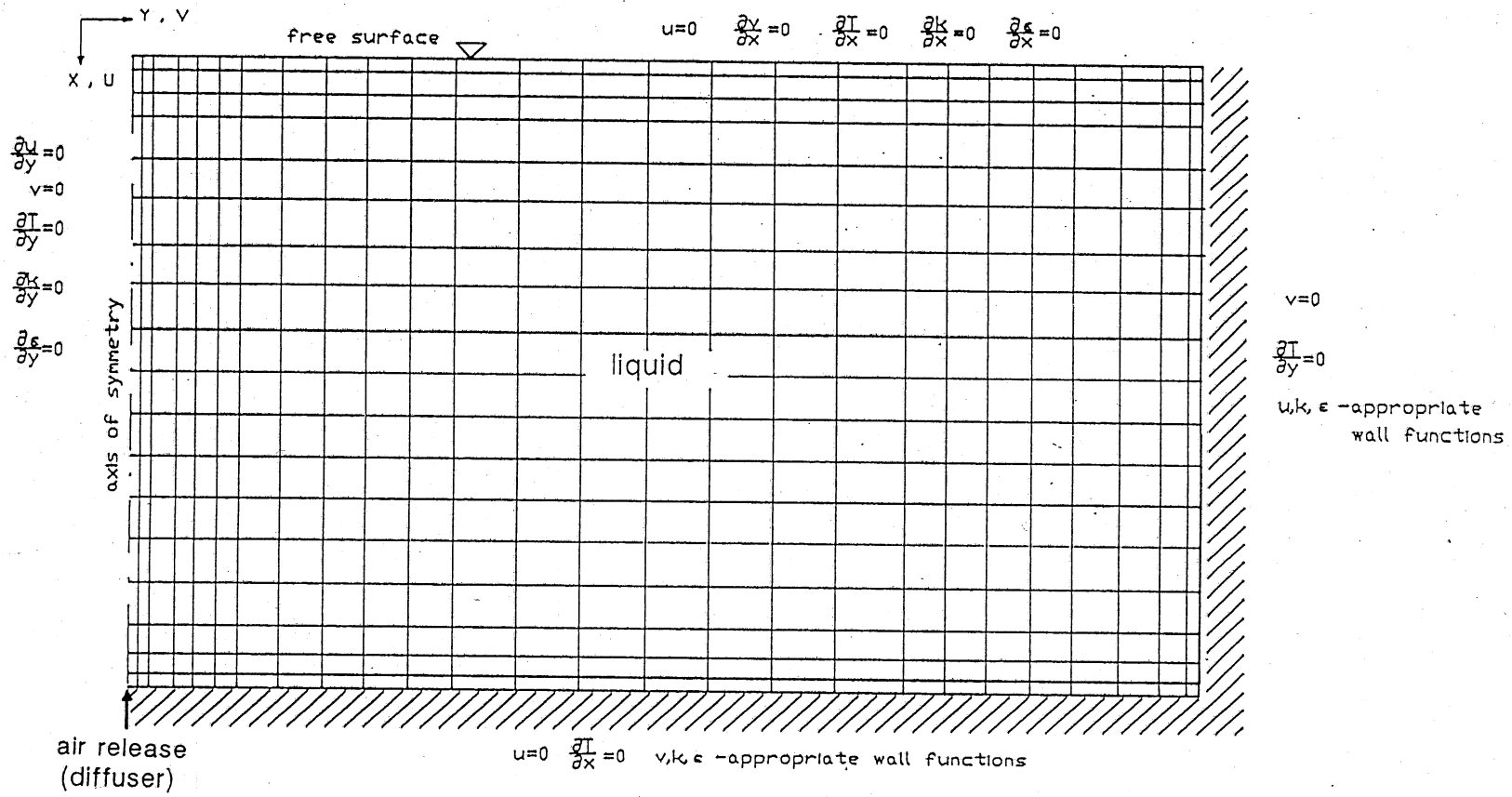

Figure 3.1 Typical computational grid and boundary conditions

3.3.1. *The PSI model*

The PSI (Particle as a Source In cell) model represents the numerical treatment of the gaseous phase. The method was first proposed by Migdal and Agosta [1967]. The basic idea of the method is to treat a particle (in this context – a bubble) as a source of momentum or energy in the fluid flow field.

The elliptic equation in Cartesian coordinates for the conservation of a general variable φ can be written in two dimensions as:

$$\frac{\partial(\varphi\rho)}{\partial t} + \frac{\partial}{\partial x}(\rho u\varphi) + \frac{\partial}{\partial y}(\rho v\varphi) = \frac{\partial}{\partial x}(\Gamma \frac{\partial\varphi}{\partial x}) + \frac{\partial}{\partial y}(\Gamma \frac{\partial\varphi}{\partial y}) + S_\varphi + S_\varphi^b \qquad (3.42)$$

where u = velocity in x direction, v = velocity in y direction, ρ = density, Γ = diffusion coefficient, S_φ = source term, S_φ^b = additional source term due to the presence of the bubbles in the flow field. (When Eqn. 3.42 represents a momentum equation then there is an additional pressure term.) S_φ^b is obtained by solving the Lagrangian equation for the corresponding bubble variable φ^b.

The solution procedure for Eq. (3.42) can be the same for single phase and two phase flow (Eulerian treatment), because the influence of the bubbles is expressed through an additional source term. The additional source term here is a drag force resulting from the movement of the bubbles in the fluid flow. Mass and energy transfer between bubbles and liquid are considered small enough to be neglected.

Accordingly, the only equations in which the presence of air bubbles are introduced in the fluid flow are the momentum equations, given as Eq. 3.5, which can be written now as

$$\frac{\partial\overline{u_i}}{\partial t} + u_j \frac{\partial\overline{u_i}}{\partial x_j} = -\frac{1}{\rho_r}\frac{\partial\overline{p}}{\partial x_i} + \frac{\partial}{\partial x_j}(\nu \frac{\partial\overline{u_i}}{\partial x_j} - \overline{u_i'u_j'}) + g_i\beta(\overline{T}_r - \overline{T}) + \text{DRAG FORCE} \qquad (3.43)$$

where the drag force remains to be evaluated.

This method was previously used by Sharma [1977] for the computation of gas–particle flows in orifices and venturis, by Crowe et al. [1977] for gas–droplet flows with application to spray cooling, by Sharma et al. [1980] for the computation of the swirling gas–particle flows in pulverized coal classifiers, by Lockwood et al. [1980] for the prediction of pulverized coal–fired furnaces, by Durst et al. [1984] for the study of the flow of different particles in fluid flow.

The behavior of the bubbles in the turbulent flow cannot be quantified satisfactorily [Azbel, 1981]. Herein the possible influence of the bubbles on the turbulence of the fluid flow is therefore neglected. The same approach has been taken by other investigators e.g. by Durst [1984] and Crowe [1977] in the case of particulate flow

The computational procedure to solve the air bubble plume problem has the following steps:

1. Solve a fluid flow field without bubbles.
2. Calculate the velocity and trajectory of the bubbles in the fluid flow field.
3. Evaluate the new source terms due to the bubbles.
4. Solve the fluid flow field with new source terms and repeat the procedure until it converges.

Since the flow is unsteady, this procedure has to be repeated for each time step.

3.3.2. *Motion of the bubbles in the fluid flow*

Equation of motion

The equation of motion for a spherical bubble with an equivalent diameter d_b in a turbulent fluid flow is [Azbel, 1981]:

$$\frac{\pi d_b^3 \rho_b}{6}\frac{dv_b}{dt} = \frac{\pi d_b^3 \rho}{6}\frac{dv}{dt} + \frac{1}{2}\frac{\pi d_b^3 \rho}{6}\left(\frac{dv}{dt} - \frac{dv_b}{dt}\right) + \frac{1}{2} c_D \rho A_b |v - v_b|(v - v_b) - \frac{1}{6}\pi d_b^3 \rho g \qquad (3.44)$$

where ρ_b = density of the bubble, ρ = density of the fluid, v_b = absolute velocity of the bubble, v = absolute velocity of the fluid, A_b = area of the bubble, c_D is the drag coefficient which varies as a function of bubble Reynolds number

$$Re_b = \frac{\rho d_b |v - v_b|}{\mu} \qquad (3.45)$$

and Grashof number

$$G = \frac{g\,\mu^4}{\rho\,\sigma^3} \qquad (3.46)$$

where μ = dynamic viscosity of the water, σ = surface tension.

According to Peebles and Garber [1953] $c_D(Re_b,G)$ can be specified as follows:

$$
\begin{aligned}
c_D &= 24\ Re_b^{-1} && \text{for } Re_b < 2 \\
c_D &= 18.7\ Re_b^{-0.68} && \text{for } 2 \le Re_b \le 4.02\ G^{-0.214} \\
c_D &= 0.6145\ \frac{d_b}{2}|v - v_b| - 2 && \text{for } Re_b \ge 4.02\ G^{-0.214}
\end{aligned}
\qquad (3.47)
$$

The first term on the righthand side of Eqn. (3.44) corresponds to the acceleration of the water, the second term is equivalent to the inertia of a virtual mass attached to a bubble, the third term is a drag force and the fourth term is the buoyancy force acting on a bubble. More about the equation of motion can be found in Appendix C.

Bubble velocity and trajectory

In the PSI method [Crowe, 1977] the total air mass release rate is distributed over several computational control volumes. The air mass fraction in each control volume consists of a number of bubbles of various diameters. The velocity and trajectory of a limited number of bubbles, taking into account appropriate mass fractions are then calculated.

If the total mass flow rate of bubbles is $\dot{m}^b$, if the mass fraction of bubbles at location j (in horizontal direction) is f_j, and if the mass fraction of bubbles of class i with diameter d_i is f_i, the number flow rate of spherical bubbles $\dot{N}^b_{ij}$ $[s^{-1}]$ of class i at the location j is according to Durst et al. [1984]

$$\dot{N}^b_{ij} = \frac{6\ \dot{m}^b}{\pi\ \rho_b\ d_i^3} f_i f_j \qquad (3.48)$$

The equation of motion (3.44) can be rewritten, for a bubble of class i at the location j as

$$
\begin{aligned}
\frac{\pi d_b^3 \rho_b}{6} \frac{dv^b_{ij}}{dt} &= \frac{\pi d_b^3 \rho}{6} \frac{dv}{dt} + \frac{1}{2} \frac{\pi d_b^3 \rho}{6} \left(\frac{dv}{dt} - \frac{dv^b_{ij}}{dt}\right) \\
&+ \frac{1}{2}\ c_D \rho A^b_i |v - v^b_{ij}| (v - v^b_{ij}) - \frac{1}{6}\ \pi d_b^3 \rho g
\end{aligned}
\qquad (3.49)
$$

with c_D given by Eq. (3.47) and v^b_{ij} = bubble velocity of class i at location j, A^b_i = area of the bubble of the class i.

Eq. (3.49) is solved by a Runge–Kutta method.

The bubble position after time interval Δt is:

$$x = x_0 + (v^b_{ij} + v^b_{ij0})\ \Delta t/2 \tag{3.50}$$

where x represents a coordinate in the direction of bubble motion, and subscript $_0$ refers to the beginning of the time interval.

The gas is presumed to follow the isothermal expansion law so that

$$\rho_b = \frac{\rho_t(H_d - z)}{H_t} \tag{3.51}$$

where ρ_t = gas density at the pressure of one atmosphere, H_t = atmospheric pressure head and H_d = absolute pressure head at the level of the air release (diffuser), z = distance above the air release.

The momentum source term due to the bubbles

The transfer of momentum between the rising bubbles and the ambient liquid is through the bubble drag force. If we consider one class of bubbles i and one location j and assume a constant bubble diameter along the trajectory, the bubble momentum source term S^b_{ij} in equation (3.42) applied to any control volume is [Durst et al., 1984]

$$S^b_{ij} = \frac{1}{V_{cv}} \dot{N}^b_{ij}\ \rho\ \frac{A^b_i}{2} \int_{t_{in}}^{t_{out}} c_D(v - v^b_{ij})\,|v - v^b_{ij}|\ dt \tag{3.52}$$

where t_{in} and t_{out} = times at which the bubble enters and leaves the control volume, respectively and V_{cv} = volume of the control volume. Durst et al. [1984] proposed for more efficient calculation of the source term that velocities be averaged over the residence time of the bubble in the control volume. Following that idea and using experimental evidence [Yip et al., 1970] that a bubble will reach terminal velocity very soon after it is released from the diffuser, a different (and simpler) equation can be used to evaluate the drag force:

$$S^b_{ij} = \frac{1}{V_{cv}} \dot{N}^b_{ij}\ \frac{\pi d_b^3}{6}\ \rho\ g\ (t_{out} - t_{in}) \tag{3.53}$$

Instead of evaluating a drag force as in Eq. (3.52) one evaluates a buoyancy force in Eq. (3.53).

The total bubble source term for bubbles of all classes which pass through the control volume CV, can then be expressed as:

$$S^b_{cv} = \sum_i^{cv} \sum_j^{cv} S^b_{ij} \tag{3.54}$$

Summation over the control volume is designated by $\sum^{cv}$. The term S^b_{cv} corresponds to the term S^b_{φ} in the flow Eq. (3.42).

The mass fraction f_j of bubbles at the location j and the mass fraction f_i of bubbles with diameter i are specified according to the experimental results by other authors. In extensive experimental work Barczewski [1983] found that the air mass fractions over the bubble plume width (f_j here) follow a Gaussian distribution. Bubble size distributions (f_i here) have been fitted with log–normal distributions rather successfully by Silberman [1957] and Azbel [1981]. The bubbles are introduced in a finite number of control volumes corresponding to the position and width of the diffuser. In each control volume a finite number of bubbles is introduced so that the log normal distribution is satisfied. More about the formation of bubbles and their sizes can be found in Appendix B.

3.4. Numerical model validation and results

Results obtained with the numerical model described above have been compared with measurements in two steps. The first step was the verification of the fluid flow model with experimental data obtained for water jets, and a second step was the comparison of the model predictions with measurements for air bubble plumes.

Andreopoulos et al. [1986] performed laboratory experiments on the vertical plane buoyant jets in shallow water. The prediction of the model, shown as a solid line, of the decay of the centerline velocity W made dimensionless with the exit velocity W_0 is shown in Figure 3.2 for nonbuoyant conditions. The height z is made dimensionless with the jet virtual origin z_0 and the exit width B. The value of $(z - z_0)/B = 100$ corresponds to the surface, or the region of the jet impingement. In addition to the to the measurements from Andreopoulos et al. [1986] for the vertical plane jet in a shallow water, marked with a square, the data by Gutmark et al. [1976] for a jet impinging on a wall are also presented and marked with a star. The fact that there is a good agreement between calculations and both measurements indicates that jets impinging on free surface and on a wall do indeed behave rather similarly. Accordingly the treatment of the free surface with a "rigid lid" assumption is correct, as found by McGuirk and Rodi [1977].

When the jet deflects at the surface it spreads horizontally as a surface jet. It has been shown [Hossain and Rodi, 1980; Celik and Rodi, 1984; Rodi, 1985; Nakatsuji et al., 1989] that the k–ϵ model with constants as presented in Table 3.3 has difficulties in taking into account the damping effect of the free surface and the density interface. The performance of such a basic k–ϵ model is compared with steady state measurements by Andreopoulos et al. [1986] in Figure 3.3.

The poor performance of the basic k–ϵ model in the prediction of the surface velocities as seen in Fig. 3.3 lead to the use of the buoyancy–extended version of the k–ϵ turbulence model as proposed by Hossain and Rodi [1980], derived by simplifying modeled transport equations for the Reynolds stresses, turbulent heat fluxes and temperature fluctuations. The buoyancy source terms in these equations are retained in the process of

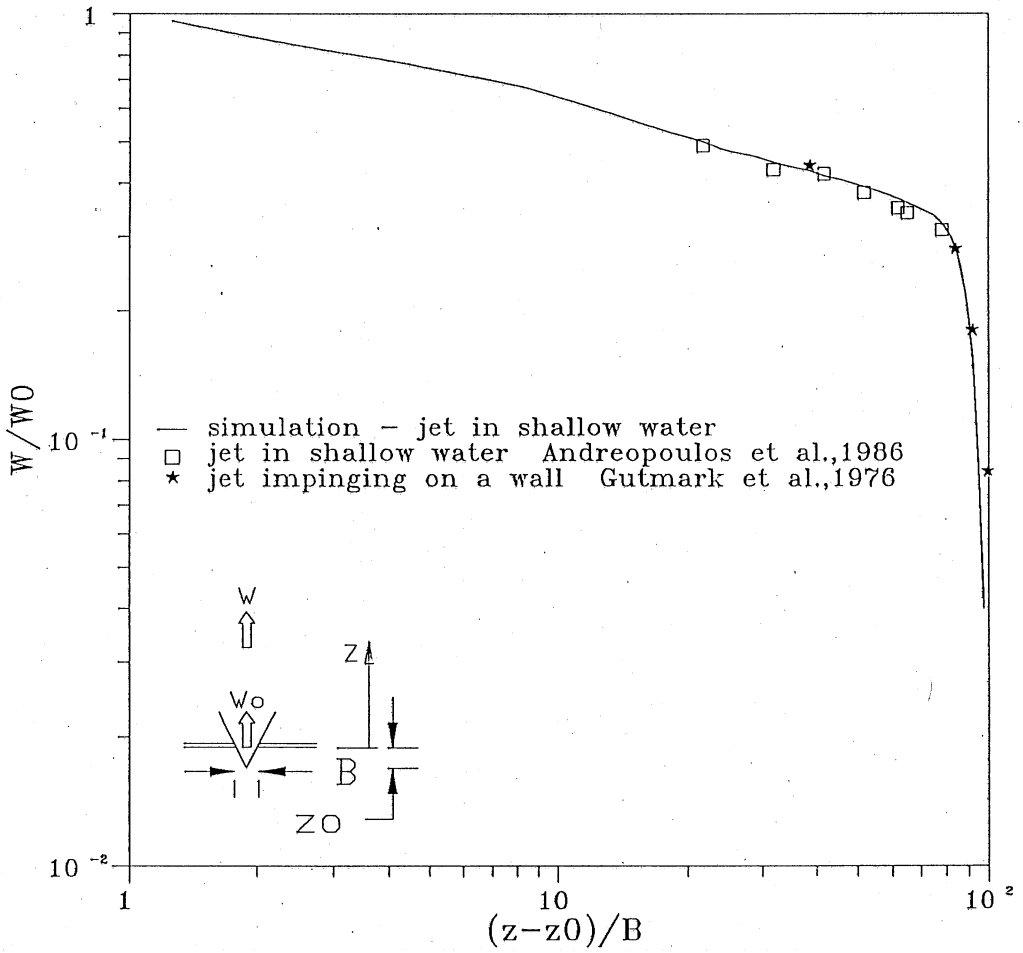

Figure 3.2 Prediction of the jet centerline velocity (F = ∞, Re = 2367)

simplifying them to algebraic expressions. The turbulent kinetic energy k and rate of its dissipation ϵ appearing in the algebraic expressions for these quantities are determined from transport equations for these quantities, which also contain buoyancy terms. The difference to the basic k–ϵ model is that the parameters c_μ and σ_t now depend on stratification and on surface damping:

$$c_\mu = \omega \frac{\overline{v^2}}{k} \quad ; \quad \sigma_t = \frac{\omega}{\alpha} \tag{3.55}$$

with

$$\omega = \frac{1 - c_2 + \frac{3}{2} c_2 c_2' f}{c_1 + \frac{3}{2} c_1' f} \frac{1 - \frac{1 - c_3}{1 - c_2 + \frac{3}{2} c_2 c_2' f} \frac{1 - c_{2_T}}{c_{1_T}} \alpha B}{1 + \frac{1 - c_3}{c_1 + \frac{3}{2} c_1' f} \frac{1}{c_{1_T}} B} \tag{3.56}$$

$$\alpha = \frac{1}{c_{1_T} + c_{1_T}' f + 2(1 - c_{3_T}) RB} \; ; \; B = \beta g \frac{k^2}{\epsilon^2} \frac{dT}{dy} \tag{3.57}$$

$$\frac{\overline{v^2}}{k} = \frac{2}{3} \frac{c_1 - 1 + \frac{P+G}{\epsilon}(c_2 - 2c_2 c_2' f) + \frac{G}{\epsilon}(3 - c_2 - 2c_3 + 2c_2 c_2' f)}{c_1 + 2c_1' f + \frac{P+G}{\epsilon} - 1} \tag{3.58}$$

Where P and G are defined already, as Eqns. 3.24 and 3.25 for a plane symmetric case and as Eqns. 3.34 and 3.35 for an axisymmetric case, respectively.

The diffusion constants σ_k and σ_ϵ in the k–ϵ equations are also replaced by buoyancy–dependent functions for reasons explained in detail in Hossain and Rodi [1980]:

$$\sigma_k = \frac{\omega}{c_k} \quad ; \quad \sigma_\epsilon = \frac{\omega}{c_\epsilon} \tag{3.59}$$

The damping function f is given as:

$$f = \frac{1}{5} \frac{k^{3/2}}{\epsilon} \left[\frac{1}{y} + \frac{1}{(H - y) + 0.04\, k_s^{3/2}/\epsilon_s} \right] \tag{3.60}$$

where y is a distance from the bottom, H = total depth, the subscript s refers to the surface.

For the constants appearing in the above buoyancy extensions of the k–ϵ model the following values have been adopted from Gibson and Launder [1978]:

Table 3.4 Constants in buoyancy–extended k–ϵ model

c_k	c_ϵ	c_1	c_2	c_3	c'_1	c'_2	c_{1T}	c_{2T}	c_{3T}	c'_{1T}	R
0.24	0.15	2.2	0.55	0.55	0.5	0.3	3.0	0.5	0.5	0.5	0.8

At the free surface, symmetry conditions are retained for all the dependent variables but the dissipation ϵ. The surface value ϵ_s is assumed to be related to the surface value of the turbulent kinetic energy k_s and to a typical length scale of the shear layer, for which the depth H is taken :

$$\epsilon_s = a \frac{k_s^{3/2}}{H} \tag{3.61}$$

Nakatsuji et al. [1989] found, after extensive testing of the model versus measurements, that the value of 1.0 for the constant a is appropriate.

The prediction of the buoyancy modified k–ϵ turbulence model as presented above for the same experiment as given in Fig. 3.3 is shown in Figure 3.4. It can be seen that this model predicts the velocities more correctly.

Vertical velocities in the liquid phase of a bubble induced vertical plume were measured by Goossens [1979] in a water filled tank of 1.25 m diameter and 0.25 m depth. The air was released at the bottom of the tank and created an axisymmetric flow field. The air diffuser was 2.6 cm in diameter. Air release rates of 2.85×10^{-5} m^3/s, 5.73×10^{-5} m^3/s and 8.6×10^{-5} m^3/s were used. The water in the tank was isothermal. Profiles of vertical water velocities measured by Goossens in several horizontal planes are compared with simulation results in Figs. 3.5, 3.6 and 3.7. All simulations started with a quiescent tank (zero velocity) at the time the air release was turned on, and were continued to approximately 320 seconds. At that time quasi–steady state conditions had been reached. The match between measurements (represented by symbols) and simulation results (solid lines) are best for the smallest air release rate (Fig.3.5). The worst fit between measurements and simulations is at the highest air release rate (Fig. 3.7) and closest to the release point.

Profiles of steady state horizontal velocities measured by Goossens [1979] in a different tank of 1.25 m diameter and 1.25 m depth with Q_{air} = 0.23 l/s are shown in Figure 3.8. The prediction of the model is shown to be good.

All the simulations presented so far were for a steady state and for isothermal receiving water. To evaluate model performance over time, and to obtain the information on the development of the flow field in a stratified water body, experiment No. 2 (see Table 4.1 and Figures 4.1 and 4.3) was

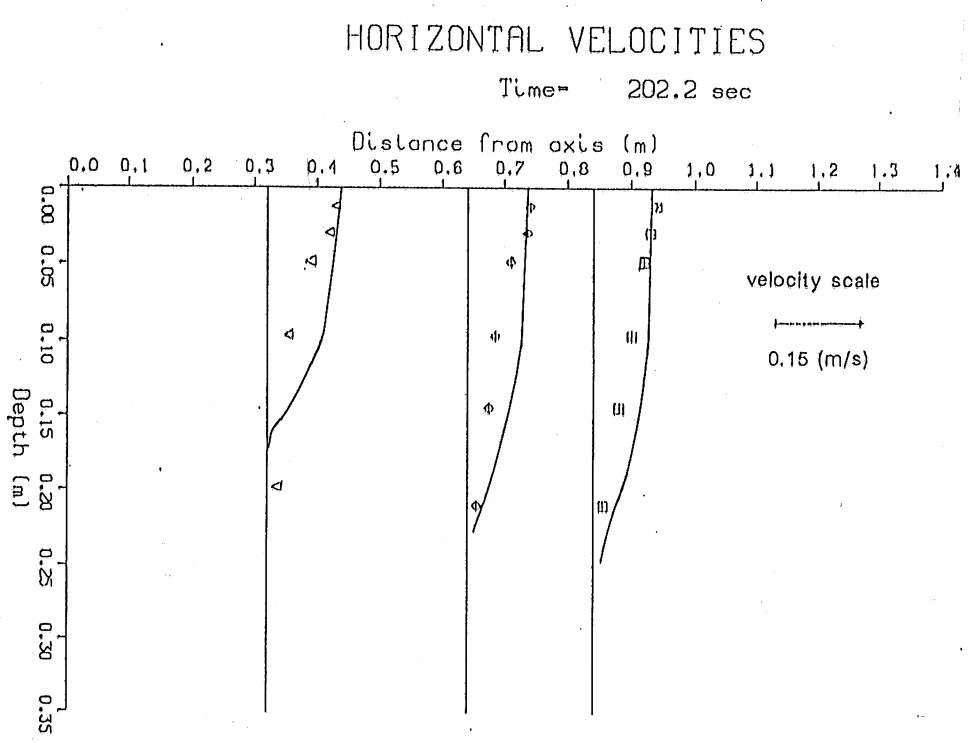

Figure 3.3 Simulation of Andreopoulos et al. [1985] experiment (symbols) with a basic k–ϵ model (solid line). Re = 2367, F = ∞

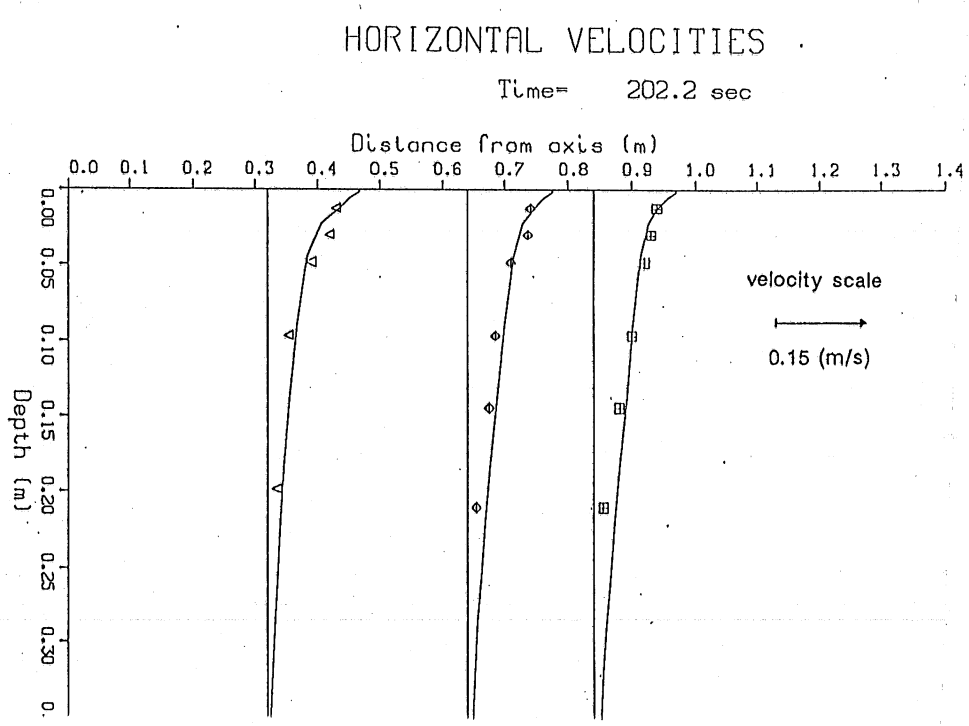

Figure 3.4 Simulation of Andreopoulos et al. [1985] experiment (symbols) with buoyancy extended k–ϵ model (solid line). Re = 2367, F = ∞

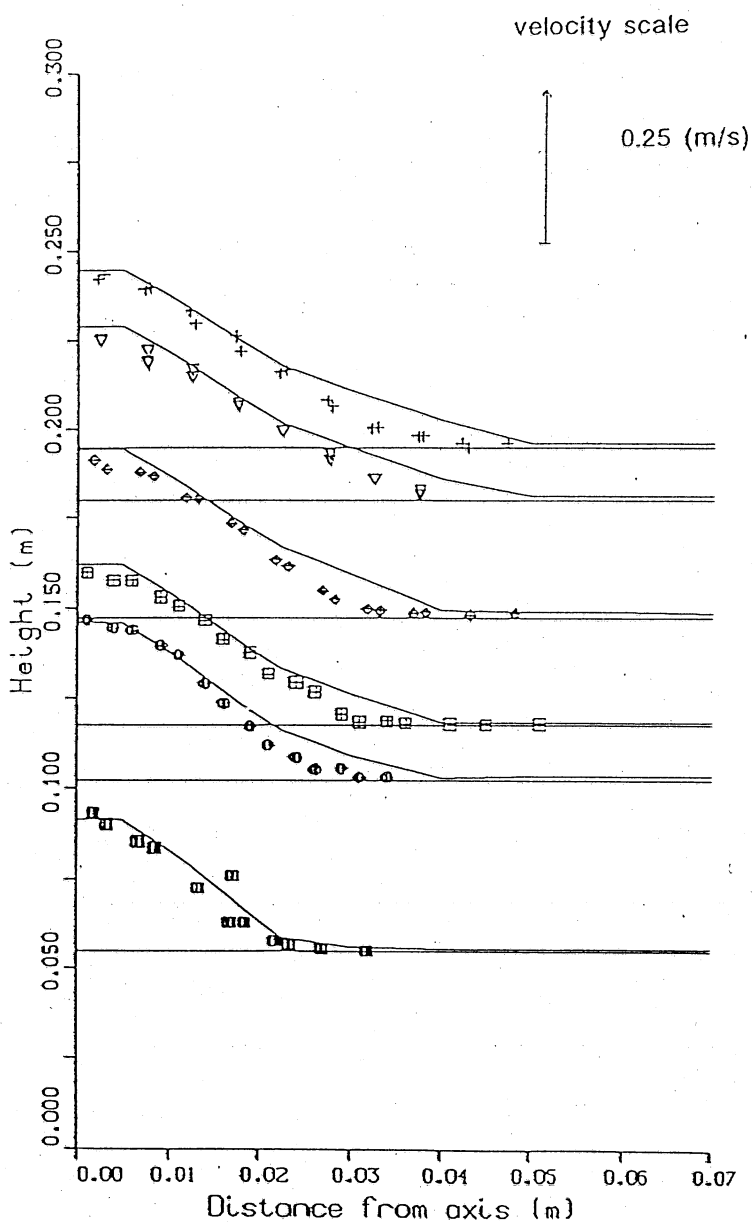

Figure 3.5 Simulation of the experiment with air bubbles with $Q_{air} = 2.85 \times 10^{-5}$ m^3/s

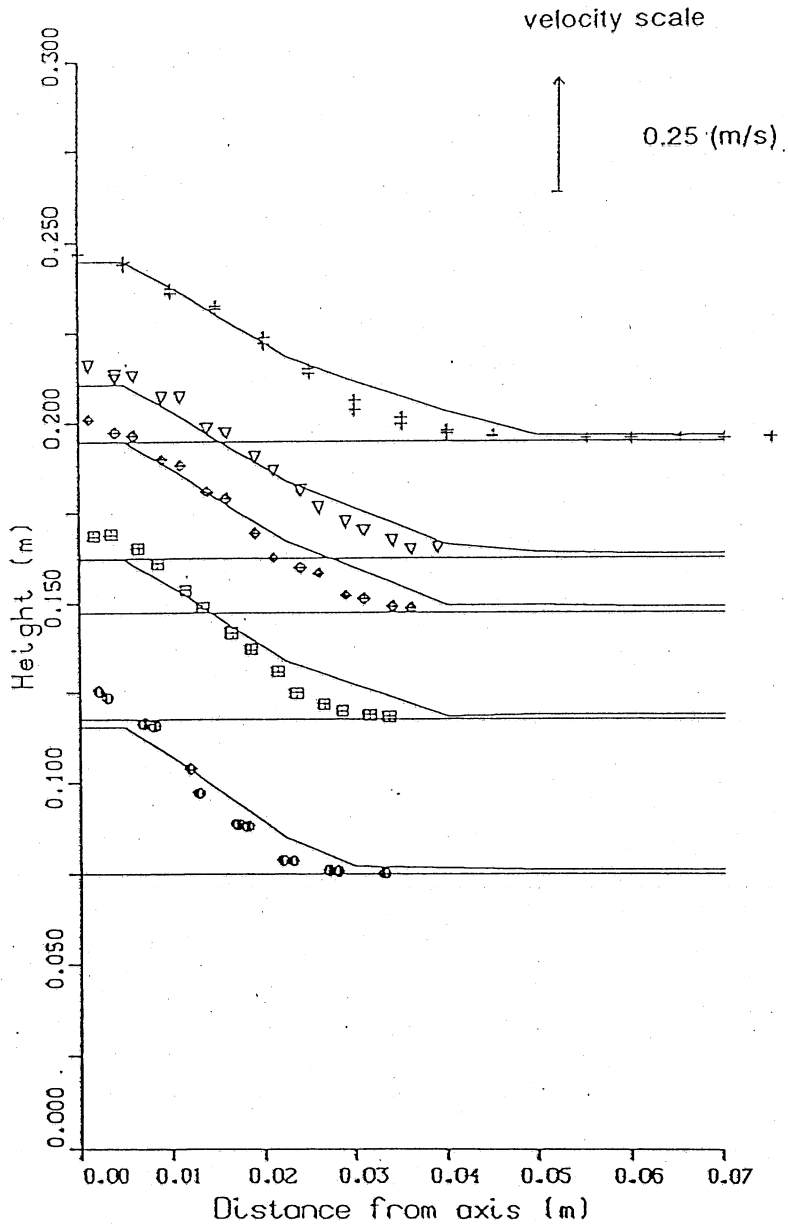

Figure 3.6 Simulation of the experiment with air bubbles with $Q_{air} = 5.73 \times 10^{-5}$ m^3/s

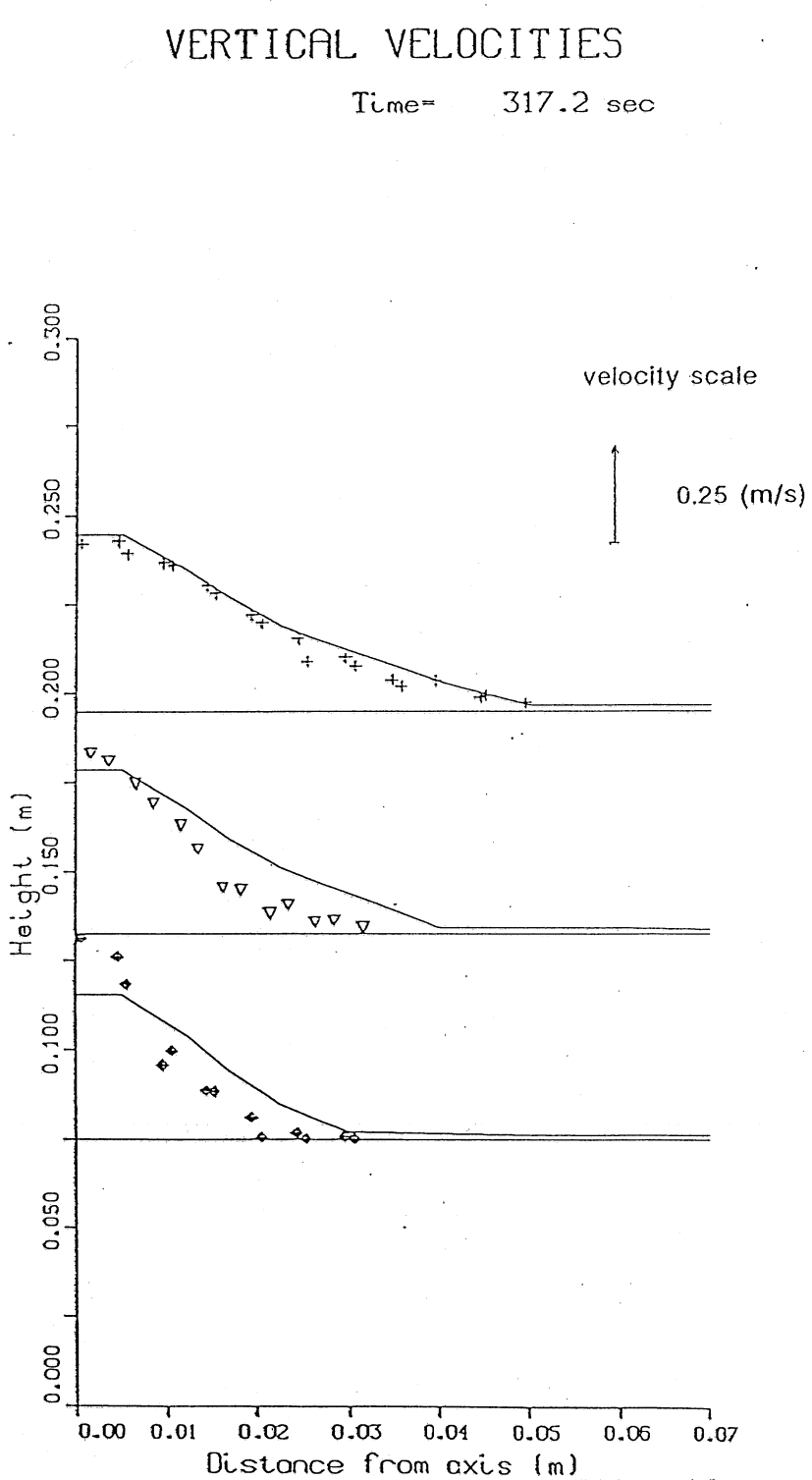

Figure 3.7 Simulation of the experiment with air bubbles with $Q_{air} = 8.6 \times 10^{-5}$ m^3/s

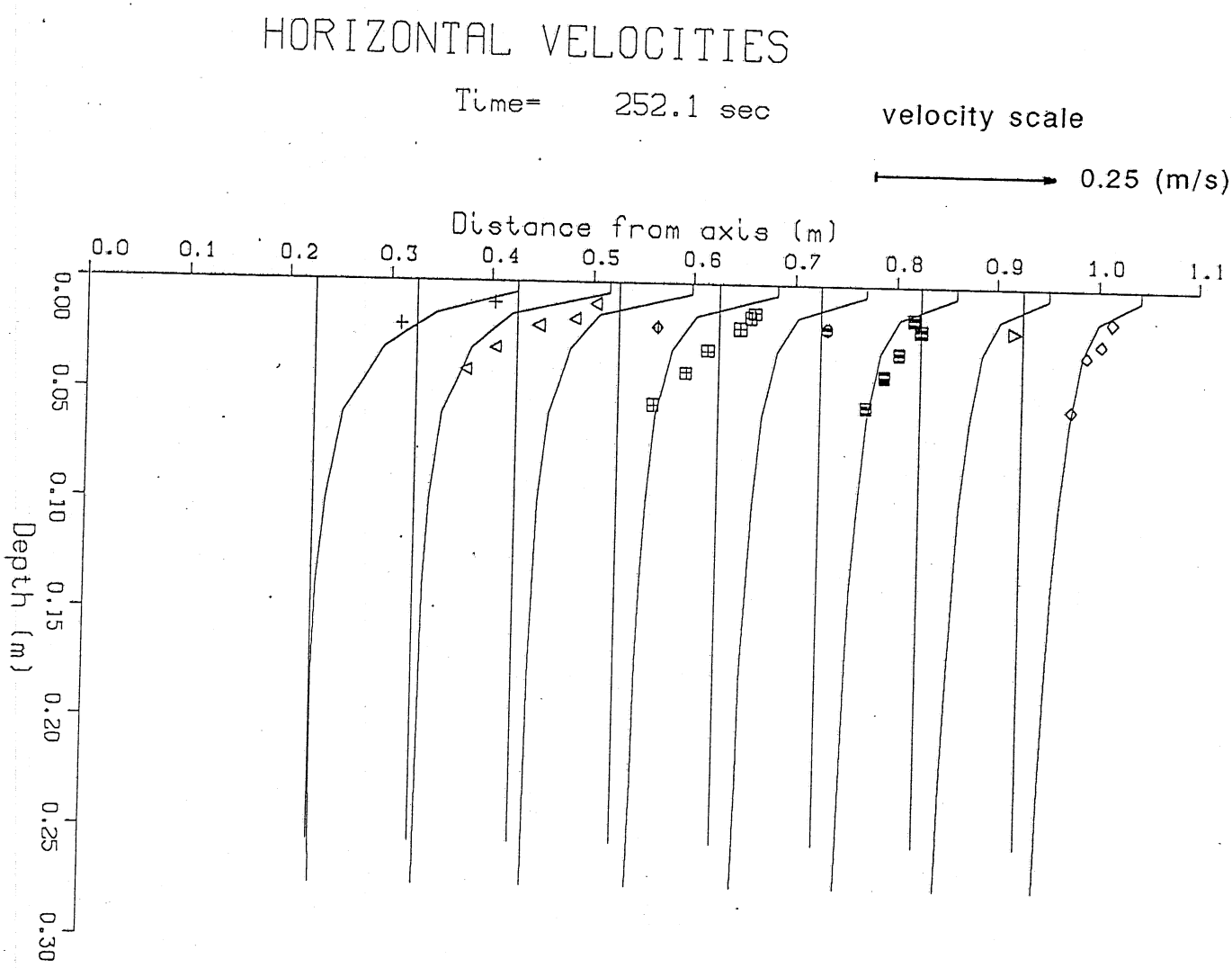

Figure 3.8 Simulation of the experiment with air bubbles with $Q_{air} = 2.3 \times 10^{-4}$ m^3/s

simulated. The results of the simulation, in terms of the flow field and temperature contours, are shown in Figures 3.9 to 3.11. Each of the figures is representing a plane of radial symmetry with a bubble plume axis on the left hand side. The entire process of destratification is shown starting from the very first motion of the water induced by the air release, for t=0.2 s, up to the stage when the entire tank was well mixed, for t=607 s. It can be seen that the mixing progresses from the surface down resulting in the depletion of the surface layers. At the same time the thermocline (which can be taken roughly as the isotherm with a temperature of 18° C) deepens. When the thermocline reaches the depth of the diffuser it becomes stationary and "erosion" starts from above it until the entire tank is well mixed. The very same behavior is observed in measurements (see Figures 4.2 to 4.11).

Temperature time series predicted by the simulation are compared with experiments in Figure 3.12 at several depths. It can be seen that the model predicts faster changes in the temperature field than measured due to a higher rate of mixing. This is a known problem. Franke, Leschziner and Rodi [1987] found that a buoyancy–extended version of a k–ϵ model of turbulence, although it captures all essential elements of the interaction between shear and buoyancy, has a mixing level which is too high, leading to an excessively fast erosion of the stratification. They explained that this mismatch may be related to the fact that the mixing process is essentially a three–dimensional process where the third velocity component may produce additional damping effects.

Although the simulation of experiment No. 2 shows the main features of the destratification by an air bubble plume, one question of interest is how the size of the ambient water pool affects the process. To resolve this question a second set of experiments was performed in a cylindrical basin with 4.52 m diameter and depth of 1.0 m. For one of those experiments, No. 5 (see Table 4.2 and Figures 4.1 and 4.6), a detailed analysis of the measurements was performed (see Chapter 4).

Figures 3.13 to 3.16, present the results of the numerical simulation of experiment No. 5. The process of destratification is shown sequentially in the velocity vectors, streamlines and temperature contours, starting from the very beginning at t=0.1 sec to the quasi steady state at t=500 sec.

Before discussing the elements of the flow field displayed in Figures 3.13 to 3.16 one should remember that the simulated rates of mixing are higher then the measured ones. Therefore processes are developing faster and with a higher intensity in the simulation, but since the relationship between the governing parameters are predicted correctly, one can use the results to analyze the flow field.

The mixing starts with only a small region affected by the air release (t=10 sec). As time progresses the mixing region spreads over the entire water body. The highest velocities are in the vicinity of the air bubble plume. When the cold water from hypolimnion reaches the surface it spreads and after some distance it plunges. This can be seen at t=35 sec when

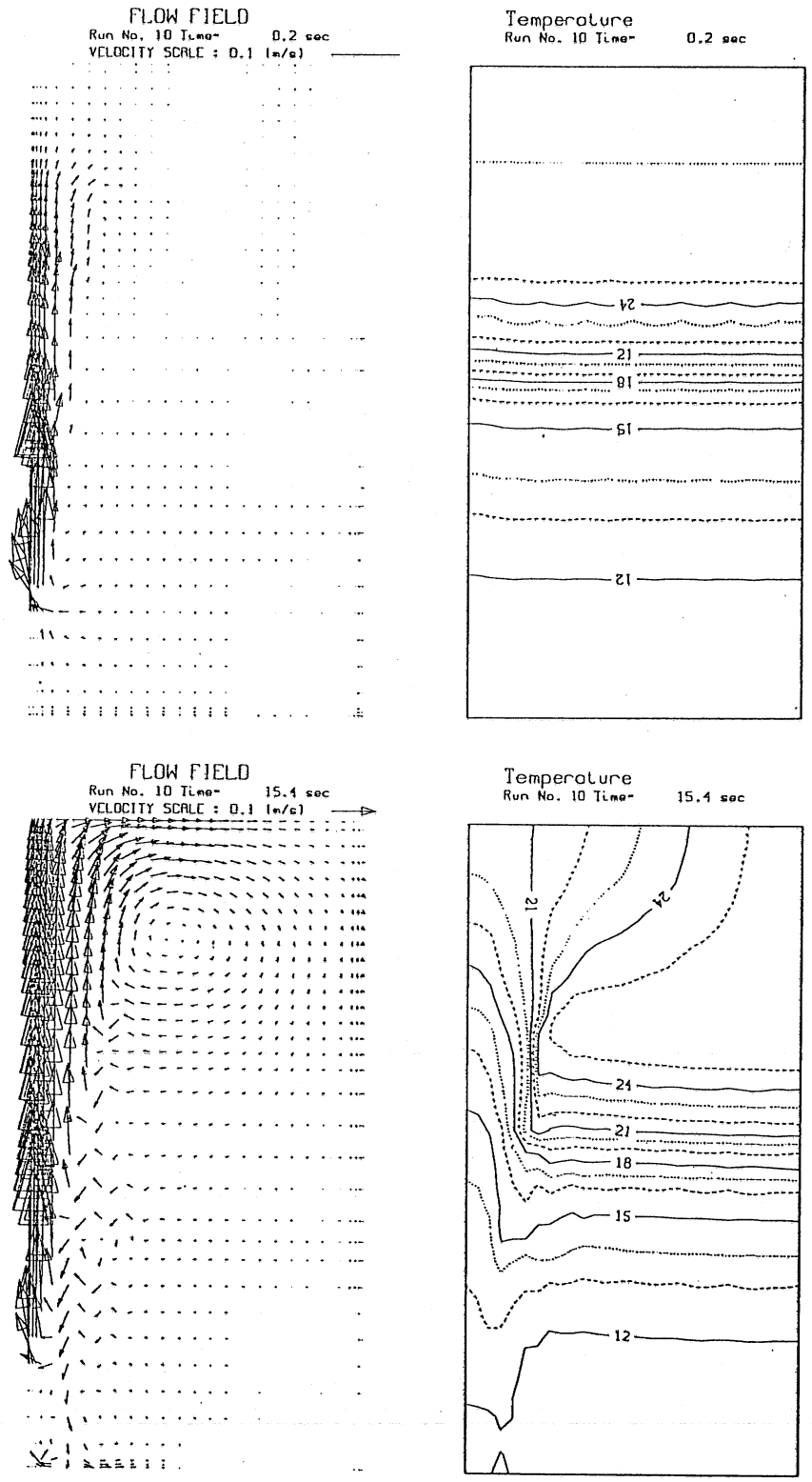

Figure 3.9 Simulation of the experiment No. 2, t=0.2s and t=15.4 s

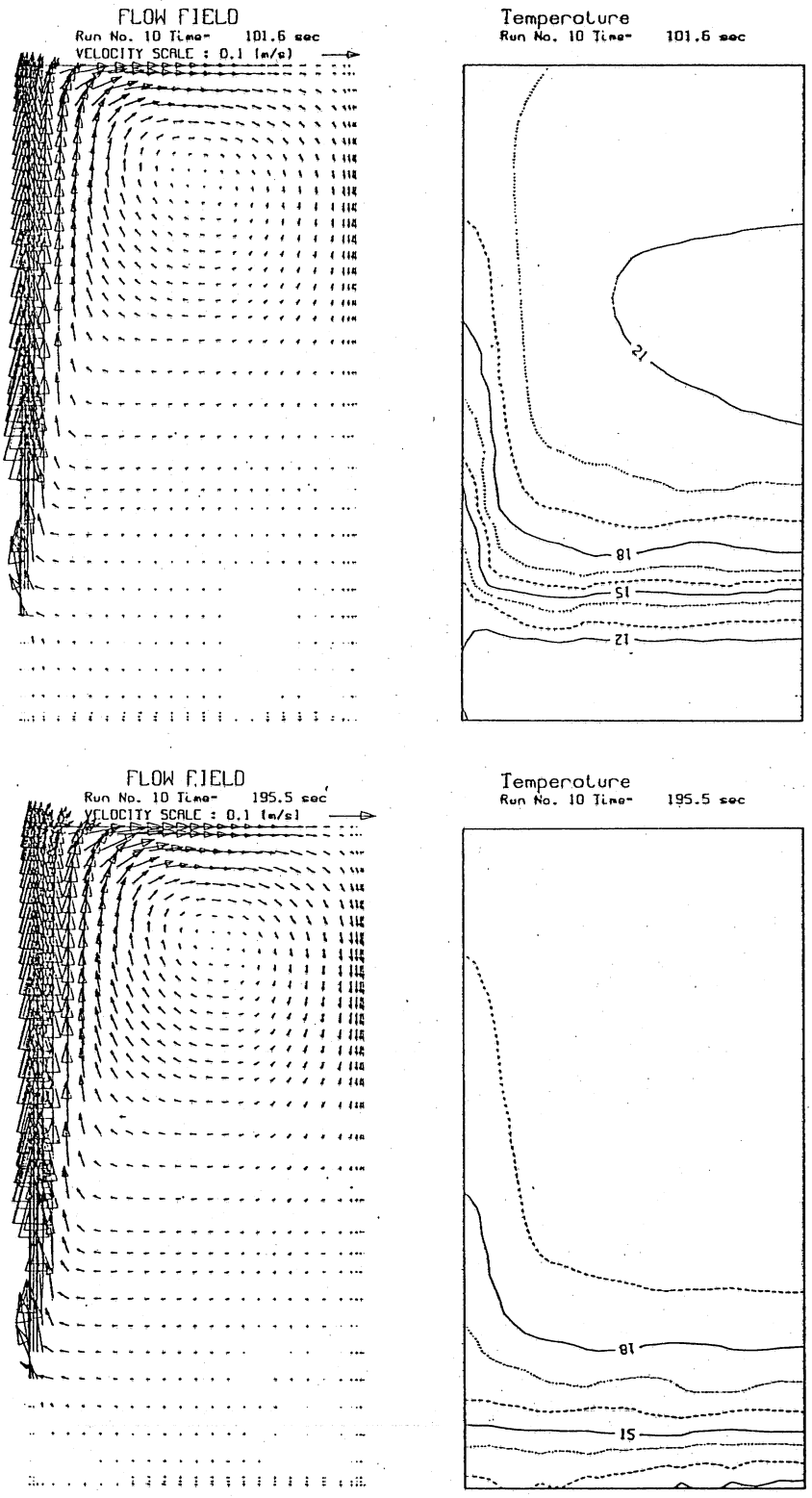

Figure 3.10 Simulation of the experiment No. 2, t=101.6s and t=195.5s

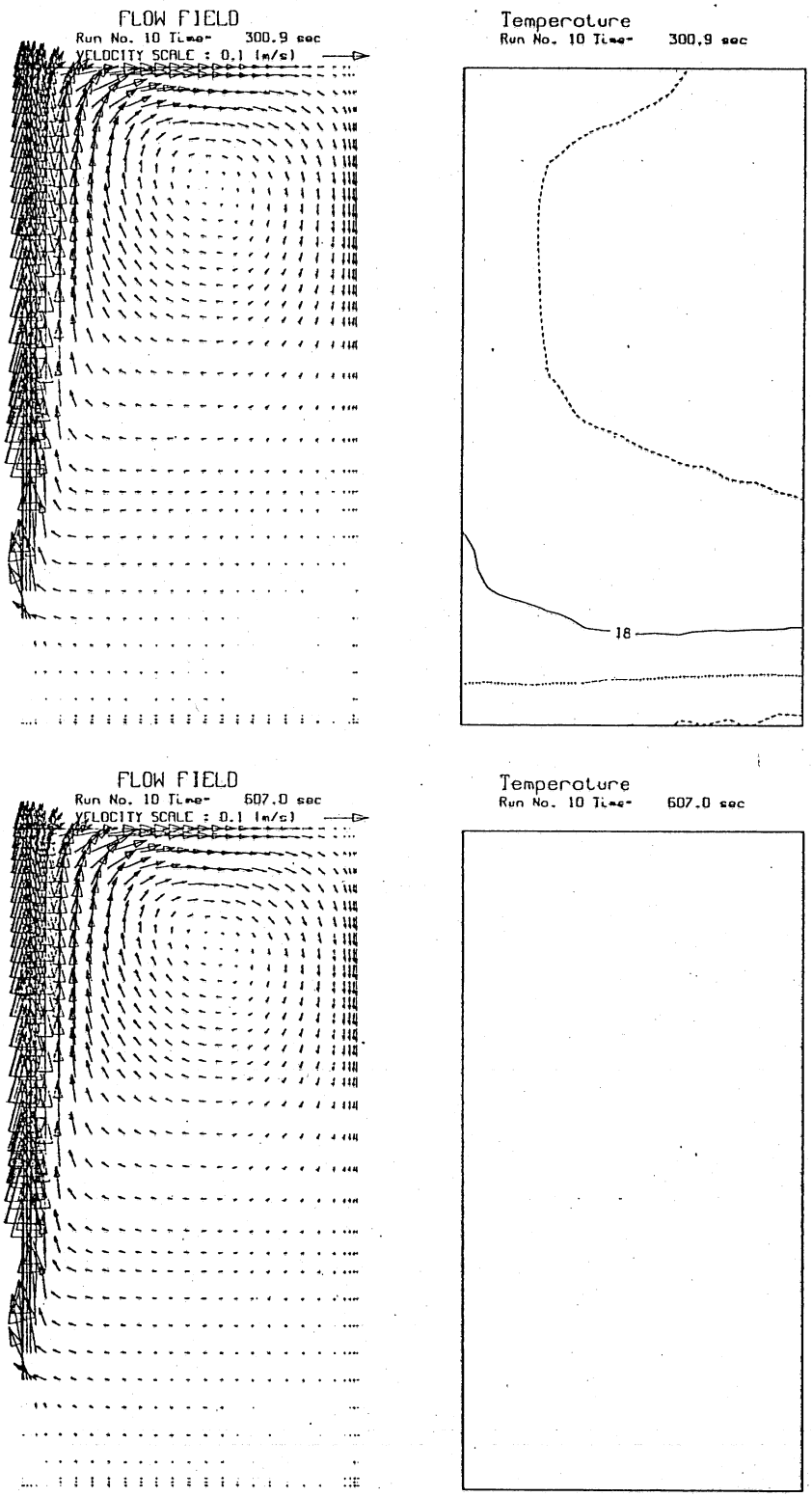

Figure 3.11 Simulation of the experiment No. 2, t=300.9s and t=607.0s

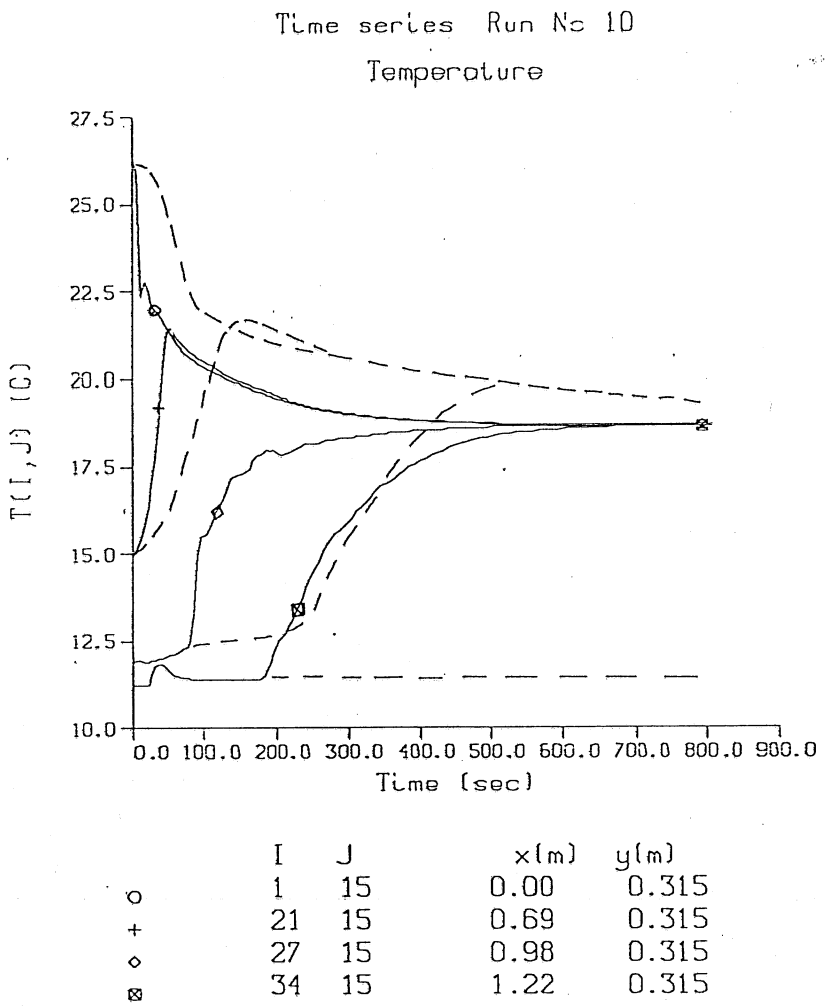

Figure 3.12 Comparison of the simulated time series (solid line) with measurements (dotted line) for experiment No. 2

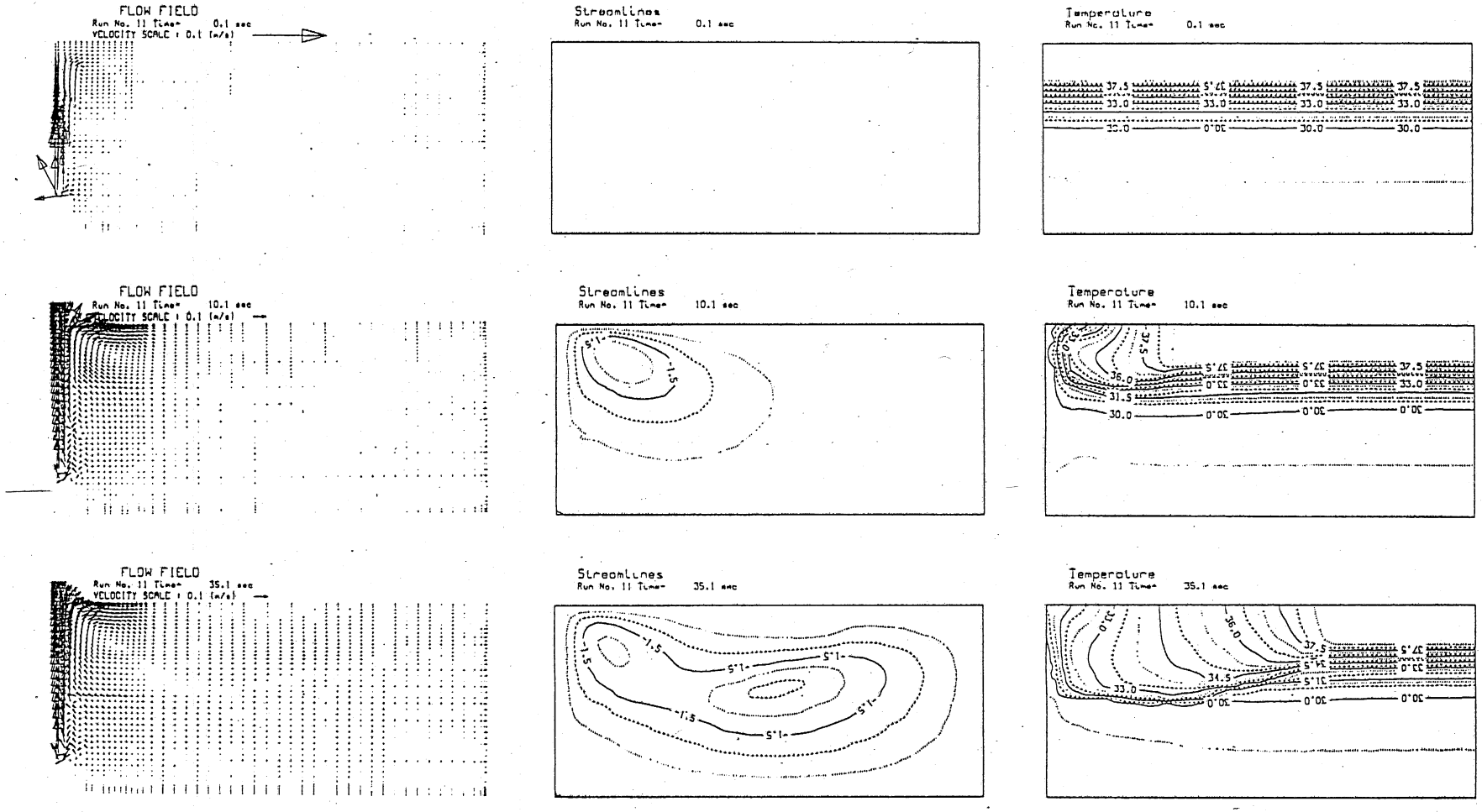

Figure 3.13 Simulation of the experiment No. 5, t=0.1; 10.0 and 35.1s

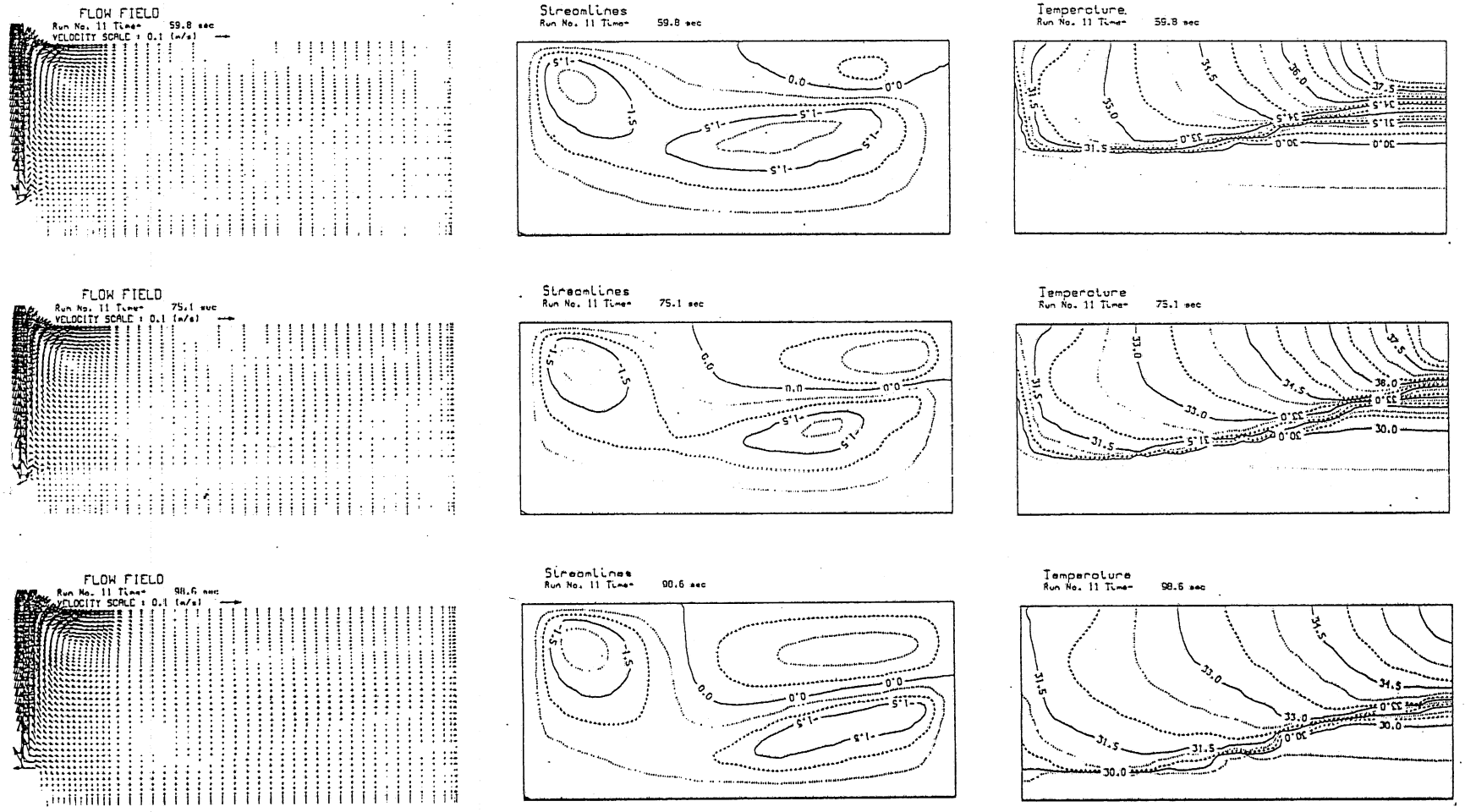

Figure 3.14 Simulation of the experiment No. 5, t=59.8; 75.1 and 98.6s

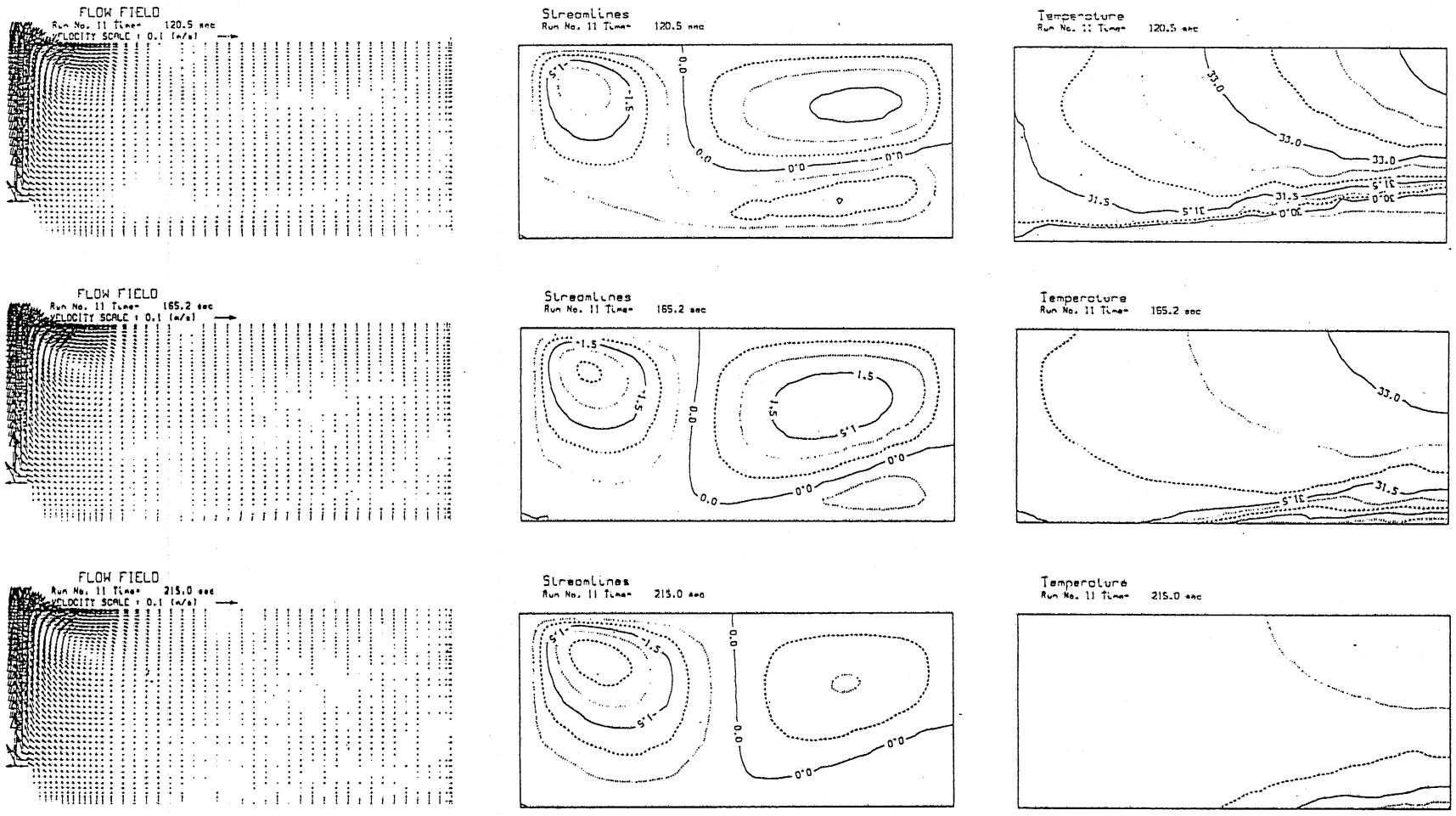

Figure 3.15 Simulation of the experiment No. 5, t=120.5; 165.2 and 215s

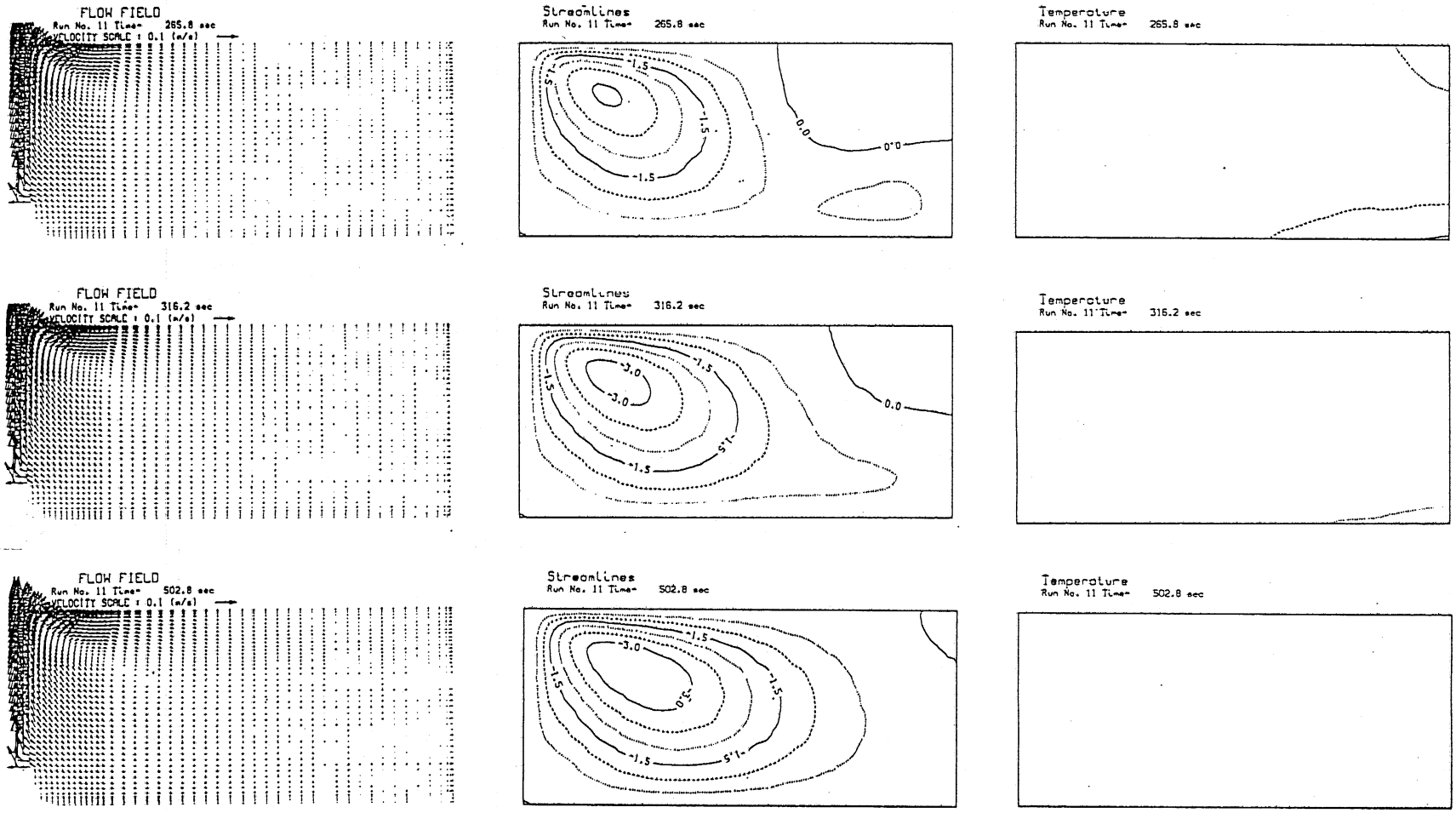

Figure 3.16 Simulation of the experiment No. 5, t=265.8; 316.2 and 502.8s

streamlines are moving away from the surface. As the process continues the plunging phenomenon becomes more evident. The stagnation streamline (with a zero value) appears, indicating clearly that there is a flow in a two opposite directions above and below it. The flow below the stagnation streamline is called interlayer flow and it is directed from the bubble plume outwards. The flow on the surface (on the right hand side up) can be considered as epilimnetic flow, and it is directed towards the bubble plume, as is the flow close to the bottom (hypolimnion). In the region after the plunging (farfield), the streamlines are more or less parallel over the entire depth. Because of the limited size of the water body recirculation occurs. In full scale lakes, where the ratio between the depth and the width is about 50 times bigger (ex. Lake Calhoun, Minneapolis) the streamlines in the farfield would be really parallel.

The stagnation streamline clearly divides the entire flow domain in two regions, nearfield and farfield. The size of the nearfield is of the order of the diffuser's depth and it appears as a big eddy like motion over the entire water depth. The nearfield becomes practically isothermal very soon after the air release starts. The dividing process between the nearfield and farfield is the plunging of the heavy surface jet. The plunging progresses down to the position of the thermocline where it spreads in two directions, towards the farfield becoming the interlayer flow, and back towards the vertical bubble plume becoming the return flow. The interlayer flow slides over the thermocline which cuts off the epilimnetic flow from the hypolimnetic flow. Accordingly, the assumptions used in Chapter 2 are correct.

As the time progresses the position of the stagnation point on the surface does not change much. It is mostly unaffected by the mixing in the epilimnion, erosion of the thermocline from above and its deepening over time. The interlayer created by the bubble plume slides above the thermocline in the farfield which means also that the thermocline cuts off the surface flow (epilimnion) from the bottom current (hypolimnion).

As the lowering of the thermocline is accompanied by mixing above it, density difference between the radial surface jet and the ambient water decreases. Eventually the momentum of the surface jet prevails over its negative buoyancy and the nearfield spreads. The entire flow domain becomes one continuous eddy (vortex ring).

The foregoing description of the development of the flow field is confirmed by the analysis of the measurements described in the following Chapter 4. As an example a comparison between the computed and measured plunging point distance is presented in Figure 3.17. The stagnation point in the analysis of the experimental data (Chapter 4) was defined as the position of the largest gradient of the surface temperature. Velocities were not measured. A comparison of streamlines and temperature contours in Figures 3.13 to 3.16 shows that the stagnation point coincided more or less with the maximum temperature gradient.

Figure 3.17 shows that the position of the stagnation point is predicted well up to about 200 sec when it reaches a distance about equal to depth.

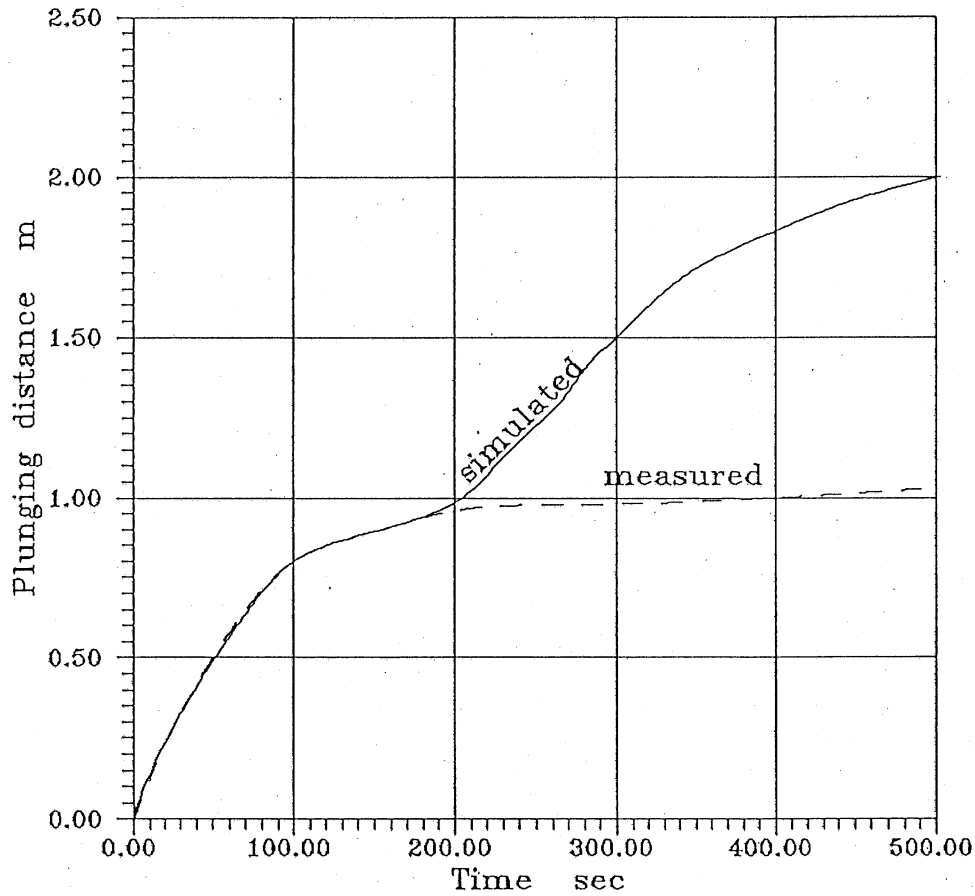

Figure 3.17 Comparison between simulated (solid line) and measured plunging distance (dotted line) for experiment No. 5

Afterwards the mathematical model predicts, as expected, a higher rate of mixing resulting in a faster spread of the stagnation distance than measured. Because the stagnation point is predicted well initially one could argue that the proposed k–ϵ model performs well for the bigger density differences, found at the beginning of the air bubbles induced circulation. The other line of thinking, which is more likely, is that at the initial period the negative buoyancy of the surface jet prevails over the mixing processes. Once the plunging phenomena establishes the general flow pattern (e.g. Figure 3.15) the mixing takes over. The plunging establishes two flow regions, nearfield and farfield. Then three eddy like circulation regions are seen. One is in nearfield and spreads over the entire depth. The other two rollers are in the epilimnion and the hypolimnion. They are flat compared to the one in the nearfield. As the mixing in these eddy–like motions is predicted at a higher rate than measured the well mixed condition (steady state) will occur earlier then measured.

Of particular interest is the parameter controlling the plunging, and accordingly the flow pattern in the startified water body. Experience with stratified flows (e.g. Jirka and Harleman, 1979) shows that the densimetric Froude number F, defined as $F = u/\sqrt{h(\Delta\rho/\rho)}$ where h = characteristic length, can be often taken as a governing parameter. The evaluation of the densimetric Froude number at the point which can be considered as the beginning of the plunging F_p is done in a few steps. At first the beginning of the plunging was evaluated. It has to be pointed out here that there is a difference between a stagnation point, at which horizontal velocity is zero and a point where horizontally dominated flow begins to turn to a to vertical flow. Such a point is found by comparing the steady–state streamlines (t=502 s), with streamlines for time steps presented in Figures 3.13 to 3.16. It can be seen that all the streamlines are practically parallel at the region of surface impingement. The diverging occurs at some distance which is considered as the beginning of plunging. The values of the densimetric Froude number F_p were evaluated from numerically calculated velocities and temperatures and presented as a time series in Figure 3.18. The value of F_p is in the range 0.6–0.7 which is in agreement with experimental results given in Chapter 4, and also with results for nonseparated plunging flows in general [Akiyama and Stefan, 1987].

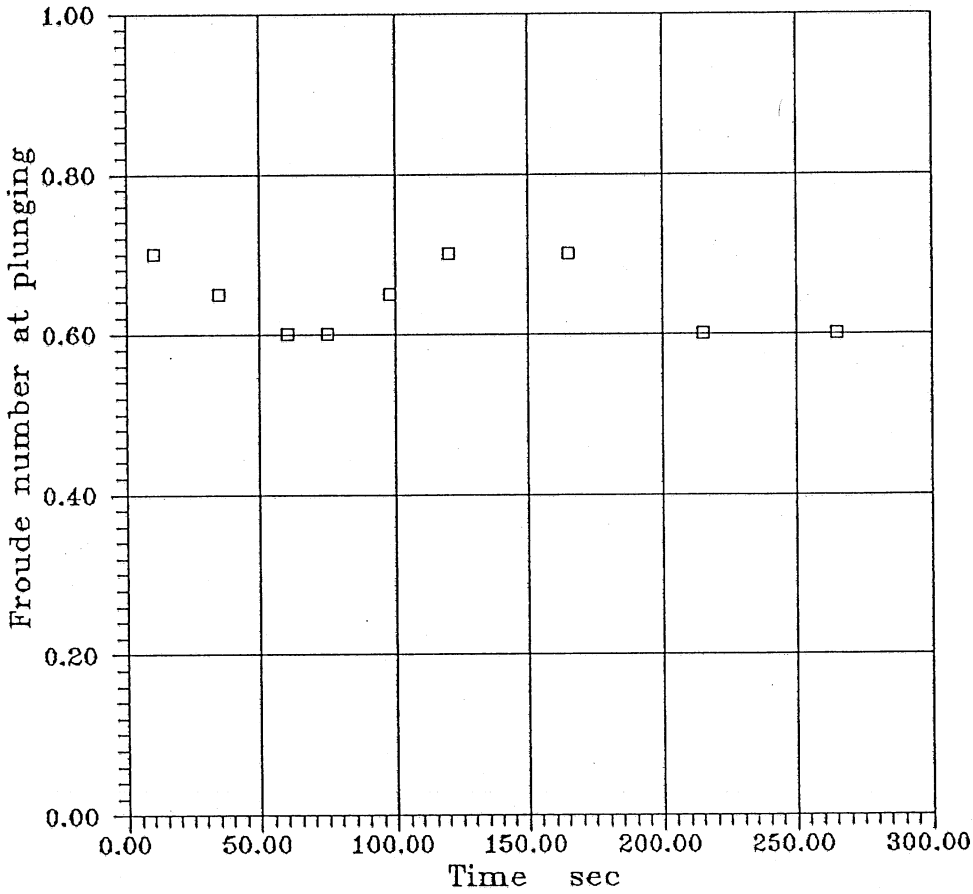

Figure 3.18 Densimetric Froude number F_p at the beginning of the plunging for the experiment No. 5

3.5. Conclusions

A 2–D model for the circulation induced by an air bubble plume was presented. The numerical model results compare well with a steady–state laboratory experiment. The numerical model predicts higher rates of mixing relative to measurements. Therefore processes are developing faster in the simulation than in reality, but slowly enough so that the relationship between the governing parameters is predicted correctly. The model results can therefore be used to analyze the flow field.

Results show clearly the existence of a nearfield and a farfield. The horizontal extent of the nearfield is of the order of the diffuser's depth of submergence. The nearfield consists of an eddy like motion over the entire depth. The nearfield becomes practically isothermal very soon after the air release starts. The process dividing the nearfield from the farfield is the plunging of the heavy surface jet. Upon reaching the position of the thermocline the plunging flow spreads in two directions, towards the farfield becoming the interlayer flow, and back towards the vertical bubble plume becoming the return flow. The interlayer flow slides over the thermocline which separates the epilimnetic from the hypolimnetic flows. The beginning of the plunging occurs when the value of the densimetric Froude number in the radial surface jet is in the range of 0.6 to 0.7.

4. EXPERIMENTAL STUDY

4.1. Overview

Air bubble plumes in water have been the subject of numerous experimental studies. In most cases, the plume itself was the main focus of interest and the ambient water was isothermal [Kobus, 1968; Cederwall and Ditmars, 1970; Milgram, 1983; Laureschen and Rowe, 1987]. Only a few authors [Rayyan and Speece, 1977; Graham, 1978; McDougall, 1978; Goossens, 1979; Kranenburg, 1979; Asaeda and Imberger, 1988] analyzed the interaction of the bubble plume with a stratified environment. More about can be found in the Literature review, Section 1.3.

The experiments presented here were conducted to better understand some of the physical processes and to produce data which are useful to verify a mathematical models presented in Chapter 2 (Integral model) and in Chapter 3 (2D model). The time evolution and spatial distribution of water temperatures were measured. The data were analyzed to identify stratified flow patterns and to calculate entrainment rates. Of particular interest were the development of the upwelling region, temperature structure in the farfield and water entrainment by the bubble plume.

4.2. Experimental equipment, instrumentation and procedures

Experiments were performed in a rectangular tank with dimensions 1.1x1.1x1.4 m, and in a cylindrical basin 4.5 m in diameter and 1.0 m deep. Water temperature stratification was established in each experiment before the air was released. Water temperature measurements commenced with the initiation of air release (time t=0) and continued until the water body was well mixed.

Experiments in the rectangular tank

The experimental set up is schematically shown in Figure 4.1a. The tank walls were thermally insulated by 2.5 cm thick styrofoam to avoid natural convection. A 1.25 cm thick lucite port window in the side wall permitted visual observations. Thermal stratification was produced by filling the tank from the bottom with a carefully adjusted mixture of heated and cold city water.

Compressed air was injected through a stone diffuser 1.2 cm in diameter and 3.5 cm in length. All experiments were run with the air injection in the center of the tank but diffuser's depth was varied. The air flow rate was measured with a rotameter. Temperature profiles were measured with a vertical chain of 16 thermistors 0.3 m from the plume axis and recorded by an Apple II computer. Experiments typically lasted 10 minutes until total mixing had occurred. The water flow pattern was visualized by dyes of various colors which were injected through small plexiglas tubes in selected locations of the flow field.

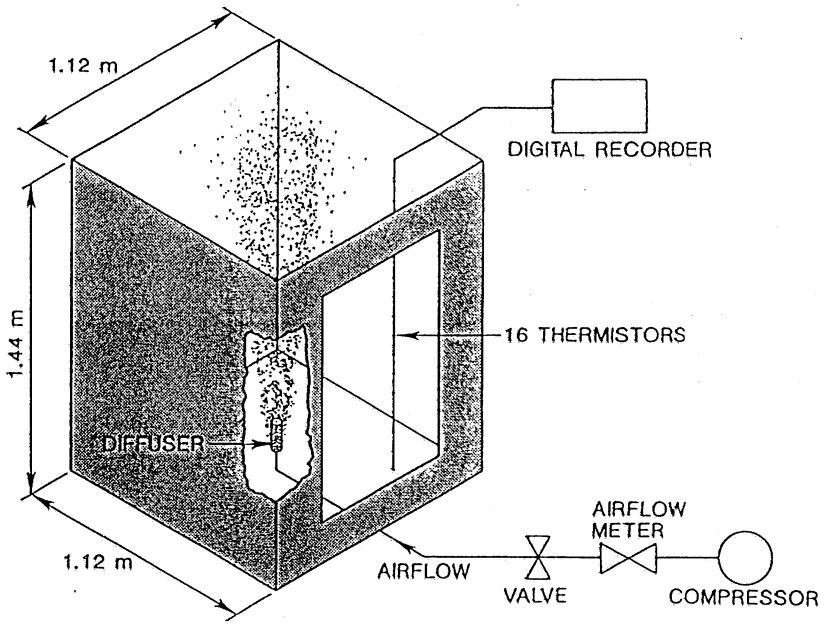

a) rectangular tank

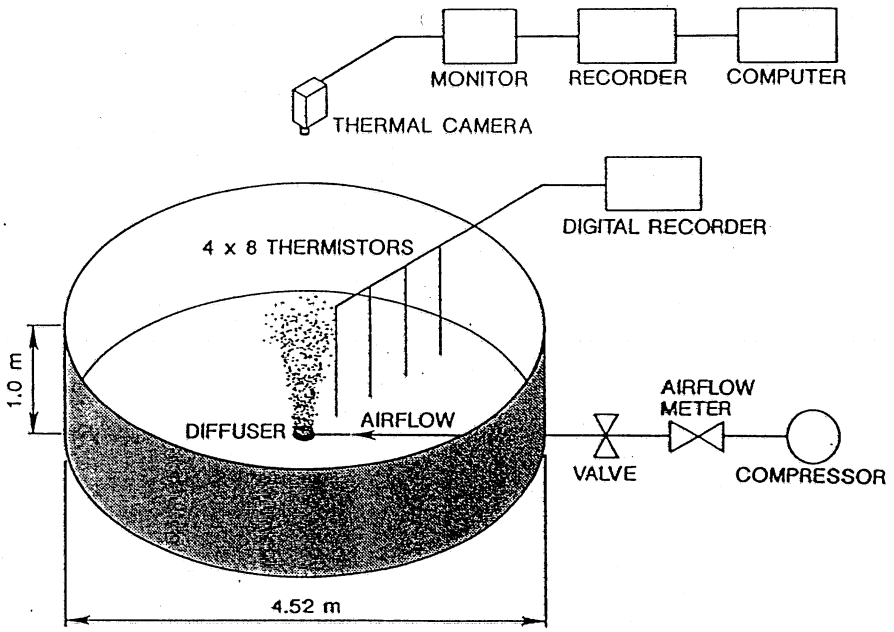

b)cylindrical basin

Figure 4.1 Experimental set–ups in rectangular tank (up) and cylindrical basin (bottom)

Table 4.1 gives the air release rate at atmospheric conditions (Q_{air}), diffuser's submergence depth (H), total water depth (H_t) and the initial (maximum) water temperature differential from surface to bottom ($\Delta T_{t=0}$) for several experiments.

Table 4.1. Experiments performed in the rectangular tank

Experiment No	Date	Q_{air} [l/s]	H [m]	H_t [m]	$\Delta T_{t=0}$ [°C]	Q_{air}/A [l/s/m^2]
1	4/13/88	0.045	0.89	1.14	14.1	0.036
2	3/21/88	0.067	0.97	1.22	15.1	0.053
3	3/7/88	0.10	0.89	1.10	18.0	0.080
4	4/14/88	0.1331	0.93	1.26	13.2	0.106

Experiments in the cylindrical basin

The cylindrical basin had a volume about ten times larger then the rectangular tank. The initial thermal stratification was established by electrically heating the surface water and gently pumping the warmed water to a lower depth. After enough time, the induced circulation produced an upper heated mixed layer. The bottom and the side walls of the basin were thermally insulated. A stone diffuser of 5 cm diameter was installed at a depth of 0.83 m. Some of the experiments (No. 5, 6, 7 and 8) were performed with a thermally insulated cover and some (No. 9 and 10) with an open water surface. The setup is shown schematically in Figure 4.1b.

Vertical temperature profiles were measured by four sets of 8 thermistors positioned at distances of 0.2 m, 0.8 m, 1.4 m and 2.0 m from the center of the basin. This thermistor arrangement gave information on the temperature stratification evolution in a vertical plane through the axisymmetric flow field.

For the last two experiments (No. 9 and 10) an AGEMA thermal camera and thermography recording system were used to obtain a continuous two–dimensional array of surface temperatures. Measurement resolution was about 1.3x1.3 cm. Surface temperatures were scanned at 0.5 seconds interval and stored digitally for analysis. Temperature fields were computed at 5 sec intervals by averaging measurements made every 0.5 sec for 2 sec. Averaging was done to reduce measurement noise.

Table 4.2 gives a list of experiments performed in the cylindrical basin.

Table 4.2. Experiments performed in the cylindrical basin

Experiment No	Date	Q_{air} [l/s]	H [m]	H_t [m]	$\Delta T_{t=0}$ [°C]	Q_{air}/A [l/s/m^2]	
5	8/10/88	0.133	0.81	1.0	9.8	0.008	covered surface
6	8/4/88	0.3	0.81	1.0	5.1	0.019	covered surface
7	8/8/88	0.353	0.81	1.0	10.2	0.022	covered surface
8	8/5/88	0.458	0.81	1.0	5.0	0.029	covered surface
9	8/17/88	0.155	0.83	1.02	9.6	0.010	open surface,Te=26.7°C
10	8/16/88	0.392	0.83	1.02	9.0	0.024	open surface,Te=26.3°C

Te = equilibrium water temperature based on room climate conditions

4.3. Experimental results

4.3.1. *Water temperature records*

Water temperature profiles and time series measured in the rectangular tank are shown in Figures 4.2 to 4.5 for the rectangular tank and in Figures 4.6 to 4.11 for the cylindrical tank. Complete data for all experiments are given in Appendix E.

An typical example showing most of the features is shown in Figure 4.4. The water temperature profiles and time series in Fig. 4.4 confirm the flow pattern shown in Fig. 1.1 and 2.1. For example, the temperature profiles at times t=145s and t=447s show a thermal instability, i.e. water at the surface is colder than that below the surface. This indicates that the measurements were made in the nearfield where the cold water entrained by the bubble plume from the lower half of the tank was still present at the water surface. The duration of the thermal instability can be seen in the water temperature time series records at depths of h=0.01 m and h=0.65 m.

Mixing induced by the bubble plume eventually leads to completely uniform temperatures in the tank. The deepening of the isothermal layer slows considerably when the thermocline depth reaches that of the air release. In the example, it took less then 500 seconds to reach that depth (h=0.97 m). To mix the tank fully (h=1.21 m) required more then 1500 seconds.

The effect of the bubble plume on water surface temperatures was recorded by the thermal camera oriented along the axis of the bubble plume (Figure 4.1b) The 24 images of water surface temperature in Figure 4.12 show the sequential growth of the upwelling region at time intervals of approximately 50 sec, starting with the inception of air injection. The area shown is about 2.0 m by 2.0 m with the axis of the bubble plume near the center. The dark shades in the center indicate cold water ($\approx$ 30 °C) coming from below. The undisturbed water surface is represented by lighter shades ($\approx$ 38 °C). The pictures are slightly distorted causing the upwelling region to

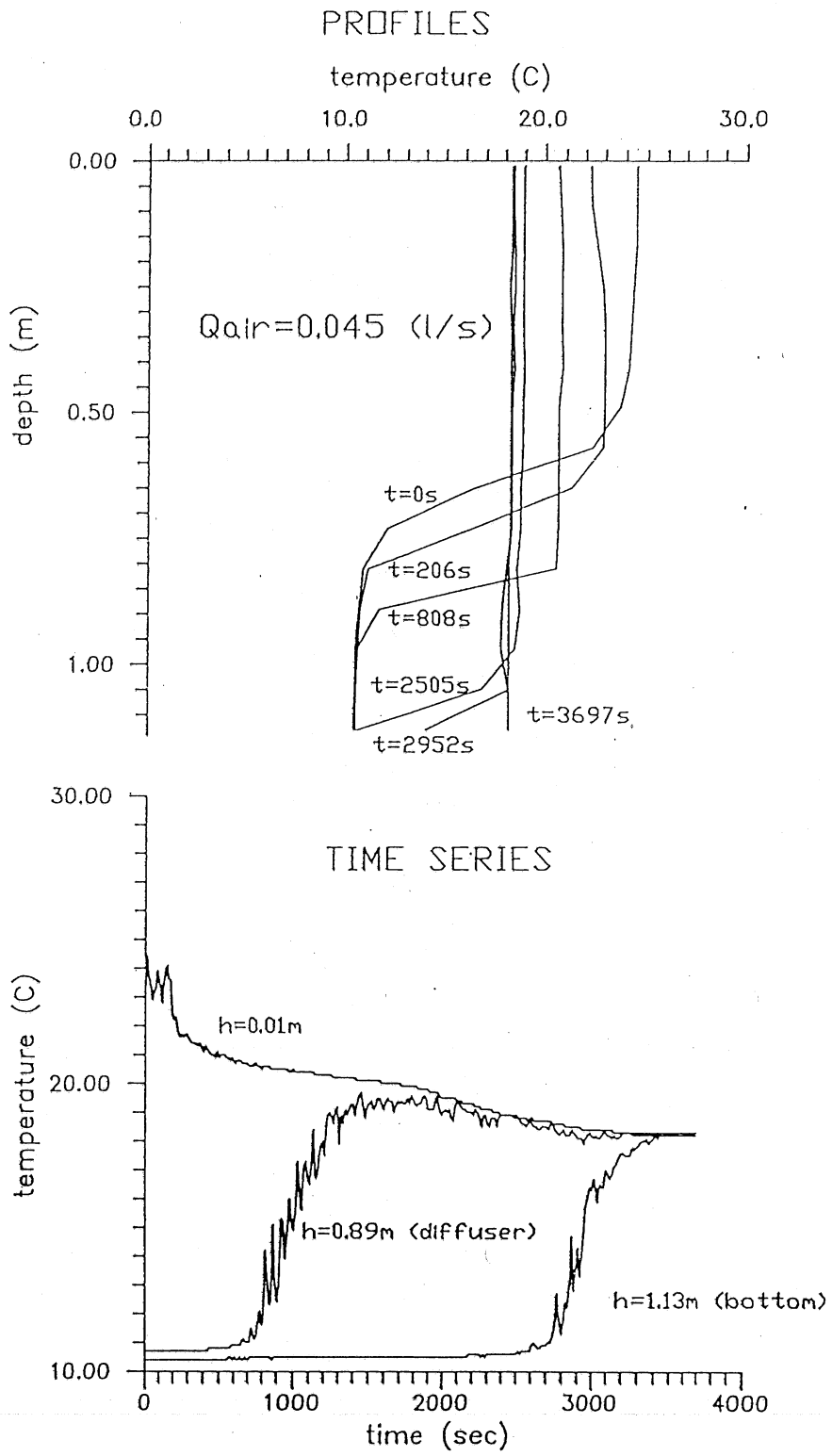

Figure 4.2 Water temperatures measured in experiment No. 1

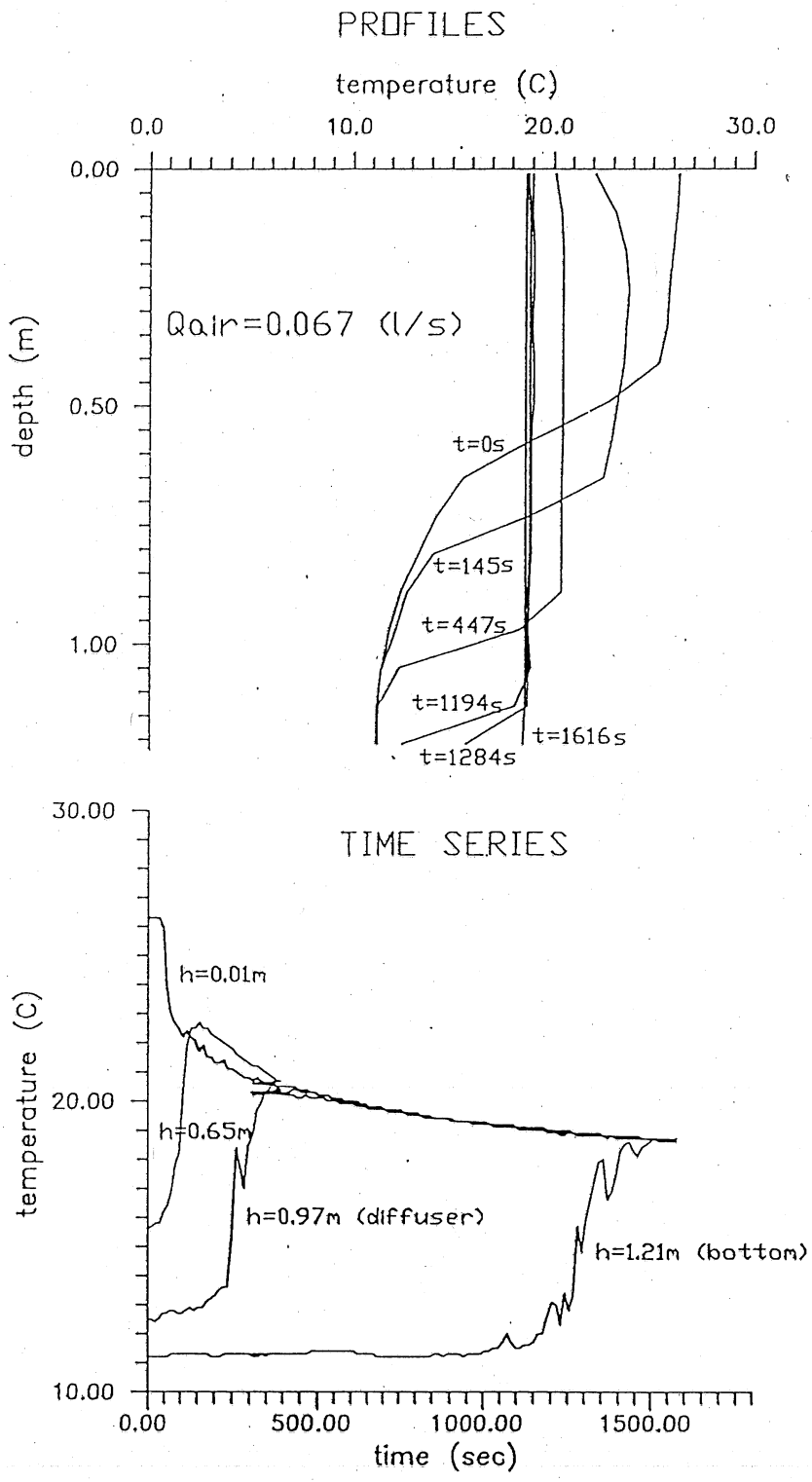

Figure 4.3 Water temperatures measured in experiment No. 2

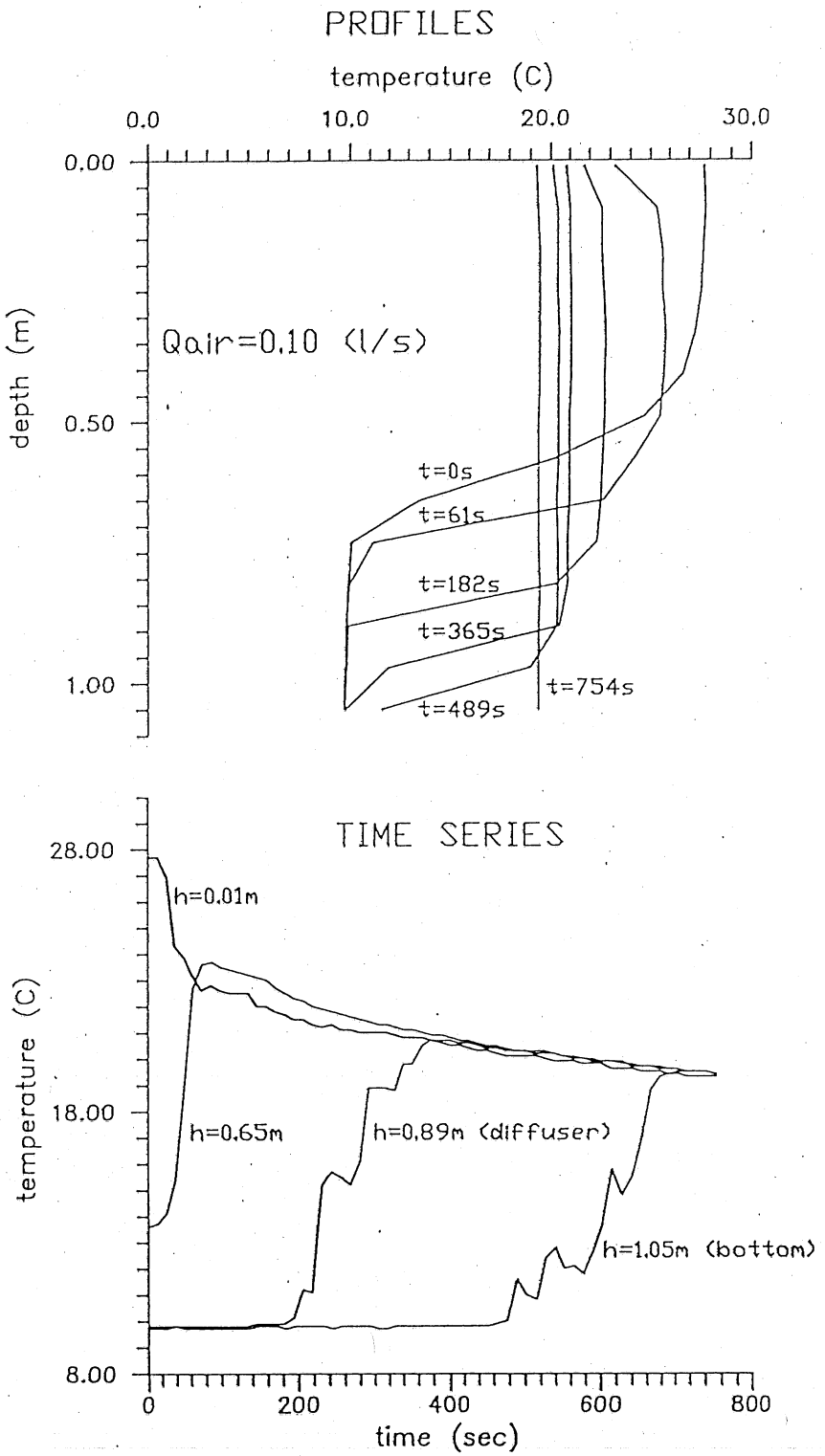

Figure 4.4 Water temperatures measured in experiment No. 3

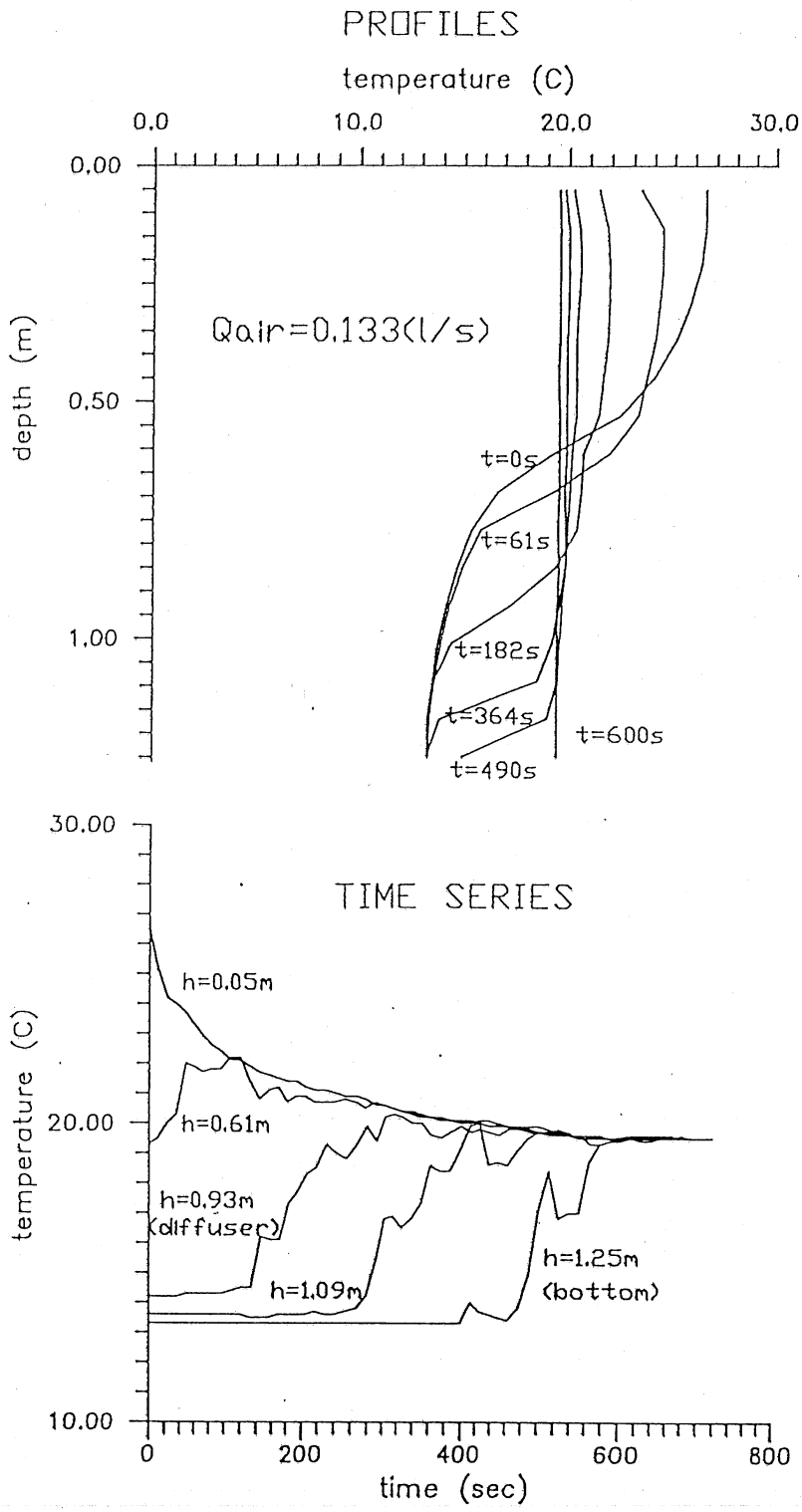

Figure 4.5 Water temperatures measured in experiment No. 4

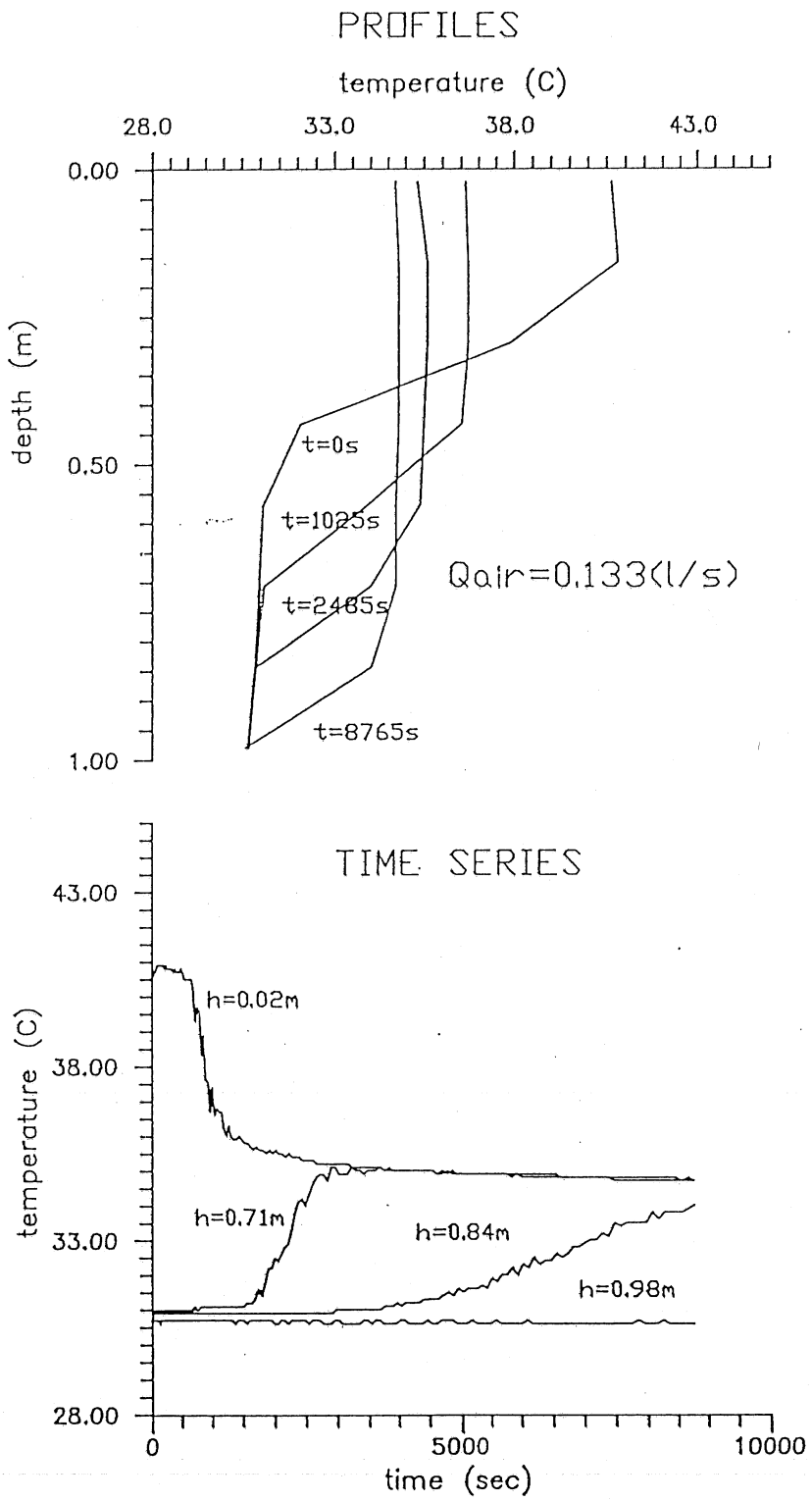

Figure 4.6 Water temperatures measured in experiment No. 5

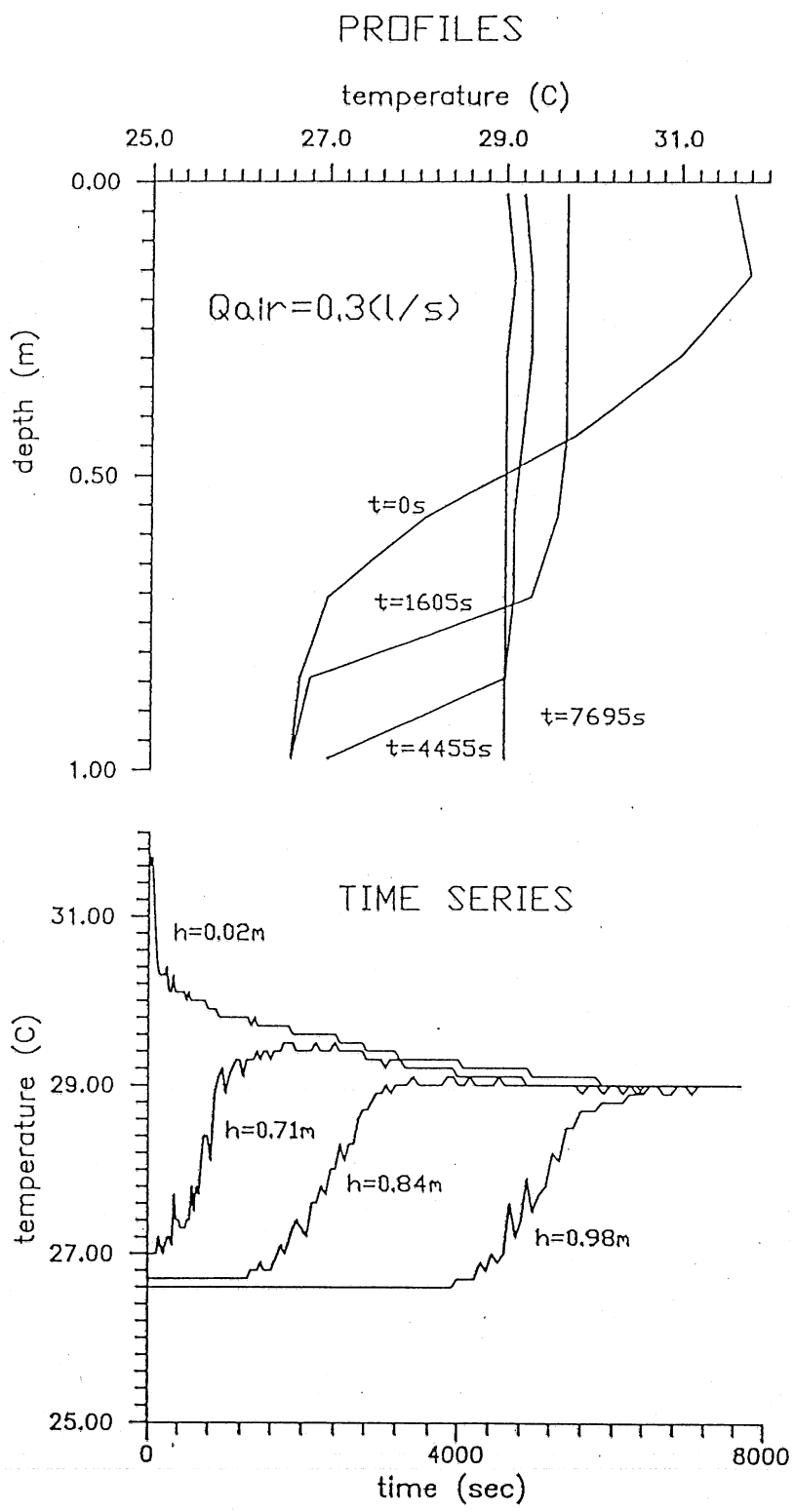

Figure 4.7 Water temperatures measured in experiment No. 6

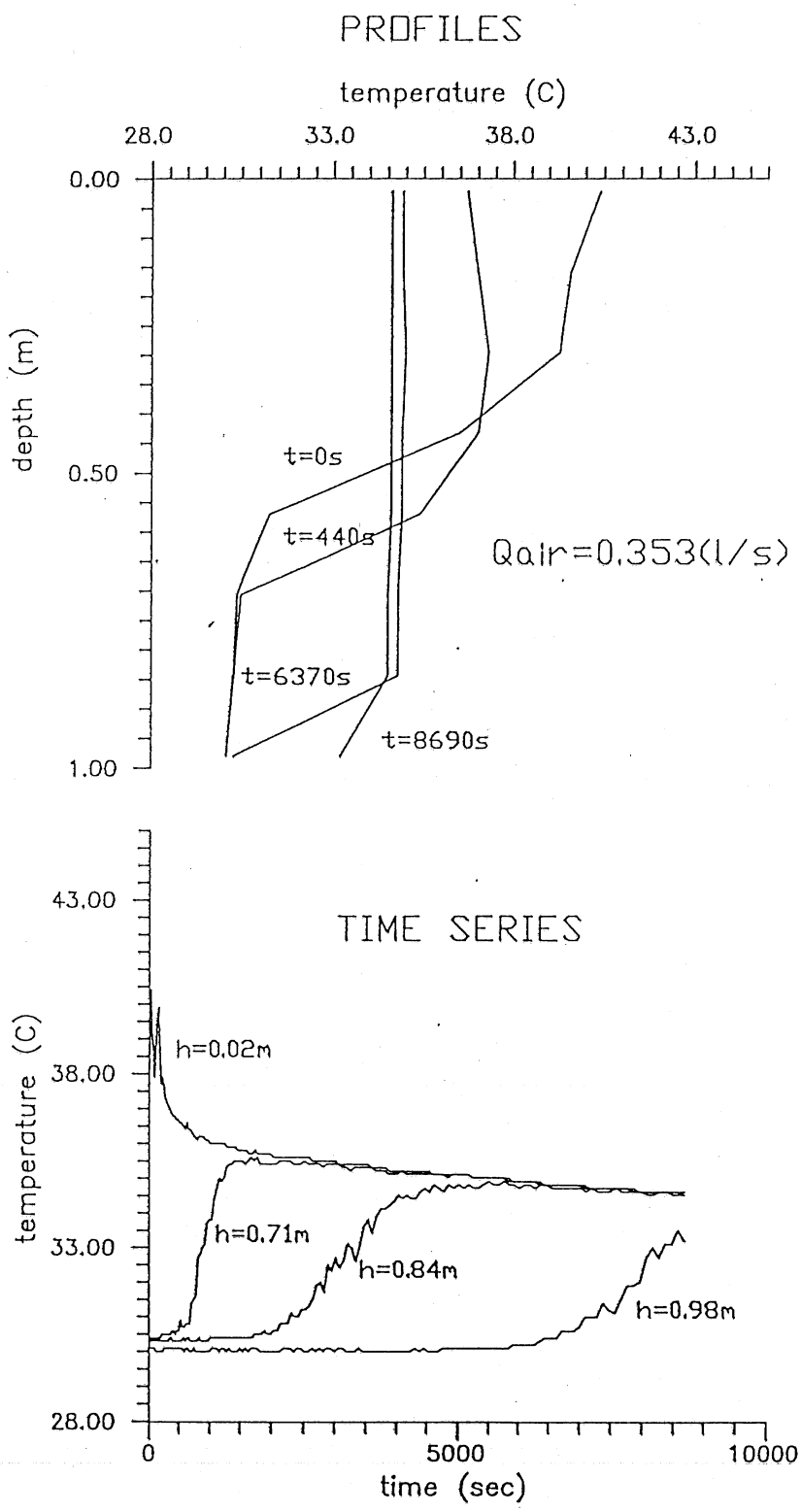

Figure 4.8 Water temperatures measured in experiment No. 7

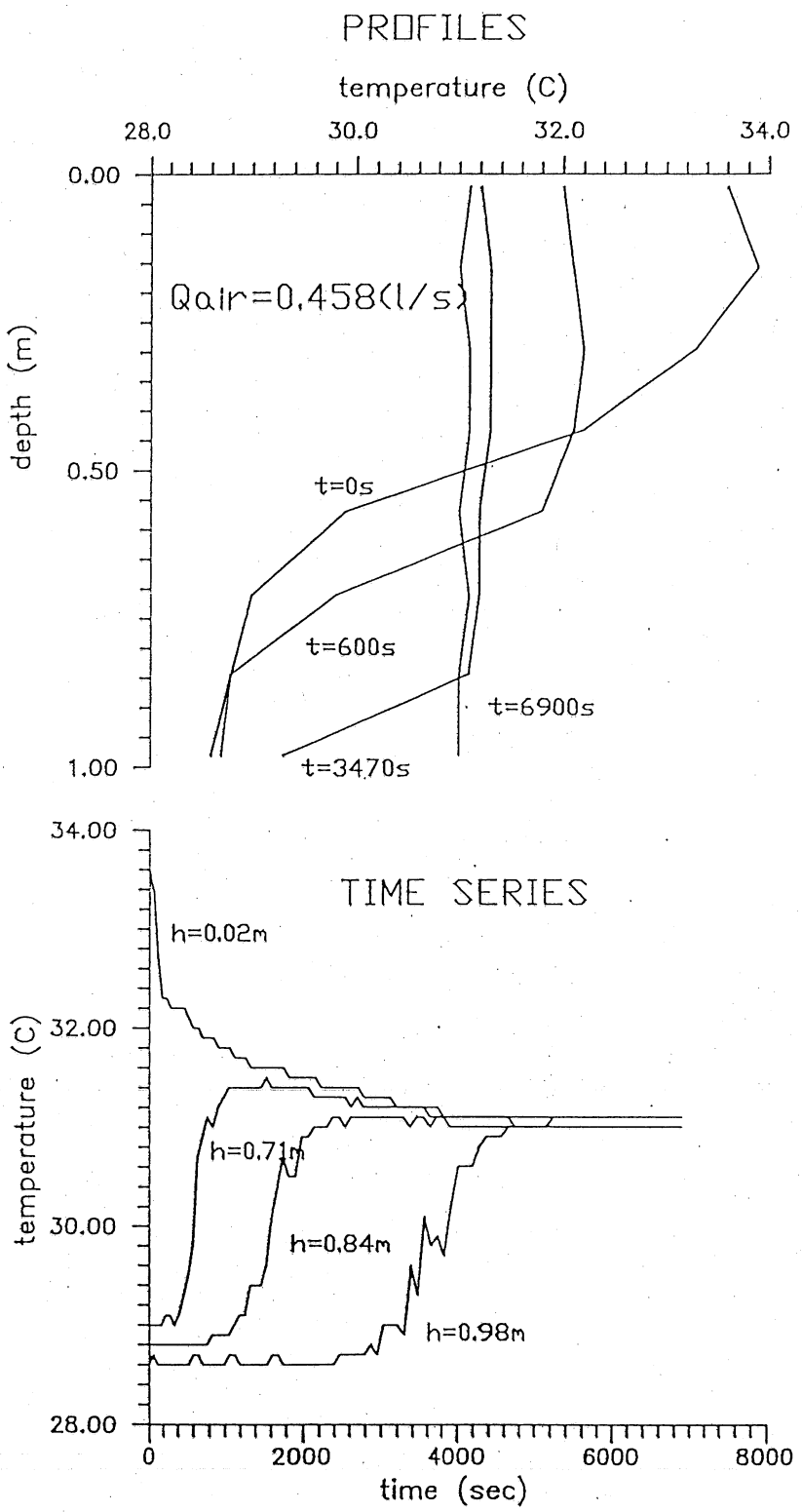

Figure 4.9 Water temperatures measured in experiment No. 8

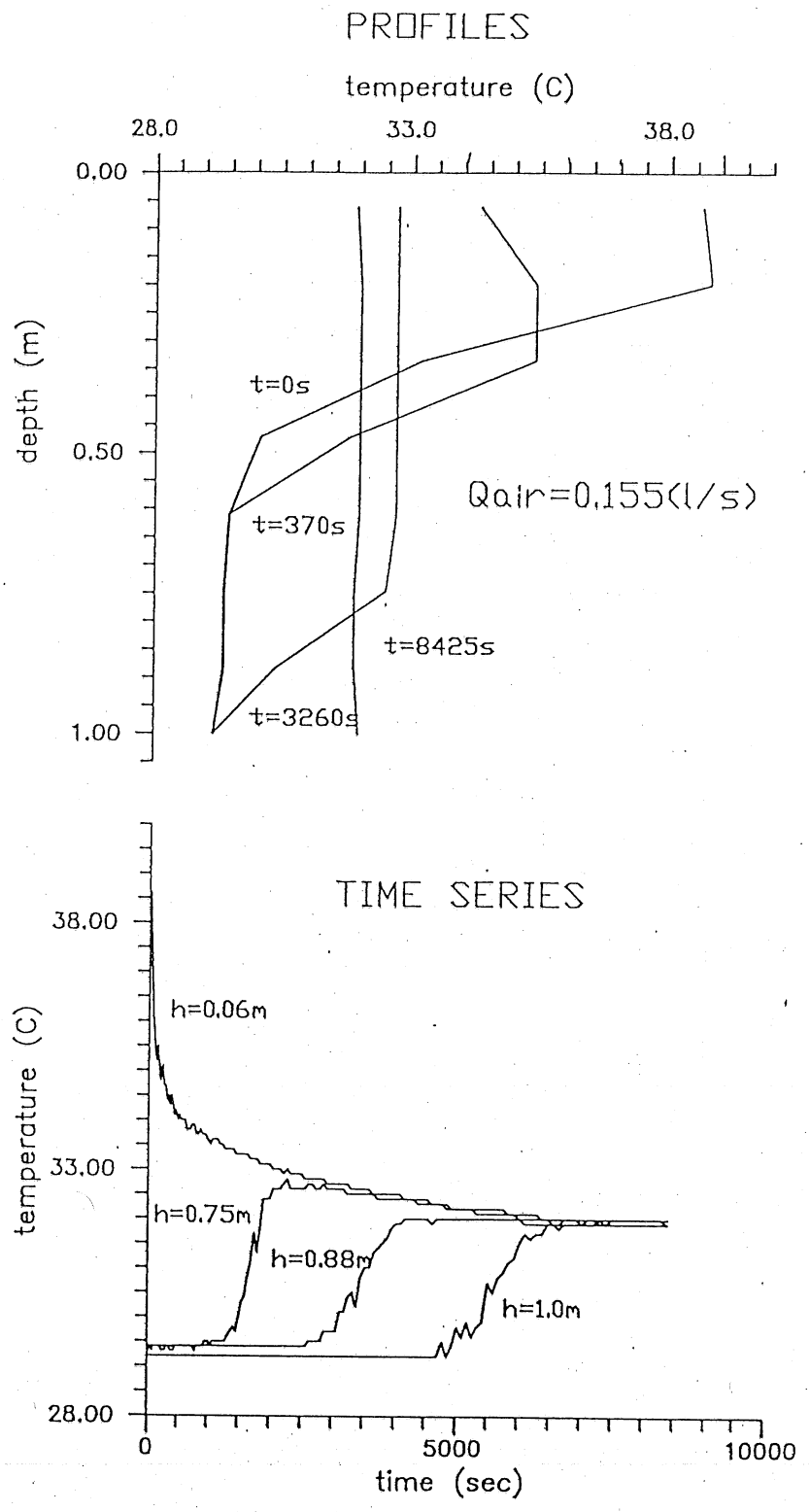

Figure 4.10 Water temperatures measured in experiment No. 9

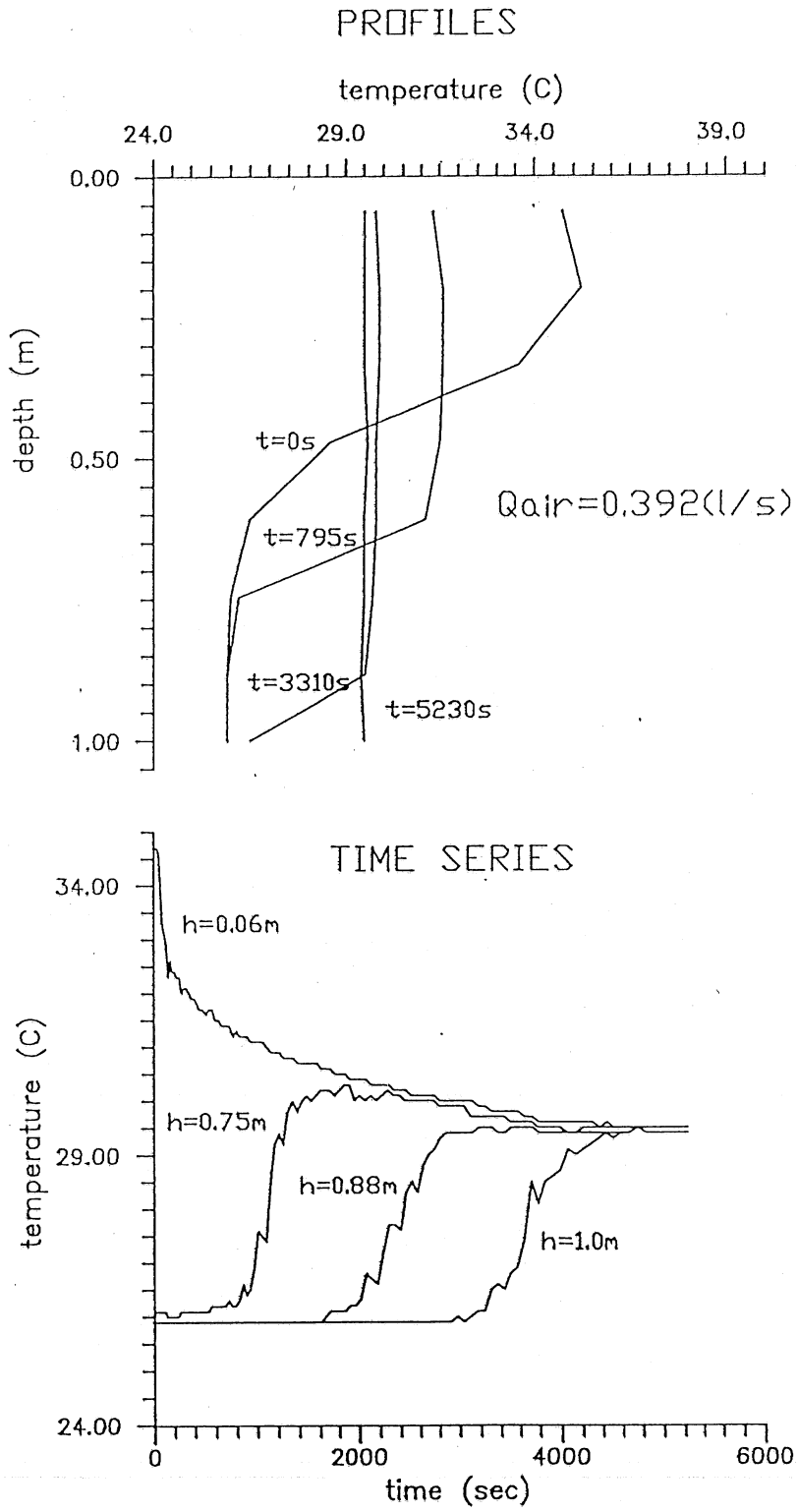

Figure 4.11 Water temperatures measured in experiment No.10

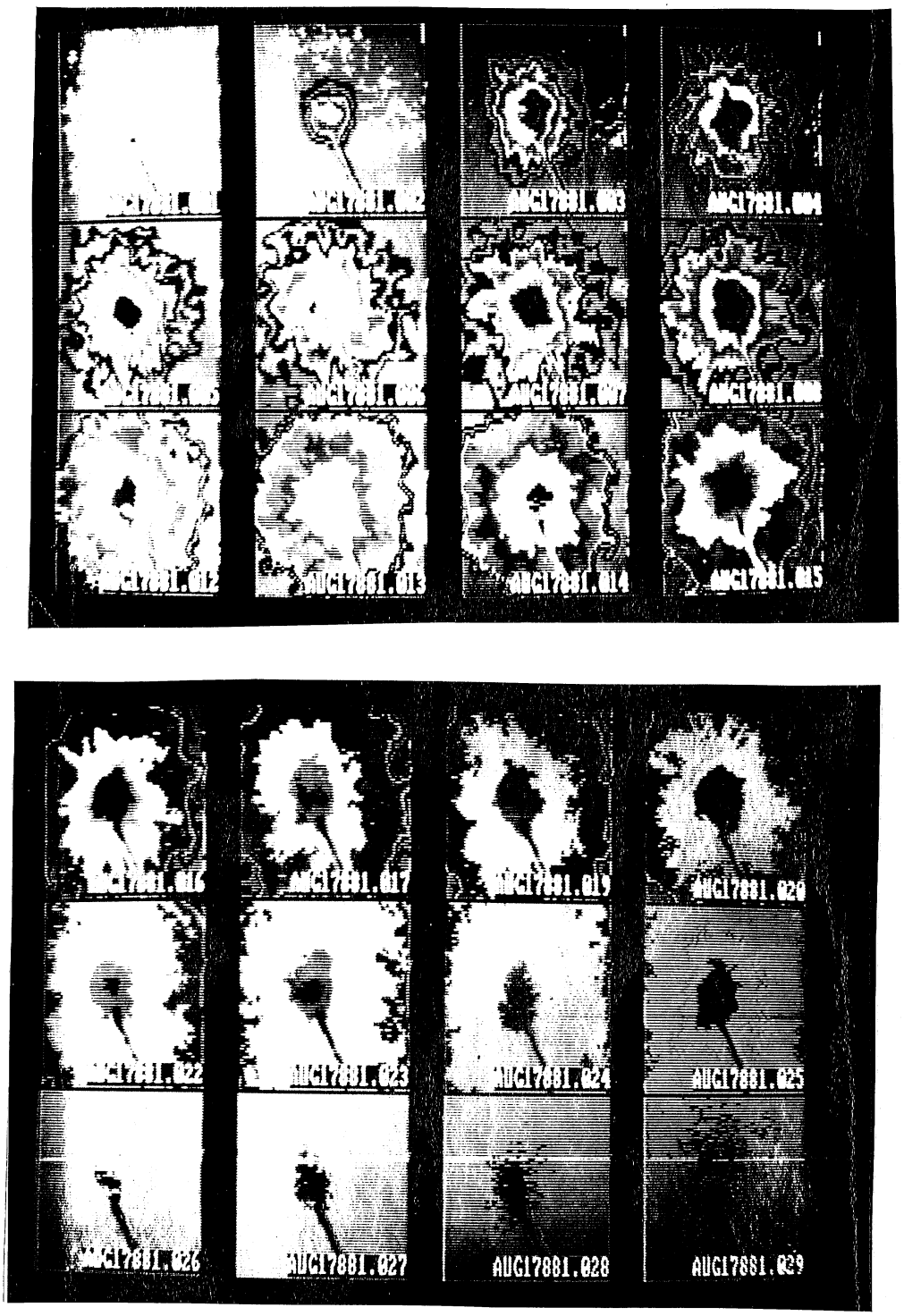

Figure 4.12 Development of upwelling region on the water surface as recorded from overhead by thermal (infrared) scanning. The sequence starts when the bubble plume is turned on (upper left corner).

appear slightly elliptical when it is actually circular (axisymmetric around the center of the plume). Instantaneous images show large random deviations from exact axial symmetry, as shown at the top of Figure 4.13. This is of course due to the turbulence in the air bubble plume. When the data are averaged over 2 minutes the axisymmetrical nature (appearing elliptic) of the flow is more obvious as is shown out at the bottom of Figure 4.13. (The umbilical line from the center of the basin to the lower right of the images is a bundle of instrumentation cables suspended over the water surface).

4.3.2. *Plunge line*

Since the upwelled colder water has a higher density then the ambient water it cannot maintain itself on the water surface and "plunging" occurs at the stagnation point shown in Figure 3.1. In the data analysis the plunging point is defined as the position where the steepest gradient of surface water temperature occurs with respect to radial distance. In Figure 4.13 (bottom) this corresponds to the narrowest spacing of isotherms. In time, the the plunge line travels from the axis of the bubble plume (when the air is turned on) radially outward. Figure 4.14 shows the position of the plunge line (radial distance from the plume axis) as a function of time. To obtain this information, the temperature distribution along a radius was calculated for each time record and the location of the highest temperature gradient was determined and plotted. A line has been fitted to the data in Fig.4.14. After a rapid initial outward migration, the plunging point assumes a fairly stationary position at a horizontal distance from the plume axis roughly equal to the depth of the basin. After that quasi–steady period the plunge point continues to move slowly outward. To explain this behavior it is necessary to recall that the plunge point is the stagnation point of the horizontal flow on the surface (Figure 3.1). At this point the buoyant force due to the stratification in the farfield produces a horizontal pressure gradient which balances the momentum of the surface jet. As the farfield stratification weakens due to vertical mixing, the nearfield spreads outwards.

In a lake where the farfield is much bigger then in a laboratory tank, stratification in the farfield is maintained for a long time and the plunge point establishes itself at a virtually fixed distance from the plume, approximately equal to the depth of the lake [Goossens, 1979]. In the laboratory experiments (Fig. 4.14) the plunge line also migrated to a distance approximately equal to the basin depth. It did not stay there very long, however, because the farfield surface water became depleted.

It can be concluded that the experiments confirmed the existence of a nearfield and a farfield. The horizontal extent of the nearfield was found to be approximately one water depth as previously seen in field experiments.

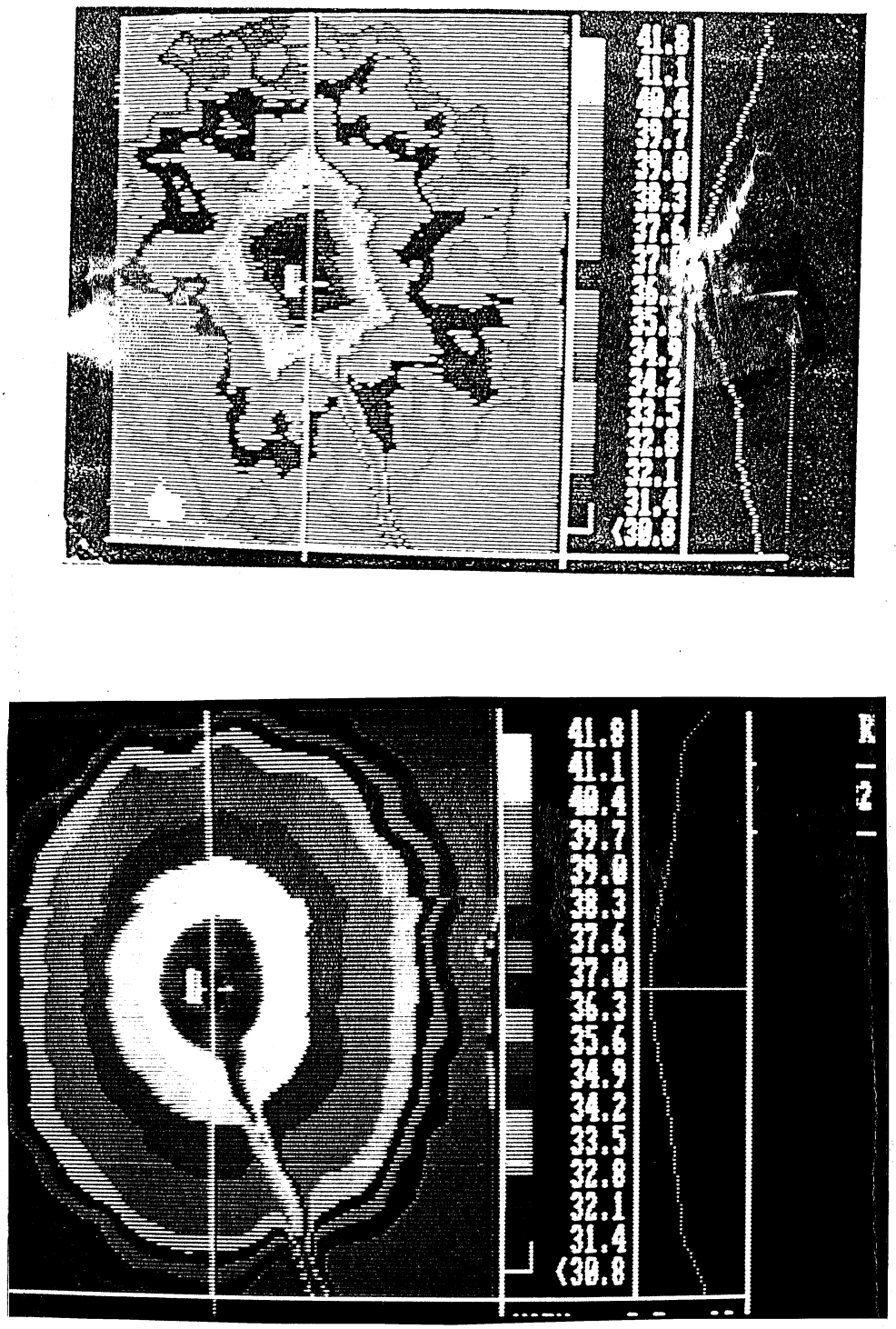

Figure 4.13 Instantaneous and 2 min average image of water surface temperatures obtained by thermal camera

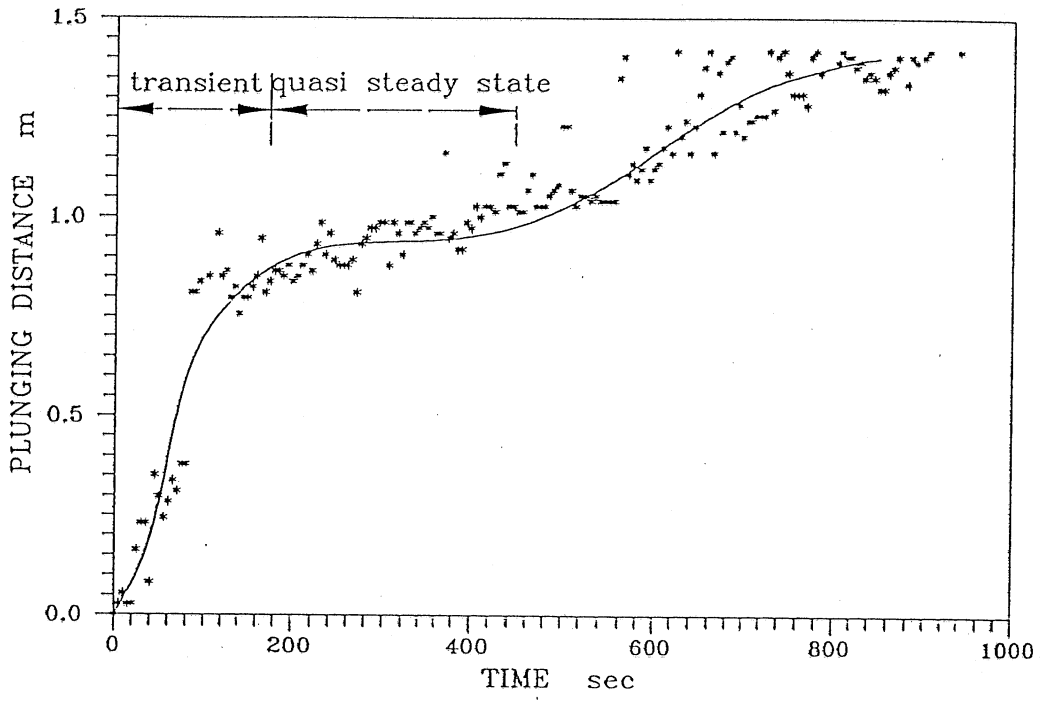

Figure 4.14 Distance to plunge line as a function of time (experiment No. 9). Experimental data and a fitted line are shown.

4.3.3 *Farfield layer structure*

Isotherms were interpolated linearly from the temperatures measured by thermistors at 32 locations distributed in 4 verticals (Figure 4.1b). There was no thermistor chain in the plume axis. The isotherms were used to analyze the progression of destratification over time. Figure 4.15 shows an example of isotherms at the beginning of air injection (t = 0), after some destratification has occurred (t = 270 sec) and when the destratification is far advanced (t = 595 sec). Operation of the bubble plume causes entrainment of water from the surface (epilimnion) and the) bottom (hypolimnion) and thickening of the intermediate depth layer as shown schematically in Figure 2.1. Figure 4.15 confirms the existence of these mechanisms: the 35 °C isotherm rises upwards and the 30 °C moves downwards. The development of this process in time is shown in Figure 4.16. Figure 4.16 depicts the farfield only. The farfield changes in extent over time as the plunge point moves. Volumetrically averaged isotherm depths are plotted in Figure 4.16 against time. In it, a number of features are evident: (a) the colder isotherms descend in time indicating water entrainment by the plume from the hypolimnion, (b) the interlayer (inflow) occurs primarily above the thermocline region where the vertical temperature gradient is strongest; (c) as time progresses, the uppermost portion of the hypolimnion becomes part of the interlayer; the top portion of the hypolimnion is entrained into the interlayer causing the average temperature in the interlayer to decrease, d) as the interlayer grows the epilimnetic layer (uppermost) decreases significantly in thickness.

The upper and lower boundaries of the interlayer are difficult to determine. The lower boundary has has been defined as the depth at which an isotherm starts to rise significantly (indicating strong vertical mixing). The upper boundary has been placed where adjacent isotherms at about constant rate (indicating identical volumetric rates of depletion). The boundaries are accordingly marked in Figure 4.16. Information from Figure 4.16 is presented in Figure 4.17 in the form of a three layer model.

4.3.4 *Entrainment*

The volumetric flow rates into and out of the epilimnion, hypolimnion and interlayer were computed from their changes in thickness using the conservation of mass principle. These results are shown in Figure 4.18. The vertical dashed line marks the time when the quasi–steady state period ends.

The flow rates shown in Figure 4.18 are horizontal and occur across the boundary between nearfield and farfield (Fig. 2.1). Horizontal entrainment rates from the epilimnion (Q_e) and the hypolimnion (Q_{hy}) and flow into the interlayer (Q_i) are shown (see Fig. 2.1 for definitions).

To evaluate entrainment by the vertical air bubble plume, a slightly different approach has to be taken. In Figure 4.15, it can be seen that the thermocline separates processes such as plunging and interlayer flow from the hypolimnion. In other words the hypolimnion is unaffected by nearfield and

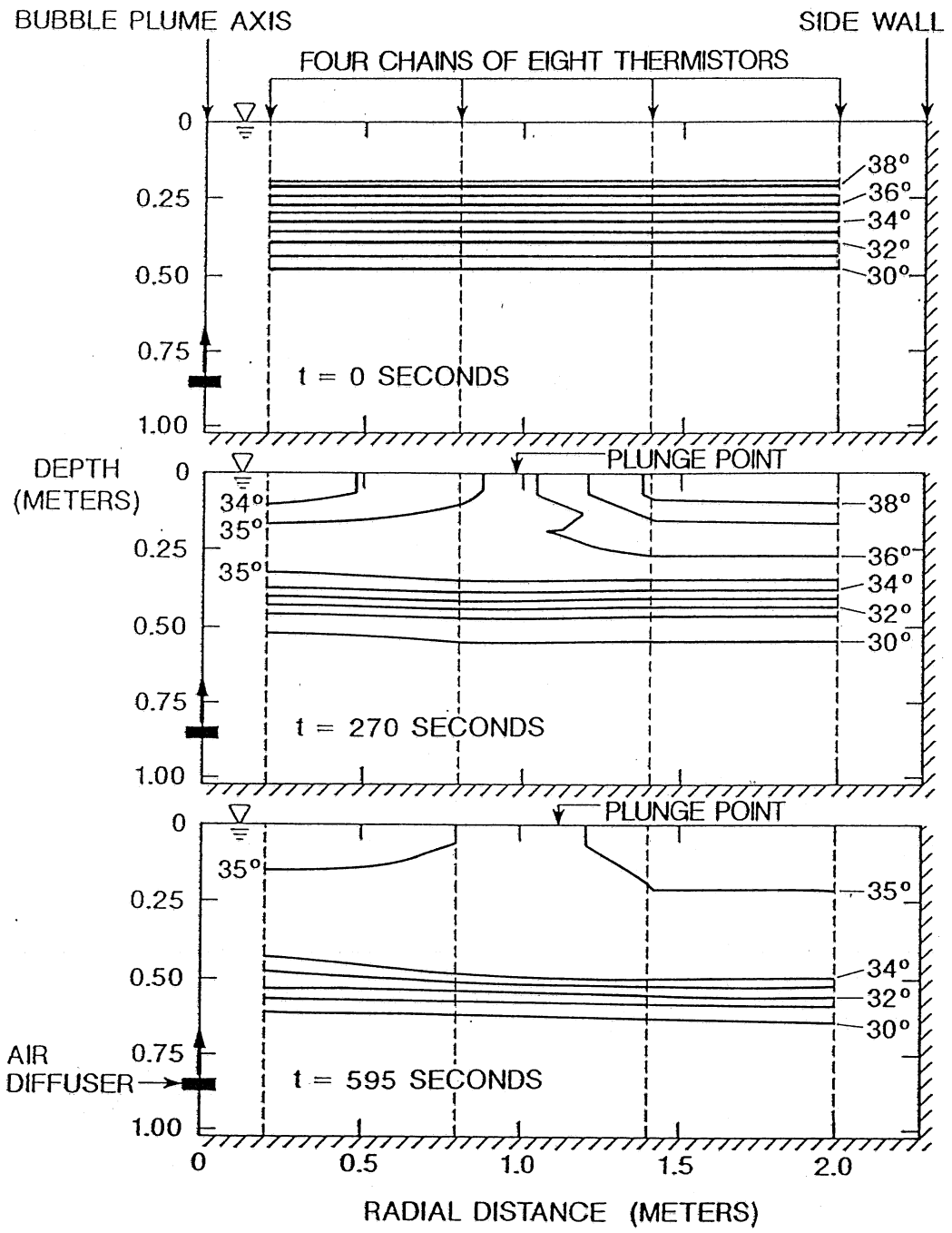

Figure 4.15 Isotherms in the circular basin at 3 instants. t=0 beginning of air injection. (Experiment No. 9)

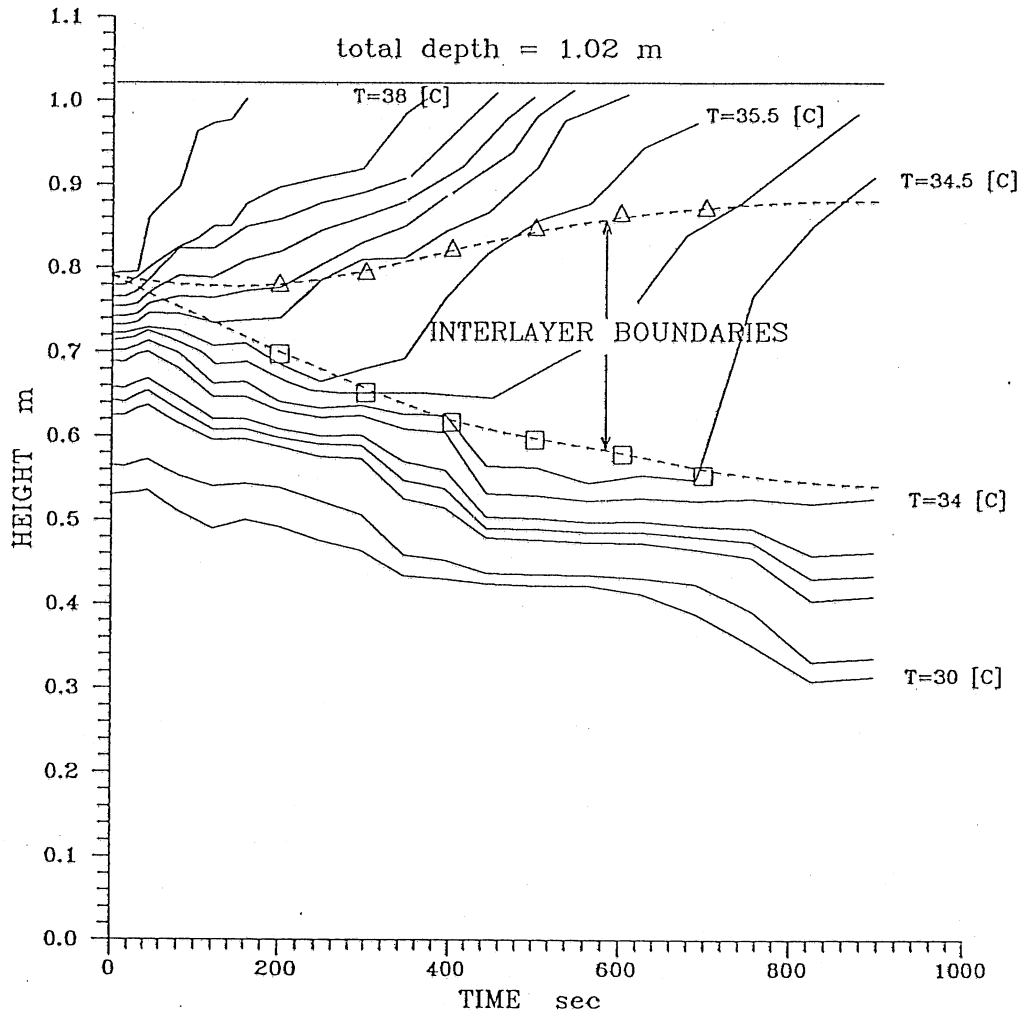

Figure 4.16 Depths of the isotherms in the farfield (Experiment No. 9)

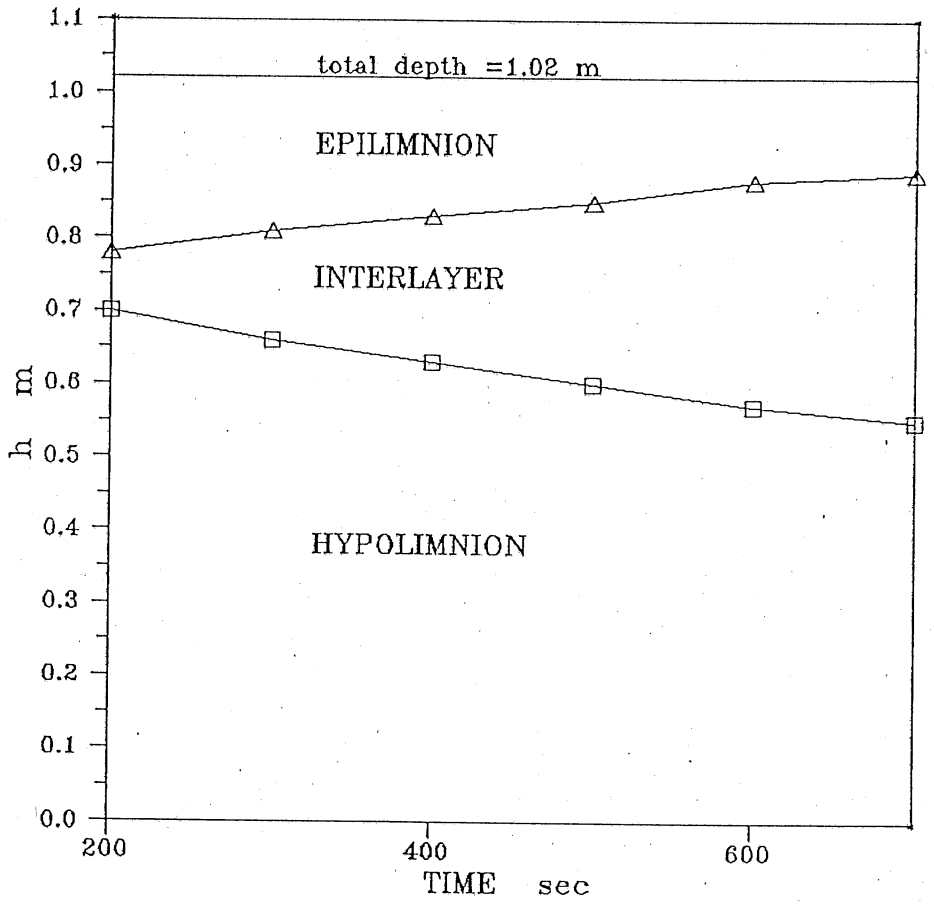

Figure 4.17 Thicknesses of epilimnion, interlayer and hypolimnion in farfield over time (Experiment No. 9)

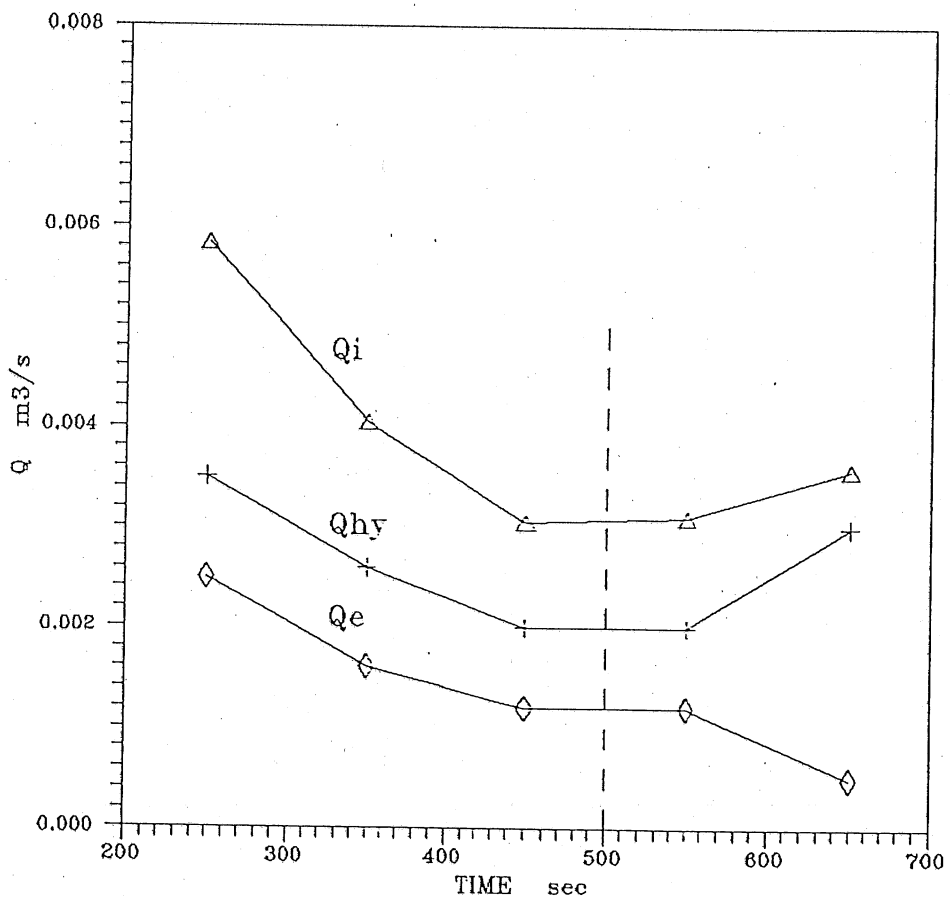

Figure 4.18 Flow rates out of the epilimnion (Q_e) and hypolimnion (Q_{hy}) and into the interlayer (Q_i) in the farfield (see Fig. 3.2 for definitions). Experiment No. 9

farfield phenomena. Accordingly, the hypolimnion can be considered as continuous over the entire basin. This implies that entrainment from the hypolimnion should be the same as entrainment observed in isothermal conditions. Figure 4.19 shows a comparison between experimental results obtained in stratified water with equations by Kobus [1973] and Goossens [1979] (Eqn. 2.3) for isothermal conditions. Field study and laboratory data are presented. The laboratory data are approximately 2/3 of the values given by Kobus' [1973] equation (the range is from 1/2 to 1). The differences are largest at the lower airflow rates when density stratification would be expected to have the strongest influence. Overall, the results indicate that without committing a large error, one can treat the region in the vicinity of the plume (nearfield) as isothermal, especially when the air flow rates are significant.

When the flow rates Q_{hy} (from the entire basin) and Q_e (from the farfield) are added, the sum is, of course, more than the interlayer flow Q_i (evaluated from the farfield data). This imbalance is due to two reasons:First, the nearfield grows in time (see Figure 4.14) and this requires more water coming in ($Q_{hy} + Q_e$) than going out (Q_i). The second reason is revealed by a look at Figure 2.1. Within the control volume II there is a return flow Q_{rt} and an outflow Q_o. The total entrainment by the plume Q_w must be balanced by the sum of $Q_{hy}+Q_{rt}-Q_o$.

Entrainment coefficients

Entrainment coefficients used in the nearfield model can be divided in two groups. (1) Entrainment coefficients used to close integral equations for the vertical bubble plume and horizontal surface jet [Goossens, 1979] are of universal nature and very close to the ones obtained by the other researchers. They are not a subject of this analysis. (2) Two additional coefficients needed in the nearfield model are c_1, entrainment coefficient of the surface plunging flow and c_2, the ratio of return flow to hypolimnetic flow. Goossens [1979] put value of c_2 in the range 1–8 and stated that the exact value has to be determined experimentally. It has found in Chapter 2, by calibration of the numerical model with field data that c_1 is approximately constant and equal to 0.05; c_2 was found to be close to 1.0 for most cases.

To evaluate c_1 and c_2 from the experiments, the information presented in Figures 4.17 and 4.18 was used. Additional information is required, namely the total flow rate and the thickness of the surface jet at the plunging point. For this purpose, equations (2.6) and (2.7) were used. The results of the evaluation of the coefficients is shown in Table 4.3.

Table 4.3. Flow rates, entrainment coefficients (c_1 and c_2) and densimetric Froude number at plunging point (F_p) for Exp. No.9

time [sec]	Q_e	Q_i	Q_{hy} [m^3/s]	Q_w+Q_o	c_1	Q_{rt} [m^3/s]	$H-Z-h_{hy}$ [m]	c_2	F_p
250	0.0025	0.006	0.0045	0.027	**0.09**	0.024	0.19	**14.0**	**0.6**
350	0.0016	0.004	0.0035	0.027	**0.06**	0.025	0.23	**14.2**	**0.6**
450	0.0012	0.003	0.0025	0.027	**0.04**	0.025	0.26	**16.9**	**0.6**

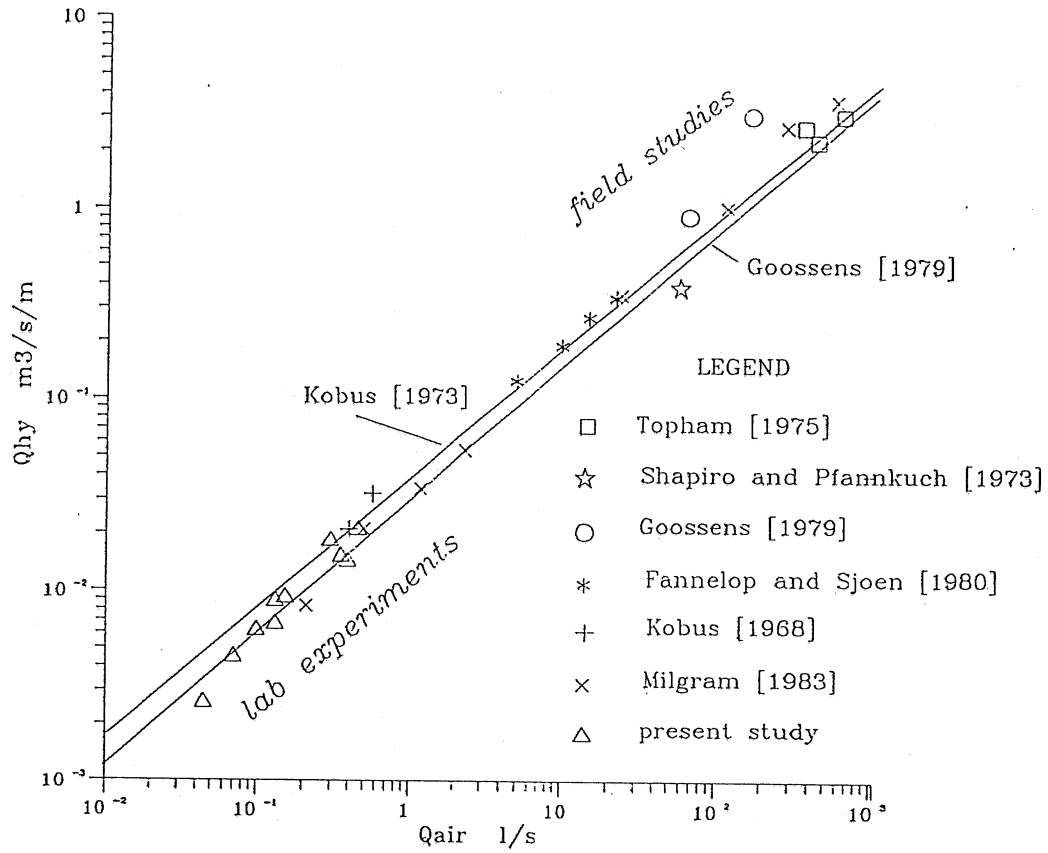

Figure 4.19 Entrainment from hypolimnion (Q_{hy}) as a function of air flow (Q_{air})

It can be seen that the entrainment coefficient c_1 is very close to the value obtained by the numerical model calibration with field data. This is not surprising, knowing that the value lies in the range from 0.01 to 0.08 determined experimentally by Akiyama and Stefan [1987] for nonseparated plunging flows. Densimetric Froude number at plunging F_p is also of the order found by Akiyama and Stefan [1987] (0.57–0.89). The coefficient c_2 is, however, much bigger than was obtained from field studies (Chapter 2) but not so much out of the range given by Goossens [1979]. This result indicates that there is much more return flow in the laboratory than in the larger scale field studies. This is in qualitative agreement with results published for buoyant jets [Lee, 1980; Jirka and Harleman, 1979] where it was found that for the same densimetric source Froude number the return flow is reduced as the depth of the ambient water increases. Another way of looking at this results is to say that for the same depth, the return flow increases with increase of the densimetric Froude number.

4.3.5 *Deepening of the "mixed layer"*

The position of the air release in aeration–mixing installations is usually at some distance above the maximum depth of the lake. One common reason is so as not to mix the entire water column, or not to entrain dissolved or suspended materials from the bottom of the lake. The air bubble plume as a method of artificial destratification permits the maintenance of a sharp thermocline at a chosen depth [Knoppert et al., 1970]. The experiments performed by the authors show that the mixing process will reach below the level of air injection if air is released long enough. However, the deepening of the thermocline (the region with steepest density gradient) progresses significantly more slowly after the thermocline passes the depth of the air diffuser (see Fig.4.2 to 4.11). The deepening of the thermocline below the diffuser is caused by the horizontal shearing generated by the flow towards the plume along the upper edge of the thermocline. Figure 4.20 shows the rate of descent of the thermocline near the depth of air injection as derived from the experimental water temperature data where h = distance from the thermocline to the air diffuser, h_0 = initial distance from air diffuser to thermocline. The thermocline is defined as the depth at which the vertical water temperature gradient is maximum. It can be seen that the rate of deepening of the thermocline diminishes once it reaches the air injection point (diffuser). A dimensionless time τ is defined as $\tau = 2.9 \times 10^6 \, Q_{air}^{1.86} \, V^{-0.7} \, t$ to present all experimental data where Q_{air} is in [m^3/s], V is in [m^3], t is in [sec].

The process of the deepening in the region below the diffuser can be analyzed in a way similar to the mixed layer deepening by wind in lakes by considering the ratio between lifting power of the plume and the potential energy attributable to the greater density of the water below the diffuser, which acts against it.

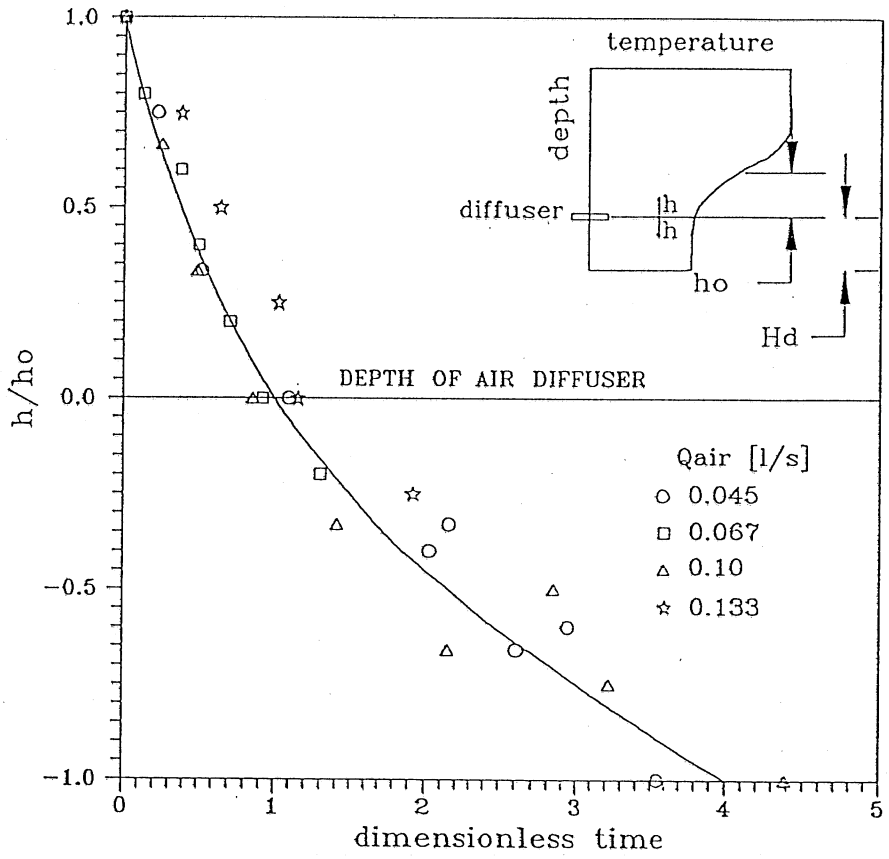

Figure 4.20 Deepening of the thermocline with time – experiments in the rectangular tank

This ratio can be expressed, for an axisymmetric diffuser as

$$\frac{g\,\Delta\rho h\, R_d^2 \Pi\, dh/dt}{Q_{air}(\rho - \rho_{air})gH_d} = \beta(t) \qquad (4.1)$$

where Q_{air} = volumetric air flow rate, g = acceleration due to gravity, R_d = average radius of the region below diffuser, dh/dt = entrainment velocity, $\Delta\rho$ = density difference at the thermocline, ρ = water density, ρ_{air} = air density, H_d = distance from diffuser to the bottom.

In equation (4.1) the only unknowns are h(t) and $\beta(t)$. The function $\beta(t)$ can be obtained from the experiments and the function h(t) can then be expressed for any specific aeration rate and the lake depth (with appropriate scaling).

Equation (4.1) can be rewritten as:

$$\beta(\tau_a) = \frac{\Delta\rho\, d(h^2)/d\tau_a}{h_o\, \rho\, H_d} \qquad (4.2)$$

where τ_a = dimensionless time expressed as

$$\tau_a = \frac{t\, Q_{air}}{h_o R_d^2 \pi} \qquad (4.3)$$

and $h_o = h(t=o)$

β versus τ_a from the tank experiments is shown in Figure 4.21. A second order polynomial which represents the best fit (r = 0.88) is

$$\beta(\tau_a) = 0.00632 - 0.0741\tau_a + 0.2061\ \tau_a^2 \qquad (4.4)$$

With equation (4.4) equation (4.1) can be written as

$$h(t) = \left(\frac{h_o gH_d}{\Delta\rho}\right)^{1/4} (0.01264\ \tau_a - 0.0741\ \tau_a^2 + 0.137\ \tau_a^3\ )^{1/4} \qquad (4.5)$$

4.4. Use of the experimental information in a three-layer simulation model

One objective of the experiments described herein was to provide data to validate the basic assumptions of the lake mixing model developed by Goossens [1979] and modified as presented in Chapter 2.

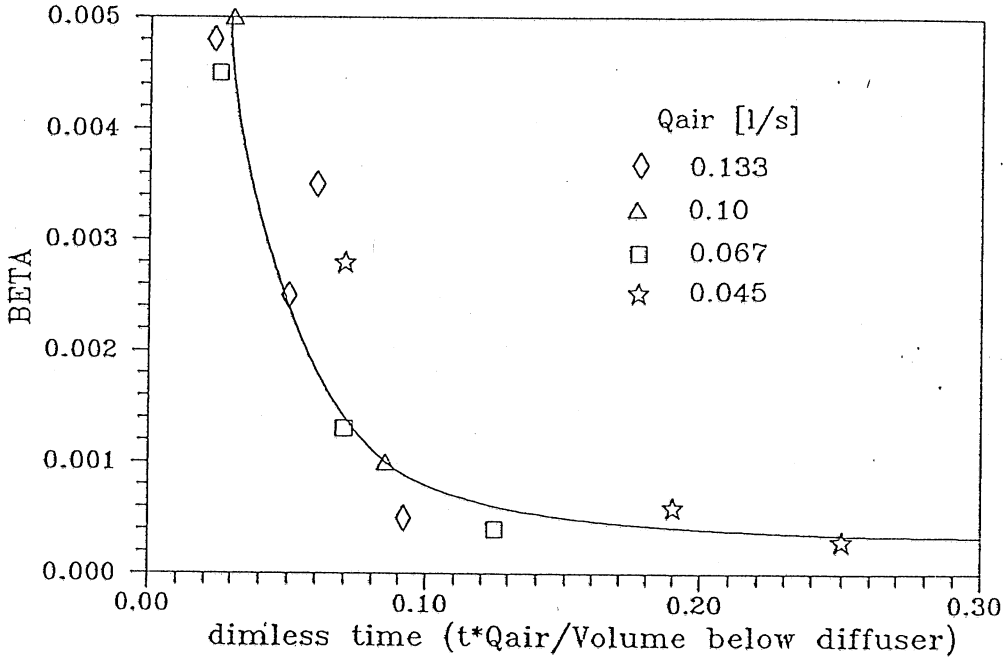

Figure 4.21 Parameter β versus time

Indeed the experimental results indicate:

(1) There is a distinct nearfield and farfield divided by a plunging region – stagnation point.
(2) The horizontal dimension of the nearfield is of the order of the depth of the water above the air injection.
(3) The nearfield initially grows rapidly until it reaches a quasi–steady position. A second much slower growth phase occurs later due to the limited volume of the farfield.
(4) Entrainment from the hypolimnion follows the relationship observed by other authors under isothermal conditions.
(5) A three layer structure in the farfield is fairly well defined.
(6) The plunging flow entrainment coefficient c_1 lies in the range determined by other investigators.
(7) The return flow entrainment coefficient c_2 is found to be much larger than in field studies. Return flow should be related to the existence of the plunging phenomena rather then to the hypolimnetic flow.
(8) Water is also entrained from below the air injection level.

Overall the experimental findings justify the basic assumptions of the numerical model.

5. SYNTHESIS OF ANALYSIS, SIMULATIONS AND EXPERIMENTAL FINDINGS FOR THE NEARFIELD FLOW

5.1. Overview

In the previous chapters the interaction of an air bubble plume and a stratified environment has been analyzed by use of a composite one–dimensional model (Chapter 2), a two–dimensional model (Chapter 3) and experiments (Chapter 4).

Although the region of practical interest is the farfield, the region which controls the flow and mixing is the nearfield. Denser hypolimnetic water entrained by the air bubbles reaches the surface where it spreads radially until it reaches a distance where the densimetric Froude number is about 0.6. Then it plunges to the depth of the neutral buoyancy. It has been shown here that the water flow induced by the air bubbles in the stratified water can be explained as a special case of negatively buoyant surface jets. The relative importance of the governing parameters is shown.

5.2. Flow field description

The flow field induced by an air bubble plume in a stratified water body is governed by the quantity of air released, the submergence depth of the diffuser, the strength of the stratification and the geometry of the basin.

Asaeda and Imberger [1988] described three types of interaction between a bubble plume and a linearly stratified environment and two types for a two layered stratification. The interaction then depends on a bubble plume number introduced by Asaeda and Imberger [1988] for two–layer systems

$$P\Delta = \frac{(g')^{1.5}\, h_\ell^{1.5}\, H_t}{g\, Q_{air}} \left[\frac{h_u}{H_t} \right]^3 \tag{5.1}$$

and for a linearly stratified system

$$P_N = \frac{N^3\, H_t^4}{g\, Q_{air}} \tag{5.2}$$

where g' is a reduced acceleration due to gravity $= g\ \Delta\rho/\rho_r$, with $\Delta\rho$ = density difference between the two layers, ρ_r = reference density, g = acceleration due to gravity, h_ℓ = thickness of the lower layer, h_u = thickness of the upper layer, H_t = total depth, and Q_{air} = gas release rate at atmospheric conditions, N = buoyancy frequency $= [-g\rho_r^{-1}d\rho_a/dz]^{0.5}$, ρ_a = ambient density.

According to Asaeda and Imberger [1988], the vertical flow of water induced by the bubble plume in a two layer stratification, impinges at the interface and a horizontal intrusion occurs at that depth when $P\Delta > 30$. This is the case of a very strong stratification and a weak bubble plume. For $P\Delta < 30$, the strong bubble plume induced flow in a weakly stratified ambient breaks through the interface and an air–water mixture reaches the free surface, where it spreads horizontally and plunges after some distance. The first regime was observed in the laboratory with a strong stratification obtained with salt [McDougall, 1978; Asaeda and Imberger, 1988]. In a linearly stratified fluid, three well defined regions of flow were evident; the upmoving flow core consisting of a mixture of air bubbles and dense fluid, an annular downdraft and beyond that the intrusion flows. At very large gas flow rates a single intrusion was observed. As the flow rate was decreased, the buoyancy flux was insufficient to carry lower fluid to the surface and multiple intrusions were observed, exiting the downdraft region at equally spaced elevations. At very low gasflow rates the intrusions became unsteady and much less well defined. The values of the P_N number for the first regime were <300, for the second $300<P_N<1000$ and $P_N>1000$ for the third regime.

Summer stratification in lakes and reservoirs can be considered two–layered. In practical applications of the bubble plume as a lake destratification device, the bubble plume numbers $P\Delta$ are typically less than 1.0 (Table 5.1) and the bubble plume effect is very strong relative to the density stratification. Direct observations of the flow field were made by Goossens [1979] in a field study and in a laboratory study with a thermally obtained stratification described in Chapter 4.

TABLE 5.1. $P\Delta$ Values in Field Studies

Lake	H_t (m)	H_ℓ (m)	g' (ms^{-2})	Q_{air} (m^3s^{-1})	$P\Delta$	Source
Calhoun	24.0	14.0	0.0232	0.059	0.5	Shapiro et al. [1973]
Petrusplaat	12.4	8.0	0.0123	0.17	0.01	Goossens [1979]
Shikazawa	10.0	7.0	0.0127	0.077	0.02	Ito [1972]
Maarsseveen	18.9	9.8	0.019	0.042	0.4	Knoppert et al.[1970]

The previous classifications are valid for a wide range of air flow rates and stratification conditions. It has been shown (Chapters 2, 3 and 4) that the flow field which develops in lake destratification consists of two distinct regions: a nearfield which is in a vicinity of the air bubble plume and the bulk of the water body called farfield. The farfield imposes a boundary conditions on a nearfield.

The ratio of the momentum of the water flow induced by the bubble plume to the stratification forces controls the different flow configurations. Similar flow fields develop when a buoyant water jet is released vertically in shallow water as observed and analyzed by Lee et al. [1974], Jirka and Harleman [1979], Lee and Jirka [1981], Lee [1980] and Andreopoulos et al. [1985]. They found that under high momentum, low buoyancy and shallow water conditions, the energy input by the buoyant jet into the receiving water may be so strong that the buoyancy contained in the discharge is not sufficient to establish a stable stratified flow. Recirculation cells are set up near the release point, leading to the re–entrainment into the vertical water flow. This configuration is termed unstable, as opposed to the stable one where there is no re–entrainment into the vertical water flow [Jirka and Harleman, 1979]. The unstable case results in a roller of size 2.5 to 3.0 H. The stable case results in an internal hydraulic jump, after which (there is some energy loss) the flow continues to spread on the surface radially outwards.

The extreme case of stable conditions, with a buoyancy approaching zero and leading to the occurrence of the unstable configuration, corresponds to the release of air bubbles in isothermal water. The release of air bubbles in stratified water represents the other extreme with a positive density difference (buoyant jets in contrary have a lower density then the ambient water), resulting in a plunging flow rather than in an internal hydraulic jump. Figure 5.1 shows similarities between the flow pattern of the stable case for a buoyant water jet with a flow pattern which occurs when the air bubbles are released in stratified water.

5.3. Flow field analysis

The nearfield mixing characteristics have been studied in considerable detail by Jirka and Harleman [1979] for a plane slot buoyant jet and by Lee et al. [1974], Lee [1980], Lee and Jirka [1981] for an axisymmetric buoyant jet.

The same line of approach has been adopted here for an air bubble plume. The features of the four regions, shown in Fig.5.1, are separately presented and the solutions are coupled to give the description of the nearfield flow characteristics.

The formulation of the problem is for a steady state and incorporates the dynamic interaction of four nearfield regions: the vertical water flow induced by the air release, the surface impingement region, the surface buoyant jet and the radial internal hydraulic jump.

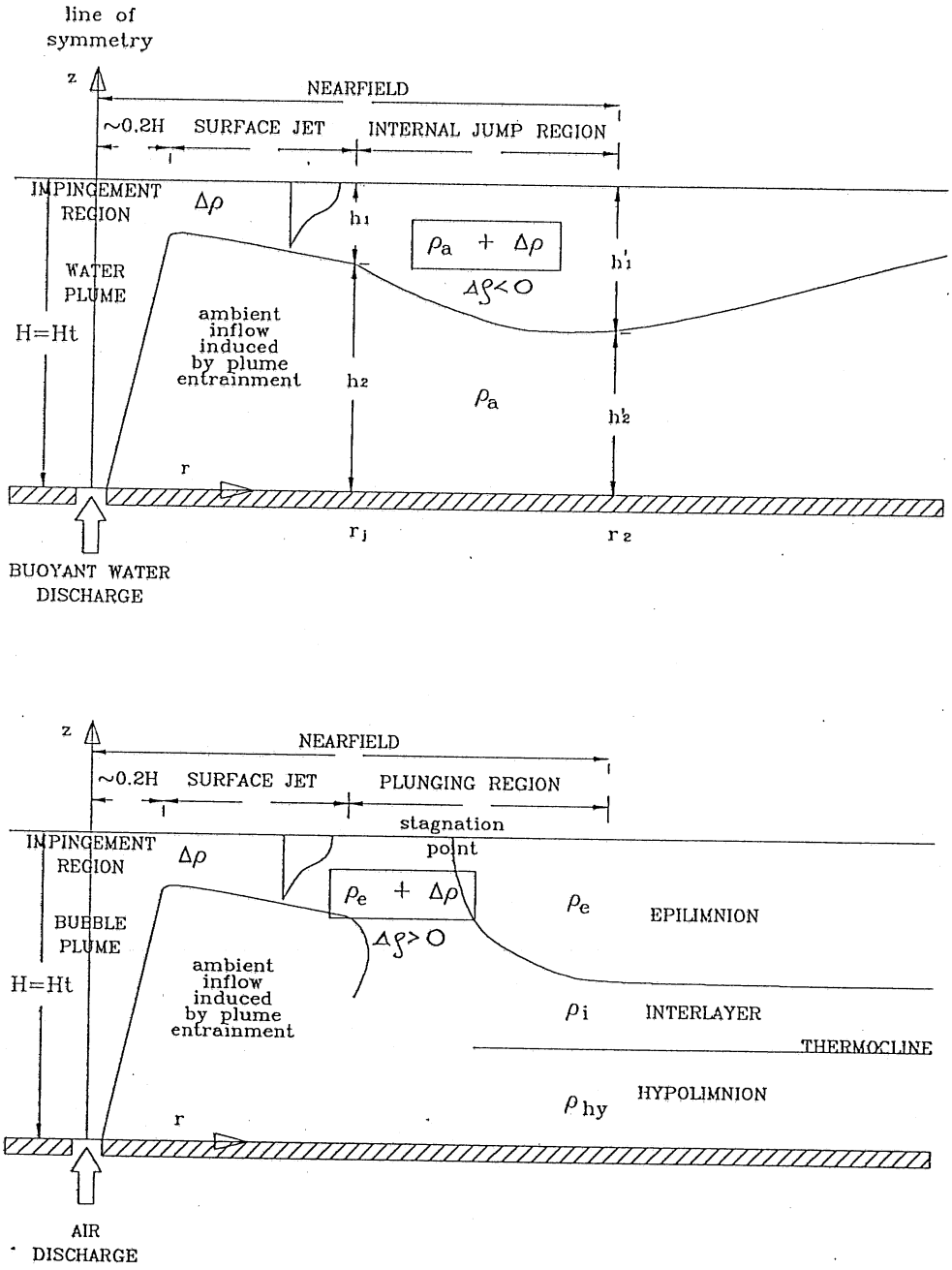

Figure 5.1. Nearfield regions

For reason of convenience the nearfield is analyzed as a linearly stratified system. Accordingly the only parameter describing the stratification is a temperature gradient dT/dz or density gradient $d\rho_a/dz$).

Bubble Plume Region

Equations used to describe the flow are the horizontally integrated equations of conservation of mass, momentum and buoyancy [Morton et al., 1956] in a form appropriate for a bubble plume. The horizontal profiles of the vertical velocities and density deficiency are assumed to be fully Gaussian:

$$u(r,z) = U(z)\, e^{-r^2/b^2} \quad ; \; \rho_a(z) - \rho_p(r,z) = \Delta\rho(z)\, e^{-r^2/\lambda^2 b^2} \tag{5.3}$$

where z = height measured upward from the diffuser, r = radius, U = centerline velocity, b = plume radius, ρ_a = ambient density, ρ_p = mean density of the plume, $\Delta\rho$ = density difference at the plume centerline, λ = ratio of gas containing radius to plume radius (called also a dispersion coefficient).

The gas is presumed to follow the isothermal expansion law

$$\rho_g(z) = \frac{\rho_T(H_B - z)}{H_T} \tag{5.4}$$

where ρ_T = gas density at a pressure of one atmosphere, H_T = atmospheric pressure head (= 10.2 m), H_B = pressure head at the level of gas release, $H_B = H_T + H$, H = submergence depth of diffuser.

The integral plume equations will involve the local mean fraction $f(r,z)$, which is given by

$$f(r,z) = \frac{\rho_a(z) - \rho_p(r,z)}{\rho_a(z) - \rho_g(z)} \tag{5.5}$$

The gas volume flux, the liquid volume flux, the momentum flux and the buoyancy per unit height respectively, are expressed in terms of local properties as

$$q(z) = 2\pi \int_0^\infty [u(r,z) + \Delta u_b] f(r,z) r\, dr \tag{5.6}$$

$$Q(z) = 2\pi \int_0^\infty u(r,z)[1 - f(r,z)] r\, dr \tag{5.7}$$

$$M(z) = 2\pi\gamma \int_0^\infty \Big\{ u^2(r,z)\rho_a(z)[1 - f(r,z)] +$$

$$[u(r,z) + \Delta u_b]^2 \rho_g(z) f(r,z)\Big\} r dr \tag{5.8}$$

$$B(z) = 2\pi g \int_0^\infty [\rho_a(z) - \rho_g(z)] f(r,z) r dr \tag{5.9}$$

where Δu_b = bubble relative (slip) velocity. Momentum amplification coefficient γ is the ratio of the total momentum flux to the momentum carried by the mean flow. Whereas for the single phase plumes, such as thermal plumes, Yih [1981] estimated that the turbulent fluctuations carry approximately 6% of the momentum flux the measurements by Milgram and Van Houten [1982] indicate that for the extremely turbulent flow associated with bubble plumes the turbulence carries approximately 50% of the momentum flux.

Closure of the integral plume equations requires a relationship between local plume properties and the rate of increase with height of the liquid volume flux. Accordingly conservation of mass for the water is written as

$$\frac{dQ}{dz} = 2\pi\alpha b(z) U(z) \tag{5.10}$$

and conservation of momentum as

$$\frac{dM}{dz} = B(z) \tag{5.11}$$

where α = entrainment coefficient.

Now the conservation of buoyancy is concerned with two separate effects: first, the effect of the stratification $d\rho_a/dz$ in the environment, and second, the increase in the volume flow rate of gas with height. It is helpful to isolate these two effects by considering first an ordinary plume rising in a stratified environment [McDougall, 1978]. Conservation of buoyancy then yields

$$\frac{dB}{dz} = \pi b^2(z) U(z) \frac{d\rho_a}{dz} \tag{5.12}$$

Second, consider a bubble plume rising in an unstratified environment. There, the conservation of gas flux at any height z can be related to the source conditions as

$$q(z) = \frac{Q_{air}\, p_a}{(H_B - z)\rho_r g} \tag{5.13}$$

where p_a = atmospheric pressure.

By using the equations (5.4) to (5.13) and the profiles mentioned above, the equations of conservation of mass, conservation of momentum and conservation of buoyancy in the stratified environment can be respectively written as:

$$2\alpha U(z)b(z) = \frac{d}{dz}\left[U(z)b^2(z)\left\{1 - \frac{\lambda^2\Delta\rho(z)}{[1+\lambda^2][\rho_a(z) - \rho_g(z)]}\right\}\right] \quad (5.14)$$

$$g\lambda^2\Delta\rho(z)b^2(z) = \frac{d}{dz}\gamma b^2(z)\left\{U^2(z)\left[\frac{\rho_a(z)}{2} - \frac{\lambda^2\Delta\rho(z)}{1+2\lambda^2}\right] + \frac{\lambda^2 u_b \rho_g(z)\Delta\rho(z)}{\rho_a(z) - \rho_g(z)}\left[\frac{2U(z)}{1+\lambda^2} + {}_\Delta u_b\right]\right\} \quad (5.15)$$

$$\frac{d}{dz}\left\{\frac{\pi\lambda^2\Delta\rho(z)b^2(z)gU(z)}{[1+\lambda^2][\rho_a(z) - \rho_g(z)]}\right\} = -\pi b^2(z)U(z)N^2(z) + \frac{d}{dz}\left\{\frac{Q_{air}p_aU(z)}{[H_B - z][1+\lambda^2][\rho_a(z) - \rho_g(z)]}\right\} \quad (5.16)$$

The values for the coefficients α, λ, and γ are given by Poon [1985]:

$$\alpha(B_u) = 0.136\left[\frac{B_u}{54.2 + B_u}\right]^{0.5}$$
$$\gamma(B_u) = 1.0 + \frac{16.2}{B_u^{1.30}} \quad (5.17)$$
$$\lambda(B_u) = 1.2\left[\frac{B_u}{71 + B_u}\right]$$

where $B_u = \{\rho_r/[\sigma(Q_{air}^4 g^3)^{0.2}]\}^{0.5}$ is called Weber number for the plume, σ = surface tension.

It should be pointed out that the effect of the stratification enters through the first term on the right hand side of Eqn. (5.16) [McDougall, 1978]. For $N = 0$ or $\rho_a(z) = \text{const}$ Eqns. (5.14) to (5.16) transform to the equations for the isothermal case given by Milgram [1983] and Poon [1985].

Eqns. (5.14) to (5.17) were solved using the Newton–Raphson method [Poon, 1985]. The model's prediction of the laboratory and field measurements of the flow rates induced by the bubble plume under isothermal conditions, by various authors, is shown in Appendix B in Figure B.6.

Surface Impingement and Buoyant Surface Jet Region

When the plume impinges on the free surface, the dynamic pressure causes a surface hump, which gives rise to a radial pressure gradient and horizontal spreading of the mixed discharge. Intense turbulent mixing occurs in this region. Figure 5.2 shows the results of two separate experiments conducted to visualize the phenomenon. Instead of attempting to describe the complicated flow details or perform a control volume analysis [Lee and

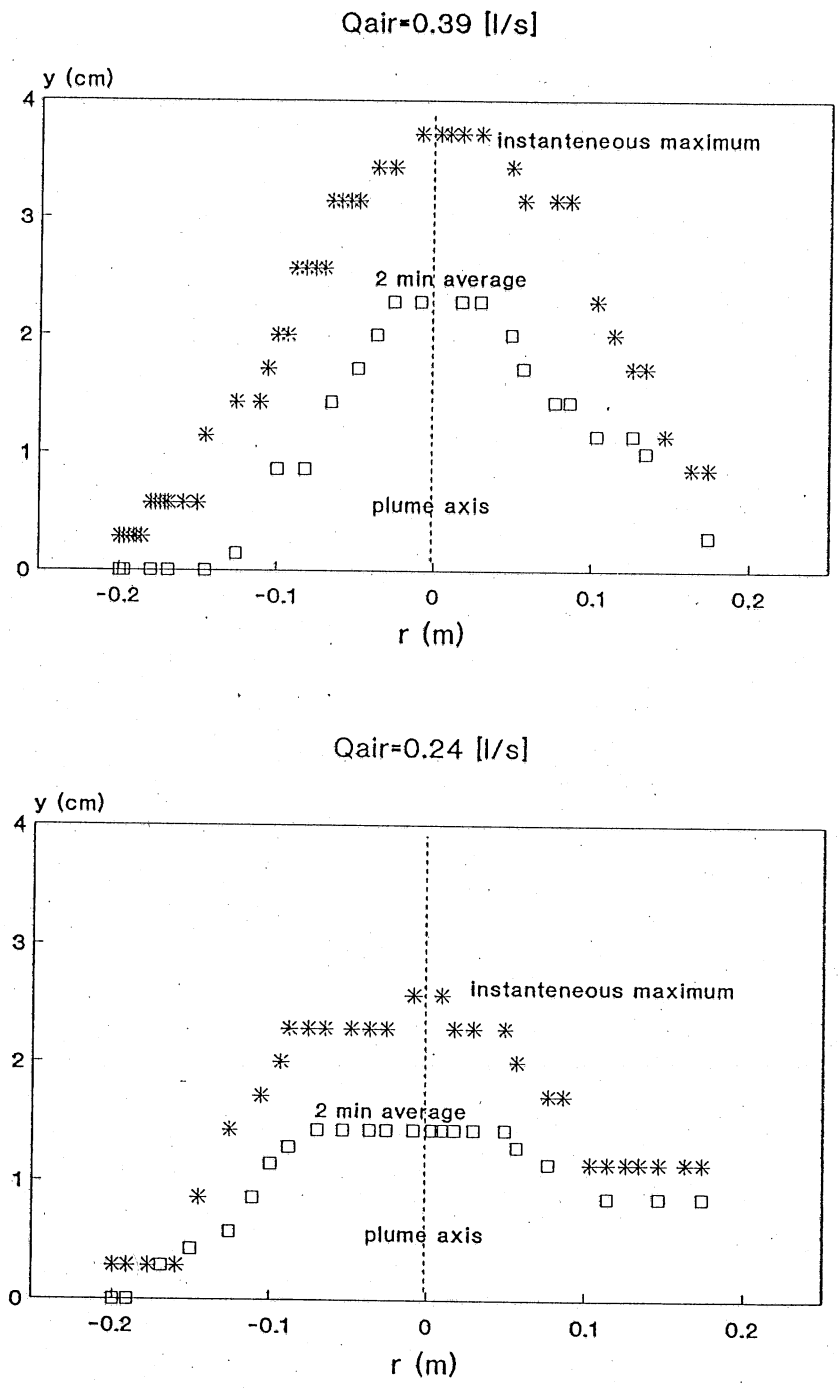

Figure 5.2 Measured water surface elevation above an air bubble plume, H=1.0 m

Jirka, 1981] the analysis presented here proceeds with a radial surface jet. The equations used to describe the surface radial jet are the ones developed by Goossens[1979] and presented in Chapter 2, as Eqns. (2.10) and (2.11). Goossens [1979] did analyze the surface impingement region experimentally and accordingly the effect of the impingement is included in the spreading and in the momentum coefficient. The equations are for the isothermal radial jet. An additional transport equation is solved in order to evaluate the heat transport along the radial surface jet.

Internal Hydraulic Jump Region

The flow in the internal hydraulic jump region is analyzed as a general two–layer system with a distinct interface, and with constant density of the upper layer ρ_1 and lower layer ρ_2. The upper and lower layer depths before the jump ($r = r_J$) are h_1, h_2, respectively, and the conjugate jump depths at the end of the jump ($r = r_2$) are h_1', h_2'.

By neglecting interfacial and bottom shear stresses, assuming hydrostatic pressure and uniform velocity distributions, and an average head of $(h_1 + h_1')/2$ over the jump length an approximate momentum analysis of an internal hydraulic jump leads to [Lee et al., 1974]
Upper layer:

$$F_1^{*2} r_1^2 \left[\frac{1}{r_1 h_1} - \frac{1}{r_2 h_1'}\right] = \frac{\rho_1}{\rho_a} \left(\frac{r_1 + r_2}{2}\right)\left(\frac{h_1 + h_1'}{2}\right)[h_1' + h_2' - h_1 - h_2]\frac{1}{h_1^3} \quad (5.18)$$

Lower layer:

$$F_2^{*2} r_1^2 \left[\frac{1}{r_1 h_2} - \frac{1}{r_2 h_2'}\right] = \left(\frac{r_1 + r_2}{2}\right)\left(\frac{h_2 + h_2'}{2}\right)\left[\frac{\rho_1}{\rho_a}(h_1' - h_1) + \frac{\rho_2}{\rho_a}(h_2' - h_2)\right]\frac{1}{h_2^3} \quad (5.19)$$

where F_1^* and F_2^* are free surface Froude numbers defined as

$$F_1^{*2} = \frac{(Q_1/2\pi r_1 h_1)^2}{g h_1} \quad \text{and} \quad F_2^{*2} = \frac{(Q_2/2\pi r_2 h_2)^2}{g h_2} \quad (5.20)$$

Transformation from a linear stratification to a two layered system is done by taking ρ_2 and ρ_1 as the average densities over the thicknesses from 0–0.8H, and 0.8–H respectively, starting from the bottom. This division is used because of the experimental evidence [Kobus, 1968; Milgram, 1983] that the vertical plume starts to spread horizontally at the distance approximately equal to 0.8H. The additional simplification can be done by defining ρ_1 as

$$\rho_1 = \rho_2 + \Delta\rho \quad (5.21)$$

ρ_1 can be bigger or smaller than ρ_2. $_{\Delta}\rho < 0$ corresponds to a buoyant jet released to the stratified environment, and $_{\Delta}\rho > 0$ corresponds to the bubble plume case. By introducing the Bousinesq approximation, $\Delta\rho << 1$ (a condition satisfied by most submerged buoyant discharge applications) the upper layer change is equal to [Lee and Jirka, 1981]

$$f\left(\frac{h_1'}{H}\right) = \frac{4F_1^2\left(1 - \frac{r}{r_J}\frac{h_1'}{h_1}\right)}{\frac{r_2 h_1'}{r_J h_1}\left(1 + \frac{r_2}{r_J}\right)\left(1 + \frac{h_1'}{h_1}\right)\left(1 - \frac{h_1'}{h_1}\right)}$$

$$- \frac{4F_2^2\left(1 - \frac{r_2}{r_J}\frac{H - h_1'}{h_2}\right)\frac{h_2}{h_1}}{\frac{r_2}{r_J}\frac{(H - h_1')}{h_1}\left(1 + \frac{r_2}{r_J}\right)\left(1 + \frac{H - h_1'}{h_2}\right)\left(1 - \frac{h_1'}{h_1}\right)} + 1 = 0 \qquad (5.22)$$

where, after Sadler and Higgins [1963]

$$r_2 = r_J + 4\,(h_1' + h_1) \qquad (5.23)$$

Densimetric Froude numbers in the upper and lower layer, F_1 and F_2, respectively, are defined as

$$F_1^2 = F_1^{*2}/(\Delta\rho/\rho_2) \quad ; \quad F_2^2 = F_2^{*2}/(\Delta\rho/\rho_2) \qquad (5.24)$$

Defining the critical state as that which is conjugate to itself, $h_1' \to h_1$, $h_2' \to h_2$, $r_1 \to r_J$ we have the criterion for criticality:

$$F_1^2 + F_2^2 = 1 \qquad (5.25)$$

The flow is supercritical upstream of the jump, $F_1^2 + F_2^2 > 1$, and usually, but not necessarily, subcritical downstream of it, $F_1^2 + F_2^2 < 1$.

In general, the governing equation for the conjugate jump height h_1', possesses two solutions that lie within the physically feasible range $0 < h_1' < H$. One of these can be discarded by energy considerations. However, for high densimetric Froude numbers of the upper layer F_1 (or large values of h_1/h_2) Eqn. (5.22) does not yield a solution. The nonexistence of a solution can be interpreted physically as a hydrodynamically unstable solution [Jirka and Harleman, 1979]. Under these high momentum conditions, the buoyancy contained in the upper layer flow is not sufficient to establish stable conjugate downstream conditions, leading to a breakdown of the stratified flow and re-entrainment into the vertical water flow.

5.4. Results

A computer program was written based on the equations presented above to obtain information about the influence of the governing parameters of the fluid flow on the nearfield mixing. It has been shown that the flow field is governed by the quantity of air released, the submergence depth of the diffuser and the strength of the stratification. A large number of numerical simulations were made by varying Q_{air} in the range from $1x10^{-4}$ to 1 m^3/s, by varying H from 1 to 30 m and by varying ΔT from 3 to 20°C. ΔT is the temperature difference between the bottom and the surface. (The temperature at the bottom was kept constant at T = 10°C.)

The effect of the stratification on the development of the vertical water flow rate was evaluated first. Figure 5.3 shows an example where for a fixed depth and air flow rate the strength of the linear stratification is changing. It can be seen that the stratification does not affect the initial development of the plume substantially as was also found by Morton et al. [1956]. As the plume rises it is slowing down, more in the stronger stratification, but not significantly. For a typical temperature difference in the summer stratification of lakes of about 10 °C it can be seen in Fig. 5.3 that the velocity at the surface is within 0.02 m/s of that for an isothermal case. For practical purposes the effect of the stratification can therefore be neglected in the treatment of the vertical water flow induced by the air release. This result is not surprising since the driving force of the plume is the buoyancy of the air bubbles which is of the order of ρ_a/ρ_{air} and which will not change significantly for the relatively small changes of density of the ambient water as a result of the stratification. The same conclusion was reached in Chapter 4 based on the experimental data.

A more general analysis of the effect of stratification on plume development, can be made by means of the P_N number defined in Eqn. (5.2). Figure 5.4 shows the height H_p at which the intrusion will occur under stratified conditions. H_p is divided by the diffuser depth H and plotted versus the bubble plume number P_N. The criterion for the intrusion is occurrence of a negative water centerline velocity. The results show that the effect of the stratification becomes important for P_N values around 10^3. For P_N values of that magnitude or larger $H_p < H < 1$ which means that the intrusion occurs at some depth bellow the surface. With ΔT = 10 °C and H = 30 m, the average value of $N^3H_t^4/g$ is about 1.0. Therefore, in order for the stratification to suppress the bubble plume development ($P_N \approx 10^3$) Q_{air} has to be smaller than 0.001 m^3/s. This flow rate is at least one order of magnitude smaller then the typically used air flow rates (see Table 5.1).

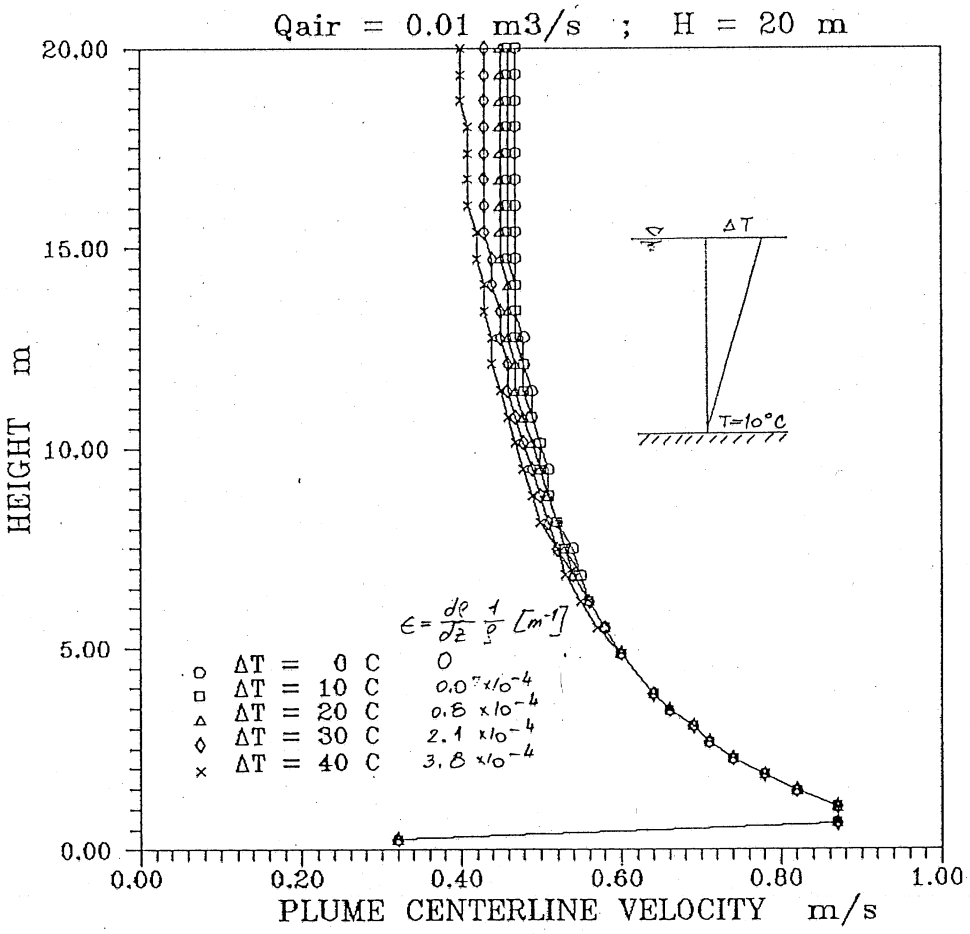

Figure 5.3 Example of the effect of a linear stratification on the vertical water flow velocity induced by the air bubble plume

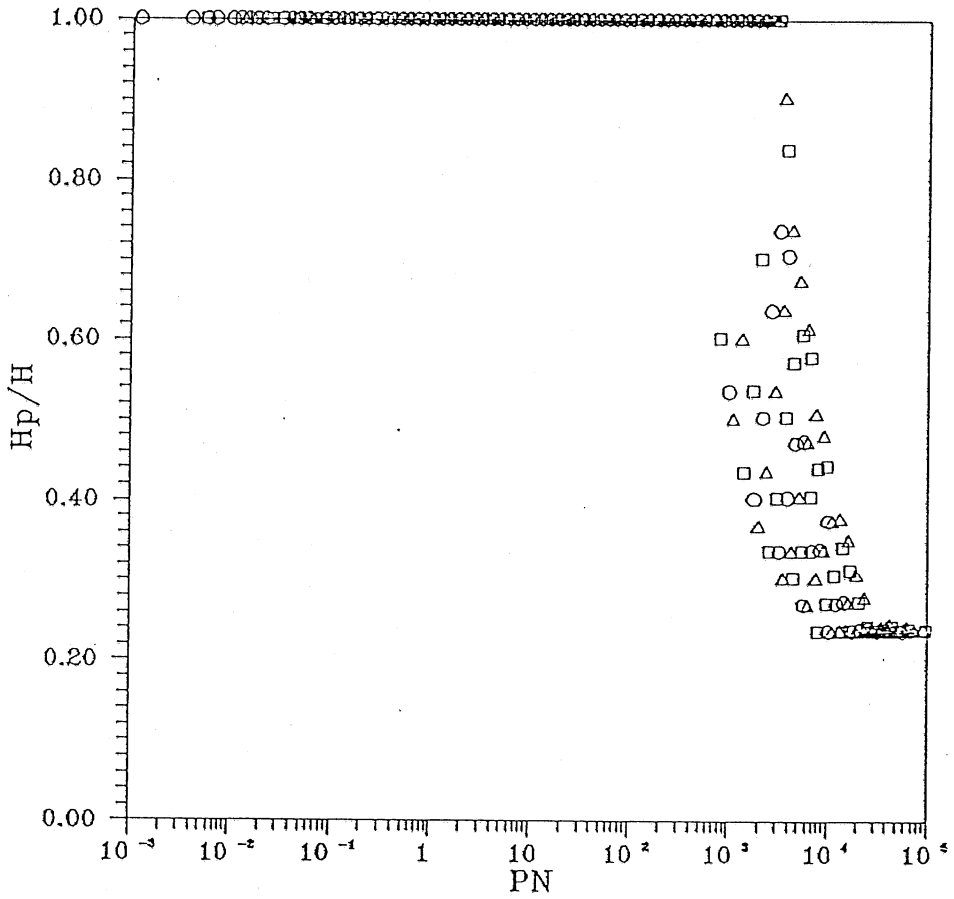

Figure 5.4 Dimensionless height H_P/H of the first intrusion (interflow) induced by the bubble plume versus bubble plume number P_N

This proves that the stratification will not have a significant effect on the plume development in lake destratification practice. Fig. 5.4 also shows that the intrusion always occurs at heights larger than 0.24 H meaning that the buoyancy of the plume prevails over the stratification below 0.24 H. It has to be pointed out that $H_p/H < 1$ does not mean that the water flow will not reach the surface. It only means that the intrusion will start at some intermediate depth and that the plume is retarded by the stratification. As the air bubbles will rise to the surface, some water will always be entrained towards the surface. The rate will be smaller when intermediate intrusions occur. The value of $P_N \approx 10^3$ when the stratification starts to take over the buoyancy of the air bubble plume is in agreement with experimental findings by Asaeda and Imberger [1988].

Similarities as well as differences exist between the flow fields induced by vertical buoyant jets and bubble plumes released in stratified environments. Results for buoyant jets are well established through analytical and experimental studies [Lee et al., 1974; Jirka and Harleman, 1979; Lee and Jirka, 1981; Andreopoulos et al., 1985]. The discharge stability is solely dependent on the near–field behavior of the jet, that is the dynamic interaction of the buoyant jet region, the surface impingement region and the internal hydraulic jump region. The stability is independent of the farfield geometry of the receiving medium [Jirka and Harleman, 1979].

The main flow regimes for vertical buoyant jets (obtained by analysis analogous to the one described previously for the bubble plume and verified by experiments) are reproduced in Figure 5.5 [Lee and Jirka, 1981]. Fig. 5.5 shows that for a given submergence H/D, where D = diameter of jet, the unstable domain is approached by increasing the source densimetric Froude number F_0. The pure plume (zero F_0) falls within the stable discharge domain. The pure jet however ($F_0 \rightarrow \infty$) falls into the unstable domain. In that case it has been found experimentally that the size of the recirculating cells is about 2.5 – 3.0 H and **independent of the H/D ratio or source momentum** [Lee et al., 1974; Jirka and Harleman, 1979; Jirka and Lee, 1981; Andreopoulos et al., 1985]. The same cell sizes have to be observed also for air bubble plumes released into isothermal environments. This also has to be the limiting size (upper bound) of the plunging distance for the case of bubble plume mixing in a stratified environment considering that isothermal conditions (well mixed) are a steady state conditions.

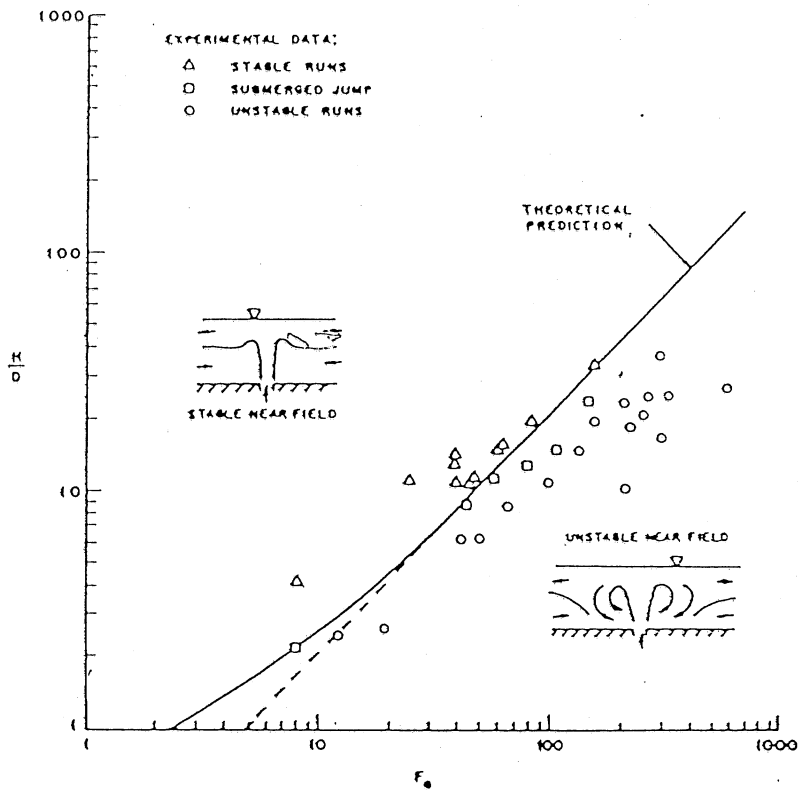

Figure 5.5 Stability of vertical round buoyant discharge in shallow water (after Lee and Jirka, 1981)

In the computations for the horizontal surface jet the unstable regime manifests itself by the inability to find the second conjugate depth of the internal hydraulic jump. As the radial surface jet is heavier then the water below, it cannot maintain itself on the surface and it plunges. Of course the jet will spread horizontally as long as momentum of the flow prevails over the negative buoyancy. The parameter describing the phenomenon is densimetric Froude number. Akiyama and Stefan [1987] found for nonseparated flows a value of the densimetric Froude number at the plunging point in the range from 0.57 to 0.89 with an average value of 0.68. In the study described herein the the next step in the calculation procedure was to implement $F_p < 0.7$ as a criterion to find the plunging position. Simulations of the plunging distance for temperature differences occuring during the experiment No. 9 (see Table 4.2) are presented in Figure 5.6. Each time period during destratification in Exp. 9 was described with temperature difference between surface and bottom. As the plunging distance was evaluated for each time period (see Fig.4.14) the relationship r_p versus ΔT was established and marked (symbols) in Figure 5.6. It can be seen that calculated values (solid line) are in agreement with measurements (symbols).

The stratification in experiment No. 9 was essentially two–layered. In the analysis a linear stratification, with the same maximum temperature difference ΔT was used. Nevertheless agreement between calculations and measurements is good. This suggests that the vertical distribution of the stratification is less important than the maximum density difference itself.

Figure 5.7 shows plunging distance r_p normalized with a thickness of the surface radial jet at the end of the surface impingement region h_w versus a densimetric Froude number evaluated the same point, F_w. The end of the surface impingement region is taken to be at approximately 0.2 H [Kobus, 1973]. The results show the increase of the normalized plunging distance with an increase of F_w, as observed for the nonseparated plunging flows [Akiyama and Stefan, 1987]. As the relationship between H and h_w is not exactly linear (Lee and Jirka, 1981, showed that for the buoyant jets may vary about 10% for the different source conditions) the relationship between F_w and r_p normalized with H have some scatter as shown in Figure 5.8. The limiting value of $r_p/H \approx 3$ is also shown.

The flow rate at the plunging point Q_p controls the entrainment from the surface layers in the farfield (epilimnion). This entrainment is found to be approximately constant, or $Q_e = 0.05\ Q_p$ (already shown in Chapters 2, 4 and by Akiyama and Stefan, 1987). The relationship between Q_p normalized with a flow rate at the end of surface impingement region Q_w versus F_w is shown in Figure 5.9.

The water plunges until it reaches the depth of neutral buoyancy, noted here as Z_p (measured from the surface). For the linear stratification the

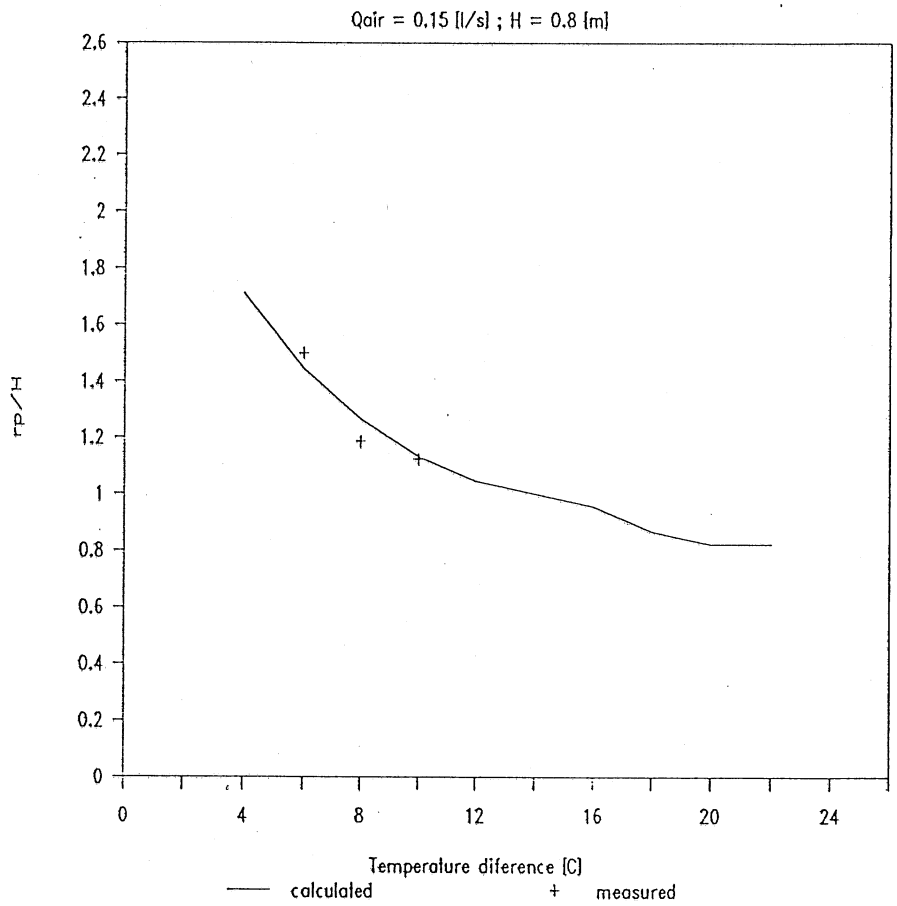

Figure 5.6. The evaluation of the plunging distance versus temperature difference for the linear stratification under experimental conditions

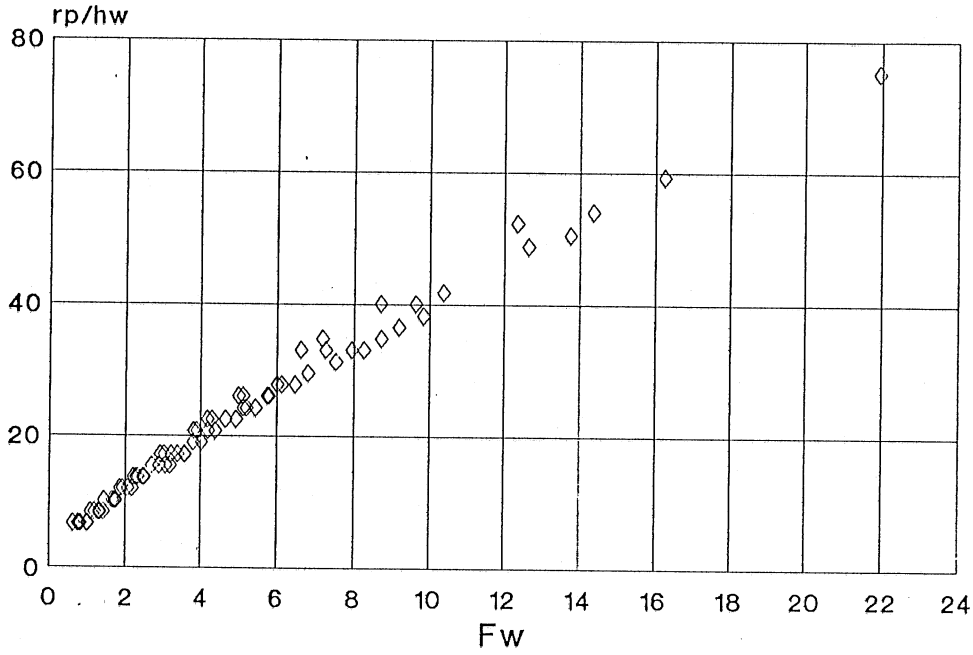

Figure 5.7. Dimensionless plunging distance, normalized with a radial jet thickness at the end of the surface impingement region, versus a densimetric Froude number at the same point

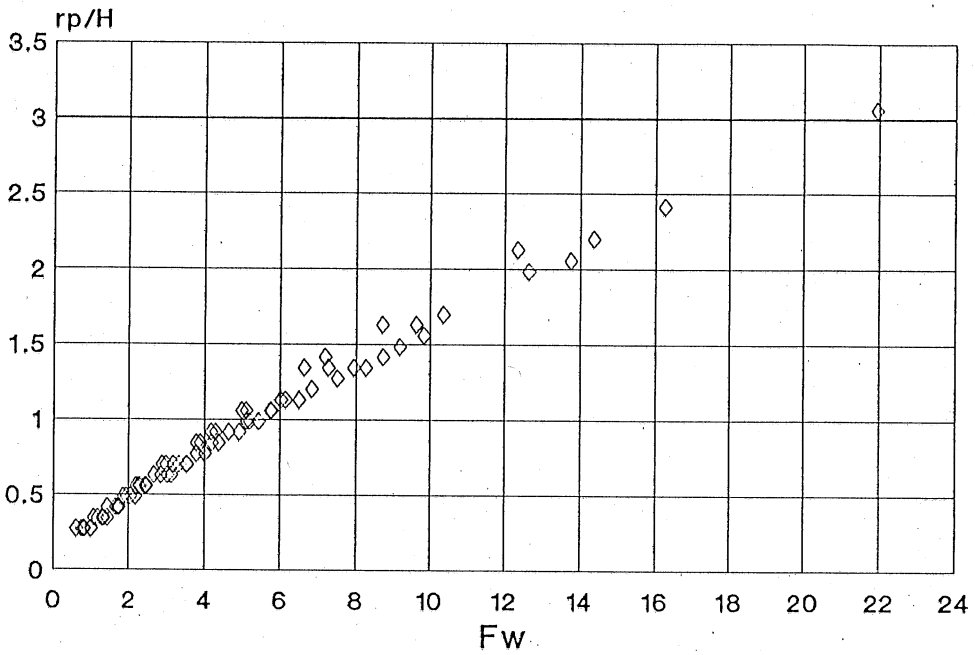

Figure 5.8 Dimensionless plunging distance, normalized with a diffuser's depth, versus a densimetric Froude number evaluated at the end of the surface impingement region

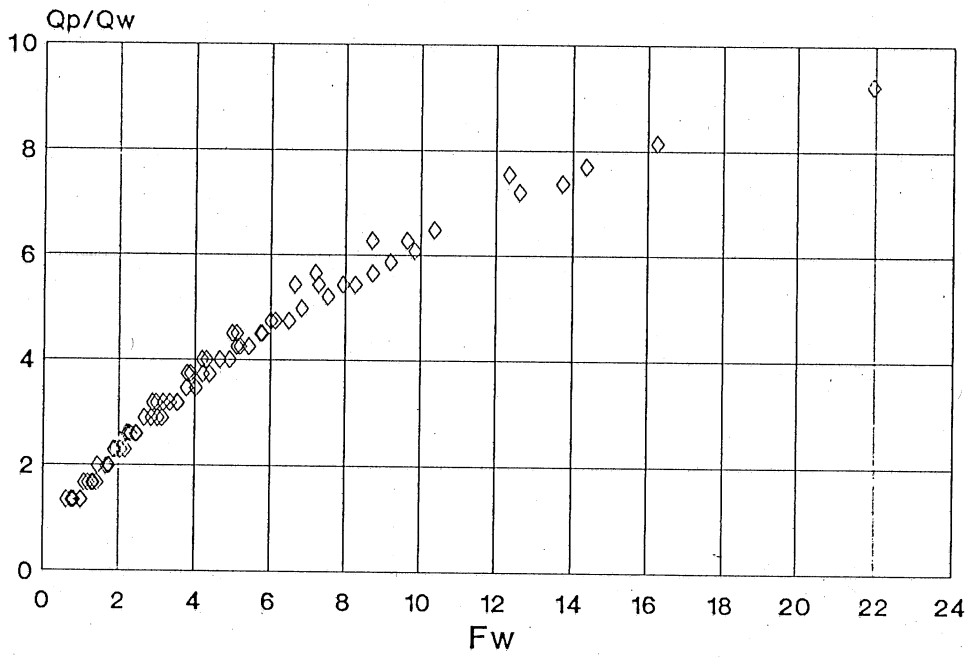

Figure 5.9 Dimensionless flow rate at a plunging point, normalized with a radial jet flow rate at the end of the surface impingement region, versus a densimetric Froude number at the same point

relationship between Z_p normalized with r_p versus F_o is shown in Figure 5.10. For the two layered stratification the point of neutral buoyancy is at the position of the thermocline. At that point the spreading of the water occurs in two directions, towards the bubble plume as a return flow Q_{ret}, and in the opposite direction (towards to the rest of the water basin), called the interlayer flow Q_i.

For the evaluation of Q_i it is not necessary to evaluate Q_{ret} because the equation of continuity applied for the farfield gives $Q_i = Q_e + Q_{hy}$ where Q_e can be evaluated as stated before ($Q_e = 0.05\ Q_p$) and the hypolimnetic flow Q_{hy} is approximately equal to the water flow rate of the bubble plume at the depth of the point of neutral buoyancy (or thermocline). This has been shown in Figure 4.19.

The discussion above stress is the main features governing the entire flow field. Of course, for a more detailed evaluation of the complete geometry of the layers in the farfield one can use a numerical model as presented in Chapter 2 and 3. The time required to mix the entire farfield volume V completely is then

$$t \geq V / Q_i \tag{5.26}$$

5.5. Conclusions

Release of air bubbles in stratified receiving water can be analyzed as a special case of a buoyant jet.

The flow field is controlled in the nearfield. The farfield geometry has a significant influence on the bulk mixing characteristic at the discharge. The parameters affecting the flow field in the nearfield are the air release rate, submergence depth of the diffuser and maximum temperature difference. A temperature difference does not have an important influence on the vertical water flow induced by the air bubbles but rather on the radial surface jet and plunging point. The plunging phenomenon here follows the same pattern as observed for nonseparated plunging flows. A thermocline (for two layered stratification) cuts off surface effects (plunging) from the flow in the hypolimnion.

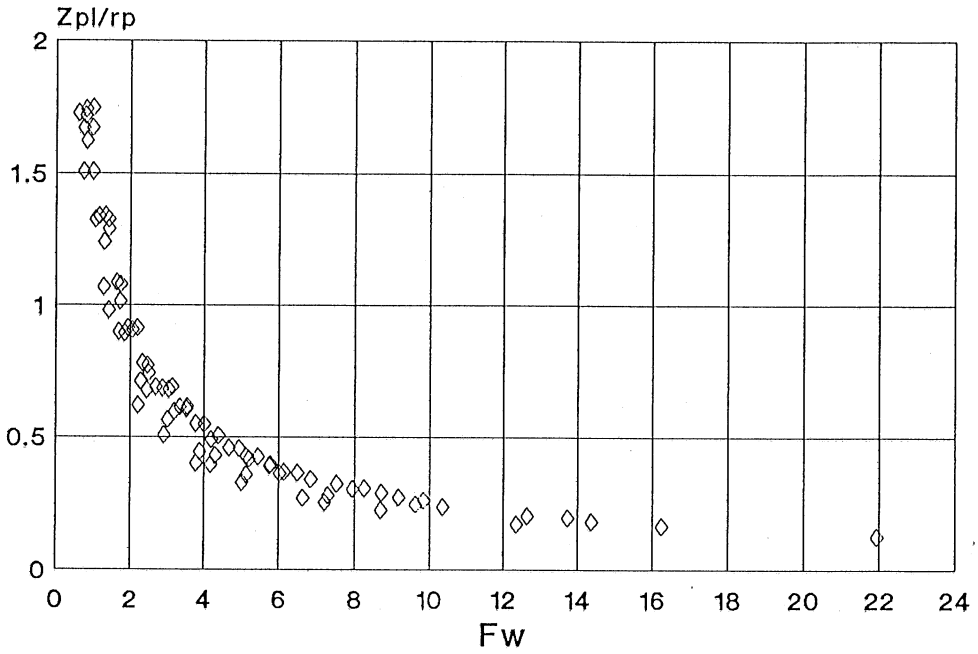

Figure 5.10 Dimensionless plunging depth, normalized with a radial jet thickness at the end of the surface impingement region, versus a densimetric Froude number at the same point

6. SUGGESTIONS FOR DESIGN OF AIR BUBBLE DESTRATIFICATION SYSTEMS

Destratification of a lake by an air bubble system depends on several parameters including the rate and distribution of the air flow, meteorological conditions, timing of the process, and the geometry of the lake. Interactions are complicated and the selection of a system for a specific lake or reservoir is not a simple matter. It should be made in several steps. The preliminary sizing of the destratification system can be done by the semi–empirical method proposed by Davis [1980] where the only inputs required are the geometry of the lake and the initial temperature profile based on which a stability parameter is calculated. This stability parameter is the only reference to the stratification in the lake. Energy input by the air bubble system necessary to overcome that stability with some energy loss is then determined. In principle, the same approach for the sizing of the system is proposed by Patterson and Imberger [1989].

The use of the stability parameter, defined as the difference in the potential energy of the lake/reservoir for the stratified and the well mixed conditions, as the main parameter in the sizing of the destratification system has important shortcomings, as stated by Fast [1981]. The stability is a relative, not an absolute measure, due to the fact that it greatly depends on the temperature profile. Based on the nonlinear relationship between density and temperature, temperature profiles having the same shape, but one of them shifted just a few degrees, will result in a very different stability parameter value. It has also been shown [Fast, 1968] that the yearly stability curve is directly related to water levels in the lake or reservoir. Therefore, if the water volumes change as a result of inflow and outflow, then changes in stability during destratification are not a suitable measure of destratification efficiency. Similarly, as pointed out by Fast [1981], it is difficult to compare efficiencies between lakes which have different water volumes and basin geometries. Therefore a stability parameter based approach can only give a preliminary aerator design. Evaluation of the preliminary system in terms of its interaction with specific lake or reservoir characteristics has to be done with a dynamic model, as proposed here in Chapter 2 or by Patterson and Imberger [1989]. Only in that type of simulation can the performance of the selected system be seen in connection with weather and timing of the operation.

7. CONCLUSIONS AND RECOMMENDATIONS FOR FURTHER RESEARCH

As a result of the research described here, a better understanding has been gained of the nature of the flow that results from the presence of a bubble plume in a stratified water body. The flow field begins as a turbulent vertical plume induced by rising bubbles. The plume entrains ambient water of varying temperatures (densities) and when it reaches the surface, it is deflected horizontally and becomes an unstable and eventually plunging flow.

Chapter 1 describes the air bubble destratification technique in the broad context of the lake restoration techniques. The literature points out the shortcomings of current research in this field.

The experiments presented in Chapter 4 were conducted to better understand the governing physical processes and to provide data to verify the mathematical models presented in chapters 2 and 3. The time evolution and and spatial distribution of water temperatures were measured in the experiments. Of particular interest were the development of the upwelling region and the temperature structure in the farfield and the quantification of water entrainment by the bubble plume. It was found that there is a distinct nearfield and farfield divided by a plunging region which is characterized by a stagnation point of the radial surface velocity. The horizontal dimension of the nearfield is of the order of the diffuser's depth of submergence. The plunging phenomenon follows the same pattern as found for plunging flows by other authors. A three layer structure in the farfield is well defined. It includes flows the epilimnion and hypolimnion towards the air bubble plume and an interlayer flow away from the bubble plume. The thermocline isolates the hypolimnion from surface effects and as a result, the entrainment from the hypolimnion approximates that found under isothermal conditions. Entrainment from below the diffuser depth also occurs, but at significantly lower rate.

The computer model presented in Chapter 2 can be used as a practical tool in the analysis of air bubble system in stratified lakes or reservoirs. The importance of weather factors relative to the strength of an air bubble mixing system is demonstrated by synoptic simulation of heat transfer into and within a lake with circulation and mixing caused by the upwelling water plume created by the rising bubbles. In addition, the simulations demonstrated that the effectiveness of an air bubble destratification system with a given air flow rate is strongly dependent on the number of air release points. The seasonal timing of the release and total air flow rate are also important.

Even though a one dimensional model such as that presented in Chapter 2 can give a good prediction of the bulk effects of the mixing process, the details of the flow field, especially its development in time, can not be ascertained. The 2–D model presented in Chapter 3 shows the finer structure of the flow during the dynamic destratification process and therefore offers a better understanding of the interaction of the various governing parameters. The approach taken in modeling the flow induced by the air bubbles uses an internal buoyancy force but treats the water phase as a continuum in which the bubbles are moving under the influence of the buoyancy. The inability of the basic k–ϵ turbulence model to predict the flow field under these conditions has been demonstrated. However, the buoyancy–extended version of the k–ϵ model can be and was used successfully. The model takes into account the damping effect of the free surface and the density interface. It was found, that even though this model contains all essential elements of the interaction between shear and buoyancy, unrealistically high rates of mixing are predicted, resulting in accelerated destruction of the stratification. As a result the breakdown of destratification as predicted by the model is faster then that measured, but the pattern of the events is in accordance with measurements. The development of the flow is illustrated by means of velocity vectors, streamlines and isotherms. It was found that plunging occurs where the densimetric Froude number has a value of about 0.6 to 0.7, the same as that for plunging flows in general. The water plunges until it reaches a depth of neutral buoyancy, which for two layered stratification is the position of the thermocline.

It was shown in Chapter 5 that the flow field induced by the air release can be placed in the more general context of water jets and plumes. The relative importance of the governing parameters of the flow field was identified and presented. Nearfield events control the development of the flow field. Farfield geometry has a significant influence on the bulk mixing characteristics of the system. The parameters affecting the flow in the nearfield are the air release rate, the submergence depth of the diffuser, and the density gradient. The strength of the stratification is found have of negligible influence on the vertical plume development but significant impact on the extent of the radial surface jet and the characteristics of the plunge region. The parameter controlling the plunging phenomenon is the densimetric Froude number at the plunge point.

Some practical suggestions for the design of an air release destratification system are given in Chapter 6. Steps are suggested for selection of an appropriate system for a given lake.

The research presented here can serve as a basis for both experimental and numerical analysis of line diffusers. A comparison of the efficiency of point diffusers which are the subject here and line diffusers may be of interest. The results of the 2–D model showed that more work is required in the modeling of the turbulence in the presence of the stratification. The present models predict artificially high mixing levels which may lead to incorrect predictions in unsteady simulations.

REFERENCES

Abraham, G., Theoretische beschouwingen over zoutbestrijding bij schutsluizen door luchtbellengordijnen, *De Ingenieur*, Vol.84, O9–O17, 1972a.

Abraham, G., Jets and plumes issuing into stratified fluid, *Proc.* First Int. Symp. on Stratified Flows, Novosibirsk, 3–34, 1972b.

Akiyama, J. and H.G. Stefan, Onset of underflow in slightly diverging channels, *Jour. of Hyd. Eng.*, ASCE, Vol. 113, No. 7, pp. 825–844, 1987.

Andreopoulos, J., A. Praturi and W. Rodi, Experiments on vertical plane buoyant jets in shallow water, *J. Fluid Mech.*, Vol. 168, pp.305–336, 1986.

Asaeda, T. and J. Imberger, Structures of bubble plumes in stratified environments. Environmental Dynamics Report ED–88–250, Center for Water Research, Univ. of Western Australia, Nedlands, WA 6009, 1988.

Ashton, G.D., Numerical Simulation of Air Bubble System, *Can. J. Civ. Eng*, Vol.5, 231–238, 1978.

Ashton, G.D., Air bubbler systems to suppress ice, US Army Corps of Eng., Cold Regions Research and Engng. Lab., Special Report No. 210, 1974.

Azbel, D., *Two–phase flows in chemical engineering*, Cambridge University Press, Cambridge, 1981.

Baines, W.D. and G.F. Hamilton, On the flow of water induced by a rising column of air bubbles, *Proceedings* of the 8th Congress in Montreal, IAHR, 7D1–7D21, 1959.

Barczewski, B., A new method for air concentration measurements in air bubble plumes, *Proceedings* of 20th IAHR Congress, Moscow, 278–287, 1983.

Benzing, R.J. and J.E. Myers, Low Frequency Bubble Formation at Horizontal Orifices, *Ind. Eng. Chem.*, Vol.47, p.2087, 1955.

Bernhardt, H., Aeration of Wahnbach Reservoir without changing the temperature profile, *J. Amer. Water Works Assoc.*, Vol.9, 943–964, 1967.

Boehmke, J.R., Effects of Aeration on Lake Cachuma, California 1980–1982, *Proc.* of 3rd Annual Conf. North Amer. Lake Management Society, Knoxville, Tennessee, 18–20, oct. 1983.

Brevik, I., Two Dimensional Air–Bubble Plume, *Journal of the Waterway, Port, Coastal and Ocean Division*, ASCE, Vol.103, WW1, 101–115, 1977.

Brunn, P.M., Discussion on Engineering challenges of dredged material disposal, *Journal of Waterways, Harbors and Coastal Eng. Division*, ASCE, Vol.101., WW4, 461–463, Nov. 1975.

Bryan, J.C. and H.J. Garber, Formation of Bubbles at Submerged Orifices, *Proceedings* AIChE Symposium on Mechanics of Bubbles and Drops, Detroit, November 1955.

Burns, F.L. and I.J. Powling, eds., Destratification of lake and reservoirs to improve water quality, *Proceedings* of a Joint U.S./Australia seminar and workshop, Melbourne, Australia, February 1979, Australian Government Publishing Service, Canberra, 1981.

Cederwall, K. and J.D. Ditmars, Analysis of Air–Bubble Plumes, W.M. Keck Laboratory of Hydraulics and Water Resources, California Institute of Technology, Report No.KH–R–24, 1970.

Celik, I. and W. Rodi, Simulation of free–surface effects in turbulent channel flows, *J. PhysicoChemical Hydrodynamics*, Vol.5, No. 3/4, pp.217–227, 1984.

Cheremisinoff, N.P., *Encyclopedia of Fluid Mechanics*, Vol.3, Gulf Publishing Company, 1986.

Chuang, S.C. and V.W. Goldschmidt, Turbulent Diffusion of Small Gas Bubbles in an Axi–Symmetric Water Jet, FWPCA–16070 D.E.P., 1970.

Clift, R. and W.H. Gauvin, Motion of Entrained Particles in Gas Stream, *The Canadian Journal of Chemical Engineering*, Vol.49, 439–448, 1971.

Clift, R., J.R. Grace and M.E. Weber, *Bubbles, Drops and Particles*, Academic Press, 1978.

Cooke, G.D., E.B. Welch, S.A. Peterson and P.R. Newroth, *Lake and Reservoir Restoration*, Butterworth Publishers, 1986.

Cook, T.L. and F.H. Harlow, VORT: A computer code for Bubbly Two–Phase Flow, Los Alamos National Lab., LA–10021–MS, US–32, 1984.

Crowe, C.T., M.P. Sharma and D.E. Stock, The Particle–Source–In Cell (PSI–CELL) Model for Gas–Droplet Flows, *Journal of Fluids Engineering*, ASME, Vol.99, 325–332, 1977.

Crowe, C.T., Two–fluid versus trajectory models: range of applicability, *Proceedings* AIAA/ASME Fluid Mechanics, Plasma Dynamics, and Lasers – 4th Conference, Atlanta, 91–95, 1986.

Crowe, C.T., REVIEW:Numerical Models for Dilute Gas–Particle Flows, *Journal of Fluids Engng.*, ASME, Vol.104, No.3, 297–303, 1982.

Datta, R.L., D.H. Napier and D.M. Newitt, The properties and Behavior of Gas Bubbles Formed at a Circular Orifice, *Trans. Inst. Chem. Engr.*, Vol.28, p.14, 1950.

Davidson, J.F. and B.O.G. Shuller, Bubble Formation at an Orifice in an Inviscid Fluid, *Trans. Inst. Chem. Enrg.*, Vol 38, p.335, 1960.

Davidson, J.F. and B.O.G. Shuller, Bubble Formation at an Orifice in a Viscous Liquid, *Trans. Inst. Chem. Enrg.*, Vol 38, p.144, 1960.

Davidson, J.F. and D. Harrison, *Fluidized Particles*, Cambridge University Press, NY, 1963.

Davidson, L. and E.H. Amick, Formation of Gas Bubbles at Horizontal Orifices, *AIChE Journal*, Vol.2, p.337, 1956.

Davis, J.M., Destratification of reservoir – a design approach for perforated – pipe compressed – air systems, *Water Services*, 497–504, 1980.

Ditmars, J.D., Mixing of density–stratified impoundments with buoyant jets, W. M. Keck Laboratory, Cal. Inst. of Tech., Pasadena, Calif., Report No. KH–R–22, 1970.

Durst, F., A.M.K.P. Taylor and J.H. Whitelaw, Experimental and Numerical Investigation of Bubble–Driven Laminar Flow in an Axisymmetric Vessel, *Int.Journal Multiphase Flow*, Vol.10, No.5, 557–569, 1984.

Durst, F., B. Schonung, K. Selanger and M. Winter, Bubble–driven liquid flows, *J.Fluid Mech.*, Vol.170, 53–82, 1986.

Durst, F., D. Milojevic and B. Schonung, Eulerian and Lagrangian predictions of particulate two–phase flows: a numerical study, *Appl. Math. Modeling*, Vol.8, 101–115, 1984.

EPA–440/5–81–003, Clean Lakes Program Guidance Manual, 1981.

Fannelop, T.K. and K. Sjoen, Hydrodynamics of underwater blowouts, In *Proc.* AIAA 18th Aerospace Sci. Meeting, Pasadena, 1980.

Farrell, G.J., Buoyancy Induced Plunging Flow Into Reservoirs and Coastal Regions, Ph.D. Thesis, University of Minnesota, 1986.

Farrell, G.J. and H.G. Stefan, Buoyancy Induced Plunging Flow Into Reservoirs and Coastal Regions, St. Anthony Falls Hydraulic Lab., University of Minnesota, Minneapolis, Project Report No. 241, 1986.

Fast, A.W., Artificial destratification of El Capitan Reservoir by aeration, Part 1: Effects on chemical and physical parameters, Calif. State Dept. of Fish and Game, Fish. Bull. 141, 1968.

Fast, A.W., The effects of artificial aeration on lake ecology, Water Pollut. Control Res. Ser. 16010 EXE 12/71, U.S. Environmental Protection Agency, 1971a.

Fast, A.W., Effects of artificial destratification on zooplankton depth distribution, *Trans. Am. Fish. Soc.*, Vol.100, 355–358, 1971b.

Fast, A.W., Discussion on the efficiency calculation based on stability, *Proceedings*, Joint U. S./Australia seminar and workshop, Melbourne, F.L. Burns and I.J. Powling, eds., pp. 344–353, 1981.

Ferziger, J.H., Simulation of incompressible turbulent flows, *Journal of Computational Physics*, Vol.69, No.1, 1–48, 1987.

Ford, D.E. and H.G. Stefan, Thermal Predictions Using Integral Energy Model, *Journal of Hydraulics Division*, ASCE, Vol.106, HY1, 39–55, 1980.

Franke, R., M.A. Leschziner and W. Rodi, Numerical simulation of wind–driven turbulent flow in stratified water bodies, *Proc.* of 3rd Int. Symposium on Stratified Flows, Calif. Inst. of Technology, Pasadena, session A–9, 1987.

Gibson, M.M. and B.E. Launder, On the calculation of horizontal non–equlibrium turbulent flows under gravitational influence, *J. Heat Transfer*, ASME, Vol. 98, C1, pp. 81–87, 1976.

Godon, A.M. and J.H. Milgram, Mixing of Fluids in Tanks by Gas Bubble Plumes, *Jour. of Fluids Eng.*, ASME, Vol.109, 186–193, 1987.

Goossens, L.H.J. and J.A. Van Pagee, Modeling of the Near Field Due to Air Injection in Big Reservoirs, *Proceedings* of the 17th Congress, IAHR, Vol.1, 551–559, 1977.

Goossens, L.H.J., *Reservoir Destratification with Bubble Column*, Delft University Press, 1979.

Graham, D.S., Experimental Results of Destratification by Buoyant Plumes, *Proc.* of 2nd Conf. on Waste Heat Management and Utilization, Univ. of Miami, Miami Beach, pp. X–A–20–X–A–38, 1978.

Graham, D.S., Discussion on Destratification of Lakes Using Bubble Columns, *Journal of the Hydraulic Division*, ASCE, Vol.106, HY6, 1129–1132, 1980.

Gutmark, E. and I. Wygnanski, The two–dimensional turbulent jet, *J. Fluid Mechanics*, vol. 73, pp. 465–495, 1976.

Gutti, S.R., Movement of Small Gas Bubbles in a Smoothly Decelerating Liquid, Grumman Aerospace Corp., Bethpage, N.Y., Research Department, Memorandum RM–499J, 1971.

Hinze, J.O., *Turbulence*, 2nd edition, McGraw–Hill, New York, 1975.

Henderson–Sellers, B., *Engineering Limnology*, Pitman Publishers, 1984.

Holland, J.P., Review of Design Guidance on Hydraulic Destratification, *Proc.* of 3rd Annual Conf. North Amer. Lake Management Society, Knoxville, Tennessee, 549–551, oct. 1983.

Hossain, M.S. and W. Rodi, Mathematical modelling of vertical mixing in stratified channel flow, *Proc.* 2nd Int. Symp. on Stratified Flows, Trodheim, Norway, 1980.

Hughes, R.R., A.E. Handlos, H.D. Evans and R.L. Maycook, The Formation of Bubbles at Simple Orifices, *Chem. Eng. Prog.*, Vol.51, p.557, 1955.

Hussain, N.A. and B.S. Narang, Analysis of two–dimensional air bubble plumes, *AIChE Journal*, Vol.23, No.4, pp. 596–601, 1977.

Hussain, N.A. and B.S. Narang, Simplified Analysis of Air–Bubble Plumes in Moderately Stratified Environments, *Journal of Heat Transfer*, Vol.106, 543–551, 1984.

Hussain, N.A. and R. Siegel, Liquid jet pumped by rising gas bubbles, *Journal of Fluids Engng.*, ASME, 49–57, 1976.

Hutchinson, G.E., *A Treatise on Limnology*, Vol.1, John Wiley & Sons, New York, 1957.

Imberger, J. and J.C. Patterson, A dynamic reservoir simulation model, DYRESM: 5. In: *Transport Models for Inland and Coastal Waters*, ed. H. B. Fischer, pp. 310–361, Academic Press, New York, 1981.

Ito, H., Pressure losses in smooth pipe bends, *J. Basic Eng. Trans. M.E.*, Vol. 82, pp. 131–143, 1960.

Ito, T., Mixing method of stratified water layer in reservoir, *Proc.* First Int. Symp on Stratified Flows, Novosibirsk, 1972.

Jirka, G.H. and D.R.F. Harleman, Stability and mixing of a vertical plane buoyant jet in confoned depth, *J. Fluid Mechanics*, Vol. 94(2), pp.275–304, 1979.

Johnson, P.L., The Influence of Air Flow Rate on Line Diffuser Efficiency and Impoundment Impact, *Proc.* Symp. Surface Water Impoundments, Minneapolis, ASCE, 900–912, 1980.

Johnson, P.L., Thoughts on selection and design of reservoir aeration devices, *Proc.* of 3rd Annual Conf. North Amer. Lake Management Society, Knoxville, Tennessee, 537–541, Oct. 1983.

Kalio, G.A. and D.E. Stock, Turbulent particle dispersion :a comparison between Lagrangian and Eulerian modeling approaches, *Proc.* AIAA/ASME Fluid Mechanics, Plasma Dynamics and Lasers – 4th Conference, Atlanta, 23–34, 1986.

Kipke, K., Problems in mixing technology, *German Chemical Engng.*, Vol.6, 119–128, 1983.

Klug,P. and A. Vogelpohl, Bubble formation with superimposed liquid motion at single–hole plates and sieve plates, *Ger. Chem. Engng.*, 311–317, 1983.

Knoppert, P.L, J.J. Rook, T. Hofker and G. Oskam, Destratification experiments at Rotterdam, *J. Amer. Water Works Assoc.*, vol.62, 448–454, 1970.

Kobus, H.E., Analysis of the flow induced by air–bubble systems, *Proceedings* of the 11th International Conference in Coastal Engn., London, 1016–1031, 1968.

Kobus, H.E., *Bemessungsgrundlagen und Anwendungen fur Luftschleier im Wasserbau*, Erich Schmidt Verlag, 1973.

Kobus, H.E., On the Use of Air–Bubble Screens as Oil Barriers, *Proceedings* of 16th Congress in Sao Paulo, IAHR, 356–363, 1975.

Kobus, H. and B. Barczewski, Durch Luftblasen erzeugte Auftriebsstrahlen, *Waserwirtschaft*, Heft 11, 393–400, 1983.

Kranenburg, C., On the destratification of lakes and reservoirs using bubble column, Lab. of Fluid Mech., Dept. of Civil Eng., Delft Univ. of Technology, Report No. 78–1., 1978.

Kranenburg, C., Destratification of Lakes Using Bubble Columns, *Journal of Hydraulic Division*, ASCE, Vol.105, HY4, 333–349, 1979.

Larsen, I., Pneumatic Barriers Against Salt Water Intrusion, *J. of Waterways and Harbors Div.*, ASCE, Vol.86, WW3, 49–61, 1960.

Laureshen, C.J. and R.D. Rowe, Modeling of plane bubble plumes, ASME, HTD–Vol.70., Buoyant Plumes, Presented at 24th National Heat Transfer Conference and Exhibition, Pittsburgh, 15–21, 1987.

Lee, J.H.W., Jirka G.H. and D.R.F. Harleman, Stability and mixing of a vertical round bouyant jet in shallow water, M.I.T. Parsons Lab. for Water Resources & Hydrodynamics, rep. 195, 1974.

Lee, J.H.W., Stability and mixing of a round buoyant discharge in shallow water, *Proc.* Second Int. Symp. on Stratified Flows, Trodheim, Norway, pp. 881–897, 1980.

Lee, J.H.W. and G.H. Jirka, Vertical round buoyant jet in shallow water, ASCE, *J. of Hydraulic Division*, Vol. 107, No. HY12, pp. 1651–1675, 1981.

Leibson, I., E.G. Holcomb, A.G. Cacoso and J.J. Jacmie, Rate of Flow and Mechanics of Bubble Formation From Single Submerged Orifices, *AIChE Journal*, Vol.2, p.296, 1956.

Levich, V.G., *Physicochemical Hydrodynamics*, Prentice–Hall Inc., N.J., 1962.

Lockwood, F.C., A.P. Salooja and S.A. Syed, A prediction method for coal–fired furnaces, *Combustion and Flame*, Vol.38, 1–15, 1980.

Lorenzen, M.W. and A.W. Fast, A guide to aeration/circulation techniques for lake management, USEPA Report No. 6003–77–004, 1977.

Maruyama, T., N. Kamishima and T. Mizushina, An Investigation of Bubble Plume Mixing by Comparison with Liquid Jet Mixing, *Journal of Chemical Engineering of Japan*, Vol.17, No.2, 120–126, 1984.

Migdal, D. and D.V. Agosta, A source flow model for continuum gas–particle flow, *J. Appl. Mech.*, ASME, Vol.35, No.4,, p.860, 1967.

Miksis, J.M., J.M. Vanden–Broeck and J.B. Keller, Rising Bubbles, *J.Fluid Mechanics*, Vol.123, 31–41, 1982.

Milgram, J.H. and R.J. Van Houten, Plumes from sub–sea well blowouts, In *Proc.* of the 3rd Intl Conf., BOSS, Vol.I, 659–684, 1982.

Milgram, J.H., Mean Flow in Round Bubble Plumes, *J.Fluid Mechanics*, Vol.133, 345–376, 1983.

Morton, B.R., G. Taylor and J.S. Turner, Turbulent Gravitational Convection from Maintained and Instantaneous Sources, *Proc.* Royal Society, Vol.234, 1–23, 1956.

McDougall, J.T., Bubble Plumes in Stratified Environments, *J.Fluid Mechanics*, Vol 85(4), 655–672, 1978.

McGuirk, J.J. and W. Rodi, A Mathematical model for the vertical jet discharging into shallow lake, *Proc.* 17th IAHR Congress, Baden–Baden, Paper A72, 1977.

McKeogh, E.J., S.M. Fraser and D.A. Ervine, Velocity and Turbulence Measurements in Air/Water Flows Using Laser Doppler Anemometry, *Proc.* of 20th Congress in Moscow, IAHR, 264–269, 1983.

Nakatsuji, K., Y. Fujisaki and A. Murota, Application of an algebraic stress model to plane buoyant surface jet, *Proc.* of XXIII Congres of IAHR, Ottawa, Canada, A–285–A292, 1989.

Pastorok, R.A, T.C. Ginn and M.W. Lorenzen, Evaluation of aeration /circulation as a lake restoration technique, EPA 600/3–81–014, U.S. Environ. Prot. Agency, Corvallis, Oregon, 1980.

Pastorok, R.A., M.W. Lorenzen, and T.C. Ginn, Environmental aspects of artificial aeration and oxygenation of reservoirs: A review of theory, techniques and experiences, U. S. Army Corps of Engineers, Waterways Experiment Station, Vicksburg, MS, Technical Report E–83–3, 1982.

Patankar, S.V. and D.B. Spalding, A Calculation Procedure for Heat, Mass and Momentum Transfer in Three–Dimensional Parabolic Flows, *Int. J. Heat Mass Transfer*, Vol.15, p.1787, 1972.

Patankar, S.V., *Numerical Heat Transfer and Fluid Flow*, McGraw–Hill, New York, 1980.

Patterson, J.C. and J. Imberger, Simulation of bubble plume destratification systems in reservoirs, *Aquatic Sciences*, 51(1), pp. 3–18, 1989.

Peebles, R.N. and H.J. Garber, Studies on the motion of gas bubbles in liquids, *Chem. Eng. Prog.*, Vol.49, pp.88–97, 1953.

Poon, Y.C., Modelling of Round Bubble Plumes, M.Sc. thesis, University of Calgary, Alberta, 1985.

Proceedings of Joint United States/Australia Seminar and Workshop, Destratification of Lakes and Reservoirs to Improve Water Quality, Melburne, Australia, editors: Burns, F.L. and I.J. Powling, feb.1979.

Rabiger, N. and A. Vogelpohl, Bubble Formation in Stagnant and Flowing Newtonian Liquids, *Ger.Chem.Eng.*, Vol.5, 314–323, 1982.

Rabiger, N. and A. Vogelpohl, Calculation of Bubble size in the Bubble and Jet Regimes for Stagnant and Flowing Newtonian Liquids, *Ger. Chem. Engng.*, Vol.6, 173–182, 1983.

Rayyan, F. and R.E. Speece, Hydrodynamics of Bubble Plumes and Oxygen Absorption in Stratified Impoundments, *Prog.Wat. Tech.*, Vol.9, 129–142, 1977.

Reischman, M.M., J.M. Holzmann and N.H. Hughes, Digital Image Analysis of Two Phase Flow Data, Naval Ocean Systems Center, San Diego, Technical Report 502, 1980.

Riley, M. and H.G. Stefan, Dynamic Lake Water Quality Model "MINLAKE", St.Anthony Falls Hydraulic Laboratory, Project Report No.263, 1987.

Riley, M. and H.G. Stefan, MINLAKE: A dynamic lake water quality simulation model. *Ecological Modeling*, Vol. 43, pp. 155–182, 1988.

Rodi, W., Turbulence models and their application in hydraulics– a state of the art review, IAHR, Delft, 1980.

Rodi, W., Calculation of stably stratified shear–layer flows with a buoyancy–extended k–ϵ turbulence model, in *Turbulence and diffusion in stable environments*, ed. J.C.R. Hunt, Clarendon Press, Oxford, 1985.

Rowe, R.D., J.Y.C. Poon and C.J. Laureshen, A simple method for predicting bubble plume properties, *Proc.* XXIII IAHR Congress, Ottawa, Canada, pp. D–23–D–30, 1989.

Sadler, C. and M. Higgins, Radial free surface flow, S.M. Thesis, Dept. of Civil Eng., Massachusetts Institute of Technology, Cambridge, Mass., 1963.

Sami, S.M., Bubble Rise Velocity in Stagnant and Flowing Liquids, *Proc.* of Int.Conference on Physical Modeling of Multi–Phase Flow, Coventry, England, BHRA Fluid Engineering , 185–198, 1983.

Shapiro, J. and H.O. Pfannkuch, The Minneapolis Chain of Lakes–A Study of Urban Drainage and its Effects 1971–1973, Interim Report No.9, Limnology Research Center, University of Minnesota, Minneapolis, 1973.

Sharma, M.P., Numerical and experimental study of gas–particle flows in orifices and venturis: application to flow meter design, Ph.D. thesis, Washington State University, 1977.

Sharma, M.P., D.K. Cornelius, J.G. Rice and D.R. Dougan, Numerical computation of swirling gas–particle flows: application to pulverized coal classifiers, *Proc.* ASME Winter Annual Meeting, Paper No. 80–WA/HT–31, 1980.

Silbermann, E., Production of Bubbles by the Desintegration of Gas Jets in Liquid, *Proc.* of Fifth Midwestern Conf. on Fluid Mech., Minneapolis, 263–284, 1957.

Speece, R., C. Givler, R. Aubert, J. Crate, R. Caire and R.H. Siddiqi, Hypolimnion Oxygenation Studies in Clark Hill Lake, *Jour. of Hydr. Div.*, ASCE, Vol.108, HY2, 225–244, 1978.

Stefan, H.G. and D.E. Ford, Temperature dynamics in dimictic lakes, ASCE, *Jour. of Hydr. Div.*, Vol. 101, No. HY1, pp. 977–113, 1975.

Stefan, H.G. and M.J. Hanson, Predicting dredging depths to minimize nutrient recycling in shallow lakes, in USEPA/NALMS, Restoration of Lakes Inland Waters, 440–5–81–010, 1981.

Stefan, H.G., S. Dhamotharan and F.R. Schiebe, Temperature/sediment model for a shallow lake, ASCE, *Jour. Environmental Engineering*, Vol. 108, No. EE4, 1982.

Takeshi, I., Mixing method of stratified water layer in reservoirs, *Proc.* First Int. Symposium on Stratified Flows, Novosibirsk, 567–577, 1972.

Tekeli, S. and W.H.C. Maxwell, Behavior of Air Bubble Screens, Technical Report UILU–ENG–78–2019, University of Illinois at Urbana – Champaign, 1978.

Tolland, H.G., Destratification/aeration in reservoirs, Tech.Rep.No. TR50. Water Research Center, Medmenham, U.K., 1977

Topham, D.R., Hydrodynamics of an oil well blowout, Beaufort Sea Tech. Rep., Inst. Ocean Sci., Sidney, B.C., No.33, 1975.

Torrest, R.S. and J. Wen, Mixing and circulation of lakes and reservoirs with air plumes, The University of New Hampshire, Water Resources Research Center, Research Report A–030–NH, 1976.

Tsang, G., Modeling Criteria for Bubble Plumes – a Theoretical Approach, *Can.J.Civ.Eng.*, Vol.11, 293–298, 1984.

Turner, J.S., *Buoyancy effects in Fluids*, Cambridge University Press, Cambridge, England, 1973.

U.S.Army Corps of Engineers, HEC–5Q, Simulation of Flood Control and Conservation Systems, Users Manual, 1982.

Van Krevelen, D.W. and P.J. Hoftijzer, Calculation of Interfacial Area in Bubble Contractors, *Chemical Engineering Progress*, Vol.46, 29–35, 1950.

Van Wijngaarden, L., Gas/Liquid flow Research in the Netherlands, *Int. J. Multiphase Flow*, Vol.10, No.1, 107–111, 1984.

Valentin, F.H.H., *Absorption in Gas–Liquid Dispersions*, London, 1967.

Wen, J. and R.S. Torrest, Aeration Induced Circulation from Line sources. I: Channel flows, *Journal of Environmental Engineering*, ASCE, Vol.113(1), 82–98, 1987.

Wilkinson, D.L., Two Dimensional Bubble Plumes, *Journal of Hydraulics Division*, ASCE, Vol.105, HY2, 139–154, 1979.

Zic, K. and H.G. Stefan, Lake destratification by air bubble columns, St.Anthony Falls Hydraulic Laboratory, Project Report No. 265, 1987.

Zic, K. and H.G. Stefan, Lake aerator effect on temperature stratification analyzed by MINLAKE Model, *Lake and Reservoir Management*, 4(2), NALMS, 85–90, 1988.

Zic, K. and H.G. Stefan, Metereological effects on lake destratification, Submitted to *Water Resources Research*, 1989a,

Zic, K., H.G. Stefan, and C. Ellis, Laboratory study of bubble plume stratification, Submitted to *Jour. Hydraulic Research*, IAHR, 1989b

Zic, K., Destratification with air bubble column: Addendum to the user's manual for the lake water quality simulation program MINLAKE, St. Anthony Falls Hydraulic Laboratory, External Memorandum No. M–218, 1989c.

Zic, K. and H.G. Stefan, Simulation of the Liquid Circulation Induced by Air Bubble Plume, University Of Minnesota Supercomputer Institute Report 89/159, 1989d.

Yip, F.C, J.E.S. Venart and G.W. Govier, The Motion of Small Air Bubbles in Stagnant and Flowing Water, *Canad. Journal of Chem. Eng.*, Vol.48, 229–235, 1970.

APPENDICES

APPENDIX A. List of Symbols

Roman Symbols

A – horizontal area of the control volume

A_b – cross–sectional area of the equivalent spherical bubble

A_i^b – cross sectional area of the equivalent spherical bubble with a diameter d_i

b – width of the bubble plume

C – bubble concentration

C_a – bubble concentration in the plume axis

C_D – drag coefficient

c_p – specific heat

c_1, c_2 – cefficients

$c_\mu, c_{1\varepsilon}, c_{2\varepsilon}$ – empirical coefficient in k–ϵ model

D_0 – orifice diameter

d_b – diameter of equivalent spherical bubble

$\bar{d}_b$ – average diameter of the equivalent spherical bubble

E – stability parameter, constant

g – acceleration due to the gravity

G – production or destruction rate of turbulent energy by buoyancy forces

g_i – acceleration due to the gravity in i direction

Gr – Grashof number

H – submergence depth of the diffuser

k – turbulent kinetic energy; coefficient

K – turbulent diffusion coefficient

K_z – vertical diffusion coefficient

L – turbulence length scale

$\dot{m}_b$ – total mass flow rate of bubbles

$\dot{N}_{ij}^b$ – number flow rate of bubbles of class i at starting location j

N_o – number of orifices

p – instantaneous hydrostatic pressure

$\overline{p}$ – mean pressure

p' – fluctuating component of the pressure

p_s – overall pressure

P – production rate of turbulent energy from the mean flow

Pr – Prandtl number for laminar flow

q – volumetric air flow rate per meter at atmospheric pressure

q_0 – volumetric air flow rate at orifice

Q_{air} – total volumetric gas release rate at atmospheric pressure

Q_{g0} – total volumetric gas rate at orifice

Q_w – total volumetric water flow rate at the surface induced by bubble column

Q_e – volumetric water entrainment rate from epilimnion

Q_h – volumetric water entrainment rate from hypolimnion

Q_i – volumetric water flow rate in the interlayer

r – radial coordinate

Re – Reynolds number

Re_b – bubble Reynolds number

S_ϕ – source term for a variable ϕ

S_ϕ^b – source term for a variable ϕ due to the bubbles

S_{ij}^b – bubble source term in a control volume

S_{cv}^b – total momentum source term in a control volume as a result of all the bubbles passing through it

t – time

T – temperature, thickness of the outflowing stream measured from the surface

$\overline{T}$ – mean temperature

T' – fluctuating part of the temperature

t_{in} – time the bubble enters the control volume

t_{out} – time the bubble leaves the control volume

Δt – time interval

u – fluid velocity in x direction

u_e – velocity in the epilimnion

u_i – instantaneous velocity in i–direction (i=x,y,z)

$\bar{u}_i$ – mean velocity in i–direction

u_i' – fluctuating velocity in i–direction

u_0 – surface velocity of the horizontal jet

u_r – radial velocity

u_* – shear velocity

$\overline{u_r' u_z'}$ – Reynolds stress

$\overline{u_i T'}$ – turbulent heat transport

v – fluid velocity in y direction

v_b – bubble velocity

v_{g0} – gas velocity at the orifice

V – turbulent velocity scale

V_b – bubble volume

V_c – chamber volume

w – fluid velocity in z direction

$\bar{w}$ – mean fluid velocity in z direction

w_{st} – bubble rise velocity

We – Weber number

We_0 – orifice Weber number

x – coordinate

x_i – general coordinate (i=x,y,z)

y – coordinate

y_p – distance from the near wall grid point to the wall

y^+ – boundary layer coordinate

z – coordinate

Greek Symbols

α – thermal diffusivity, spreading coefficient of the jet

α_{eff} – effective thermal diffusivity $= \frac{\alpha}{Pr} + \frac{\nu_t}{\sigma_t}$

β – thermal expansion coefficient

Γ – general diffusion coefficient

δ_{ij} – Kronecker delta

ϵ – turbulent energy dissipation

ϵ_k – empirical coefficient

ρ – water density

ρ_b – density of the bubble

ρ_g – gas density

ρ_p – density of the particle

ρ_r – reference density

$\Delta\rho$ – density difference

φ – general variable

μ – molecular dynamic viscosity of the fluid

ν – molecular kinematic viscosity of the fluid

ν_g – molecular kinematic viscosity of the gas

ν_t – turbulent or eddy kinematic viscosity

ν_{eff} – effective diffusivity $= \nu + \nu_t$

σ – surface tension

σ_b – standard deviation of the bubble diameter

σ_t – turbulent Prandtl number

σ_ϵ – empirical coefficient

τ_a – dimensionless time for entrainment below diffuser in the case of axisymmetric flow

Super and Subscripts

– time average

′ deviation from a time averaged mean

o initial or reference value

APPENDIX B

Review of Bubble Dynamics

B.1 Bubble formation

The formation of gas bubbles from a single orifice submerged in a liquid has been discussed in numerous studies. Extensive references were given by Wallis [1969], Clift et al. [1978], Azbel [1981] and Ghosh [1986]. However the development of a general theory for bubble size for a two–phase system has not been succesful [Azbel, 1981].

Ghosh [1986] summarized the principal factors influencing the bubble size as follows:

1) the orifice size and shape,
2) the chamber volume below the orifice,
3) the volumetric gas flow rate through orifice,
4) the physical properties of the liquid.

Orifice size and shape is one of the most important factors. At low gas flow rates, the volume of the bubbles varies linearly with orifice diameter D_o [Datta et al., 1950; Van Krevelen and Hoftijzer, 1950; Benzing and Myers, 1955]. At high gas flow rates, some experimental data indicate that the bubble volume V_b varies as D_o^n, where n is approximately 1.5 to 2.0 [Quigley et al., 1955; Leibson et al., 1956; Davidson and Amick, 1956]. But some other data have reported insignificant influence of orifice diameter, especially, in a study of bubble formation in jets [Van Krevelen and Hoftijzer, 1950; Bryan and Garber, 1955; Davidson and Shuler, 1960]. The frequency of bubble formation at higher gas flow rate increases with a decrease in orifice diameter; the frequency varies as D_o^{-m} where, m is 1/3 to 1/2 [Bryan and Garber, 1955; Davidson and Amick, 1956].

The single bubble formation is subdivided usually into two different regimes: bubbling (with smaller gas flow rates) and jetting (with higher gas flow rates), to which different laws are applicable [Wallis, 1969]. Rabiger and Vogelpohl [1983] developed a model for a single orifice which is valid for the entire gas throughput range. Their approach is based on the experimental finding that in a jet regime single or double bubble formation always occurs. A gas jet does not occur. In the detachment step the bubbles move at constant velocity, which roughly corresponds to their rise velocity. The disintegration of the primary bubble in the jetting regime is caused by the induction of fluid flow into the bubble by the severance of the filament connecting the bubble to the capillary. Above a critical gas

throughput, this fluid breaks up the bubble and thus initiates the disintegration of the bubble into secondary bubbles. Equation for prediction of the diameter of the primary bubbles is given as

$$\frac{g\Delta\rho d_b^3\pi}{12}[2 - 3(\frac{D_o}{d_b})^2] = D_o\sigma\pi +$$

$$+ c_D\rho K \frac{d_b^2\pi}{8}[2(\frac{4Q_{go}}{D_o^2\pi} - w_k)(\frac{D_o}{2d_b})^2 + v_{bo}]^2 \quad (B.1)$$

where

$$c_D = \frac{24}{Re} + \frac{4}{Re^{0.5}} + 0.4 \quad (B.2)$$

$$Re = \frac{vd_b\rho}{\mu} \quad (B.3)$$

$$v = 2\frac{Q_{go}}{D_o^2\pi}[1 + (\frac{D_o}{2d_b})^2] \quad (B.4)$$

$$v_{bo} = (\frac{4gd_b}{3c_D})^{0.5} \quad (B.5)$$

For secondary bubbles as

$$\frac{1}{4}v_{rz,crit}^2 = B + \frac{4\sigma}{D_o\rho} + \frac{4}{D_o\rho}[12\mu(K_2 - K_3v_{rz,crit}) +$$
$$+ 0.1\rho D_o v_{rz,crit}]A \quad (B.6)$$

where

$$v_{rz,crit} = \frac{2}{D_o}[\frac{2d_b}{\rho}(\sigma - 3\mu w_{st})]^{0.5} \quad (B.7)$$

$$A = \{2d_bg + 2K_4[K_1/(1 + w_k/w_{st})]^{0.5} - 4v_{rz,crit}^2) + 1\}^{0.5} \quad (B.8)$$

$$B = (gH - \frac{K_1Q_{go}}{1 + w_k/w_{st}})(1 + \frac{2d_b}{D_o}) \quad (B.9)$$

$$K_1=20\ 000 \qquad K_2=265 \qquad K_3=650 \qquad K_4=0.8 \quad (B.10)$$

and g = acceleration due to gravity; $\Delta\rho$ = density difference between fluid and gas; d_b = equivalent bubble diameter; D_o = orifice diameter; σ = surface tension; ρ = fluid density; Q_{go} = volumetric gas rate at orifice; w_k = mean velocity of flowing fluid; μ = dynamic viscosity of the fluid; w_{st} = bubble rise velocity; H = submergence depth of the orifice.

Both equations (B.1) and (B.6) have to be solved iteratively.

Klug and Vogelpohl [1983] showed that as in the case of the orifice, two different regimes can be distinguished in the process of the bubble formation at perforated plates: the bubbling regime at low gas volumetric rates, and the jetting regime at high flow rates. Individual bubbles are

formed in the bubbling regime, while a continuous jet is supposed to form in the jetting regime, its head disintegrating into single bubbles. The transition between bubbling and jet regime is found to be about the value of 2 of the orifice Weber number given in the form:

$$We_0 = \frac{v_{g0}^2 \rho D_0}{\sigma} \tag{B.11}$$

where v_{g0} = gas velocity at the orifice.

Figure B.1 shows significant influence of the hole spacing (given as the distance between holes t) on the bubble diameter. The case with $t \to \infty$ corresponds to the single orifice. Two conclusions can be obtained from Figure B.1. Sudden drops in bubble diameter occur on sieve plates with hole spacings of 15 mm and 6 mm (or expressed in the hole diameters, 15 D_0 and 6 D_0). In addition bubble diameters approach a constant value at larger Weber numbers but the bubbles are considerably smaller from the plate with close spacing then for the plate with large spacing. This effect may be attributed to the dispersive action of the generated shear field. Since the ascending bubbles are much nearer to one another at close hole spacing, larger shear stresses result and hence also smaller limiting values of the stable bubble diameter [Klug and Vogelpohl, 1983]. As can be seen, for smaller spacing, or for higher Weber numbers (higher flow rates) bubble size is independent of gas throughputs. These measurements and explanations agree with measurements and conclusions of Silberman [1957] and Kobus [1968] that the bubble size does not depend on the orifice size for flow rates of practical interest.

In aeration devices typical orifice (single hole) diameters are from 0.1 mm to 1.0 mm (and usually with fine spacing) and Q_{g0} = 0.01 – 0.1 l/s [Goossens, 1979]. This gives orifice Weber numbers in the range of 3 to 260. In the other words, orifice size can be practically dropped as a parameter in the analysis of pactical applications of air bubble systems.

Chamber volume is generally defined as the volume of the gas supply system between the orifice and the control valve, where the pressure drop is very large. Hughes et al. [1955] found the bubble volume to be independent of the chamber volume for the cases of small chamber volume and low gas flow rate or large chamber volume and high gas flow rate. Tadaki and Maeda [1963] provide the following criterion for the required chamber volume V_c below the orifice:

$$\frac{4V_c \rho_g}{\pi D_0^2 p_s N_0} > 8 \tag{B.12}$$

where ρ_g = gas density ; p_s = overall pressure ; N_0 = number of dispersed orifices. Depending on the volume two types of gas flow can be defined: constant flow (very small chamber volume) and constant pressure (chamber of large volume).

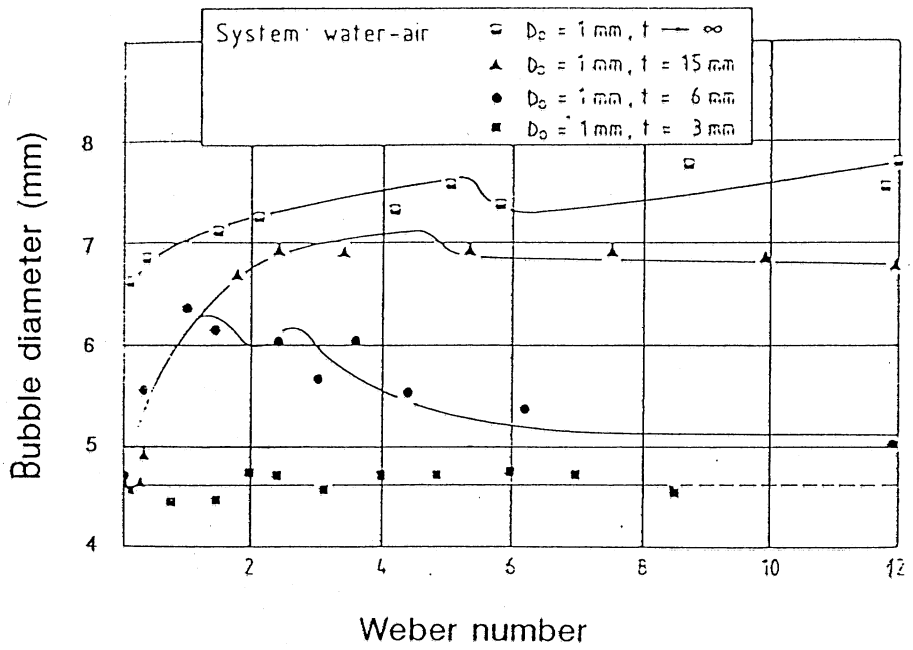

Figure B.1 Secondary bubble diameter at different sieve plates (after Klug and Vogelpohl, 1983)

Gas flow rate is an important parameter which controls the bubble size and frequency of bubble formation in the system. Although the effect of the gas flow rate was already mentioned in the context of the orifice size and shape some additional observations can be presented here for the gas flow rate itself. At small flow rate, bubble volume remains independent of the gas flow rate; the final bubble volume is controlled by the buoyancy and surface tension forces [Azbel, 1981]. At high gas flow rates and for low liquid viscosity, bubble volume has been found to vary as $Q_{go}^{1.2}$ [Davidson and Harrison, 1963]. For viscous fluids, initially both bubble volume and frequency increase with an increase in gas flow rate, but after a particular gas flow rate is exceeded frequency becomes constant and the bubble volume only increases linearly [Klug and Vogelpohl, 1983; Rabiger and Vogelpohl, 1983]. With a further increase in the gas flow rate, the system reaches a turbulent regime caused by the dynamic interaction of the continuous liquid phase with the turbulent gas jet. In this regime, the frequency and size of bubbles formed become independent of the orifice size and fluid properties [Leibson et al., 1956; Azbel, 1981].

Physical properties of the fluid show contradictory effects in different studies. Fluid viscosity μ which imposes a viscous drag force at the gas bubble–fluid interface is a principal factor to determine the bubble size. Davidson and Shuler [1960] found bubbles to be larger in high viscosity fluids. On the other hand Datta et al. [1950] found a slight decrease in bubble volume with an increase in viscosity of the fluid. After Ghosh [1986] this difference can be explained by the fact that the apparent effect of viscosity is often influenced by the effect of other variables in a particular system. Density of the gas has a very negligible influence on the bubble formation process [Ghosh, 1986]. At high gas flow rates, gas density acts through the gas momentum imposed on the interphase. The liquid density ρ affects both upward buoyant force and downward inertial force. The net effect of these two opposing forces is a weak dependency of bubble volume on liquid density [Ghosh, 1986]. At low gas flow rate, surface tension of the fluid is very important in determining the bubble size. Bubble volume has been found to increase linearly with an increase in surface tension [Datta et al., 1950]. As the gas flow rate increases, the effect of surface tension on the bubble formation process is found to be less and less significant [Ghosh, 1986].

The previous discussion can be summarized by the classification given by Valentin [1967] who defined several bubble formation regimes according to the orifice Reynolds number given as:

$$Re_o = \frac{D_o v_{go}}{\nu_g} \tag{B.13}$$

where v_{go} = gas velocity at orifice, ν_g = kinematic viscosity of the gas. The classification is given in the Table B.1.

Increasing the gas flow rate increases the orifice Reynolds number and produces a change from a free to a forced convection. Above an orifice Reynolds number of about 5000, the orifice diameter ceases to have much effect and bubble size is determined mainly by gas flow rate and fluid

properties [Valentin, 1967]. For typical values of the gas flow rate and orifice diameter in (mentioned before) the range of the orifice Reynolds number is $3x10^4$ to $7x10^7$. Therefore according to Table B.1 applications are in the range in which the bubble size is independent of orifice diameter (agrees with previous conclusions based on the orifice Weber number).

Table B.1 Bubble Regimes [After Valentin, 1967]

Regime	Orifice Reynolds No.	Characteristics
Constant volume	0 – 200	Bubble diameter constant; frequency of bubble formation increases with Re
Slowly increasing volume	200 – 1000	Frequency of bubble formation becomes relatively constant; bubble volume increases with gas flow rate
Constant frequency (laminar)	1000 – 2100	Constant frequency of bubble formation dependent on orifice diameter; bubble volume increasing with increasing gas rate; bubbles begin to break up
Turbulent range	2100 – 10000	Considerable spread of bubble size due to break–up of large bubbles; bubble size is independent of orifice diameter
Jet gassing	> 10000	Fully developed turbulence

B.2. Bubble shape and size

The shape of rising bubbles is determined by the pressure distribution along their interface layed, the shape is therefore determined by the mutual interaction of surface tension, viscosity, lift and inertial forces. Clift et al. [1978] provided a diagram which correlates the shape of bubbles and drops with dimensionless numbers combining those properties:

Reynolds number: $$Re = \frac{\text{inertial force}}{\text{viscous force}} = \frac{\rho \Delta v_b d_b}{\mu} \qquad (B.14)$$

Weber number: $$We = \frac{\text{inertial force}}{\text{surface tension force}} = \frac{\rho(\Delta v_b)^2 d_b}{4\sigma} \qquad (B.15)$$

Eotvos number: $$Eo = \frac{\text{lift force}}{\text{surface tension force}} = \frac{g\Delta\rho d_b^2}{\sigma} \qquad (B.16)$$

Morton number: $$Mo = Eo\,\frac{16\ We^2}{Re^4} = \frac{g\mu^4\Delta\rho}{\rho^2\sigma^3} \qquad (B.17)$$

The diagram is reproduced in Figure B.2. For typical values of fluid and air bubble properties it can be obtained Re ≈ 700, Eo ≈ 0.5 and Mo ≈ $2x10^{11}$. From Figure B.2 then follows that the air bubbles are mainly in the wobbling regime. As the bubbles are rising in the direction of the free surface the hydrostatic head steadily reduces, so that the volume of the bubble increases during its upwards flow. This expansion results in the generation of additional eddies in the surrounding fluid. The paths of the bubbles become erratic because of more frequent collisions. The formation of eddies by the expansion of the bubbles and their collisions enhance the turbulence [Cheremisinoff, 1986].

From the discussion in section B.1 it follows that with an increase of the air flow rate (controlled by orifice Weber or Reynolds numbers) the mean bubble diameter depends neither on the air flow rate nor on the orifice size. According to measurements by Tekeli and Maxwell [1978], Azbel [1981], Idogawa [1987] in intensive mass–bubbling operations, bubbles of a fairly uniform size are formed in a gas–fluid mixtures, this being result of a breaking up and coalescing of bubbles, which in turn is due to the dynamic interaction between the fluid and gas. In mass bubbling the equivalent bubble diameter is practically independent of the flow system, so, for example, increasing the orifice 100 times increases the bubble diameter only twice for an air–water system [Azbel, 1981]. The commonly used approach to treat the size of bubbles for such a case is with the appropriate distribution function. The distributions were found to be normal, but more often log–normal. For some cases with very low gas flow rates and low velocity in the fluid Reichmann and Holzmann [1980] found even bimodal distributions which usually occur only for the jetting regime [Klug and Vogelpohl, 1983]. Bubble size distributions have been fitted with log–normal distribution rather successfully by Leibson [1956], Silberman [1957], Leutheusser et al. [1973], and several other authors cited by Azbel [1981].

The bubble diameter density distribution obeys then the logarithmic–normal law described by the equation

$$f(y) = \frac{1}{y \ln\sigma_b (2\pi)^{0.5}} \exp\left[- \frac{(\ln y - \ln \overline{d}_b)^2}{2(\ln\sigma_b)^2} \right] \qquad (B.18)$$

where $\overline{d}_b$ = average bubble diameter and σ_b = standard deviation of the bubble diameters. The standard deviation σ_b is found to be, according to citations in Azbel [1981], independent of the equipment diameter and independent of the properties of the system over a wide range of gas flow rates, and related to the average bubble diameter as given in Figure B.3.

Starting from the equation of relative motion of a gas–bubble in a gas–fluid mixture (see Appendix C) Azbel [1981] states that the most likely state of the bubble will be determined by a minimum of energy dissipation, which leads to the equation for the average bubble diameter

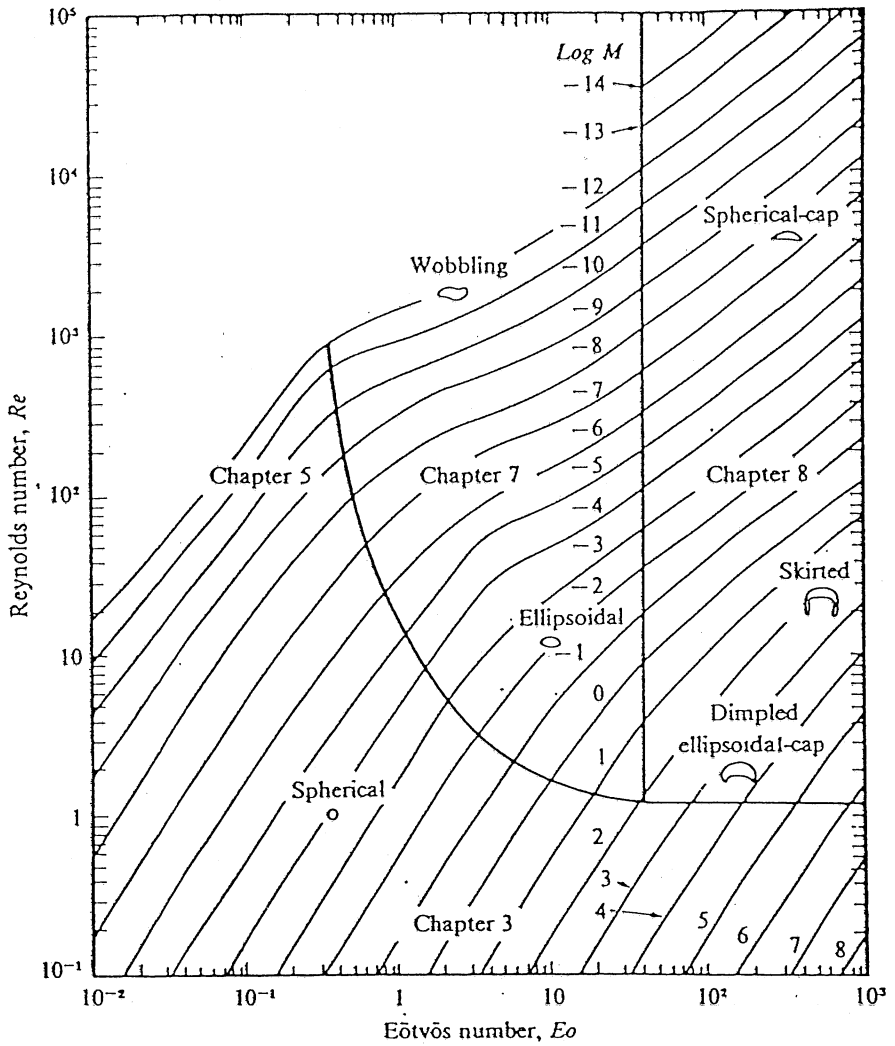

Figure B.2 Shape regimes for bubbles and drops (after Clift et al. 1978)

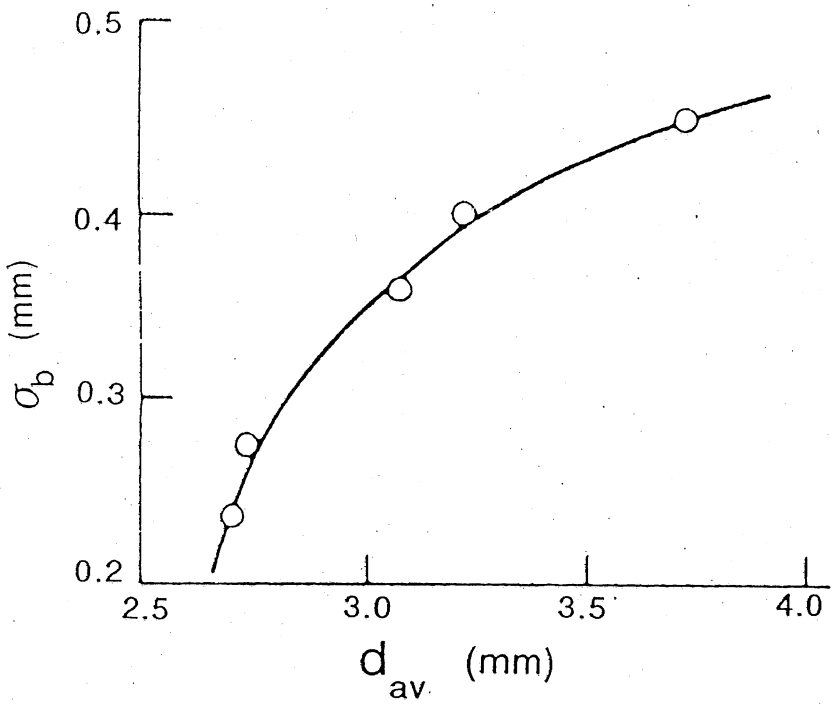

Figure B.3 The standard deviation of the bubble diameter versus the mean bubble diameter (after Azbel, 1981)

$$\overline{d}_b = \frac{C_D \Delta v_b^2}{2\ g} \tag{B.19}$$

where C_D = drag coefficient ; Δv_b = relative bubble velocity ("slip velocity").

As typical values are $C_D = 0.4$ and $v_b = 0.3$ (m/s) the mean equivalent bubble diameter in the turbulent flow is about 2 mm. This value agrees well with measurements by Tekeli and Maxwell [1978], Goossens [1979].

It has been found that a maximum stable equivalent bubble diameter is about 8 mm [Kocamustafaogullari et al., 1985]. The most important breakup mechanisms are classified as high shear stress and turbulent fluctuations in the surrounding continuous fluid [Kocamustafaogullari et al., 1985].

Bubble concentration in the air bubble plume

Mathematical or numerical models of air bubble plumes need information on the concentration (void ratio) of air in the plume. Using an optical technique Barczewski [1983] performed extensive experimental work on plane symmetric plumes, and developed a semi – empirical model which allows the calculation of the bubble concentration in the plume axis C_a, if the air intake is known as :

$$C_a = 0.66\left[\frac{q^2}{g(z+z_0)^3}\right]^{0.25} \tag{B.20}$$

where z = elevation from the air source (m), $z_0 = 0.2$ (m), q = volumetric air flow rate per meter. Experimental data for C_a from Barczewski [1983] and Goossens [1979] are shown in Figure B.4. With a Gaussian distribution air concentration is given [Barczewski, 1983]

$$C = C_a \exp(-x/\lambda b)^2 \tag{B.21}$$

where λb = width of the concentration distribution, b = width of the plume itself, x = horizontal distance from the vertical axis. Kobus and Barczewski [1983] found that the dispersion coefficient λ is

$$\lambda = 0.87 \exp\left\{-0.154\left[\frac{\Delta v_b}{(g\, q_0)^{1/3}}\right]^{1.5}\right\} \tag{B.22}$$

where $\Delta v_b = 0.35$ (m/s), q_0 = volumetric air flow rate per meter at the source.

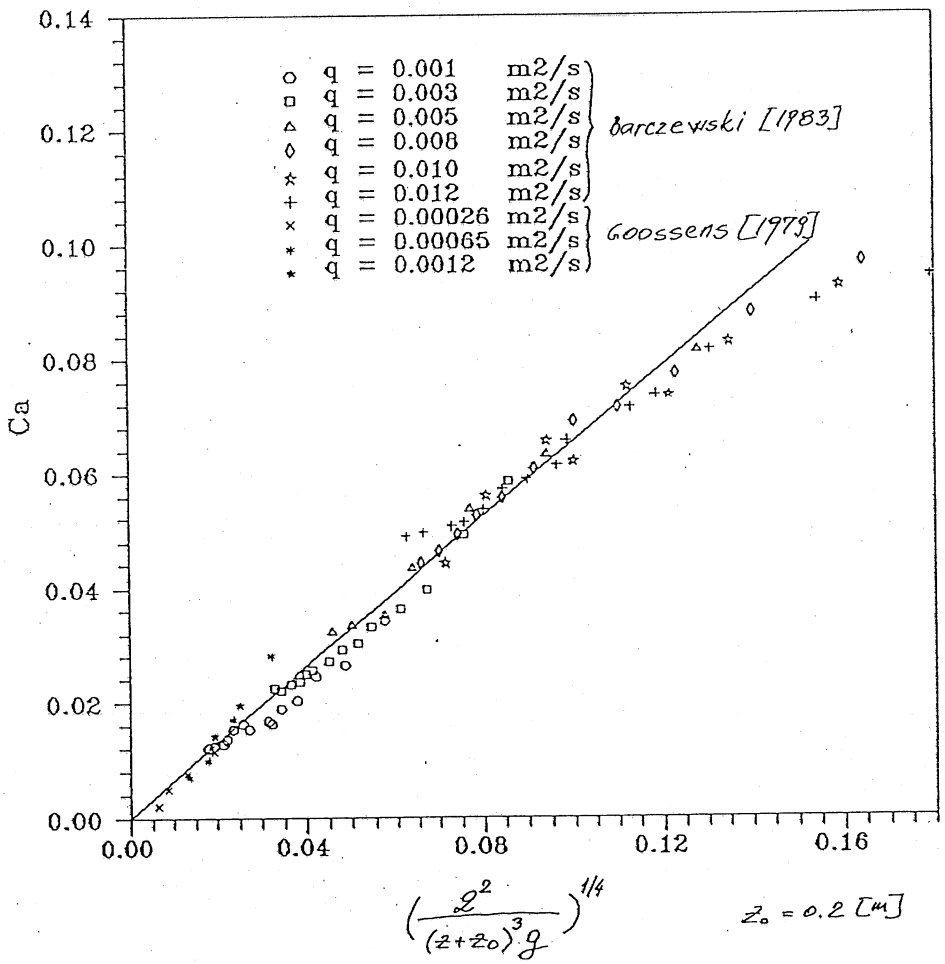

Figure B.4 Bubble concentration in the air bubble plume

B.3. Bubble plume properties

The general properties of the bubble plume will be described by applying the concept of an integral theory. Within an integral formulation (see Chapter 5) the values for four parameters are required. These are the bubble "slip velocity" (also called terminal velocity) Δv_b, the gas/water velocity radius ratio λ, the entrainment coefficient α and the ratio of the total momentum flux to the momentum flux carried by the mean flow γ. Analysis of their values over a wide range of source conditions can show the main features of the air bubble plume.

Figure B.5a shows the bubble "slip velocity" Δv_b as a function of the equivalent spherical bubble diameter. As the mean observed diameter of the bubbles in the air bubble plume is about 2 mm, a commonly chosen value for Δv_b is 0.3 m/s [Kobus, 1968; McDougall, 1978; Goossens, 1979; Milgram, 1983].

It has been found [Rowe et al., 1989] that the entrainment coefficient α, momentum amplification factor γ and dispersion ratio λ depend only on a dimensionless number called the bubble Reynolds number:

$$Re_b = \frac{\rho \overline{q}}{\mu H} \tag{B.23}$$

where $\overline{q}$ is the height averaged volumetric gas flow rate and H is the submergence depth of the diffuser. Figure B.5b shows such a relationships. At very low rates of air release (i.e. $Re_b \to 0$), the structure of the plumes may be approximated by single bubbles rising one after the other. In this limit, the entrainment coefficient and the dispersion ratio become zero while the momentum amplification factor becomes large without limit. At very high rates of air flow (i.e. $Re_b \to \infty$), the structure of bubble plumes is analogous to the that of single–phase plume due to the fact that the air bubbles are widely distributed within the plume in a manner analogous to that in which buoyancy occurs in a single–phase plume. In this limit, the dispersion ratio and the momentum amplification factor have essentially the same values as those upon which most single–phase plume investigations have been based [Kotsovinos and List, 1977; George et al., 1977]. The entrainment coefficient, however, is larger then that for a single–phase plume of 0.082 [Chen and Rodi, 1980]. Similar higher values for the entrainment coefficient α were obtained by Tekeli and Maxwell [1978] and Milgram [1983]. Between these two extremeties, the dispersion ratio and the entrainment coefficient were found to increase with increasing value of Re_b but the inverse was found for the momentum amplification factor. As more bubbles are formed and widely dispersed within the plume at high gas flow rates, the momentum associated with the buoyancy force of the rising gas bubbles imparted to the surrounding liquid is increased thus enhancing the turbulence intensities to the liquid, which in turn enhances the entrainment at the plume interface through the action of turbulent eddies. At the same time, the mean flow in the plume is much increased because of this large quantity of momentum transfer from the gas bubbles, so the turbulent velocities remain relatively small in comparison to their mean counterparts, which results in a small ratio

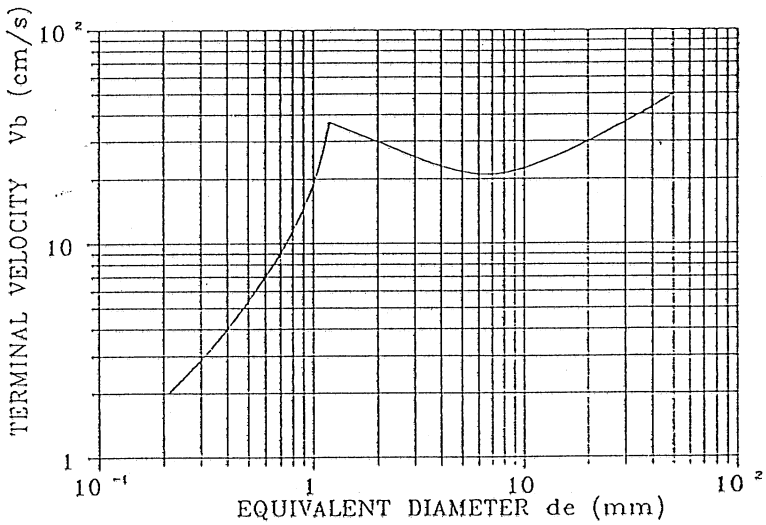

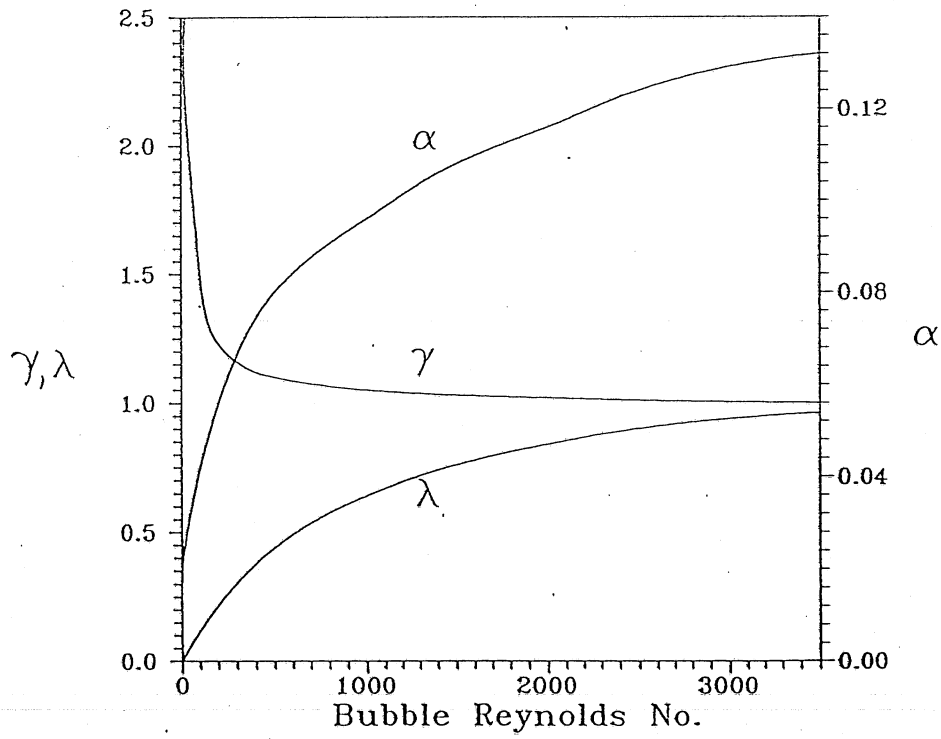

Figure B.5 Bubble terminal velocity versus bubble equivalent diameter (top) and integral bubble plume model parameters versus bubble Reynolds number (bottom)

of the averages of the squared turbulent vertical velocity to the mean vertical velocity. This reasoning [Rowe et al., 1989] is supported by the experiments by various authors. Serizawa [1975] found that the phenomenon of turbulence in an air bubbles plume for the higher gas flow rates may be described as the competition among the following effects and others:

1) Decrease in the effective volume of the liquid phase for energy dissipation due to the volume occupied by the suspended bubbles – this effect is to increase the turbulent intensity.

2) Energy dissipation associated with the lateral relative motions or rotations of bubbles – the turbulent intensity may be decreased in order to supply this energy dissipation.

3) An energy–absorbing character of bubbles– bubbles may act as a kind of energy absorber.

Serizawa also found that over the large portion of any cross section most of the various local parameters were uniformly distributed in the radial direction. Uniform distributions of the local parameters follow from the intensified turbulent transport of the transferable quantities.

Chuang and Goldschmidt [1970] measured attenuation of turbulence intensity (defined as the ratio between a fluctuating and mean velocity component) from 0.24–0.36 to 0.24–0.32 due to the presence of bubbles in an axisymmetric turbulent jet. The increased level of turbulence which they observed in the axial direction in the absence of the bubbles conforms with the findings of Kotsovinos [1977], who found the intensity of turbulence fluctuations of temperature dropping as the turbulent jet became a plume.

Tekeli and Maxwell [1978] had measured the intensity of turbulent fluctuations of fluid velocity for plane symmetric and axisymmetric bubble plumes. No variation among the different cross sections or the different tests was found. The maximum $u'/u_m \approx 0.37$ is higher then the 0.22 to 0.28 reported for turbulent jets [Kotsovinos, 1977] but it is lower then the 0.5 reported by Kotsovinos [1977] for a thermal plume.

Examples of integral models from literature

Kobus [1973] found that the water velocity in the bubble plume axis u_a and the bubble plume width b, at some vertical distance z from the diffuser in isothermal receiving water, can be calculated as

$$u_a(z) = \frac{\sqrt[3]{g Q_{air} H_o}}{S_Q^{1/3}} \, 3.6 \, \left(\frac{H_o}{H_o + H}\right)^{2/3} \left[\frac{1}{(1 - z^*)(z^* + 0.05)}\right]^{1/3} \qquad \text{(B.24)}$$

$$\frac{b^*}{z^* + 0.05} = 0.1 \, S_Q^{3/8} \qquad \text{(B.25)}$$

where

$$z^* = \frac{z}{H_o + H} \; ; \; b^* = \frac{b}{H_o + H} \tag{B.26}$$

$$S_Q = \text{Tanh}\left(\frac{\sqrt[3]{g Q_{air} H_o}}{\Delta u_b}\right) \; ; \; \Delta u_b = 0.25 \text{ (m/s)} \tag{B.27}$$

where Q_{air} = air release rate under atmospheric conditions, H = submergence depth of diffuser and H_o = 10.0 m.

The integral model presented in Chapter 5 transforms, for isothermal receiving water, into a model developed by **Poon [1985]**, which in turns represents a slight modification of the model presented by **Milgram [1983]**.

Figure B.6 shows a comparison between the predictions of the centerline velocity by the models by Kobus [1973] and Poon [1985] versus the measurements performed by Kobus [1968], Topham [1975], Fannelop and Sjoen [1980], Milgram and Van Houten [1982], Milgram [1983] as presented by Milgram [1983]. The solid line is a line fitted through measured data. Having in mind that the range of the air flow rates used in the measurements by the listed authors vary in the range from 0.0004 m^3/s to 0.66 m^3/s and that the diffuser depths vary in the range from 4.7 m to 60 m the predictions can be considered satisfactory.

Mass transfer

Mass transfer is actually the transfer of oxygen into the water across the gas/liquid interface. The interface is either between the water body and the atmosphere or between the water and bubbles travelling upward through the water body.

In the application of the air bubble plume as a destratification device the mass transfer is usually neglected [Nielsen, 1974; Goossens, 1979; Patterson and Imberger, 1989]. To justify this, an analysis is done here by the use of the concept of the capture coefficient f_{CD}. The capture coefficient represents the mass fraction of oxygen captured by the water during the bubbles ascent, or:

$$f_{CD} = \frac{\textit{mass transfer over the height}}{Q_{air} \; 0.21 \; \rho_{air}} \tag{B.28}$$

where Q_{air} = uncompressed volume flow rate of air, ρ_{air} = mass density of air. After Hogan [1970]

$$f_{CD} = \frac{32.24}{d_b} \left[\frac{D_L \; H}{\Delta u_b} \right]^{1/2} \frac{C_{sat} - C}{\rho_{air}} \tag{B.29}$$

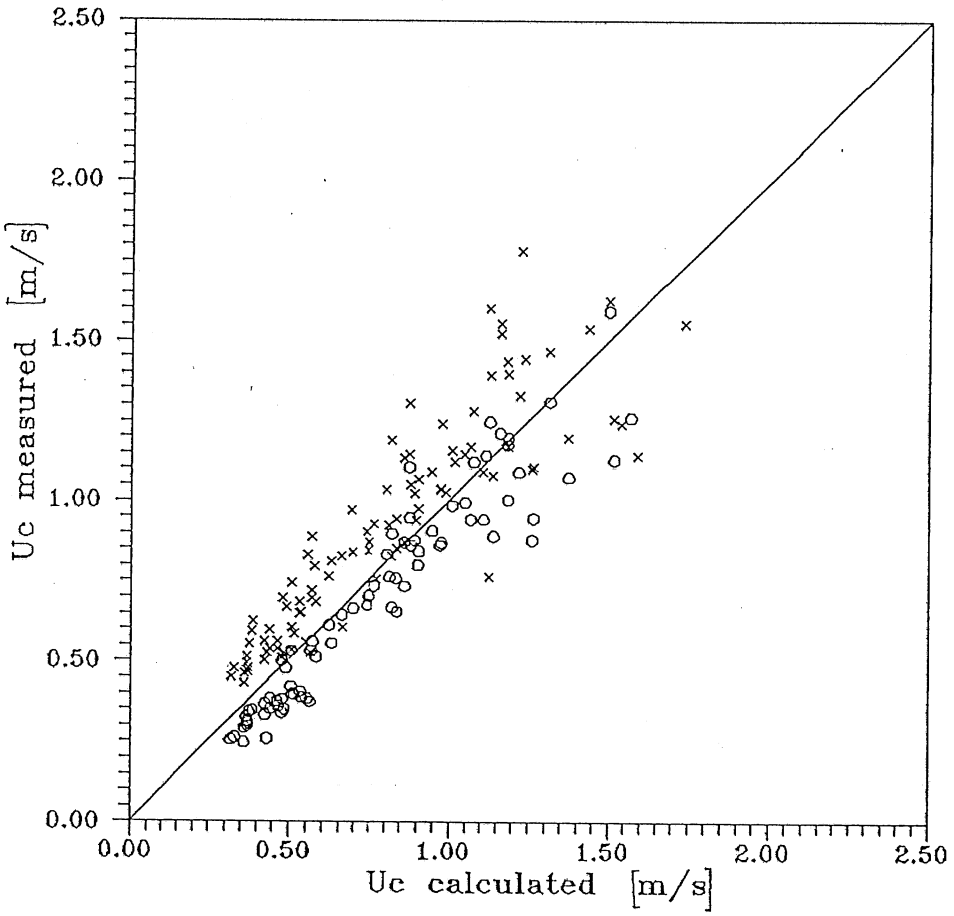

Figure B.6 Performance of integral models by Kobus [1973] and by Poon [1985], represented by crosses and circles, respectively, versus measurements.

where H = diffuser's depth in ft, C_{sat} = dissolved oxygen saturation concentration in mg/l, C = dissolved oxygen concentration in mg/l, D_L = diffusion coefficient = 2.41×10^{-5} cm^2/s for T = 25 °C, Δu_b = bubble terminal velocity = 30 cm/s, d_b = bubble diameter in cm, ρ_{air} = air density = 1025 mg/l. The saturated dissolved oxygen concentration can be calculated as

$$C_{sat} = 14.65 - 0.4102\ T + 7.99 \times 10^{-3}\ T^2 - 7.777 \times 10^{-5}\ T^3 \qquad (B.30)$$

where T = water temperature in °C.

The oxygen transfer on the surface can be calculated as

$$\Delta C = K\ (C_{sat} - C) \qquad (B.31)$$

where ΔC = change in dissolved oxygen in mg l^{-1} day $^{-1}$, K = surface exchange (reaeration) coefficient = 0.641 [day^{-1}] for calm weather conditions and for surface layer thickness of 1 m. Equation (B.31) is used in program MINLAKE [Riley and Stefan, 1987] which is used as a model for the farfield in Chapter 2.

The equations shown above can be applied to the case of the destratification of Lake Calhoun [Shapiro and Pfankuch, 1973]. Calculated values of the mass transfer from the air bubble plume to the water are presented in Table B.2 (z starts from the bottom).

Table B.2 Estimation of the oxygen transfer rate from the bubble plume (Example: Lake Calhoun, 1971)

z [m]	C [mg/l]	T [°C]	C_s [mg/l]	fcd [%]	mass transfer [kg/day]
9.0	8.30	22	8.67	0.001	6.1
16.5	8.60	22	8.67	0.0001	0.6
14.0	7.80	22	8.67	0.002	9.8
11.5	0.21	15	10.03	0.03	184.3
4.0	0.00	10	11.27	0.027	165.9
0.1	0.00	10	11.27	0.004	24.6
					Σ = 380 [kg/day]

Using Eq. (B.31) an oxygen transfer rate of 9500 [kg/day] at the surface (surface area = 1.7×10^6 m^2) is estimated, under condition that hypolimnetic water with C = 0.0 mg/l comes to the surface. Therefore, the mass transfer at the surface is estimated to be about 25 times bigger then

the one from the air bubble plume. Accordingly, the mass transfer from the bubbles can be, for all practical purposes, neglected in this application of the air bubble plume.

Additional information can be obtained from the results in Table B.2. Oxygen transfer from the bubble plume is about 6% of the oxygen mass released from the diffuser. As oxygen is 21% of the air mass, absolute transfer rates from the air are even smaller. This practically means that the mass transfer, even in absolute terms, can be neglected in the analysis of the air bubble plume.

APPENDIX C

Equation of motion of a bubble in a flow field

The differential equation for nonsteady rectilinear motion of a particle in a fluid has been obtained and modified by several authors [Clift et al., 1978]. Neglecting external forces, the final form of the equation for the motion of a spherical particle in a turbulent flow, with nonzero mean velocity is usually obtained as [Azbel, 1981]

$$\frac{\pi d_p^3 \rho_p}{6}\frac{dv_p}{dt} = \underbrace{\frac{\pi d_p^3 \rho}{6}\frac{dv}{dt}}_{I} + \frac{1}{2}\underbrace{\frac{\pi d_p^3 \rho}{6}\left(\frac{dv}{dt} - \frac{dv_p}{dt}\right)}_{II} + \underbrace{3\pi\nu\rho d_p(v - v_p)}_{III} + \frac{3}{2} d_p^2 \rho \pi^{0.5} \underbrace{\nu \int_{t_0}^{t} \left(\frac{dv}{dt} - \frac{dv_p}{dx}\right) \frac{dx}{(t-x)^{0.5}}}_{IV} \qquad (C.1)$$

where d_p = diameter of the particle, ρ = density of the fluid, ρ_p = density of the particle, v_p= absolute velocity of the particle, v = absolute velocity of the fluid, ν = fluid kinematic viscosity, and t = time. The meaning of the terms I, II, III and IV in Eq. (C.1) are :

I – surface force acting on the particle, resulting from the pressure variation on the surface; a direct consequence of the fluid acceleration,

II – surplus of inertia caused by the pressures resulting from the relative acceleration $\frac{dv_p}{dt} - \frac{dv}{dt}$; equivalent to the inertia of a virtual mass attached to a particle,

III – the viscous force due to the relative motion of the particle in liquid; known as linear–resistance term or Stokes term,

IV – the resistance that is due to the energy expended in setting the liquid itself in motion, called the history term or Basset term.

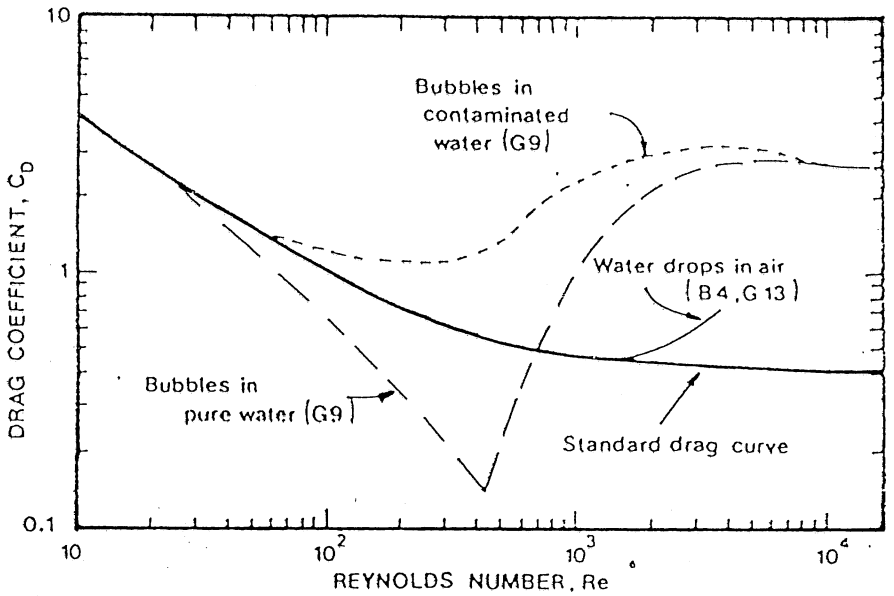

Figure C.1 Drag coefficient as a function of Reynolds number for water drops in air and air bubbles in water, compared with standard drag curve for rigid spheres (after Clift et al., 1978)

Eq.(C.1) is valid when the following relations hold [Azbel, 1981]

$$\frac{d_p^2}{\nu}\frac{\partial v}{\partial x} << (C.2)$$

$$\frac{v}{d_p^2(\partial^2 v/\partial x^2)} >> 1 \qquad (C.3)$$

where x is a linear dimension. Conditions (C.2) and (C.3) are satisfied [Azbel, 1981].

Eq. (1) is used here to analyze the motion of the air bubble with an equivalent diameter d_b and therefore instead of subscript p the subscript b will be used furthermore.

Following the procedure of Hinze [1975] Eq.(C.1) can be rewritten in the form:

$$\frac{dv}{dt} + av_b + c\int_{t_0}^{t}\frac{dv_b/dx}{(t-x)^{0.5}}dx = av + b\frac{dv}{dt} + c\int_{t_0}^{t}\frac{dv/dx}{(t-x)^{0.5}}dx \qquad (C.4)$$

where

$$a = \frac{18\nu}{[(\rho_b/\rho) + 0.5]d_b^2}$$
$$b = \frac{3}{2[(\rho_b/\rho) + 0.5]} \qquad (C.5)$$
$$c = \frac{9\nu^{0.5}}{[(\rho_b/\rho) + 0.5]\pi^{0.5}}$$

For air bubbles/water flow typical values are $\nu = 4\ x10^{-6}$ [m^2/s], $\rho_b/\rho = 1/1000$ and $d_b = 2$ [mm]. Typical values for a, b and c in Eq. (C.5) therefore are $a \approx 36$, $b \approx 11$, $c \approx 0.02$. Hence $c \ll a, b$ so that the history term in Eq. (C.1) can be neglected.

The third term in Eq. (C.1) which represents the drag force at steady state is usually expressed as

$$F_D = \frac{1}{2} C_D \rho A_b |v - v_b|(v - v_b) \qquad (C.6)$$

where A_b = projected area ; C_D= the drag coefficient and varies as a function of a bubble Reynolds number,

$$Re_b = \frac{\rho d_b |v - v_b|}{\mu} \qquad (C.7)$$

and Grashof number

$$G = \frac{g\,\mu^4}{\rho\,\sigma^3} (C.8)$$

Using the correlations of Peebles and Garber [1953]

$$C_D = 24\ Re_b^{-1} \qquad \text{for } Re_b < 2 \tag{C.9}$$

$$C_D = 18.7\ Re_b^{-0.68} \qquad \text{for } 2 \leq Re_b \leq 4.02\ G^{-0.214} \tag{C.10}$$

$$C_D = 0.6145\ \frac{d_b}{2}|v - v_b| - 2 \qquad \text{for } Re_b \geq 4.02\ G^{-0.214} \tag{C.11}$$

The three regimes represented by Eqns (C.9)–(C.11) are "Stokes", "oscillating bubble", and "Taylor–Davies", respectively.

Eq. (C.11) is a linearized combination of two higher Reynolds number regimes proposed by Cook and Harlow [1984] which is useful for numerical stability and represents the data quite well.

The additional force is the buoyancy force and is equal to

$$F_B = \frac{1}{6}\ \pi d_b^3 g(\rho_b - \rho) \tag{C.12}$$

As the density of the air bubble is of order 10^{-3} of the density of the water Eq. (C.12) can be rewritten as

$$F_B = -\frac{1}{6}\ \pi d_b^3 g\rho \tag{C.13}$$

With Eqns (C.2) to (C.13), Eq. (C.1) can be rewritten as

$$\frac{\pi d_b^3 \rho_b}{6}\frac{dv_b}{dt} = \frac{\pi d_b^3 \rho}{6}\frac{dv}{dt} + \frac{1}{2}\frac{\pi d_b^3 \rho}{6}\left(\frac{dv}{dt} - \frac{dv_b}{dt}\right) + \frac{1}{2}\ C_D \rho A_b |v - v_b|(v - v_b) - \frac{1}{6}\ \pi d_b^3 \rho g \tag{C.14}$$

APPENDIX D

Improvement of the computer code

The computer code used in the calculation of 2–D flow is the "General Purpose Computer Program for Elliptic Situations" developed by Patankar [1980]. The improvement described here is related to the problem of numerical diffusion, called also a false diffusion.

In the field of computational fluid mechanics, false diffusion is a major obstacle to the achievement of accurate and economical solutions to the governing equations [Pollard and Siu, 1982]. False diffusion arises when practitioners of computational fluid mechanics replaced the central–differencing scheme (a scheme that achieves stable, non–false diffusion affected results through the use of fine grid distributions, such that the grid Peclet number, the ratio of convection to diffusion across the grid, is less than 2) with one–sided differencing schemes which achieve stable solutions on coarse grids [Pollard and Siu, 1982]. The introduction of these schemes (commonly referred to as "upwind") afforded economical solutions but reduced the accuracy of the solutions because it introduced a truncation error. This error is commonly referred to as false or numerical diffusion. The phenomenon is discussed in more detail by Patankar [1980].

False diffusion exists only in multi–dimensional phenomena and arises because of the common practice of treating the flow across each control–cell face as locally one–dimensional. Unless the numerical mesh can be aligned fairly closely with the fluid pathlines, numerical diffusion imports increasingly important errors to the solution as the inter–nodal Peclet (or Reynolds) numbers are raised [Huang et al., 1985]. Therefore schemes that would give less false diffusion should take account of the local multi–dimensional nature of the flow. The true merit of the higher order schemes is that they approximate better the fluid property space variation, which is in reality non–linear; so they may be more accurate for relatively coarse grid [Patel et al., 1985]. There are two major "schemes": Profile Schemes which define the profile shape independent of the relative strengths of the advection, diffusion and the source terms and Physical Influence schemes which take into account specific conditions (ex. Skew Scheme by Raithby, 1976). Examples of the Profile scheme are QUICK (quadratic upstream–weighted interpolation) by Leonard [1979], with its different improvements [Pollard and Siu, 1982; Huang et al., 1985; Freitas, 1986] and the Spline Flux method by Varejao [1979].

The existing computer code uses power–law difference scheme (here and after referred to as PLDS) which is a very good approximation for a purely one–dimensional flux balance. Accordingly such a scheme performs well in flow regions in which the velocity vector aligns closely with mesh lines and in which convection is primarily balanced by streamwise diffusion rather than

cross–stream diffusion or sources [Huang et al., 1985]. In multi–dimensional flow, however, the coupling between transport processes in different directions is usually strong and such a scheme does not perform well and can produce serious numerical error. This has been acknowledged by various authors, Varejao [1979], Patankar [1980], Huang et al. [1985], Patel and Markatos [1986]. Farrell [1986] showed a dominance of the numerical over physical diffusion in some cases in the study of plunging flow in stratified reservoirs. The same was found in this study during initial trial simulations of the mixing of stratified reservoirs with buoyant jets.

A diffusion–advection scheme with a higher accuracy has been implemented in the existing computer code. The QUICK scheme has been used here after a study of the literature. The QUICK scheme although being popular due to its efficiency and relative simplicity in coding is not "problem free". Since it is a profile scheme, negative values of the coefficients can occur in the algebraic equation (Eq. D1) which defines a relationship between unknowns in one control volume. The result of this are nonphysical "wiggles". Sometimes extra terms are added to the equation to dampen out such "wiggles", but this is somewhat ad hoc. A different approach is the so–called blending which consists of adding carefully weighted contributions of some diffusive scheme [Zhu and Leschziner, 1988]. McGuirk and Sadrul Salim [1987] used an even simpler approach. They controlled the value of the variable by its physically possible maximum and minimum to prevent under– and over–shoots.

As the reason of the unphysical behavior of the solution lies in the fact that coefficients in the governing equation can have a negative value, Pollard and Siu [1982] and Freitas [1986] rewrote the equations for the coefficients in a such a manner that they are always positive. Freitas [1986] included his QUICK version in the REBUFFS code by J. A. C. Humphrey at the University of California, Berkeley. Implementation of it in Patankar's [1980] code is shown afterwards.

The another version of QUICK implemented in the existing code is the one used by Huang et al. [1986].

A general transport equation for the variable φ (Eq. 3.26) according to the notation given by Patankar [1980] can be written as

$$a_P \varphi_P = a_E \varphi_E + a_W \varphi_W + a_N \varphi_N + a_S \varphi_S + b \qquad (D.1)$$

where for Cartesian coordinates, and for Freitas' [1986] version

$$a_E = [u_e^+ \frac{1}{8} \frac{\delta x_e}{\Delta x_P} - u_e^- (\frac{1}{2} + \frac{1}{4} \frac{\delta x_e}{\delta x_{ee}})]F_e$$

$$+ [u_w^+ \cdot 0 + u_w^- (\frac{1}{4} \frac{\delta x_w}{\Delta x_p}(1 + \frac{1}{2} \frac{\delta x_w}{\delta x_e}) - \frac{1}{2} \frac{\delta x_w}{\delta x_e})]F_w + \frac{\Gamma_e^\varphi A_e^\varphi}{\delta x_e} \qquad (D.2)$$

$$a_W = [u_w^- \left(-\frac{1}{8}\right)\frac{\delta x_w}{\Delta x_P} + u_w^+ \left(\frac{1}{2} + \frac{1}{4}\frac{\delta x_w}{\delta x_{ww}}\right)]F_w$$

$$- [u_e^- \cdot 0 + u_e^+ \left(\frac{1}{4}\frac{\delta x_e}{\Delta x_P}\left(1 + \frac{1}{2}\frac{\delta x_e}{\delta x_w}\right) - \frac{1}{2}\frac{\delta x_e}{\delta x_w}\right)]F_e + \frac{\Gamma_w^\varphi A_w^\varphi}{\delta x_w} \qquad (D.3)$$

$$a_N = [u_n^+ \frac{1}{8}\frac{\delta y_n}{\Delta y_P} - u_n^- \left(\frac{1}{2} + \frac{1}{4}\frac{\delta y_n}{\delta y_{nn}}\right)]F_n$$

$$+ [u_s^+ \cdot 0 + u_s^- \left(\frac{1}{4}\frac{\delta y_s}{\Delta y_P}\left(1 + \frac{1}{2}\frac{\delta y_s}{\delta y_n}\right) - \frac{1}{2}\frac{\delta y_s}{\delta y_n}\right)]F_s + \frac{\Gamma_n^\varphi A_n^\varphi}{\delta y_n} \qquad (D.4)$$

$$a_S = [u_s^- \left(-\frac{1}{8}\right)\frac{\delta y_s}{\Delta y_P} + u_s^+ \left(\frac{1}{2} + \frac{1}{4}\frac{\delta y_s}{\delta y_{ss}}\right)]F_s$$

$$- [u_n^- \cdot 0 + u_n^+ \left(\frac{1}{4}\frac{\delta y_n}{\Delta y_P}\left(1 + \frac{1}{2}\frac{\delta y_n}{\delta y_s}\right) - \frac{1}{2}\frac{\delta y_n}{\delta y_s}\right)]F_n + \frac{\Gamma_s^\varphi A_s^\varphi}{\delta y_s} \qquad (D.5)$$

$$b = - [u_e^+ \frac{1}{2}\varphi_e + u_e^- \left(\frac{1}{4}\frac{\delta x_e}{\Delta x_E}\left(1 + \frac{1}{2}\frac{\delta x_e}{\delta x_{ee}}\right) - \frac{1}{2}\frac{\delta x_e}{\delta x_{ee}}\right)\varphi_{ee}]F_e$$

$$+ [u_w^- \frac{1}{2}\varphi_w + u_w^+ \left(\frac{1}{4}\frac{\delta x_w}{\Delta x_W}\left(1 + \frac{1}{2}\frac{\delta x_w}{\delta x_{ww}}\right) - \frac{1}{2}\frac{\delta x_w}{\delta x_{ww}}\right)\varphi_{ww}]F_w$$

$$- [u_n^+ \frac{1}{2}\varphi_n + u_n^- \left(\frac{1}{4}\frac{\delta y_n}{\Delta y_N}\left(1 + \frac{1}{2}\frac{\delta y_n}{\delta y_{nn}}\right) - \frac{1}{2}\frac{\delta y_n}{\delta y_{nn}}\right)\varphi_{nn}]F_n$$

$$+ [u_s^- \frac{1}{2}\varphi_s + u_s^+ \left(\frac{1}{4}\frac{\delta y_s}{\Delta y_S}\left(1 + \frac{1}{2}\frac{\delta y_s}{\delta y_{ss}}\right) - \frac{1}{2}\frac{\delta y_s}{\delta y_{ss}}\right)\varphi_{ss}]F_s$$

$$+ a_P^0 \varphi_P^0 + S_c \Delta x \Delta y \qquad (D.6)$$

$$a_P = [u_e^+ \frac{1}{4}\frac{\delta x_e}{\delta x_w} + u_e^- \left(-\frac{1}{8}\right)\frac{\delta x_e}{\Delta x_E}]F_e$$

$$+ [u_w^- \left(-\frac{1}{4}\right)\frac{\delta x_w}{\delta x_e} + u_w^+ \frac{1}{8}\frac{\delta x_w}{\Delta x_W}]F_w$$

$$+ [u_n^+ \frac{1}{4}\frac{\delta y_n}{\delta y_s} + u_n^- \left(-\frac{1}{8}\right)\frac{\delta y_n}{\Delta y_N}]F_n$$

$$+ [u_s^- \left(-\frac{1}{4}\right)\frac{\delta y_s}{\delta y_n} + u_s^+ \frac{1}{8}\frac{\delta y_s}{\Delta y_S}]F_s$$

$$+ \frac{\Gamma_e^\varphi A_e^\varphi}{\delta x_e} + \frac{\Gamma_w^\varphi A_w^\varphi}{\delta x_w} + \frac{\Gamma_n^\varphi A_n^\varphi}{\delta y_n} + \frac{\Gamma_s^\varphi A_s^\varphi}{\delta y_s} + a_P^0 - S_p \Delta x \Delta y \qquad (D.7)$$

and for the one derived by Huang et al.[1985]

$$a_E = [u_e^+ \frac{1}{8}\frac{\delta x_e}{\Delta x_P} - u_e^- \frac{1}{8}\frac{\delta x_e}{\Delta x_E}]F_e - \frac{1}{2}F_e + \frac{\Gamma_e^\varphi A_e^\varphi}{\delta x_e} \quad (D.8)$$

$$a_W = [u_w^- (-\frac{1}{8})\frac{\delta x_w}{\Delta x_P} + u_w^+ \frac{1}{8}\frac{\delta x_w}{\Delta x_W}]F_w + \frac{1}{2}F_w + \frac{\Gamma_w^\varphi A_w^\varphi}{\delta x_w} \quad (D.9)$$

$$a_N = [u_n^+ \frac{1}{8}\frac{\delta y_n}{\Delta y_P} - u_n^- \frac{1}{8}\frac{\delta y_n}{\Delta y_N}]F_n - \frac{1}{2}F_n + \frac{\Gamma_n^\varphi A_n^\varphi}{\delta y_n} \quad (D.10)$$

$$a_S = [u_s^- (-\frac{1}{8})\frac{\delta y_s}{\Delta y_P} + u_s^+ \frac{1}{8}\frac{\delta y_s}{\Delta y_S}]F_s + \frac{1}{2}F_s + \frac{\Gamma_s^\varphi A_s^\varphi}{\delta y_s} \quad (D.11)$$

$$\begin{aligned} b = &- [u_e^+ \frac{1}{8}\frac{\delta x_e^2}{\Delta x_P}\mathrm{GRAD}_w - u_e^- \frac{1}{8}\frac{\delta x_e^2}{\Delta x_E}\mathrm{GRAD}_{ee}]F_e \\ &+ [u_w^+ \frac{1}{8}\frac{\delta x_w^2}{\Delta x_W}\mathrm{GRAD}_{ww} - u_w^- \frac{1}{8}\frac{\delta x_w^2}{\Delta x_P}\mathrm{GRAD}_e]F_w \\ &- [u_n^+ \frac{1}{8}\frac{\delta y_n^2}{\Delta y_P}\mathrm{GRAD}_s - u_n^- \frac{1}{8}\frac{\delta y_n^2}{\Delta y_N}\mathrm{GRAD}_{nn}]F_n \\ &+ [u_s^+ \frac{1}{8}\frac{\delta y_s^2}{\Delta y_S}\mathrm{GRAD}_{ss} - u_s^- \frac{1}{8}\frac{\delta y_s^2}{\Delta y_P}\mathrm{GRAD}_n]F_s \\ &+ a_P^0 \varphi_P^0 + S_c \Delta x \Delta y \end{aligned} \quad (D.12)$$

$$a_P = a_E + a_W + a_N + a_S + a_P^0 - S_p \Delta x \Delta y \quad (D.13)$$

where:

$$u_i^+ = \frac{u_i + |u_i|}{2|u_i|} \; ; \; u_i^- = 1 - u_i^+ \; ; \; i = e,w,n,s \quad (D.14)$$

$$\mathrm{GRAD}_i = \frac{1}{x_{I+1} - x_I}(\varphi_{I+1} - \varphi_I) \; ; \quad i = e,w,n,s,ee,ww,nn,ss \quad (D.15)$$

$$I = P,E,W,N,S,EE,WW,NN,SS$$

ex. $$\mathrm{GRAD}_e = \frac{1}{x_E - x_P}(\varphi_E - \varphi_P)$$

It can be seen by the inspection of the equations that Freitas' version requires more computational work. Huang's version can be coded more efficiently maintaining previously done vectorization of the code and therefore it has been used afterwards. Control of the unphysical "wiggles" is done by using the QUICK scheme just for the velocities and not for other variables.

Two examples are presented to compare the PLDS scheme with the QUICK scheme used afterwards.

Wall driven square cavity flow

The driven cavity has been examined by numerous authors and accurate numerical data are readily available for this case. Therefore it is used as a test case to verify the performance of the code. The solutions have been obtained here as a function of the Reynolds number $Re = U_w L/\nu$ for Re = 400 and Re = 1000. For Re = 400 a uniform grid is used having 12x12 and 22x22 grid lines. Results are compared with reference data in Figure D.1, obtained with 52x52 uniform grid by Burggraf [1966]. For the case with Re = 1000 and for nonuniform grid 42x42 grid lines were condensed uniformly from the center of cavity towards the walls at the geometric rate of 1.2. Results are compared with reference data reported by Schreiber and Keller [1983] for a 180x180 mesh.

Figure D.1 shows U velocity distribution along x/L = 0.5. A very good performance of the QUICK version used here can be observed. For a coarse uniform grid (12x12) and Re = 400 is even closer to the datum than the fine grid solution with original PLDS approximation.

Convective transport of a scalar

Although it is a simple problem, convective transport of a scalar step represents a severe test because of the steepness of the φ gradient. A scalar φ is convected by the velocity inclined to the uniform mesh, as shown in Figure D.2.

Comparisons between PLDS and QUICK were done for two velocity inclinations, with uniform 12x12 mesh. The case a = 0 corresponds to an angle of 45°, a = 2 has an angle of 30°. QUICK is clearly superior to PLDS though QUICK produces slight under– and over–shoots. These anomalies are due to one of the coefficients in the finite difference equation becoming negative. In the later work these unphysical "wiggles" were controlled as described previously, and then under– and over–shoots did not occur.

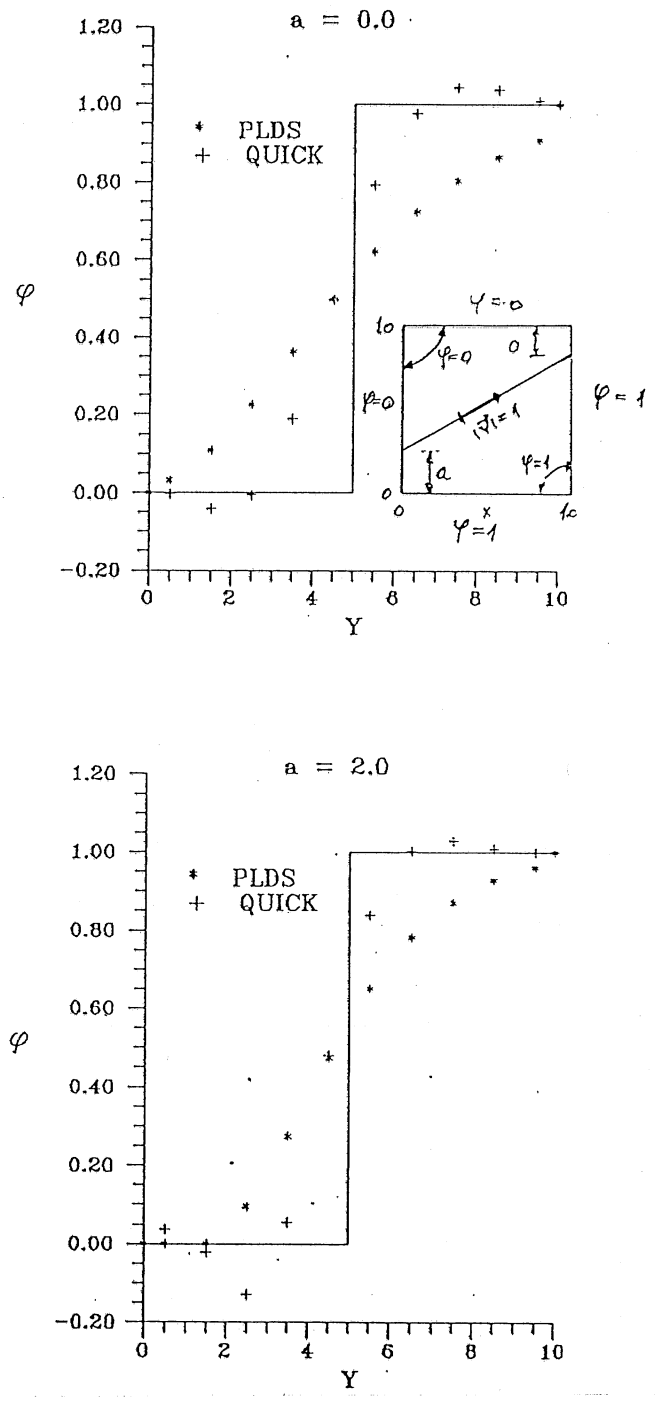

Figure D.1 Comparison of the performance of PLDS and QUICK for convective transport of a scalar.

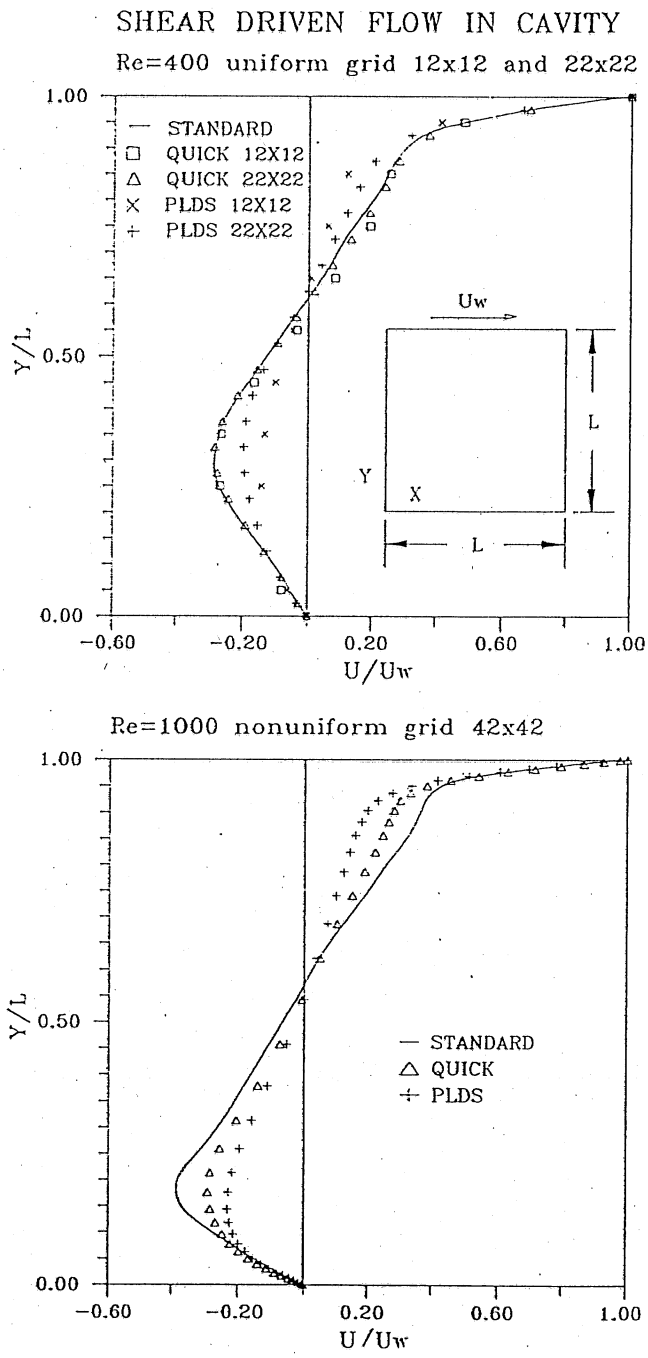

Figure D.2 Comparison of the performance of PLDS and QUICK for shear driven flow in a cavity